

# Analysis of High Latitude ULF Waves and HF Radar Performance for African Equatorial Latitude SuperDARN



UNIVERSITY OF  
**LEICESTER**

Chizurumoke Michael Michael

Radio and Space Plasma Physics Group

Department of Physics and Astronomy

University of Leicester

A thesis submitted for the degree of

*Doctor of Philosophy*

November 2020

# Abstract

Analysis of High Latitude ULF Waves and  
HF Radar Performance for African Equatorial Latitude SuperDARN

Chizurumoke Michael Michael

This thesis studies the phase evolution in ultra low frequency (ULF) waves driven by substorm-injected energetic particles drifting azimuthally around the Earth using measurements from a Super Dual Auroral Radar Network (SuperDARN) radar at high latitude. The characterisation of a case-study Pc5 ULF wave event observed by the Hankasalmi SuperDARN radar suggests an equatorward latitudinal and eastward longitudinal phase propagation with an effective azimuthal wave number of  $17 \pm 1$ , in the intermediate range of those observed in ULF waves. This wave, also detected in nearby magnetometer datasets, has been interpreted as resulting from drifting electrons of energies of  $35 \pm 5$  keV in a drift resonance condition linked to particle populations from a magnetospheric substorm. The latitudinal phase characteristics of this wave experienced temporal evolution. Statistical analysis of 18 similar ULF wave events also linked to substorm-injected particles suggested that the phase evolution in the case-study is caused by additional injected particle populations associated with the same substorm driving the wave. This resulted in an observed backscatter "bite-out". This analysis enhances our current understanding of this species of ULF waves.

The thesis also presents the predicted performance of such SuperDARN radars at African equatorial latitudes where they do not currently exist. A high frequency ray tracing simulation using realistic

ionospheres and magnetic field geometries indicates that the east-west azimuth ( $\sim 25^\circ$  range) has a significant likelihood of achieving SuperDARN-type backscatter in this sector. This is mainly due to the magnetic field geometry, as these azimuths allow the HF waves to propagate orthogonal to the geomagnetic field in the ionospheric region where irregularities are expected. These results are central to the planning of a SuperDARN-style radar for studying the equatorial ionosphere, for instance, in determining the radar characteristics such as operating frequencies, antenna boresight and azimuth coverage.

## Declaration

The following paper has been published based on the studies for this thesis:

Michael, C. M., Yeoman, T. K., Wright, D. M., Milan, S. E., and James, M. K. (2020). A ray tracing simulation of HF ionospheric radar performance at African equatorial latitudes. *Radio Science*, 55, e2019RS006936, <https://doi.org/10.1029/2019RS006936>.

## **Dedication**

In memory of my father Kenechukwu Kenneth Iloerunachi

## Acknowledgements

My heartfelt gratitude goes to my supervisor Professor T. K. Yeoman. Thank you Tim for your patience with me, your tutelage and tremendous support during this study. Your reassuring approach helped me to navigate the various challenges that I encountered during this programme. Thank you immensely. I would also like to thank my second supervisor Dr Darren Wright for his constructive ideas, support and encouragement.

I would like to thank everyone in the Radio and Space Plasma Physics group at the University of Leicester. Special thanks to Professor Steve Milan, who was always ready to help, for explaining those weird plasma dynamics and the tips on IDL. Not leaving out my office mates, past and present, Rosie, Sam W, Arrate, Harneet, Angeline, Sam T, Tom B, Mellisa and Lauren. It has been a pleasure to share the 1 by 4 room with everyone of you. Thanks to Adam, Rogers and Nahid for organising the football games at various times; those games were always a needed escape. I would also like to mention Anne, Matt, Hamed, Timothy, Padraig, Alexandra and Mick Parsons who have each been helpful to me during this period.

I would like to express my gratitude to the Nigerian Tertiary Education Trust Fund (TETFund) for funding my PhD programme through the Federal University Otuoke (FUO). Special thanks is reserved for the Management of FUO for nominating me for the scholarship.

Profound gratitude to my family especially my mother Ginikanwa Lydia Iloerunachi, Chinaecherem Ken, Ada Esther, Mmeri Deborah, my uncle Echezona Iloerunachi and Chibuzo Ndufuechi for their support and encouragement throughout my study.

Finally, my friends have been of immense support to me. I will not fail to thank Dr Doubra Egbe who had to listen to my rehearsal talks on this research even when they are uninteresting; and for the laughter that helped to ease the stress of PhD journey. I am particularly thankful to my friend Ngozi Marion for her encouragement during the period of writing this thesis and for providing me with some useful distractions. Many thanks to Elizabeth, Jonathan, Larry, Johnson, Abiola G, Tobi, Lesley, Sanita, Vivian U and Carmel for their encouragements. This thesis is a product of so much goodwill, and for this, I'm grateful. To God be the glory.

May 2020

# Contents

<b>List of Figures</b>	<b>xii</b>
<b>List of Tables</b>	<b>xxiv</b>
<b>1 Introduction</b>	<b>1</b>
1.1 Single Particle Motion in an EM Field . . . . .	2
1.1.1 Gyromotion . . . . .	3
1.1.2 Bounce motion . . . . .	5
1.1.3 Drift Motion . . . . .	9
1.1.3.1 Gradient and Curvature Drift . . . . .	10
1.2 Magnetohydrodynamics . . . . .	13
1.2.1 Maxwell's Equations . . . . .	14
1.2.2 Alfvén's Theorem . . . . .	15
1.3 The Solar wind . . . . .	17
1.4 Earth's Magnetosphere . . . . .	18
1.5 Geomagnetic Activity . . . . .	23
1.5.1 Substorms . . . . .	23
1.5.1.1 Detecting Substorms using Ground Magnetome- ter Data . . . . .	26
1.5.2 Geomagnetic Storms . . . . .	28
1.6 Magnetospheric MHD Waves . . . . .	29
1.6.1 Alfvén waves and Field Line Resonance . . . . .	31
1.6.2 ULF Waves . . . . .	33
1.6.2.1 Classifications of ULF Waves . . . . .	33
1.6.2.2 ULF Wave Sources . . . . .	34

1.7	Earth's Ionosphere . . . . .	35
1.7.1	Ionospheric Modification of ULF Waves . . . . .	37
1.7.2	Ionospheric Irregularities . . . . .	39
1.8	Radio Frequency Ray Tracing . . . . .	39
<b>2</b>	<b>Literature Review</b>	<b>44</b>
2.1	Magnetospheric ULF Waves . . . . .	44
2.2	Low- $m$ ULF Waves and Field Line Resonance . . . . .	45
2.3	High- $m$ ULF waves . . . . .	46
2.3.1	Ground-Based Observations . . . . .	48
2.3.2	Quiet Time Observations . . . . .	48
2.4	Intermediate- $m$ ULF waves . . . . .	51
2.5	Substorm-injected Particles Driven ULF Waves . . . . .	52
2.6	Previous Studies Related to HF Ionospheric Ray Tracing . . . . .	55
2.7	HF Radar Experiments at Equatorial African Longitudes . . . . .	58
<b>3</b>	<b>Instrumentation and Analysis Techniques</b>	<b>60</b>
3.1	HF Ionospheric Radar . . . . .	60
3.1.1	SuperDARN . . . . .	62
3.1.1.1	Multiple Pulse Sequence in SuperDARN . . . . .	65
3.1.2	SuperDARN Antennas . . . . .	71
3.1.3	Ionospheric Radar Backscatter . . . . .	73
3.1.4	Time-Series Analysis of ULF Waves in SuperDARN measurement . . . . .	75
3.2	Ground Magnetometers . . . . .	77
3.2.1	IMAGE . . . . .	78
3.3	Ray Tracing Model . . . . .	78
3.4	International Reference Ionosphere . . . . .	80
3.5	IGRF . . . . .	81
<b>4</b>	<b>Phase Evolution of Intermediate-<math>m</math> ULF Waves Driven by Substorm-injected Particles: a case study</b>	<b>82</b>
4.1	Introduction . . . . .	82
4.2	Data . . . . .	83

4.3	ULF Wave Event on May 13th 2016 . . . . .	86
4.3.1	Interval 1 (00:00 – 01:30 UT) Radar Observation . . . . .	95
4.3.2	Interval 2 (01.30 – 03:00 UT) Radar Observation . . . . .	97
4.4	Magnetometer Observations . . . . .	99
4.4.1	Substorm Occurrence . . . . .	99
4.4.2	Magnetometer Observation of the Pc5 ULF wave . . . . .	102
4.4.3	Magnetometer Observation of a Pc4 ULF Wave . . . . .	105
4.5	Discussion . . . . .	108
4.5.1	Driving Particles and Wave Energy . . . . .	109
4.5.2	Possible Phase Evolution . . . . .	113
4.5.3	Eastward Drifting Bite-out . . . . .	115
4.5.4	Ground Magnetometer Wave Signatures . . . . .	116
4.5.4.1	The Pc5 Wave . . . . .	116
4.5.4.2	The Pc4 Wave . . . . .	117
4.6	Summary . . . . .	119
<b>5</b>	<b>A Statistical Study of Intermediate-<i>m</i> ULF Waves Driven by Substorms</b>	<b>121</b>
5.1	Introduction . . . . .	121
5.2	Data . . . . .	122
5.2.1	Example Wave Event . . . . .	123
5.3	Substorm Observations . . . . .	125
5.4	Statistical Observations . . . . .	128
5.4.1	Wave Periods . . . . .	128
5.4.2	Wave Phase Propagation . . . . .	129
5.4.3	Driving Particle Energies . . . . .	130
5.5	Discussion . . . . .	132
5.6	Summary . . . . .	134
<b>6</b>	<b>A Ray Tracing Simulation of HF Ionospheric Radar Performance at African Equatorial Latitudes</b>	<b>135</b>
6.1	Introduction . . . . .	135
6.2	Methods . . . . .	138

## CONTENTS

---

6.2.1	Ionospheric Models . . . . .	139
6.2.2	Description of Methods . . . . .	141
6.3	Raytracing . . . . .	147
6.3.1	Ground Scatter Evaluation . . . . .	153
6.4	Geographic distribution of orthogonality . . . . .	155
6.4.1	Low Elevation Angle Operations . . . . .	156
6.4.2	Near-vertical Operations . . . . .	160
6.5	Propagation Analysis . . . . .	162
6.5.1	Orthogonality as a Function of Elevation Angle . . . . .	162
6.5.2	Elevation Angle vs Ground Range . . . . .	169
6.5.3	Orthogonality as a Function of Altitude . . . . .	171
6.6	Discussion . . . . .	174
6.7	Summary . . . . .	178
<b>7</b>	<b>Recommendations on Antenna Patterns and Array Design</b>	<b>180</b>
7.1	Introduction . . . . .	180
7.2	Elevation Radiation Pattern . . . . .	182
7.2.1	Antenna Height . . . . .	182
7.2.2	Antenna Separation . . . . .	184
7.3	Azimuthal Radiation Pattern . . . . .	184
7.4	Summary . . . . .	189
<b>8</b>	<b>Conclusions and Future Work</b>	<b>191</b>
8.1	Intermediate- $m$ ULF Wave Observations . . . . .	191
8.2	Ray Tracing Analysis of SuperDARN-style Radar Performance at African Equatorial Latitudes and Applications . . . . .	194
	<b>References</b>	<b>196</b>

# List of Figures

1.1	Schematic illustration of the trajectory of a particle with non-zero $v_{\parallel}$ . . . . .	5
1.2	Diagram illustrating a $q > 0$ particle moving into a region of converging magnetic field with increasing field strength. The small arrows show direction of the Lorentz force on the particle as it gyrates along the $z$ -axis (Figure courtesy of Steve E. Milan). . . . .	6
1.3	Diagram showing positive and negative charges experience $\mathbf{E} \times \mathbf{B}$ drift (Figure courtesy of Steve E. Milan). . . . .	10
1.4	Diagram showing ion and electron drifting due to a gradient in magnetic field strength perpendicular to the magnetic field direction, resulting in a $\mathbf{j}$ due to their opposite direction of drift (after, Baumjohann & Treumann, 1997). . . . .	11
1.5	Schematic illustrations of the three major configurations of a single particle motion due to the morphology of the magnetic field. Taken from Kivelson & Russell (1995). . . . .	12
1.6	An illustration that magnetic field is modified as it is transported with the plasma in the frozen-in flux approximation. (Figure courtesy of Steve E. Milan) . . . . .	17
1.7	A diagram depicting magnetic cavity formation from the Earth's magnetic field as the solar wind streams towards the Earth. Figure taken from (Chapman & Bartels, 1940). . . . .	19
1.8	Illustration of different regions of the Earth's magnetosphere. Taken from (Frey, 2007). . . . .	20

## LIST OF FIGURES

---

1.9	Illustration of reconnection at the magnetopause for northward and southward IMF orientation from a sunward view. The dashed lines represent external magnetosheath while the solid lines represent internal magnetospheric field lines. Reconnection occurs at high latitude, poleward of the cusp in northward IMF orientation as seen in the left while at low latitude during southward IMF shown in the middle and a tilted neutral line from the component reconnection model in the right. Taken from (Frey, 2007). . . . .	22
1.10	Schematic diagrams illustrating the near-earth neutral-line (NENL) substorm model based on Figures 13.21, 13.22 and 13.23 of Kivelson & Russell (1995). Taken from James (2015). . . . .	25
1.11	Illustration of a substorm current wedge in the top panel and the likely variation of magnetic bays in the North and East components of the geomagnetic field close to the substorm current wedge in the bottom panel. From Clauer & McPherron (1974). . . . .	27
1.12	Illustration of MHD wave modes in a cold plasma approximation. Taken from Kivelson & Russell (1995) . . . . .	30
1.13	Illustrations of fundamental and second harmonic frequency resonances of a field line in closed dipolar geomagnetic field. The top parts show field line displacements due to Alfvén wave while the lower diagrams illustrate the variation in electric field $\mathbf{E}$ and magnetic perturbation $\mathbf{b}$ along the geomagnetic field lines across the conjugate points in the northern and southern ionospheres (Hughes, 1983). . . . .	32
1.14	Illustration of a typical ionospheric mid-latitude electron density profile for day and night time. Taken from (Rishbeth, 1988). . . .	36
1.15	Schematic illustration of the ionospheric rotation (after, Hughes & Southwood, 1976). . . . .	38

## LIST OF FIGURES

---

2.1	This figure, taken from Mager <i>et al.</i> (2019), shows the state of the solar wind and magnetosphere for 16–24 UT on 22 November 2014 during the interval in which they reported an intermediate- $m$ wave observed simultaneously from a radar and spacecraft. Where (a) and (b) represent the density ( $n_{sw}$ ) and velocity ( $V_{sw}$ ) of the solar wind; (c) the $B_z$ component of the interplanetary magnetic field (IMF $B_z$ ); (d) ASY-H and SYM-H geomagnetic indices (1 min high-resolution global storm indexes); (e) AU and AL auroral indices; (f) horizontal component of the magnetic field BH according to AMD geomagnetic station (Mager <i>et al.</i> , 2019, and therein). The gray stripes denote the interval of the reported wave event and the arrow denotes the substorm onset. . . . .	52
2.2	This figure, taken from James <i>et al.</i> (2013), shows that a clear majority of substorm-injected particles driven waves propagate equatorward as indicated by a plot of latitudinal phase gradient for the waves against the magnetic latitude separation of the waves from the substorm onset positions. . . . .	53
2.3	Variation of (a) Azimuthal wave numbers, $m$ of ULF waves versus the distance from substorm onset position for comparison with (b) $m$ relative to the substorm location when the substorms have expanded to their largest size. Where green data points denote events in which the substorms have expanded in the westward direction while orange data points denote eastward expansion. They ( a and b) also show the eastward expanding (red) and westward expanding (blue) wave events placed into $15^\circ$ bins shown by square symbols. Likewise, (c) and (d) show latitudinal phase gradient, $l$ , against latitudinal separation of substorm UV aurora and observed wave in green at the substorm onset time (c) and after expansion (d). The red square points in (c) and (d) represent the green data points for $2.5^\circ$ bins. From James <i>et al.</i> (2013) . . . . .	54
2.4	RTI plot from a broad-beam HF zenithal radar at Korhogo in Côte d’Ivoire, an African equatorial location. Note that the axes labels have been re-created after the original. From Farges <i>et al.</i> (1999) .	59

## LIST OF FIGURES

---

3.1	Fields of view of the SuperDARN radars as of 24 June 2018 in the (a) Northern and (b) Southern Hemispheres. Created from the VT-SuperDARN Radar FOVS tool . . . . .	63
3.2	A diagram showing the seven-pulse sequence transmitted by the SuperDARN radars for normal operation mode (from McWilliams, 2001). . . . .	66
3.3	Simplified illustration of how a typical radar transmits pulse and receives echo (adapted from Bryson <i>et al.</i> , 2007). . . . .	67
3.4	A schematic diagram of a two-pulse transmission sequence (adapted from McWilliams, 2001). . . . .	68
3.5	The top panel (a) shows a plot of a complex autocorrelation function (ACF) measurement from Pykkvibær SuperDARN radar (see Table 3.1), while the middle panel (b) shows the phase (crosses) and fitted phase (solid line) of the ACF which aliases at $\pm\pi$ . The bottom panel (c) shows the Doppler spectrum obtained from a Fast Fourier Transform (FFT) of the ACF from which the three main parameters of SuperDARN radars (backscattered power, velocity and spectral width) are derived. Taken from McWilliams (2001). . . . .	70
3.6	A schematic diagram describing the radar backscatter from field-aligned plasma irregularities for a monostatic system following Schlegel (1996). $k_i$ and $k_s$ denote the incident and scattered radar wave-vector, $\delta = 90 \pm \alpha$ , where $\alpha$ is the aspect angle and the $\lambda_{irr}$ represent the scale size of the irregularities. . . . .	74
3.7	A schematic illustration of possible propagation modes and regions from where ionospheric backscatter (and other backscatter sources such as the ground) are received. From Milan <i>et al.</i> (1997a) . . . . .	75
3.8	Map of IMAGE magnetometer stations in geographic coordinates. (Taken from IMAGE, 2019c) . . . . .	79

## LIST OF FIGURES

---

4.1	Field-of-view and data coverage from Channel A of the SuperDARN radar at Hankasalmi, Finland during the wave activity interval, onset at 01:00 UT in magnetic latitude-magnetic local time coordinates. The outline inside the FOV indicates the beam that Channel B is restricted to. The radial dashed lines are separated by 1 h local time, with local midnight being marked by the vertical dashed line. The positions of the IMAGE magnetometer stations used are highlighted. The ionospheric velocities are colour-coded such that red (negative) and blue (positive) represent velocities away from the radar and towards the radar respectively. . . . .	84
4.2	Hankasalmi beam 9 SuperDARN radar velocity measurements as a function of magnetic latitude. The ionospheric velocities are colour-coded such that red (negative) and blue (positive) represent velocities away from the radar and towards the radar respectively.	87
4.3	Hankasalmi beams 3 - 9 SuperDARN radar velocity measurements as a function of Radar range gate. The ionospheric velocities are colour-coded such that red (negative) and blue (positive) represent velocities away from the radar and towards the radar respectively, while the black lines indicate drifting bite-out features. . . . .	88
4.4	Similar to Figure 4.1 except that here shows wave activity onset at 00:50 UT before (left panel), 01:50 UT during (middle panel), and 02:50 UT after (right panel) the appearance of the bite-out. The vertical outlines inside the FOV indicates beams 5 and 9 while curved black outline in middle panel describes the spatial extent of bite-out. . . . .	89
4.5	(a) SuperDARN radar velocity measurement from Hankasalmi beam 9 for the current ULF wave event. Red (negative) indicate ionospheric velocities away from the radar and blue (positive) for velocities towards the radar. (b) Velocity data availability. Colour code shows percentage data occupancy in each cell over the 3-hour wave activity interval. . . . .	90
4.6	Fourier power spectrum of beam 6 range gate 27 showing two clear dominant frequencies. . . . .	91

## LIST OF FIGURES

---

4.7	Fourier (a) amplitude and (b) phase at 0.75 mHz peak frequency of the ULF wave derived from the ionospheric drift velocity measurement for all the cells with 50% and above data availability over the 3-hour (00:00-03:00 UT) interval across all the beams as a function of geomagnetic latitude and longitude. The black outline indicates beam 9. . . . .	92
4.8	Fourier (a) amplitude and (b) phase at 0.75 mHz peak frequency of the ULF wave derived from the ionospheric drift velocity measurement along beam 9, and Fourier (c) amplitude and (d) phase across beams 5-11 of the Hankasalmi SuperDARN radar at $\sim 70^\circ$ latitude as a function of geomagnetic longitude. The dotted line in (d) is a linear fit to the longitudinal phase variation. . . . .	93
4.9	Fourier phase at 0.75 mHz peak frequency of the ULF wave derived from the ionospheric drift velocity measurement as a function of Magnetic Local Time (MLT). The figure is presented in magnetic latitude-magnetic local time coordinates. The bold outline inside indicates the radar FOV. The radial dashed lines are separated by 1 h local time, with local midnight being marked by the vertical dashed line, while the black arrowheads show azimuthal direction of wave propagation. . . . .	94
4.10	Interval 1 Fourier (a) amplitude and (b) phase as a function of geomagnetic latitude and longitude across beams with clear wave activity that meet the 50 percent data occupancy. The black outline in (b) indicates beam 9. . . . .	95
4.11	Interval 1 - Fourier (a) amplitude and (b) phase at 0.75 mHz frequency of the ULF wave derived from the ionospheric drift velocity measurement along beam 9, and Fourier (c) amplitude and (d) phase across beams 5-11 of the Hankasalmi SuperDARN radar at $\sim 70^\circ$ latitude as a function of geomagnetic longitude. The dotted line in (d) is a linear fit to the longitudinal phase variation. . . . .	96
4.12	Similar to Figure 4.10, but for Interval 2 (01:30-03:00 UT) with peak frequency 0.74 mHz. . . . .	97
4.13	Similar to Figure 4.11 but for Interval 2 (01:30 - 03:00 UT) analysis. . . . .	98

4.14	Unfiltered IMAGE X-component magnetometer data during the substorm interval. The IMAGE stations covering decreasing latitudes from top to bottom panels. The last panel shows HAN station data bandpass filtered between 20-200 s to highlight Pi2 pulsation activity. The light green outlines indicate onset of substorm expansion phase and subsequent bursts. . . . .	100
4.15	Magnetic field bay of mid-latitude IMAGE (a) X-component and (b) Y-components during the substorm. The data is the same as in previous Figure 4.14 and subsequent Figure 4.16 but for selected two mid-latitude stations between 18:00 and 23:59 UT interval on 12th May 2016. The top and middle panels are unfiltered X- and Y-components from the OIJ and HAN stations of the IMAGE array, while the bottom panels are HAN station but with a 200-20 s band-pass filter applied to illustrated the Pi2 pulsation activity (onset times marked with light green solid lines) associated with the substorm expansion phase onset at about 20:10 UT. . . . .	102
4.16	Similar to Figure 4.14 but for Y-component (east-west component at the earth’s surface) and interval of 23:00 UT 12th to 03:30 UT 13th, May 2016. The last panel shows HAN station data bandpass filtered between 20-200 s to highlight Pi2 pulsation activity indicated by the light-green outline. The light-blue and yellow highlight a long period wave activity and a short period wave respectively. . . . .	103
4.17	IMAGE Y-component magnetometer data between the intervals 02:00 UT – 03:00 UT on May 13th, 2016. The IMAGE stations covering decreasing latitudes from top to bottom panels. The data is bandpass-filtered between 20-150 s to highlight a Pc4 pulsation activity observed in the magnetometer data. . . . .	104
4.18	Similar to Figure 4.19 but for the Pc4 ULF wave observation at 8.3 mHz peak Fourier spectra in the IMAGE Y-component magnetometer data between the interval 02:00–03:00 UT on May 13th, 2016. . . . .	106

## LIST OF FIGURES

---

4.19	Latitudinal variation of (a) amplitude and (b) phase and equivalent longitudinal (c) amplitude and (d) phase profiles for the Pc5 ULF wave observation at 0.77 mHz peak Fourier spectra in the IMAGE Y-component magnetometer data between the interval 00:00–03:00 UT on May 13th, 2016. . . . .	107
4.20	A graphical representation of the drift resonance condition for the Pc5 ULF wave event. . . . .	112
4.21	A graphical representation of the drift-bounce resonance condition for the Pc4 ULF wave event. The side labelled A represents wave particle energy driven through a drift-bounce resonance interaction while B represents wave driven through a drift resonance. . . . .	118
5.1	Hankasalmi beam 8 SuperDARN radar velocity measurements as a function of magnetic latitude. The ionospheric velocities are colour-coded such that red (negative) and blue (positive) represent velocities away from the radar and towards the radar respectively. . . . .	124
5.2	Fourier (a) power and (b) phase at dominant 0.83 mHz frequency of the wave event shown in Figure 5.1 across beams 4 to 10 as a function of geomagnetic latitude and longitude. The black outlines indicate beam 8. . . . .	125
5.3	Similar to Figure 5.2 except that it is the one dimensional version of Fourier (a) power, (b) phase along beam 8 and Fourier (c) power and (d) phase across beams 5-10 at $\sim 71^\circ$ latitude as a function of geomagnetic longitude. . . . .	126
5.4	Unfiltered IMAGE X-component magnetometer data over the time interval of the wave event in Figure 5.1. The IMAGE stations are the same as those used in Chapter 4 (See Table 4.1). The last panel shows HAN station data bandpass filtered between 20-200 s to highlight Pi2 pulsation activity. The light green outline indicates substorm activity. . . . .	127
5.5	Histogram showing the periods of the waves studied placed into 500 s bins. . . . .	128

## LIST OF FIGURES

---

5.6	Wave periods as a function of azimuthal wave number of each of the waves. Waves with poleward phase propagation are shown by asterisk symbols while those with with equatorward phase propagation are shown by black-shaded circle symbols. . . . .	130
5.7	Wave periods as a function of calculated particle energies for each of the waves. Waves with poleward phase propagation are shown by asterisk symbols while those with equatorward phase propagation are shown by circle symbols. The red and blue symbols indicate waves driven by a resonance with electrons and protons respectively. . . . .	131
6.1	Variation of foF2 from IRI data at the three proposed locations. The $x$ -axis indicates the three proposed location at different solar minimum and maximum intervals . . . . .	140
6.2	Map showing the Earth’s magnetic (a) inclination (I), and (b) declination (D) over the locations and field-of-views (FOVs) of the simulated radars. Each side of the FOV range 3000 km from the radar location. The Earth’s magnetic field is derived from IGRF model (Thébault <i>et al.</i> , 2015). . . . .	142
6.3	Schematic diagram illustrating ray propagation path traversing the ionosphere. The solid curve is a realistic path and the dashed line is the line-of-sight path, $h$ and $h_v$ represent the physical and virtual altitudes respectively. The angle between HF wave vector $\mathbf{k}$ and vector of geomagnetic field $\mathbf{B}$ is $\Omega$ , such that the orthogonality angle, $\alpha = \text{mod}(90^\circ - \Omega)$ , while $\delta$ is the elevation angle, $r$ is the slant range along the propagation path, $R_E$ is the radius of the Earth and $\mathbf{B}$ is the geomagnetic field ( <i>After: de Larquier et al.</i> , 2013). . . . .	144

6.4	Ray tracing for simulated HF radars at Bo Njala location from an azimuth of $90^\circ$ measured from North geographic coordinate at 8 MHz frequency and with elevation angle rays from $0^\circ$ to $90^\circ$ . The colour codes represent perpendicularity $\leq 10^\circ$ between wave vector and the geomagnetic field. Plot derived using the ionospheric profiles A, D and C parameters as shown in the top, middle and bottom panels respectively. . . . .	146
6.5	Ray tracing for simulated HF radars at Bo Njala (a), Port Harcourt (b) and Bahir Dar (c) locations, from an azimuth of $90^\circ$ measured from North geographic coordinate at 12 MHz frequency and with elevation angle rays from $0^\circ$ to $90^\circ$ . The colour codes represent perpendicularity $\leq 10^\circ$ between wave vector and the geomagnetic field. Plot derived using the ionospheric profile C parameters. . . . .	148
6.6	Same as Figure 6.5 except that it is for Bo Njala location only and the ionospheric profiles A, F and H parameters are used as shown in the top, middle and bottom panels respectively. . . . .	151
6.7	Same as Figure 6.5 except that it is for Bo Njala location only and the transmitted frequencies are 12, 16, 20 and 24 MHz as shown in first, second, third and fourth rows from top respectively. . . . .	152
6.8	Ground scatter evaluation as a function of ground range and elevation angle for transmit frequency of 12 MHz (top panel) and 16 MHz (bottom panel) using the ionospheric Profile C (at noon with medium foF2) for the Bo Njala simulated radar. . . . .	154
6.9	Spatial distribution of regions with perpendicularity, $\alpha$ (colour-coded) between radar wave vector and the Earth's magnetic field within $10^\circ$ . Plots derived from the ionospheric profile A (00 LT solar min) parameters, looking through $1 - 360^\circ$ azimuths for transmit frequencies of 12 MHz (first column), 16 MHz (second column), 20 MHz (third column) and 24 MHz (fourth column). Rays propagate from the elevation angles of $1^\circ$ to $90^\circ$ . The rows a, b and c represent Bo Njala, Port Harcourt and Bahir Dar locations respectively. . . . .	157

6.10	Same as Figure 6.9, but using ionospheric profile C (12 LT solar min) parameters. . . . .	159
6.11	Spatial distribution of regions with perpendicularity (colour-coded) between radar wave vector and the Earth’s magnetic field within 10°. Plots derived from the ionospheric profile C (12 LT solar min) parameters for near vertical elevation angles (45° - 90°), looking through 1 – 360° azimuths for transmit frequency of 12 MHz. Panels a, b and c represent Bo Njala, Port Harcourt and Bahir Dar locations respectively. . . . .	161
6.12	Evaluation of orthogonality ( $\alpha \leq 1^\circ$ ) as a function of elevation angle for transmit frequencies 12 MHz (red), 16 MHz (blue), 20 MHz (black) and 24 MHz (green). Plots derived from the solar minimum ionospheric profiles A (column 1), B (column 2), C (column 3) and D (column 4) parameters, looking through designated east-west azimuths measured from North geographic coordinate, top panels (Bo Njala, 75 – 100° azimuth), middle panels (Port Harcourt, 80 – 105° azimuth) and bottom panels (Bahir Dar, 70 – 95° azimuth). . . . .	163
6.13	Same as Figure 6.12, but using solar maximum ionospheric profiles E (column 1), F (column 2), G (column 3) and H (column 4) parameters. . . . .	167
6.14	Evaluation of orthogonality ( $\alpha \leq 1^\circ$ ) as a function of ground range and elevation angles for transmit frequency 12 MHz (column 1), 16 MHz (column 2), 20 MHz (column 3) and 24 MHz (column 4). Plots derived from the ionospheric parameters of profiles A (top panels), C (middle panels) and G (bottom panels) for Bo Njala simulated radar looking through 75–100° eastward azimuths measured from North geographic coordinate. . . . .	170

6.15	Evaluation of orthogonality ( $\alpha \leq 1^\circ$ ) as a function of altitude range $\leq 500$ km for transmit frequencies 12 MHz (column 1), 16 MHz (column 2), 20 MHz (column 3) and 24 MHz (column 4). Plot derived from the parameters of ionospheric profiles A (top panels), C (middle panels) and G (bottom panels), for Bo Njala simulated radar looking through $75 - 100^\circ$ azimuths from North geographic coordinate and at different classifications of elevation angles ( $\delta$ ). Altitude bins are 5 km wide. . . . .	173
7.1	Elevation radiation pattern for a Rankin-type single type antenna using radar frequency of 12 MHz. (a) Antenna height for a normal height (black - 7.5 m, 12.5 m masts), reduced height (blue - 5 m, 10 m masts), reduced height with lower reflector (green), and reduced height tilted (red). The green dot indicates cursor elevation of $31^\circ$ . (b) Antenna separation for a normal separation (black - 12 m), reduced separation (blue - 8.3 m), compromise separation one (green - 9.6 m), and compromise separation two (red - 12 m). The green dot indicates cursor elevation of $49^\circ$ . . . . .	183
7.2	Azimuthal pattern for a Standard CUTLASS radar, beam 5 and azimuth $-8.1^\circ$ off boresite with (a) 12 MHz that has a width of $8^\circ$ and (b) 20 MHz that has a width of $4.8^\circ$ . . . . .	185
7.3	Azimuthal pattern for a Standard CUTLASS radar, beam 5 and azimuth $-8.1^\circ$ off boresite with (a) 12 MHz and 8.3 m separation resulting in a width of $14.6^\circ$ , (b) 12 MHz and 9.6 m separation giving $12.6^\circ$ width, (c) 20 MHz and 8.3 m separation giving $8.8^\circ$ width, and (d) 20 MHz and 9.6 m separation giving $7.6^\circ$ width. . . . .	186
7.4	Azimuthal pattern for (a) 12 MHz 16 beams with 15.24 m separation giving a width of $8^\circ$ , and (b) 16 MHz 8 beams with 9.6 m separation and a width of $10^\circ$ . . . . .	188
7.5	Same as Figure 7.4b except that here (a) has 16 MHz 24 antennas, 8 beams at $3.24^\circ$ , resulting in a width of $6.6^\circ$ and (b) 16 MHz 24 antennas, 12 beams at $2.08^\circ$ giving a width of $6.6^\circ$ . . . . .	189

# List of Tables

1.1	Classification of ULF waves following Jacobs <i>et al.</i> (1964). . . . .	34
3.1	The geographic co-ordinates to two decimal point accuracy, bore-site and host institution's country of the SuperDARN radars as of 24 June 2019 for the northern and southern hemisphere. *PI stands for principal investigator. Adapted from the VT-SuperDARN radar information table . . . . .	64
4.1	The geographic and geomagnetic location of the IMAGE magnetometer stations used in this study. CGM stands for Corrected Geomagnetic Coordinates. Taken from IMAGE (2019b) . . . . .	85
4.2	A summary of the characteristics of the Pc5 ULF wave observations and a previous ULF wave observations with equatorward phase propagation. . . . .	112
6.1	Simulated Radar Locations . . . . .	141
6.2	Characteristics of Ionospheric Density Profiles . . . . .	141

# Chapter 1

## Introduction

The analysis explored in this thesis provides information on the dynamical processes that form an important part of space weather studies and the instrumentation required for its investigation. For instance, magnetospheric ultra-low frequency (ULF) waves are a channel for energy and momentum transfer in the dynamic interactions and processes occurring in the Earth's magnetosphere, and between the magnetosphere and the interplanetary space plasma environment. Such waves are described by magnetohydrodynamic (MHD) theory. They can accelerate particles in the inner magnetosphere, which can result in the energisation and decay of the Earth's radiation belts. Such particle acceleration and energisation, in extreme space weather circumstances, can cause operational anomalies and damage on satellite systems and electrical power grids, thereby resulting in a huge economic loss (e.g., Rostoker, 1994; Odenwald, 2007; Lam *et al.*, 2012; Baker *et al.*, 2013; Lam, 2017; Lanzerotti, 2017). In-situ measurement from spacecraft, HF coherent radars and ground-based magnetometer observations can provide data to characterise the frequencies, powers, scale lengths and polarisations of these MHD waves (e.g., Wright *et al.*, 2001; Ponomarenko *et al.*, 2005; Rae *et al.*, 2005; Yeoman *et al.*, 2016). This thesis has investigated the evolution in phase propagation of the intermediate- $m$  ( $m$  number of  $\sim 10$ ) type of such ULF waves driven by substorm-injected particles, as observed in the ionosphere by a Super Dual Auroral Radar Network (SuperDARN) radar at Hankasalmi, Finland. The  $m$  number is the azimuthal wave number of the ULF wave. It is an im-

## 1.1 Single Particle Motion in an EM Field

---

portant factor for assessing the contribution of ULF wave-particle interactions to the dynamics inside the Earth's magnetosphere (Chisham & Mann, 1999; Murphy *et al.*, 2018). It also indicates the azimuthal scale size of a magnetospheric ULF wave. The azimuthal wave number  $m$  can be determined by calculating the phase difference between two-point observations of a ULF wave at the same latitude but which are separated in azimuth (Chisham & Mann, 1999; Yeoman *et al.*, 2012; Murphy *et al.*, 2018). Likewise, this thesis has applied high frequency (HF) ray tracing to predict the performance of SuperDARN-style radars operating at African equatorial latitudes for the planning of such radars in the region. In this first chapter, basic concepts of plasma physics, the terrestrial magnetosphere and ionospheric radio wave propagation are presented. Chapter 2 discusses previous literature related to the analysis performed for this thesis while Chapter 3 provides information on the instrumentation and data employed in the study. Chapter 4 presents results on the analysis of the phase evolution in a case-study intermediate- $m$  ULF wave event. Chapter 5 presents a statistical analysis examining the type of phase evolution observed in the case-study wave. Chapter 6 applies HF ray tracing to simulate the performance of SuperDARN-style radars at equatorial latitudes of the African longitude sector. Following the ray tracing results, Chapter 7 demonstrates the implications for antenna array design. Lastly, Chapter 8 provides the summary of work done and areas for future research.

The analysis presented in this thesis are of intrinsic scientific interest. They also have a significant economic impact due to their applications in, for example, global satellite and navigation systems, space hardware, and communications systems.

## 1.1 Single Particle Motion in an EM Field

The Earth's space environment is dominated by matter in plasma state. A plasma refers to a gas of charged particles that comprises equal numbers of free positive and negative charge carriers (Baumjohann & Treumann, 1997). The motion of such particles in an electromagnetic field can be described mathematically as,

$$m \frac{d\mathbf{v}}{dt} = q(\mathbf{E} + \mathbf{v} \times \mathbf{B}) \quad (1.1)$$

## 1.1 Single Particle Motion in an EM Field

---

where  $m$  is the mass of the particle,  $\frac{d\mathbf{v}}{dt}$  is the rate of change of the particle's velocity,  $\mathbf{v}$ ,  $q$  is the charge,  $\mathbf{E}$  is the electric field and  $\mathbf{B}$  is the magnetic field.

In equation 1.1, derived by combining Newton's second law of motion,  $\mathbf{F} = m\mathbf{a}$  with the Lorentz forces,  $\mathbf{F} = q(\mathbf{E} + \mathbf{v} \times \mathbf{B})$ ; other forces, such as the gravitational force, are not considered because they are small compared to the electromagnetic forces.

We consider charged particle motion in the presence of magnetic field. The systems being focused on here are ones where the mean free paths are large, and as such, are regarded as collisionless. Examples of such systems are the solar wind and the Earth's magnetosphere. To do this, we consider various configurations of electric field  $\mathbf{E}$  and magnetic field  $\mathbf{B}$ . Also we assume that the fields are in a steady state. This implies that they vary on timescales that are long compared to the period of the gyrating particles. The three fundamental motions of such a single charged particle in electric and magnetic fields, namely gyromotion, bounce motion and gradient curvature drift are discussed in this section.

### 1.1.1 Gyromotion

In this treatment we assume an absence of electric field (i.e.  $\mathbf{E} = 0$ ), and a steady magnetic field in the  $\hat{z}$  direction. This means that the field is not changing in space and time. To examine the motion of a charged particle under this circumstance we apply Equation 1.1. As shown by equation 1.1, the direction of magnetic field force is perpendicular to  $\mathbf{v}$  and  $\mathbf{B}$ . As such,  $\mathbf{v}$  and  $\mathbf{B}$  components can be expressed in the Cartesian coordinate as shown in equation 1.2.

$$\begin{aligned}\mathbf{v} &= v_x\hat{\mathbf{x}} + v_y\hat{\mathbf{y}} + v_z\hat{\mathbf{z}} \\ \mathbf{B} &= B\hat{\mathbf{z}} \\ \mathbf{E} &= 0\end{aligned}\tag{1.2}$$

Equation 1.1 can be described as 1.3 based on  $\mathbf{z}$ , which shows that the rate

## 1.1 Single Particle Motion in an EM Field

---

of change of  $v_z = 0$ .

$$\begin{aligned}
 (a) \quad & \frac{dv_x}{dt} = \frac{qB}{m}v_y \\
 (b) \quad & \frac{dv_y}{dt} = -\frac{qB}{m}v_x \\
 (c) \quad & \frac{dv_z}{dt} = 0
 \end{aligned} \tag{1.3}$$

Specifically differentiating Equation 1.3(a) and on substitution from 1.3(b) will produce 1.4,

$$\frac{d^2v_x}{dt^2} = -\left(\frac{qB}{m}\right)^2 v_x \tag{1.4}$$

which is an equation for simple harmonic motion (SHM) for  $v_x$  with an angular frequency,

$$\Omega = \frac{qB}{m} \tag{1.5}$$

where  $\Omega$  is sensitive to the sign of  $q$ . This implies that ions and electrons behave differently.

The solution of Equation 1.4 is

$$v_x = v_{\perp} \cos(\Omega t + \phi) \tag{1.6}$$

where  $\phi$  is the phase at time  $t = 0$  and  $v_{\perp}$  is the particle's speed, which is perpendicular to the magnetic field direction. Substituting Equation 1.6 into 1.3(a) gives

$$\begin{aligned}
 v_y &= \frac{1}{\Omega} \frac{dv_x}{dt} \\
 v_y &= -v_{\perp} \sin(\Omega t + \phi)
 \end{aligned} \tag{1.7}$$

Equations 1.2, 1.6 and 1.7 show that the charged particle rotates in a circular path with a perpendicular speed,  $v_{\perp}$  to magnetic field,  $\mathbf{B}$  and a parallel velocity  $v_{\parallel}$  along  $\mathbf{B}$ . Both  $v_{\perp} = \sqrt{v_x^2 + v_y^2}$  and  $v_{\parallel} = v_z$  are constant, producing a motion of a helix (see Figure 1.1) with an axis known as the guiding centre. The value of  $v_{\perp}$  is determined by the particle's energy. Such a particle rotates with an angular frequency as shown by Equation 1.5. This angular frequency is known as gyrofrequency with a period, the gyroperiod,

$$\tau = \frac{2\pi}{\Omega} \tag{1.8}$$

## 1.1 Single Particle Motion in an EM Field

---

The gyroperiod is not dependent on speed. As pointed out earlier, electrons and ions behave differently. In this case, they rotate in opposite directions. Electrons rotate clockwise about the magnetic field while ions rotate anticlockwise in a motion known as gyromotion. The radius of such motion is called a cyclotron radius or gyroradius,

$$r_g = \frac{v_{\perp}}{\Omega} = \frac{mv_{\perp}}{qB} \quad (1.9)$$

which depicts that a more massive particle with a weaker field will gyrate with a bigger gyroradius than a less massive particle with a stronger field. As such,  $r_g$  depends on the magnetic field strength. In typical magnetospheric environment with a  $B$  of about 100 nT and energy  $\sim 1$  keV; gyrofrequency and gyroradii for an electron will be approximately  $1.8 \times 10^4$  rad s $^{-1}$  and 1 km respectively. While for a proton they will be about 10 rad s $^{-1}$  and 50 km.

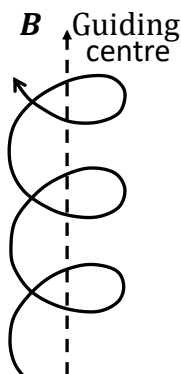


**Figure 1.1:** Schematic illustration of the trajectory of a particle with non-zero  $v_{\parallel}$ .

### 1.1.2 Bounce motion

In the last case, we considered a scenario where magnetic field is not varying in space and time. Here, we shall consider a scenario where it varies spatially but unchanged in time. By taking the scalar product with  $\mathbf{v}$  on the right-hand side (RHS) and left-hand side (LHS) of Equation 1.1,

$$m\mathbf{v} \cdot \frac{d\mathbf{v}}{dt} = q\mathbf{v} \cdot (\mathbf{v} \times \mathbf{B}) \quad (1.10)$$

## 1.1 Single Particle Motion in an EM Field

---

the RHS becomes equal to zero given that  $\mathbf{v} \cdot (\mathbf{v} \times \mathbf{B}) = 0$ . The LHS of Equation 1.10 can be expressed as

$$m \frac{d}{dt} \left( \frac{1}{2} \mathbf{v} \cdot \mathbf{v} \right) = 0 \quad (1.11)$$

Equation 1.11, which can also be written as  $\frac{d}{dt} \left( \frac{1}{2} m v^2 \right) = 0$  shows that the total kinetic energy of the particle does not vary with time. This implies that speed,

$$v = \sqrt{v_{\perp}^2 + v_{\parallel}^2} = \text{constant} \quad (1.12)$$

where  $v_{\perp}$  and  $v_{\parallel}$  are the respective components of  $\mathbf{v}$  perpendicular and parallel to  $\mathbf{B}$ . Thus, the particle speed remains constant despite the spatial variation in the magnetic field.

In certain situations, the magnetic field strength varies along the field direction. For example, in a converging configuration as shown in Figure 1.2, the field strength varies along  $\mathbf{B}$ .

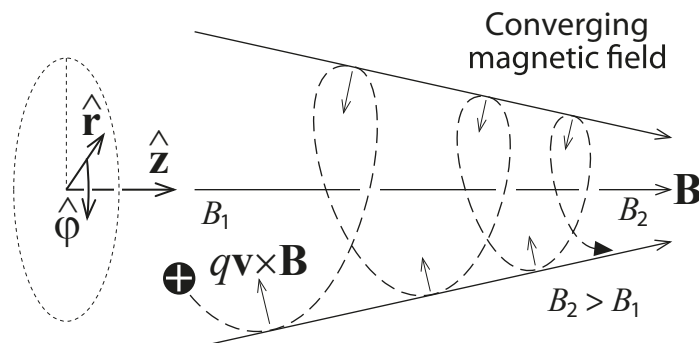


**Figure 1.2:** Diagram illustrating a  $q > 0$  particle moving into a region of converging magnetic field with increasing field strength. The small arrows show direction of the Lorentz force on the particle as it gyrates along the  $z$ -axis (Figure courtesy of Steve E. Milan).

The Lorentz force  $q\mathbf{v} \times \mathbf{B}$  is perpendicular to  $\mathbf{B}$ . Therefore, the  $v_{\perp}$  component points away from the  $\hat{z}$ -axis, which is the direction of increasing field. However,  $v_{\parallel}$  decreases until the parallel motion along  $\hat{z}$ -axis stops. At such point, known as mirror point, the direction of the particle motion reverses from the region of high

## 1.1 Single Particle Motion in an EM Field

---

field strength. This can be derived by applying a cylindrical coordinate system  $(r, \varphi, z)$ , assuming that the azimuthal component of the field  $B_\varphi$  is zero, which means that there is no twisting. Since  $\nabla \cdot \mathbf{B} = 0$ , the point at which the particle is repelled or mirrored can be shown from

$$\nabla \cdot \mathbf{B} = \frac{1}{r} \frac{\partial}{\partial r} (rB_r) + \frac{1}{r} \frac{\partial B_\varphi}{\partial \varphi} + \frac{\partial B_z}{\partial z} = 0 \quad (1.13)$$

Since  $B_\varphi = 0$ , and it is assumed that  $B \approx B_z$ , then

$$\frac{\partial}{\partial r} (rB_r) = -r \frac{\partial B_z}{\partial z} = -r \frac{dB}{dz} \quad (1.14)$$

Integrating Equation 1.14 with respect to  $r$ , assuming that  $B_r = 0$  at  $r = 0$ ,

$$B_r = -\frac{r}{2} \frac{dB}{dz} \quad (1.15)$$

The particle velocity has three components,  $v_r$ ,  $v_\varphi$  and  $v_z$ . If the azimuthal component of velocity is related to its perpendicular speed by  $v_\varphi = -v_\perp$  where  $B$  increases along  $+z$  direction as shown in Figure 1.2, then  $v_z = v_\parallel$ , from which the Lorentz force in the  $z$ -direction can be expressed as

$$F_z = -ev_\varphi B_r \quad (1.16)$$

Substituting Equation 1.15 and using  $v_\varphi = -v_\perp$

$$F_z = -\frac{ev_\perp r}{2} \frac{dB}{dz} \quad (1.17)$$

Factor in Equation 1.9, the gyroradius, such that  $r = r_g$ , then

$$F_z = -\frac{mv_\perp^2}{2B} \frac{dB}{dz} \quad (1.18)$$

Equation 1.18 is the force that acts on the particle as it moves in  $z$ -direction, reducing  $v_\parallel$  such that the motion in the  $z$ -direction is

$$\frac{dv_\parallel}{dt} = \frac{F_z}{m} = -\frac{v_\perp^2}{2B} \frac{dB}{dz} \quad (1.19)$$

Rearranging Equation 1.19 and given that  $\frac{dz}{dt} = v_\parallel$ , gives

$$dv_\parallel = -\frac{v_\perp^2}{2} \frac{dB}{B} \frac{dt}{dz} = -\frac{v_\perp^2}{2v_\parallel} \frac{dB}{B} \quad (1.20)$$

## 1.1 Single Particle Motion in an EM Field

---

Further rearranging Equation 1.20 gives

$$d(v_{\parallel}^2) = -v_{\perp}^2 \frac{dB}{B} \quad (1.21)$$

Since the total speed remains constant as shown in Equation 1.12, then

$$\frac{d(v_{\perp}^2)}{v_{\perp}^2} = \frac{dB}{B} \quad (1.22)$$

Integrating Equation 1.22,

$$\ln v_{\perp}^2 = \ln B + \text{constant}$$

or

$$\frac{v_{\perp}^2}{B} = \text{constant} \quad \left( = \frac{v_{\perp 0}^2}{B_0} \right) \quad (1.23)$$

where by measuring  $v_{\perp 0}$  and  $B_0$  at a specified initial point, the value of the constant can be determined. Equation 1.23 is known as the first adiabatic invariant. The particle mirrors at point  $B_m$ , known as the mirror point, at which  $v_{\parallel} = 0$  such that

$$B_m = B_0 \left( \frac{v}{v_{\perp 0}} \right)^2 \quad (1.24)$$

The particle motion can also be described in terms of the pitch angle,  $\alpha$  such that

$$\tan(\alpha) = \frac{v_{\perp}}{v_{\parallel}} \quad (1.25)$$

where  $v_{\perp} = v \sin(\alpha)$  and  $v_{\parallel} = v \cos(\alpha)$ . Thus, the first adiabatic invariant can be represented as,

$$\frac{v_{\perp}^2}{B} = \frac{v^2 \sin^2 \alpha}{B} = \text{constant} \quad (1.26)$$

Since  $v$  is constant, Equation 1.26 becomes

$$\frac{\sin^2 \alpha}{B} = \text{constant} \quad (1.27)$$

Thus, at  $\alpha = 90^\circ$ , which is the mirror point where  $v_{\parallel} = 0$ ,

$$B_m = \frac{B}{\sin^2 \alpha} \quad (1.28)$$

## 1.1 Single Particle Motion in an EM Field

---

Equation 1.28 shows that the point at which the particle is repelled or mirrored is dependent on the pitch angle but not on the particle's mass or charge. All particles with  $\alpha = 90^\circ$  irrespective of their type and speed will mirror in a converging magnetic field configuration.

### 1.1.3 Drift Motion

In the two previous considerations,  $\mathbf{E}$  was zero but here we shall consider the effect of electric field, resulting in a  $\mathbf{E} \times \mathbf{B}$  drift. The electric field parallel and perpendicular to  $\mathbf{B}$  can be determined. Thus, for  $\mathbf{E}$ , which is produced due to charge separation parallel to  $\mathbf{B}$ , the component of  $v_z$  in Equation 1.3, previously zero now becomes

$$\frac{dv_z}{dt} = \frac{q}{m} E_{\parallel} \quad (1.29)$$

Integrating Equation 1.29 produces

$$v_z = v_{z0} + \frac{qE_{\parallel}}{m} t \quad (1.30)$$

showing that ions and electrons move in opposite directions along  $\mathbf{B}$ , depending on the value of  $v_{z0}$ . As electrons move towards the positive charge and ions towards the negative charge, the charge separation that created the electric field is reduced, consequently  $\mathbf{E}_{\parallel}$  tends to zero.

In the case of  $\mathbf{E}$  perpendicular to  $\mathbf{B}$ , assuming  $\mathbf{B} = B\hat{\mathbf{z}}$  and  $\mathbf{E} = E_{\perp}\hat{\mathbf{y}}$ , the electric field accelerates a proton along the  $y$ -direction as illustrated in Figure 1.3 from its start at point 1. As it accelerates to point 2, the Lorentz force  $e\mathbf{v} \times \mathbf{B}$  increases, causing a turning trajectory until point 3 where  $v_y = 0$ . As such,  $e\mathbf{v} \times \mathbf{B}$  force dominates  $e\mathbf{E}$  force at point 4 to 5 where it comes to rest.

The electron also moves along the same  $\mathbf{E} \times \mathbf{B}$  direction as depicted in Figure 1.3. Thus, the resultant "hopping" cycle or motion of the particles is along the  $\mathbf{E} \times \mathbf{B}$  direction regardless of charge with drift velocity

$$\mathbf{v}_E = \frac{\mathbf{E} \times \mathbf{B}}{B^2} \quad (1.31)$$

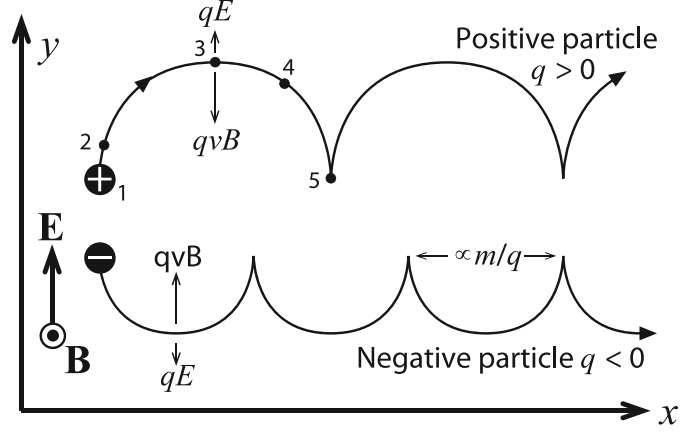


**Figure 1.3:** Diagram showing positive and negative charges experience  $\mathbf{E} \times \mathbf{B}$  drift (Figure courtesy of Steve E. Milan).

where  $\mathbf{v}_E$  is the drift where the electric field exists in the frame under consideration, which will produce a total drift,  $\mathbf{v}$  if we add the parallel component  $v_{\parallel} \hat{\mathbf{B}}$  to the RHS of Equation 1.31.

If we transform to a frame of reference moving with the  $\mathbf{E} \times \mathbf{B}$  velocity in Figure 1.3, then the motion of the particles reverts to the circular gyration around the magnetic field as described above. Thus, the electric field is a result of the frame of reference, and is zero in the frame of reference moving at the  $\mathbf{E} \times \mathbf{B}$  velocity. The electric field given that there is a plasma drift  $\mathbf{v}$ , which is the  $\mathbf{E}$  for a bulk drift of plasma perpendicular to the magnetic field in the frame illustrated in Figure 1.3 is

$$\mathbf{E} = -\mathbf{v} \times \mathbf{B} \quad (1.32)$$

### 1.1.3.1 Gradient and Curvature Drift

It has been shown in Section 1.1.2 that changes in the effect of magnetic field strength parallel to the field results in a bounce motion at a certain pitch angle. In a situation where the gradient in the magnetic field strength is perpendicular to  $\mathbf{B}$ , the particle will gyrate with a gyroradius, that can be determined by Equation

## 1.1 Single Particle Motion in an EM Field

---

1.9. Such  $r_g$  as earlier discussed, depends on the magnetic field strength. The  $r_g$  at each point in time will vary as the particle gyrates given that the magnetic field strength has a gradient in the direction perpendicular to the magnetic field. Such variation as illustrated in Figure 1.4 will result in drifts of the particles known as gradient drift with velocity,  $\mathbf{v}_{\nabla B}$  expressed following Baumjohann & Treumann (1997) as

$$\mathbf{v}_{\nabla B} = \frac{1}{2} m v_{\perp}^2 \frac{\mathbf{B} \times \nabla B}{q B^3} \quad (1.33)$$

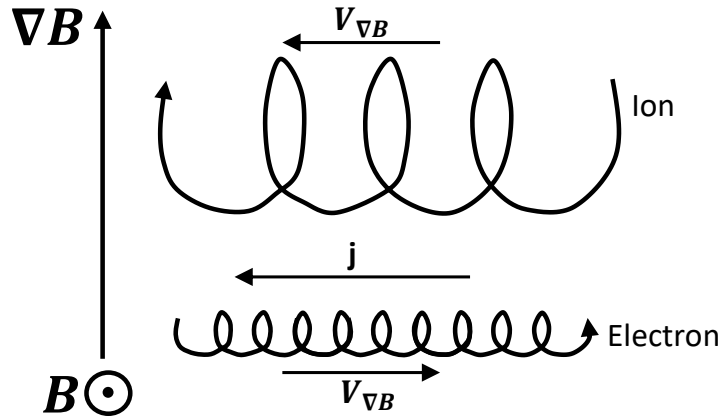


**Figure 1.4:** Diagram showing ion and electron drifting due to a gradient in magnetic field strength perpendicular to the magnetic field direction, resulting in a  $\mathbf{j}$  due to their opposite direction of drift (after, Baumjohann & Treumann, 1997).

Equation 1.33 shows that the  $\mathbf{v}_{\nabla B}$  direction is dependent on the particle charge. Thus, the gradient drift of the particles induces a current. The particle's drift is also influenced by a curved configuration such as the Earth's magnetic field lines.

The curvature drift velocity can be expressed as

$$\mathbf{v}_c = \frac{m v_{\parallel}^2}{q} \frac{\mathbf{R}_c \times \mathbf{B}}{R_c^2 B^2} \quad (1.34)$$

## 1.1 Single Particle Motion in an EM Field

---

where  $\mathbf{R}_c$  is the radius of local field line curvature. The variation in gyroradii of each circular path around the field line as the particle flows along it results in drift perpendicular to the field. Such a drift motion and the previously described gyromotion and bounce motion in the Earth's magnetosphere are illustrated in Figure 1.5. The curvature drift is also dependent on charge, the same as for gradient drift. Plasma particles in Earth's magnetosphere often experience the gradient and curvature drift together. Further information on the motion of a single charged plasma can be found in (e.g., Kivelson & Russell, 1995; Baumjohann & Treumann, 1997).

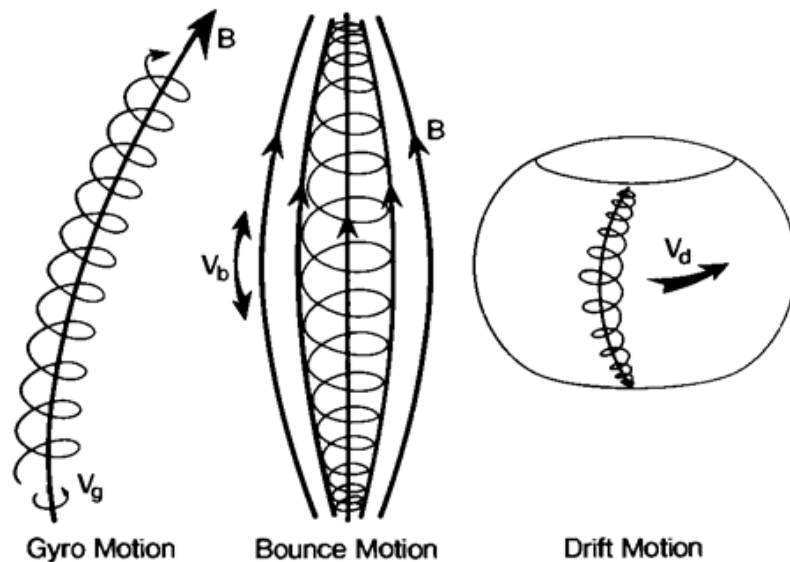


**Figure 1.5:** Schematic illustrations of the three major configurations of a single particle motion due to the morphology of the magnetic field. Taken from Kivelson & Russell (1995).

## 1.2 Magnetohydrodynamics

The last section discussed the motions of individual charged particles in constant magnetic and electric field configurations. At the start of that section, a plasma was said to be quasi-neutral, which means that it consists of equal number of ions and electrons. Quasi-neutrality is maintained mostly where the spatial scale,  $L$  of the plasma is large under certain conditions that shall be treated in the later part of this section. At such large spatial scales, a plasma is often treated as a conducting fluid and not as individual particles. The assumption that plasma is collisionless as earlier stated, also holds here. This fluid approach is known as magnetohydrodynamics (MHD). It combines electromagnetic forces and fluid dynamics to describe plasma dynamics. MHD equations rely on three basic equations; the continuity equation, the equation of motion and the equation of state as well as Maxwell's equations because of the contribution of the electric and magnetic field.

The continuity equation, also known as conservation of mass and charge, upholds the conservation of ion and electron particles, such that the number of particles flowing into an arbitrary volume,  $V$  having a surface,  $S$  must correspond to the particles flowing out through the surface. This is expressed as

$$\frac{d}{dt} \int_V \rho dV = - \oint_S \rho \mathbf{v} \cdot d\mathbf{s} \quad (1.35)$$

where  $\mathbf{v}$  is the centre of mass velocity,  $d\mathbf{s}$  is the surface element of the volume and  $\rho$  is the total mass density. Applying Gauss' divergence theorem will change the integral on the RHS of Equation 1.35 to a volume integral such that

$$\frac{\partial \rho}{\partial t} + \nabla \cdot (\rho \mathbf{v}) = 0 \quad (1.36)$$

An element of plasma in such a system responds to external forces, including gravity, the pressure from the surrounding medium and electromagnetic forces. The total momentum resulting from these external forces must be conserved and can be described by Newton's second law. It is defined as

$$\rho \frac{d\mathbf{v}}{dt} = \rho \mathbf{g} - \nabla P + \rho_q \mathbf{E} + \mathbf{j} \times \mathbf{B} \quad (1.37)$$

where  $\rho_q$  is the charge density indicating a departure from quasi-neutrality, while  $\rho$  retains its earlier definition,  $P$  is the pressure and  $\mathbf{j}$  is the current density. Comparing the magnitudes of the various terms on the RHS in a typical space plasma shows that the  $\rho\mathbf{g}$  term is negligible. Also, the  $\rho_q\mathbf{E}$  term can be neglected with respect to the magnetic field term where the motions within the plasma are significantly slower than the speed of light. Therefore, Equation 1.37 can be reduced to

$$\rho \frac{d\mathbf{v}}{dt} = -\nabla P + \mathbf{j} \times \mathbf{B} \quad (1.38)$$

Equation 1.38 is known as equation of motion, which describes essential features of the total plasma together with the continuity equation. The current density,  $\mathbf{j}$  with respect to the electromagnetic field can also be described by Ohm's law as

$$\mathbf{j} = \sigma (\mathbf{E} + \mathbf{v} \times \mathbf{B}) \quad (1.39)$$

where  $\sigma$  is the electrical conductivity of the plasma. The third basic equation for MHD is the equation of state, which describes the conservation of energy. It is expressed as

$$\frac{P}{\rho^\gamma} = \text{constant} \quad (1.40)$$

where  $P$  is the pressure,  $\rho$  retains its meaning as the plasma density and  $\gamma$  is the ratio of specific heats.

### 1.2.1 Maxwell's Equations

Maxwell's equations are expressed in differential form as

$$\begin{aligned} (a) \quad & \nabla \cdot \mathbf{E} = \frac{\rho_q}{\varepsilon_0} \\ (b) \quad & \nabla \cdot \mathbf{B} = 0 \\ (c) \quad & \nabla \times \mathbf{E} = -\frac{\partial \mathbf{B}}{\partial t} \\ (d) \quad & \nabla \times \mathbf{B} = \mu_0 \mathbf{j} + \mu_0 \varepsilon_0 \frac{\partial \mathbf{E}}{\partial t} \end{aligned} \quad (1.41)$$

Equation 1.41(a) known as Gauss's law for electricity states that the divergence in an electric field depends on charge density. This means that the source of the electric field is defined by the total charge density. Equation 1.41(b) Gauss's

law for magnetism states that the total divergence of the magnetic field is zero, meaning that there are no sources of magnetic field or no magnetic monopoles.

Equations 1.41 (c-d) define the relationship between electric and magnetic fields in varying spatial and temporal conditions. Equation 1.41 (c) also called Faraday's law denotes that the spatial variation of electric field is related to the time varying magnetic field. Lastly, Equation 1.41(d) is the Ampère-Maxwell law, which describes the relationship of varying magnetic field to currents in the plasma. The first term on RHS is the conduction current,  $\mathbf{j}$  flowing as magnetic field revolves while the second term is the displacement current. In large-scale systems such as the magnetosphere where the electric field varies slowly with time,  $\partial\mathbf{E}/\partial t$  is relatively small compared to  $\mathbf{j}$  such that it is negligible. The remaining parts of Equation 1.41(d) without the displacement current is Ampère's law, mainly used when studying space plasmas.

### 1.2.2 Alfvén's Theorem

Faraday's law presented as Equation 1.41(c) connotes that magnetic field strength will increase or decrease in a region of space where there is non-zero curl of the electric field. Applying this procedure describes the relationship between the flow of plasma and the surrounding magnetic field. For instance, if  $\mathbf{E}$  is made the subject in Equation 1.39 such that

$$\mathbf{E} = -\mathbf{v} \times \mathbf{B} + \frac{\mathbf{j}}{\sigma} \quad (1.42)$$

Taking the curl of both sides of Equation 1.42 means that we can substitute Faraday's law for the LHS, which becomes

$$\frac{\partial \mathbf{B}}{\partial t} = \nabla \times \left( \mathbf{v} \times \mathbf{B} - \frac{\mathbf{j}}{\sigma} \right) \quad (1.43)$$

Applying Equation 1.41(d) without the negligible displacement current term,  $\partial\mathbf{E}/\partial t$  gives

$$\frac{\partial \mathbf{B}}{\partial t} = \nabla \times (\mathbf{v} \times \mathbf{B}) - \frac{\nabla \times \nabla \times \mathbf{B}}{\mu_0 \sigma} \quad (1.44)$$

By replacing the vector identity  $\nabla \times \nabla \times \mathbf{B}$  with  $\nabla(\nabla \cdot \mathbf{B}) - \nabla^2 \mathbf{B}$  and considering that  $\nabla \cdot \mathbf{B} = 0$ , we get

$$\frac{\partial \mathbf{B}}{\partial t} = \nabla \times (\mathbf{v} \times \mathbf{B}) + \frac{\nabla^2 \mathbf{B}}{\mu_0 \sigma} \quad (1.45)$$

Equation 1.45 is known as the induction equation, where the first and second terms on the RHS represent convection and diffusion of magnetic fields respectively. In collisionless plasmas where the conductivity is mostly high,  $\sigma$  tends to infinity, as such the diffusive term is ignored with only the convective term remaining. The implication is that plasma as a conducting fluid is not considered to flow or diffuse across the magnetic field lines, but to move with the magnetic field. This phenomenon is known as Alfvén's theorem or the frozen-in flux approximation. The equivalent form of this approximation in terms of Ohm's law is  $\mathbf{E} = -\mathbf{v} \times \mathbf{B}$ , earlier stated as Equation 1.32, indicating that electric field is frame dependent since it has components perpendicular to the motion of the plasma frozen-in to the magnetic field but has no parallel components. In such frozen-in flux conditions, the distribution of field inside a region of plasma flowing with its embedded magnetic field is accordingly modified as illustrated in Figure 1.6. Also, if the configuration of the flow of plasma particles changes, the magnetic field within the particles consequently adopts the new configuration.

In a condition where  $\sigma$  does not tend to infinity, the behaviour of the plasma is determined by both diffusive and convective terms in Equation 1.45. The ratio of the magnitude of both terms gives the magnetic Reynolds number,  $R_m$  defined as

$$R_m = \mu_0 \sigma v L \quad (1.46)$$

where  $L$  represents the characteristic scale length of the system being described. As earlier stated,  $L$  is large in certain systems, for example, in space plasma environments such as the solar wind and Earth's magnetosphere. This implies that  $R_m \gg 1$  based on Equation 1.46, as such the convective term dominates and the frozen-in flow approximation holds. In contrast, if  $L$  is not large such that  $R_m \sim 1$ , the diffusive term cannot be ignored, so the frozen-in flow theorem breaks down.

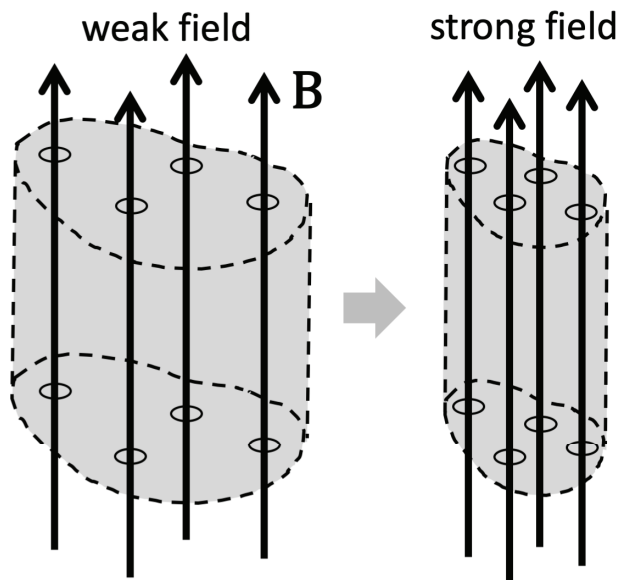


**Figure 1.6:** An illustration that magnetic field is modified as it is transported with the plasma in the frozen-in flux approximation. (Figure courtesy of Steve E. Milan)

### 1.3 The Solar wind

The magnetosphere-ionosphere system and its complex dynamics cannot be described without highlighting the role of the Sun and the solar wind as its main energy source. The Sun consists primarily of hydrogen ( $\sim 90\%$ ) and helium ( $\sim 10\%$ ) gas. It has a mass of  $1.99 \times 10^{30}$  kg, which is about 330,000 times the mass of the Earth, and a radius of 696,000 km. The Sun's atmosphere consists of three layers known as photosphere, which carries the heat energy of the Sun and has a density of about  $10^{23} \text{ m}^{-3}$ , followed by chromosphere and corona. The temperature in the photosphere is in the region of 4,200 K, representing a minimum value compared to the other layers, because the Sun's atmospheric temperature increases as the layers extend outward. Thus, the Sun's corona is higher in temperature than the photosphere, which leads to complete ionisation of the gases causing charged particles to flow out due to the pressure they experience being too high for gravity to restrain. Such charged particles of the Sun flow outward into the heliosphere along with the interplanetary magnetic field (IMF) as the

solar wind.

The solar wind is the continuous outflow of tenuous plasma at a supersonic speed, which typically ranges between  $300 \text{ km s}^{-1}$  and  $800 \text{ km s}^{-1}$  around 1 AU, from the Sun's corona (Sakao *et al.*, 2007). It comprises approximately equal numbers of electrons and ions, which are mainly protons with trace elements of ionised helium and heavier ions. The solar wind is a highly dynamic system and as such it varies in density, velocity, temperature and magnetic field properties. It also varies with temporal and spatial features like the solar cycle, heliographic latitude, heliocentric distance and rotational period and in response to shocks, waves and turbulence perturbing the interplanetary flow (SwRI, 2020). The out-flowing solar wind plasma is bound to a weak IMF, through the frozen-in phenomenon discussed earlier. Such IMF represents a part of the Sun's magnetic field that is carried into interplanetary space by the solar wind. Thus, the solar wind flows radially into the space, pervading the solar system along with the magnetic field produced by the Sun.

Subsequent sections discuss the Earth's magnetosphere and ionosphere and their dynamics, which influences, for example, the excitation and propagation of ULF waves.

## 1.4 Earth's Magnetosphere

The plasma particles in space are bound to the magnetic field of the associated geophysical environment as a result of frozen-in-flux theorem discussed in Section 1.2.2. Hence, the idea of the Earth's magnetosphere was birthed based on the knowledge that the magnetic field of the Earth and the Sun carried by the solar wind are different, so their respective plasma populations are frozen-in to their associated magnetic field. This idea was first developed by Chapman & Ferraro (1931), and is illustrated in Figure 1.7 below. The interplanetary magnetic field (IMF) carrying the solar wind plasma envelops the Earth's magnetic field, forming a cavity known as magnetosphere. The magnetosphere is the region of space overlying the Earth's ionosphere where the influence of the Earth's magnetic field is dominant (Newell *et al.*, 2001). The different regions and structure

of the Earth's magnetosphere are illustrated in Figure 1.8. These regions are characterised by plasma of different energy, composition and density.

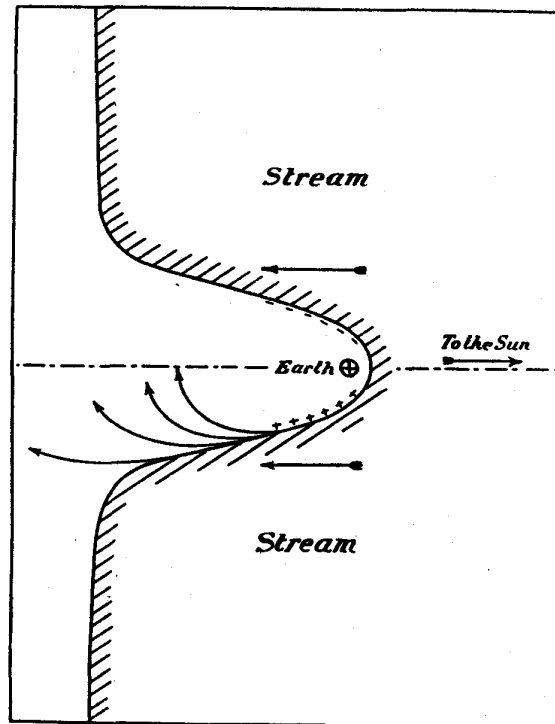


**Figure 1.7:** A diagram depicting magnetic cavity formation from the Earth's magnetic field as the solar wind streams towards the Earth. Figure taken from (Chapman & Bartels, 1940).

The boundary of the Earth's magnetic field, which confines the Earth's field within the magnetosphere is called the magnetopause as depicted in Figure 1.8. The magnetopause is approximately a surface of revolution about the Sun-Earth line ( $x$ -axis in Geocentric Solar Magnetospheric System - GSM coordinates). The magnetopause stand-off distance at the subsolar point is roughly  $10 R_E$ . The radius in the  $x = 0$  plane is  $15 R_E$ , and it continues to flare outwards, asymptoting to a radius of  $20 R_E$  further down-tail. The geocentric solar configuration changes spatially with the time depending on the solar wind dynamic pressure and the rate of transport of southward magnetic flux. The geocentric distance of the

sunward dayside is shorter than the elongated magnetotail side, which is due to the solar wind pressure being reduced on the nightside compared to the dayside. The solar wind flows with a supersonic speed towards the Earth's magnetosphere. As it approaches the magnetopause, the magnetosphere develops a shock wave known as bow shock, which reduces the solar wind speed to a subsonic level. The bow shock lies at about  $3 R_E$  sunward from the magnetopause and in between the bow shock and the magnetopause is a region called magnetosheath, comprising shocked solar wind plasma with increased plasma density and temperature but decreased speed (Frey, 2007).

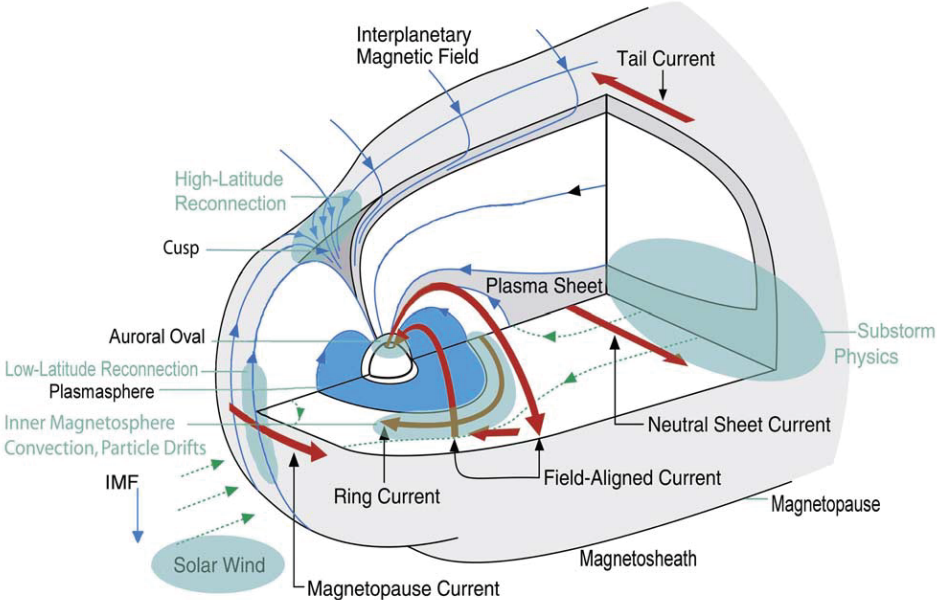


**Figure 1.8:** Illustration of different regions of the Earth's magnetosphere. Taken from (Frey, 2007).

The magnetopause also plays an important role in the process where two plasma regions that were initially segregated can bind to each other through the frozen-in magnetic field lines that connect them. Assuming frozen-in flow, then the solar wind plasma advecting with the IMF meets with the plasma of the Earth's magnetic field without mixing. As such, a current system known as the Chapman-Ferraro current is produced at the magnetopause as a result of Ampère's law. This current flows between the plasma carried by the IMF and that

of the Earth's field. Magnetic field gradients at the magnetopause usually have length scales that are similar to the particle gyroradii, leading to a breakdown of the frozen-in-flux condition, which requires that the magnetic field scale lengths are large compared to the particle gyroradii. This leads to a process known as magnetic reconnection, which describes how the solar wind plasma frozen-in to magnetic field lines of the IMF merges with the Earth's field at the magnetopause. In the open model of the magnetosphere (Dungey, 1961), often referred to as Dungey Cycle; plasma flow in and out of the terrestrial magnetosphere is mainly controlled by reconnection at the magnetopause between the Earth's magnetic field and the IMF and resultant processes in the geomagnetic tail (Cowley, 2000). Magnetic reconnection of the solar wind and the geomagnetic field lines is a continuous process and most effective when the field lines are antiparallel (Frey, 2007). The relative orientation between the arriving IMF and field lines at the magnetopause determines where reconnection occurs on the magnetopause. As illustrated in Figure 1.9, reconnection manifests in the low latitude and high latitude regions during external southward and northward IMF respectively. A reconnection following a northward IMF orientation occurs in the direction poleward of the cusp while a southward IMF model predicts the reconnection mostly associated with the Dungey cycle. The trapped plasma on the reconnected field lines known as flux tubes are transferred with flow of the solar wind in antisunward direction. Such motion of the reconnected flux tubes causes displacement of surrounding flux and results in a bulk flow of plasma towards the magnetotail. This flow is known as plasma convection. The direction of the plasma motion is perpendicular to the electric field produced in the magnetosphere due to solar wind interaction and the Earth's magnetic field. This phenomenon discussed previously in this chapter, is known as **E-cross-B** drift. Therefore, magnetic reconnection continuously occurring between the IMF and the terrestrial magnetic field drives most of the dynamics such as ULF waves that characterise the internal magnetosphere of the Earth (Milan *et al.*, 2012).

The funnel-shaped region depicted in Figure 1.8 is known as the cusp and is magnetically linked to the magnetopause (Smith & Lockwood, 1996; Frey, 2007). Ionospheric signatures of the cusp vary in size and position depending on the conditions of the external solar wind parameters as results from measurements

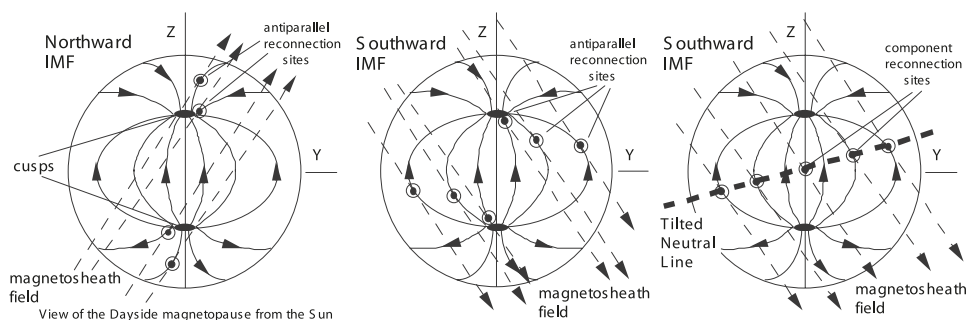


**Figure 1.9:** Illustration of reconnection at the magnetopause for northward and southward IMF orientation from a sunward view. The dashed lines represent external magnetosheath while the solid lines represent internal magnetospheric field lines. Reconnection occurs at high latitude, poleward of the cusp in northward IMF orientation as seen in the left while at low latitude during southward IMF shown in the middle and a tilted neutral line from the component reconnection model in the right. Taken from (Frey, 2007).

by low altitude spacecraft have revealed (Newell & Meng, 1994). Reconnection occurring at the magnetopause can be seen from the plasma features in the cusp as the plasma accelerates away from the magnetopause (Frey, 2007).

At the magnetotail region, in the nightside of the magnetosphere, stretched open field lines from each hemisphere reconnect again (Baumjohann & Treumann, 1997). This magnetotail reconnection occurs explosively, releasing energy and plasma in the inner magnetosphere irregularly in a process known as a substorm (e.g., McPherron, 1970; Kivelson & Russell, 1995), discussed in the subsequent section.

Inside the magnetosphere is a region called the plasmasphere, which is populated by dense, cold plasma surrounding the Earth. The boundary separating the plasmasphere from other regions of varying plasma density is known as plasmopause, which is a result of electric fields in the magnetosphere, such that decreasing magnetic activity causes it to move outward and increasing magnetic activity causes it to move inward. The plasmopause in the steady state, separates charged particle drift trajectories open to the magnetopause from those closed around the Earth (McPherron, 2005). The solar wind interaction with the magnetospheric plasma and dynamics in the magnetosphere discussed here can

result in disturbances such as substorms and geomagnetic storms.

## 1.5 Geomagnetic Activity

### 1.5.1 Substorms

A substorm is generally understood to mean a short-lived magnetospheric disturbance, in the range of two to three hours. It usually occurs following a southward turning of the IMF (McPherron, 2005). Such IMF orientation as earlier discussed, allows the interplanetary and terrestrial magnetic field lines to reconnect at the sunward magnetopause, causing energy from the solar wind to be transferred to the magnetosphere. Subsequently, part of this energy stored in the Earth's magnetotail results in the initial phase of the substorm known as the growth phase, followed by the expansion and recovery phases. During the expansion, the energy deposited in the magnetotail is released when the field lines in the inner magnetosphere relax from their outstretched, tail-like configuration and then return to a more dipolar configuration in a process referred to as dipolarisation (McPherron, 1979). This causes energisation of plasma sheet charged particles, thus, driving them deeper into the inner magnetosphere. These different phases of a substorm activity can be described from the near-earth neutral-line (NENL) model (McPherron *et al.*, 1973; Baker *et al.*, 1996). They can also be described in terms of associated auroral characteristics and morphology variations (e.g., Akasofu, 1964; Frey *et al.*, 2004; James *et al.*, 2013). The substorm phases are further discussed below based on these two descriptions.

The NENL model of the substorm phases is described using the schematic diagrams in Figure 1.10. Based on the NENL model, the night side plasma sheet becomes thin as shown in the top diagram of Figure 1.10 due to the pressure on the magnetotail during the growth phase as the flux being stored in the magnetotail increases, forming an X-line separating ions into sheets in an adiabatic process that produces a cross-tail current. As a result of this process, a new X-line is formed from tail reconnection during substorm expansion phase. The substorm expansion phase as shown in the middle diagram in Figure 1.10, starts when field lines of the initial distant neutral line (DNL) split as a result of reconnection

(Baker *et al.*, 1996), with the NENL separating field lines moving towards the Earth and a plasmoid moving tailward. A reconnection at the new X-line of the NENL drives the plasmoid further tailward as well as the X-line until it reaches a distance in the tail where the magnetosphere returns to its initial state in a process known as the substorm recovery phase. Such a substorm occurrence following the reconnection process described here can lead to injection of particles from where the substorm started to other parts of the magnetosphere. During the substorm, there are changes in the auroral morphology, in addition to the enhancement of currents in the high latitude ionospheric region and associated high latitude magnetic field strength variations due to the storage and release of energy in the magnetosphere (e.g., Voronkov *et al.*, 2003). The changes in the auroral morphology, for example, is the brightening of the auroral arc (Sakurai & Saito, 1976), which is most intense during the expansion phase, dissipating during the recovery phase when the magnetosphere returns to its quiet condition. An important geomagnetic activity index for characterising substorms is the auroral electrojet (AE).

The AE index developed by Davis & Sugiura (1966) is derived from ground-based magnetometers located around the auroral zone. It is defined as the difference between the auroral electrojet upper (AU) and lower (AL) indices. The AU and AL indices are calculated from the north-south component ( $H$ ) of the magnetic field measurements by the magnetometers. As such, the AE index uses such perturbations of ionospheric currents on the  $H$  component of the magnetic field for observing the global electrojet activity.

Such substorm occurrences discussed earlier in this section lead to variations in fields and plasma in the Earth's magnetosphere (McPherron, 2005). Energetic particles injected by substorm occurrence can result in particle acceleration processes, leading to the variations in fields and plasma in the magnetosphere. At certain conditions of parameters such as angular frequency and drift velocity, particles of such plasma can interact with magnetospheric ULF waves, leading to growth or dissipation of wave energy. For example, the energetic particles injected by a substorm can drive MHD wave modes through drift and drift-bounce resonance interactions or other wave-particle interactions (e.g., Baddeley *et al.*, 2002; James *et al.*, 2013; Yeoman *et al.*, 2016). Such wave-particle resonance

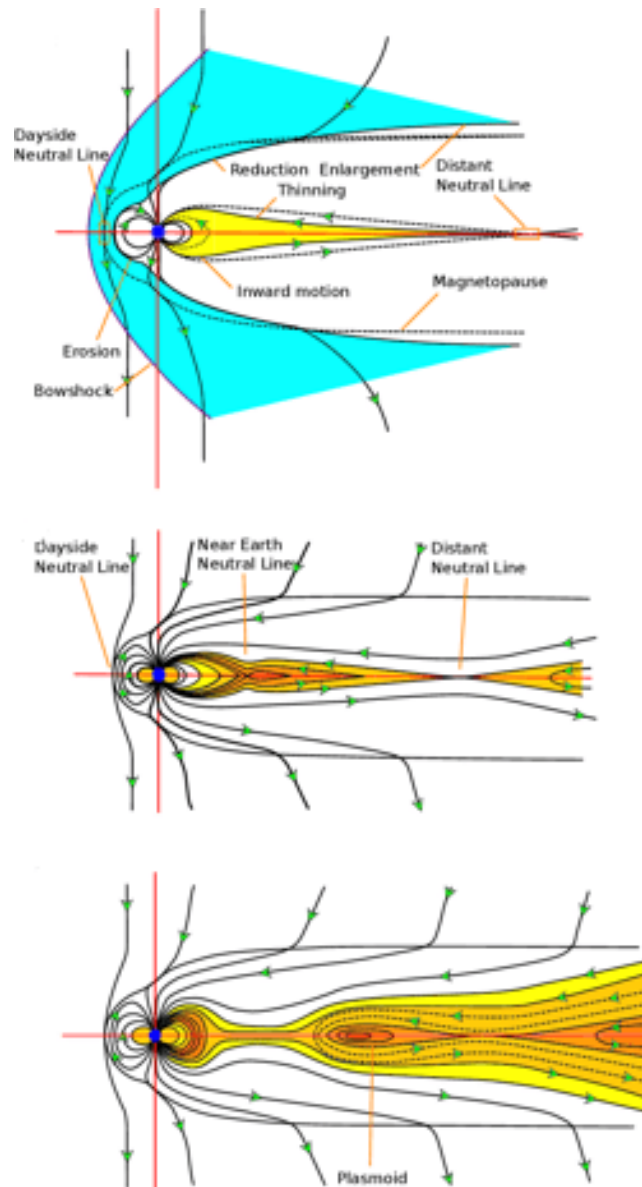


**Figure 1.10:** Schematic diagrams illustrating the near-earth neutral-line (NENL) substorm model based on Figures 13.21, 13.22 and 13.23 of Kivelson & Russell (1995). Taken from James (2015).

interactions are dependent, for example, on those parameters like the angular frequencies, the proton bounce and the proton azimuthal drift and these processes are discussed further in sections 2.3 and 2.4 and Chapter 4. Several studies exist of ULF waves driven by substorm-injected particles in the magnetosphere (e.g., Yeoman *et al.*, 2010). The waves, pre-existing in the magnetosphere are in the Alfvén continuum but become amplified or damped due to resonant interactions with particles injected by a substorm occurrence gradient-curvature drifting around the Earth as discussed previously in Section 1.1.3.1. In a similar vein, Chapters 4 and 5 of this thesis study waves due to such wave-particle interactions.

### 1.5.1.1 Detecting Substorms using Ground Magnetometer Data

Energy transferred into the magnetosphere from the solar wind is stored in the stretched tail side during the growth phase of substorm, which is explosively released during the expansion phase (McPherron *et al.*, 1973), as discussed in the last section. During the substorm, a magnetospheric cross tail current is diverted down field lines as a substorm current wedge (SCW), resulting in a westward auroral electrojet through the ionosphere as depicted in the top diagram of Figure 1.11. On the other hand, the perturbation in the geomagnetic field measured by ground magnetometers, which is due to the SCW forms a characteristic feature in mid-latitude ground magnetometer data as illustrated in the bottom diagram of Figure 1.11, showing that changes occur in the east-west and north-south magnetic fields, which depend on the relative location of the magnetic field measurement and the centre of the wedge (McPherron *et al.*, 1973; Clauer & McPherron, 1974; Lester *et al.*, 1983). The upward and downward field-aligned current (FAC) are formed such that there is a symmetric peak in the north-south component ( $H$ ) of the magnetic perturbation and anti-symmetric gradient in the east-west component ( $D$ ). The gradient in the  $D$  component indicates a positive peak near the westward FAC and a negative peak towards the eastward field aligned current. Therefore, the magnetic bay usually observed during a substorm is in response to the SCW and its magnitude and sign detected by the ground magnetometer data is dependent on the location of the station with respect to the SCW (Mann *et al.*, 2008). The dipolarisation resulting in the formation of the FAC will result

in Pederson and Hall currents in the ionosphere which can equally be seen in the magnetic perturbation observed on the Earth's surface.

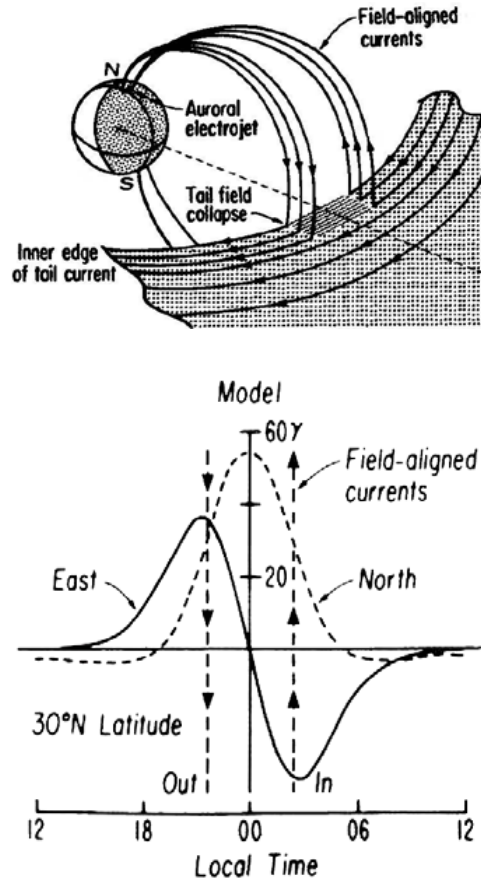


**Figure 1.11:** Illustration of a substorm current wedge in the top panel and the likely variation of magnetic bays in the North and East components of the geomagnetic field close to the substorm current wedge in the bottom panel. From Clauer & McPherron (1974).

The magnetic field perturbation detected by ground magnetometer in response to the SCW as discussed above and further description of the magnetometer data used here in Section 3.2 are applied in the studies presented in Chapter 4 of this thesis for inferring the location of substorms.

### 1.5.2 Geomagnetic Storms

Geomagnetic or magnetic storms are disturbances in the terrestrial magnetosphere resulting from a compression of the magnetosphere by enhanced solar wind activity leading to an intensification of the ring current. The connection of the compression of the magnetosphere with magnetic storm is well known for storms driven by coronal mass ejections (CMEs) but those driven by corotating interaction regions (CIRs) are not well known (Borovsky & Denton, 2006). Further discussions on the differences between the CME-driven magnetic storms and CIR-driven storms can be found in (e.g., Borovsky & Denton, 2006).

Similar to substorms, magnetic storms usually occur following a southward turning of the IMF for a prolonged time interval. According to Gonzalez *et al.* (1994), a magnetic storm is “an interval of time when a sufficiently intense and long-lasting interplanetary convection electric field leads, through a substantial energization in the magnetosphere-ionosphere system, to an intensified ring current sufficiently strong to exceed some key threshold of the quantifying storm time Dst index.” The disturbance storm time (Dst) variations represent the growth and recovery of the ring current and is applied as an index for quantifying magnetic storm intensity. Such magnetic storms are classified by intensity as weak, moderate and intense. With Dst index, weak storms are those between -30 nT and -50 nT, moderate storms are in the range of -50 nT and -100 nT and intense storms with peak Dst of -100 nT or less (Gonzalez *et al.*, 1994). There are other indices such as Kp for quantifying storms and the period of absence of magnetic storms is often referred to as a quiet period. Magnetic storms have three phases; initial, main and recovery phases, similar to substorms but have significant effects at mid and low latitudes.

The initial phase, which can last up to 16 hours, often starts with a sudden storm commencement (ssc), causing a global increase in the horizontal magnetic field due to compression of the magnetosphere by the solar wind induced shock wave. Thereafter, the horizontal field drops quickly below the pre-storm level as a result of the enhancement of the westward ring current, indicating the start of the main phase. The recovery phase begins as the horizontal field returns to pre-storm level, marked by a huge decrease in substorm activity and can last

for several days. Geomagnetic storms comprise many substorms, which has been suggested as a probable cause of ULF waves occurring during storms (McPherron, 2005). Whilst intense substorms occur frequently during geomagnetic storms, the processes that prompt substorm expansion and its connection with the formation of storm-time ring current are yet to be fully understood (Akasofu, 1977; Gonzalez *et al.*, 1994).

## 1.6 Magnetospheric MHD Waves

Magnetohydrodynamic waves in the Earth's magnetosphere can be described from the perturbation of the background magnetic field, plasma density and plasma pressure (Kivelson & Russell, 1995). Assuming that the background velocity of the plasma is zero so that  $\mathbf{v} = 0 + \mathbf{v}^1$  and the sum of the background magnetic field and perturbation is  $\mathbf{B} = \mathbf{B}_0 + \mathbf{b}$  where the background field,  $\mathbf{B}_0$  is much greater than the magnetic perturbation,  $\mathbf{b}$ . The plasma velocity is expressed in terms of background value assumed to be zero and perturbation value of  $\mathbf{v}^1$ . Substituting electric field  $\mathbf{E}$  from Equation 1.32 into 1.41(c) becomes

$$\nabla \times (\mathbf{v} \times \mathbf{B}) = \frac{\partial \mathbf{b}}{\partial t} \quad (1.47)$$

The displacement current in Equation 1.41(d) can be neglected at the frequency of ULF waves such that current density  $\mathbf{j}$  from the magnetic perturbation becomes

$$\mathbf{j} = \frac{1}{\mu_0} \nabla \times \mathbf{b} \quad (1.48)$$

where  $\mu_0$  is permeability of free space and the gradient of plasma pressure is zero. Wave equations due to the magnetic perturbations can be obtained from a Cartesian coordinate with z-axis parallel to  $\mathbf{b}$  such that

$$\begin{aligned} (a) \quad & \frac{\partial^2 \mathbf{b}}{\partial t^2} = \frac{B_0^2}{\rho \mu_0} \frac{\partial^2 \mathbf{b}}{\partial z^2} \\ (b) \quad & \frac{\partial^2 \mathbf{v}}{\partial t^2} = \frac{B_0^2}{\rho \mu_0} \frac{\partial^2 \mathbf{v}}{\partial z^2} \end{aligned} \quad (1.49)$$

## 1.6 Magnetospheric MHD Waves

Following equation 1.49, the Alfvén speed,  $v_A$  due to the velocity  $\mathbf{v}$  of the plasma associated with the magnetic perturbation  $\mathbf{b}$  is defined as

$$v_A = \sqrt{\frac{B_0^2}{\mu_0 \rho}} \quad (1.50)$$

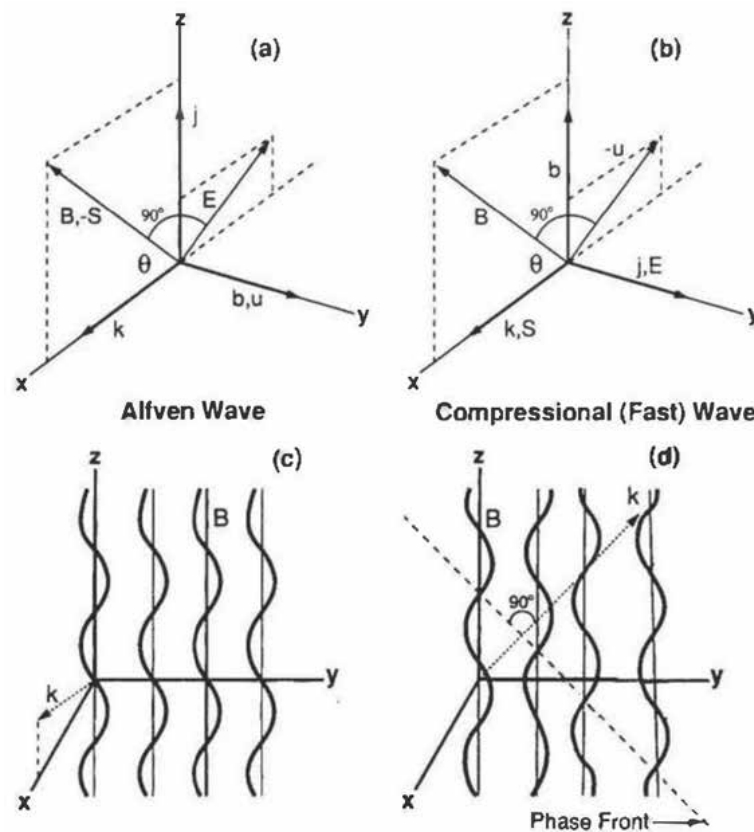


**Figure 1.12:** Illustration of MHD wave modes in a cold plasma approximation. Taken from Kivelson & Russell (1995)

Theory for the MHD wave dispersion relation is discussed in detail in (e.g., Kivelson & Russell, 1995). MHD waves in a cold plasma have two modes of propagation, namely; the shear Alfvén and fast modes. Figure 1.12 describes the features of these two modes. In the Alfvén mode, magnetic perturbation is in the perpendicular direction to the background magnetic field, but such background fields are in the same plane with the electric field and wave vector as illustrated by Figure 1.12(a). The implication is that the direction of energy flux, the Poynting

vector  $\mathbf{S} = \mathbf{E} \times \mathbf{b}$  is parallel to the background field. The angle  $\theta$  between the wave vector and magnetic field in Figure 1.12(a) indicates that phase velocity is equivalent to motion of the phase fronts illustrated in Figure 1.12(c). As such, the Alfvén mode is transverse or field-guided as depicted in Figure 1.12(c), showing the wave front in  $y$  axis while the phase front is directed along the magnetic field in the  $z$  axis. On the other hand, the fast mode illustrated in Figure 1.12(b) has current density and electric field parallel to  $\mathbf{k} \times \mathbf{B}$  while the plasma velocity vector, wave vector, magnetic perturbation and background field are in the same plane. Thus, the fast mode is not field-guided because the phase fronts travel in the direction of wave vector  $\mathbf{k}$  as described in 1.12(d). Unlike the Alfvén mode, the fast mode can transmit pressure variations given that magnetic field strength is not constant, as such, it can produce compression. Here the Poynting vector is parallel to the wave vector implying that the direction of energy flux is the same as the wave propagation and energy can be transferred across field lines. Thus, the phase velocity is independent of the direction of energy flow and wave propagation.

Another primary mode of propagation of MHD waves is the slow mode. The slow mode occurs where plasma pressure is significant compared to the magnetic pressure, also known as warm plasmas, such as in the ring current or the plasma sheet. Such modes propagate as a compressional wave that is guided along the background magnetic field with a phase speed comparable to the particle thermal speed (Fraser, 2009). Here, plasma and magnetic pressure oscillate out of phase, cancelling their effect unlike in the previous fast mode where they are in phase and as such, their effects are reinforced.

### 1.6.1 Alfvén waves and Field Line Resonance

In the last section, we noted that Alfvén waves propagate along Earth’s magnetic field lines with their associated wave energy. Such wave energy dissipates in the ionosphere by frictional forces in a closed conjugate field line. The ionosphere can reflect the waves because of its large conductivities, forming electric field nodes and magnetic field antinodes as depicted in Figure 1.13. A field line resonance

(FLR) is produced when the frequency of a driving fast mode matches the natural frequency of the Alfvén waves travelling along a field line.

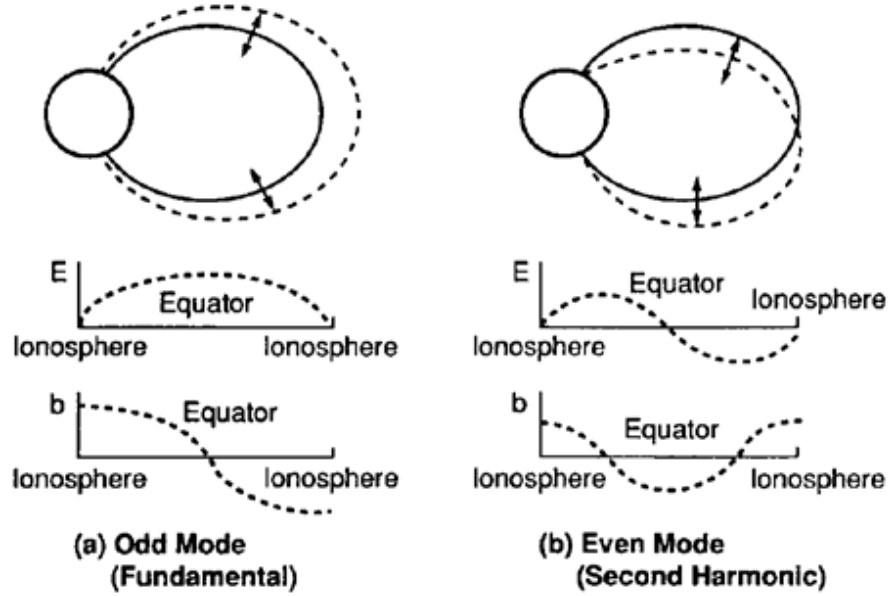


**Figure 1.13:** Illustrations of fundamental and second harmonic frequency resonances of a field line in closed dipolar geomagnetic field. The top parts show field line displacements due to Alfvén wave while the lower diagrams illustrate the variation in electric field  $\mathbf{E}$  and magnetic perturbation  $\mathbf{b}$  along the geomagnetic field lines across the conjugate points in the northern and southern ionospheres (Hughes, 1983).

The typical wavelengths of the Alfvén waves is described as  $\frac{2l}{n}$ , where  $l$  represents the length of a field line and  $n$  is the harmonic number of the wave. The frequencies of such typical wavelengths can be related as

$$f = \frac{nv_A}{2l} \quad (1.51)$$

where  $v_A$  retains its meaning as the Alfvén speed, the phase velocity of the Alfvén wave. As such, the length of the field line between the two conjugate ionospheres and the Alfvén speed as well as  $B_0$  from Equation 1.50 determines the FLR eigenfrequencies illustrated in Figure 1.13 for the first and second harmonics. The Alfvén speed is related to plasma mass density as described by Equation

1.50. Characteristics of field lines resonances are discussed further in Section 2.2 of the next chapter.

### 1.6.2 ULF Waves

Many studies spanning over seven decades have been carried out on the subject of ultra-low frequency waves, see for example, reviews by (Hughes, 1994; Fraser, 2006). Magnetic pulsations, a ULF wave manifestation, are the ground-based signatures of the MHD waves in the Earth's magnetosphere. The earliest observation of long-period waves, now known as ULF waves, was the comparison of compass measurements in Uppsala with auroral fluctuations reported in 1741 by Anders Celsius (Kangas *et al.*, 1998). While other observations of long-period pulsations were reported in the mid-19th century, ULF wave research witnessed a resurgence following increased data availability and the development of theories that describes this wave phenomena in the magnetospheric plasma especially the notable works done in 1942 by Hannes Alfvén and in 1954 by J. W. Dungey (Fraser, 2006). For example, Dungey's hydromagnetic wave equation described the propagation of ULF waves using two coupled second-order differential equations where the field geometry is symmetrical about an axis for plasmas in which the magnetic pressure is considerably greater than the plasma thermal pressure, also called a cold plasma as discussed in the last section.

#### 1.6.2.1 Classifications of ULF Waves

The classification of ULF waves based on frequency by Jacobs *et al.* (1964) harmonised various names used to categorise magnetic pulsations. ULF waves are classified into two broad categories and sub-classes based on the wave period. The first is continuous pulsations (Pc), which are oscillations characterised by quasi-sinusoidal waveform and the second category is impulsive oscillations referred to as irregular pulsations (Pi). This classification of geomagnetic pulsations based on wave period is presented in Table 1.1.

The oscillation mode of a dipole field line is classified as either a toroidal mode or a poloidal mode (Southwood & Hughes, 1983). The toroidal mode represents

Name	Period (s)	Frequency
Pc1	0.2-5	0.2-5 Hz
Pc2	5-10	0.1-0.2 Hz
Pc3	10-45	22-100 mHz
Pc4	45-150	7-22 mHz
Pc5	150-600	1-7 mHz
Pi1	1-40	0.03-1 Hz
Pi2	40-150	7-25 mHz

**Table 1.1:** Classification of ULF waves following Jacobs *et al.* (1964).

a displacement in the azimuthal direction with an azimuthal magnetic perturbation while poloidal mode represents a radial displacement with radial magnetic perturbation. ULF waves can also be classified into two groups based on their azimuthal scale length. Those with a small azimuthal scale length which give a large effective azimuthal wavenumber ( $m$ ) are commonly referred to as high- $m$  waves with absolute azimuthal wave number ( $|m| \sim 20-100$ ) and those with large azimuthal scale length, as low- $m$  waves ( $|m| \sim 0-5$ ) (Chisham *et al.*, 2007). In general, high  $m$  waves are poloidal and low  $m$  waves toroidal, although intermediate polarisations and azimuthal scale lengths are also observed. Examples of high- $m$  Pc4 and 5 wave activity are presented in subsequent chapters while the Pi2 pulsation is used to identify substorm onset in the studies presented in Chapters 4 and 5 of this thesis.

### 1.6.2.2 ULF Wave Sources

ULF waves are generated by sources external or internal to the Earth's magnetosphere (McPherron, 2005). Solar wind dynamic impulses and instability on the magnetopause are typical examples of sources of externally driven ULF waves in the Earth's magnetosphere (Yeoman *et al.*, 2006). The Earth's magnetosphere, through processes such as the field line resonance (FLR) and the cavity resonance, can transform wave energy that enters from the external sources to the wave signatures measurable on the ground. On the other hand, ULF waves driven from inside the magnetosphere can result from wave-particle interaction through the drift and drift-bounce resonance in the magnetosphere (Hughes & Southwood,

1976), and are mostly associated with high- $m$  azimuthal wave number (Mager & Klimushkin, 2008). These wave generation mechanisms are discussed more in the next chapter.

## 1.7 Earth's Ionosphere

The Earth's ionosphere is the ionised region of the Earth's upper atmosphere, stratified to layers consisting of free electrons and various ionised particles at a density that can affect radio wave propagation. This region extends from a height of about 60 km up to 1000 km (McNamara, 1991). The ionosphere contributes to the plasma population of the magnetosphere and as a result forms an important part of the ionosphere-magnetosphere dynamic interaction. It consists of more charged particles than other regions of the atmosphere as a result of ionisation. The primary source of its ionisation is solar photons as extreme ultraviolet (EUV) and x-ray radiation (Zolesi & Cander, 2014). This radiation breaks apart neutral atmospheric molecules to produce ions and free electrons.

The ionosphere has a number of distinct regions or layers mainly because of the different capacity of the constituent gases to absorb ultraviolet radiation of various wavelengths and thus ionise. These regions, in order of increasing altitude from the Earth's surface as depicted in Figure 1.14 are the D, E, F1 and F2 regions. The ionosphere behaves quite differently at different latitude zones due to the strong geomagnetic field that influences charged particles and results in an anisotropic ionospheric plasma (Buchert, 2007). The D-layer exists at altitudes of about 60 to 90 km above the surface of the Earth during the daytime as the ionisation quickly disappears at night due to the recombination of electrons and ions. The ionisation of this region is primarily due to the absorption of X-rays and Lyman-alpha emissions. It has high neutral molecule density compared to other regions and can form negative ions at night time due to relatively small ultraviolet (UV) light intensity needed to ionise them (Rishbeth, 1988). Next in ascending altitude from the Earth's surface is the E layer, which lies between the D-layer and F-layer of the ionosphere. It exists at an altitude of about 100 to 120 km above the surface of the Earth. Similar to D region, the level of ionisation falls relatively quickly at night as the electrons and ions recombine and virtually

disappear. The photo ionisation and recombination process occur more slowly in the E-layer than in the D-layer and are primarily due to X-rays and EUV, forming mainly  $NO^+$  and  $O_2^+$ . The E layer carries the biggest currents due to the differing dynamics of the ions and electrons.

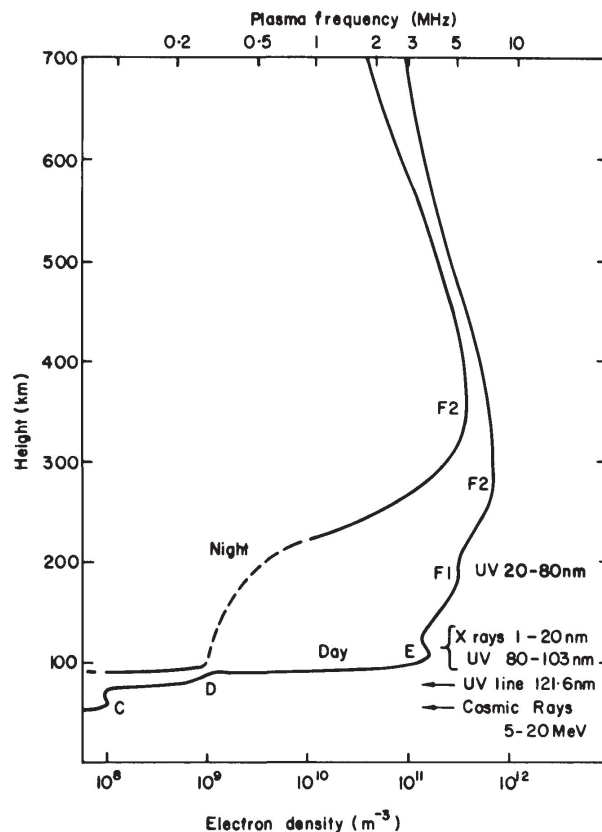


**Figure 1.14:** Illustration of a typical ionospheric mid-latitude electron density profile for day and night time. Taken from (Rishbeth, 1988).

The F-layer is the uppermost of the ionosphere regions with the highest free electron density and stretches from 130 km above the Earth's surface and upwards. It separates into two layers known as F1 and F2 layers during the day when more UV radiation is being received from the Sun resulting in increased ionospheric plasma density. However, the F1 and F2 layers recombine gradually during the night-time with ionospheric plasma density decreasing because

the ionospheric production is much less at nighttime. The F1-region consists of mainly  $NO^+$  and  $O_2^+$  and is situated below the F2 layer, between 150 km and 180 km above the surface of the Earth (Rishbeth, 1988).

### 1.7.1 Ionospheric Modification of ULF Waves

The ULF waves studies presented in the later chapters of this thesis are based on observations from ground-based HF radars and magnetometers. As such, the magnetic field measurements of ULF waves on the Earth's surface by magnetometers for example, have travelled through the ionosphere. Such passage through the ionosphere can affect or modify the structure of ULF waves. Theoretical studies have shown that the two common effects of the ionosphere on ULF waves are rotation of the polarisation ellipse and attenuation of the wave amplitude (Hughes, 1974; Hughes & Southwood, 1976). Also, observational studies such as those reported in Walker *et al.* (1979b); Pilipenko (1990) corroborated the existence of such effects.

The effect of ionospheric rotation on the magnetic field measurement of ULF waves is illustrated in Figure 1.15. Here, the horizontal variation of the field perturbation is assumed to be in the  $y$ -axis with the background magnetic field in the vertical direction, which is typical of the vertically inclined high latitude magnetic field geometries. In the magnetosphere, the magnetic perturbation  $\mathbf{b}$  is in the  $x$ -axis with Electric field  $\mathbf{E}$  in the  $y$ -axis, with energy propagating downward along with field aligned currents. This describes the characteristic configuration of an Alfvén wave propagating down in the magnetosphere toward the ionosphere. As the ULF wave enters the E region of the ionosphere as shown in Figure 1.15, increasing ion collision frequency results in the wave electric field driving a Pedersen current  $j_y$  in the  $y$ -axis perpendicular to the magnetic perturbation of the wave. Hughes (1974) shows that the magnetic field perturbation of the Pedersen current on the Earth's surface, which is in the  $x$ -axis following Ampère's law, encounters screening effect due to the Pedersen current. This screening effect of magnetic perturbations observed on the ground, resulting from the ionospheric rotation, can lead to wave polarisation and spatial integration and attenuation of the wave amplitude (Hughes, 1974). Hughes & Southwood (1976) show that such

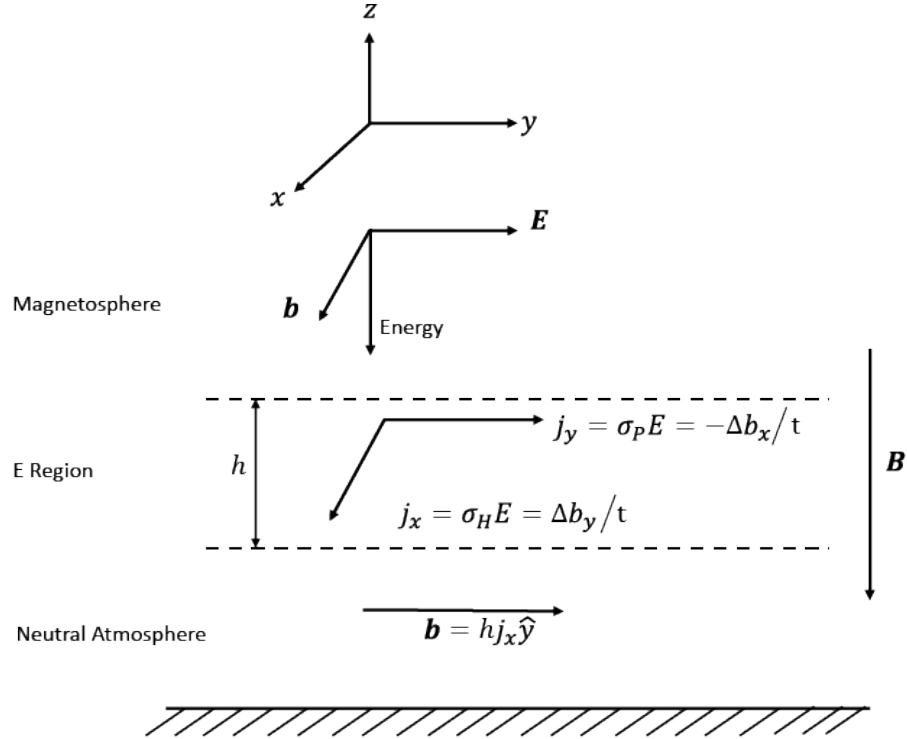


**Figure 1.15:** Schematic illustration of the ionospheric rotation (after, Hughes & Southwood, 1976).

attenuation of the wave magnetic perturbation below the ionosphere is proportional to  $e^{-kz}$ , where  $k$  is the field-perpendicular component of the wave number and  $z$  indicated as  $h$  in Figure 1.15, represents the ionospheric E-region height.

Similarly, a Hall current,  $J_x$ , is produced in the  $x$ -axis as shown in Figure 1.15 as the ULF wave propagates further down in the ionosphere. Following Ampère's law, the magnetic field of the Hall current is in the  $y$ -axis on the Earth's surface. This implies that the magnetic field measurement on the ground is rotated by  $90^\circ$  relative to the magnetosphere. As such, ground-based magnetometers observe magnetic field of the Hall current due to the ULF wave. Thus, ULF waves observed on the ground by magnetometers have undergone modification due to ionospheric screening and rotation compared to waves observed in the ionosphere, for example, from SuperDARN radars (Chisham *et al.*, 2007). The effect of the ionosphere on the ULF wave observations are discussed further in the next chapter.

### 1.7.2 Ionospheric Irregularities

The Earth's ionosphere is characterised by plasma due to ionisation mostly from the Sun's UV radiation. The density of those ionospheric plasmas is oriented in a way that its variations occur rapidly across the geomagnetic field but rarely along the fields (Perkins, 1975). Ionospheric irregularities are small-scale structures with sizes ranging from centimeters to kilometers in such plasma (Fejer & Kelley, 1980). They are field-aligned (Schlegel, 1996), and plasma instabilities in the ionosphere are a major generation process (Fejer & Kelley, 1980). For example, the varying electric current flowing in the equatorial ionosphere known as EEJ - equatorial electrojet (Onwumechikli, 1997), can cause plasma instabilities in the equatorial ionosphere.

Observations of the ionospheric irregularities using radio and radar techniques are used for studies in ionospheric physics and the magnetosphere at large. Instruments and techniques that require ionospheric irregularities for their functioning are used for the studies in this thesis. More details of such instrumentation are presented in Chapter 3.

## 1.8 Radio Frequency Ray Tracing

Ray tracing is a useful tool for studying the characteristics of high frequency (HF) radio wave propagation in the ionosphere (Croft, 1972; Davies, 1990). Such propagation can be vertical or oblique sounding of the ionosphere. The Earth's ionosphere is an anisotropic and dispersive medium and, as such, its effect on the HF (3 to 30 MHz) band is important because radio waves propagating through the ionosphere on such frequencies are normally reflected and refracted due to the ionospheric density gradients. At frequencies lower than 3 MHz radio waves propagating in the ionosphere encounter heavy absorption and on frequencies much higher than 30 MHz they are not normally reflected from the ionosphere.

The refractive capability of the ionosphere when a radio wave passes through it is important in HF ionospheric experiments. As such, radio refractive index of the ionosphere is useful in understanding radio ray tracing. The mathematical theories of radio propagation in the ionosphere in the presence of the Earth's

magnetic field were developed by Sir Edward Appleton and others, thus, the formula for the refractive index is commonly known as Appleton or Appleton-Hartree (A–H) formula (Davies, 1990).

The A–H theory is used in describing radio wave propagation in a uniform magnetised plasma and can be solved using Maxwell’s third (Faraday’s law) and fourth (Ampère-Maxwell law) equations as earlier written as Equation 1.41(c and d) for electromagnetic waves propagating in a conductor.

Taking the curl of both sides of Faraday’s law (Equation 1.41c) gives

$$\nabla \times \nabla \times \mathbf{E} = -\frac{\partial}{\partial t} (\nabla \times \mathbf{B}) \quad (1.52)$$

Substituting for  $\nabla \times \mathbf{B}$  in the RHS of Equation 1.52 from the Ampère-Maxwell law (Equation 1.41d) produces

$$\nabla \times \nabla \times \mathbf{E} + \frac{1}{c^2} \frac{\partial^2 \mathbf{E}}{\partial t^2} + \mu_0 \frac{\partial \mathbf{j}}{\partial t} = 0 \quad (1.53)$$

where  $\frac{1}{c^2}$  is equivalent to  $\mu_0 \varepsilon_0$ . Applying the vector identity  $\nabla \times \nabla \times \mathbf{F} = \nabla (\nabla \cdot \mathbf{F}) - \nabla^2 \mathbf{F}$ , and assuming that  $\nabla (\nabla \cdot \mathbf{F})$  is zero here, the wave equation in a conductor becomes

$$\nabla^2 \mathbf{E} - \frac{1}{c^2} \frac{\partial^2 \mathbf{E}}{\partial t^2} - \mu_0 \frac{\partial \mathbf{j}}{\partial t} = 0 \quad (1.54)$$

We can set  $\mathbf{j} = \underline{\underline{\sigma}} \mathbf{E}$  where  $\underline{\underline{\sigma}}$  is the conductivity tensor. Assuming that  $\mathbf{E}$  and  $\mathbf{j}$  vary in the form  $\exp [i(\mathbf{k} \cdot \mathbf{r} - \omega t)]$ , then we can relate the wave parameters together as

$$\mathbf{k} \times (\mathbf{k} \times \mathbf{E}) - \frac{\omega^2}{c^2} \mathbf{E} - i\omega \mu_0 \underline{\underline{\sigma}} \mathbf{E} = 0 \quad (1.55)$$

where the vector  $\mathbf{k}$  describes the change of phase per unit distance described by the position vector,  $\mathbf{r}$  and  $\omega$  is the change of phase in radians per unit time (see, Davies, 1990).

On the other hand, the equation of motion for an electron in an electric and magnetic field, with collisions, can be expressed as

$$m \frac{d\mathbf{v}}{dt} = (e\mathbf{E} + e\mathbf{v} \times \mathbf{B}) - m\nu\mathbf{v} \quad (1.56)$$

where the term of the left side describes the electron inertia and the terms in the right side are the Lorentz force and collisional force with  $\nu$  being the collision frequency.

## 1.8 Radio Frequency Ray Tracing

---

It is conventional to use three dimensionless parameters,  $X$ ,  $Y$ ,  $Z$  to characterise the A–H equation to describe the effect of electrical conductivity ( $\underline{\sigma}$ ). Following Davies (1990),

$$X = \frac{Ne^2}{\varepsilon_0 m \omega^2} = \frac{\omega_p^2}{\omega^2} \quad Y = \frac{eB}{m\omega} = \frac{\Omega}{\omega} \quad Z = \frac{\nu}{\omega}$$

where the frequencies  $\omega$ ,  $\Omega = eB/m$ ,  $\omega_p$  and  $\nu$  represent the frequency of incident wave, electron gyrofrequency, plasma natural frequency and electron collision frequency respectively. The parameter  $Y$  has a transverse ( $Y_T = \frac{\omega_T}{\omega}$ ) and longitudinal ( $Y_L = \frac{\omega_L}{\omega}$ ) components where  $\omega_T$  and  $\omega_L$  are a function of the direction of propagation with respect to the geomagnetic field. Substituting  $\mathbf{j} = Ne\mathbf{v}$  into Equation 1.56 gives

$$\frac{d\mathbf{j}}{dt} = \frac{Ne^2}{m}\mathbf{E} + \frac{eB}{m}\mathbf{j} \times \hat{\mathbf{B}} - \nu\mathbf{j} \quad (1.57)$$

Using  $\exp[i(\mathbf{k} \cdot \mathbf{r} - \omega t)]$  and substituting in for the dimensionless parameters above gives

$$-i\omega\mathbf{j} = \varepsilon_0\omega^2 X\mathbf{E} + \omega Y\mathbf{j} \times \hat{\mathbf{B}} - \omega Z\mathbf{j} \quad (1.58)$$

Equation 1.58 relates  $\mathbf{E}$  and  $\mathbf{j}$  in terms of  $X$ ,  $Y$  and  $Z$ , which determines the conductivity, such that where collisions are not important, then  $Z = 0$ , and if there is no magnetic field then  $Y = 0$ . Neglecting both collisions and magnetic field, Equation 1.58 reduces to

$$\mathbf{j} = i\varepsilon_0\omega X\mathbf{E} \quad (1.59)$$

The refractive index,  $n$  of an ionised medium such as the Earth's ionosphere in the A–H equation can be described from Equation 1.59, which can also be expressed as  $n = \sqrt{1 - X}$  where absorption is neglected (see, Davies, 1990). If  $n^2 = 0$  then reflection of the radio wave occurs, such that  $1 - X = 0$ , also expressed as  $\omega_p = \omega$ .

Generally, collisions and the magnetic field cannot be neglected in the ionosphere (where there are many collisions and the magnetic field is strong). However, for HF waves, the wave frequency is much greater than the gyrofrequency, so  $Y$  is extremely small. Similarly, the wave frequency is much greater than the

collision frequency so  $Z$  is extremely small. Hence, the last two terms in Equation 1.58 can be neglected. For further information on radio signals propagating through the ionosphere, see (e.g., Ratcliffe, 1959; Davies, 1990).

When a radio signal is transmitted to ambient space from a ground-based instrument such as an HF radar, some of the energy enters the ionosphere, where the waves undergo refraction, penetration or reflection back to the ground. The behaviour of the radio waves depends on the transmit frequency, the ionospheric condition as well as the elevation angle. For ionospheric related studies using radio and radar techniques, the transmit frequency is normally larger than the maximum ionospheric plasma frequency. A ray tracing technique can be used to calculate the ray paths of the wave between the transmitting and receiving ends (Bennett *et al.*, 2004). The information about the ray path is useful for determining some features of the received signal, such as amplitude, polarisation, relative phase, time of flight and Doppler shift. In the ray tracing analysis presented in Chapter 6, both collisions and magnetic field are neglected, as such, the refractive index of the ionospheric electron density can be described by Equation 1.59. More descriptions of radio ray tracing techniques used for ionospheric related studies can be found in (e.g., Croft, 1972; Bennett *et al.*, 2004).

The radio wave travelling through the ionosphere is affected by the Earth's magnetic field. An example of such an effect is the splitting of an incident wave into an ordinary (' $O$ ' mode) wave, which is left-handed with respect to the magnetic field and a right-handed extraordinary (' $X$ ' mode) wave. For the ordinary wave mode, the radio wave propagation is equivalent to the local plasma frequency where collisions and magnetic field are neglected. In oblique propagation, such effects complicate the echo structure given that these radio waves travel different paths in the ionosphere (Davies, 1990). These effects are ignored in the studies in Chapter 6 because there is no evidence of significant effects from  $O$  and  $X$  mode polarisation from SuperDARN radars (e.g., Chisham *et al.*, 2008; Yeoman *et al.*, 2008b; de Larquier *et al.*, 2013), the application under examination here. However, by point-by-point ray tracing, the ray path can still be integrated when the magnetic field is included. The numerical ray tracing allows the ionosphere to vary in three dimensions and can take into consideration the magnetoionic (propagation of radio waves in uniform magnetised plasma) effects within the

## 1.8 Radio Frequency Ray Tracing

---

limitations of quasi-optics (Bennett *et al.*, 2004). An existing and widely used program based on numerical ray tracing is Jones & Stephenson (1975).

In HF radar ionospheric related studies (e.g., Fejer & Kelley, 1980; Röttger, 2004; Hocking, 2011), applications of ray tracing calculations can be categorised into those involving system planning or analysis of experiments already carried out, and those carried out as part of an operational system or interactive experiment (Bennett *et al.*, 2004). The former category of applications of ray tracings applies to the studies presented in Chapter 6 of this thesis, where ray tracing is used for simulating HF ionospheric radar performances for three proposed SuperDARN-type radars at African equatorial latitude locations.

# Chapter 2

## Literature Review

The last chapter has described a number of theoretical concepts relevant to the studies presented in this thesis. The aim of this thesis is categorised into two broad segments. The first segment is a case study and a statistical analysis of the temporal and spatial evolution of intermediate- $m$  ULF waves driven by energetic particles injected during substorms using SuperDARN radar and magnetometer datasets. While the second segment uses a ray tracing simulation to predict the performances of three proposed SuperDARN radars at African equatorial latitudes and following the analysis, provides technical recommendations for their future development.

This chapter presents a review of some existing literature applicable to ULF waves due to wave-particle interactions observed from similar multi-instrument datasets employed in the present wave study. It also discusses previous studies relevant to HF ionospheric radar experiments at equatorial African region and some prior ray tracing modelling for SuperDARN radars at high and mid latitudes.

### 2.1 Magnetospheric ULF Waves

Ultra low frequency (ULF) waves of the Earth's magnetosphere are generated by processes in the magnetosphere and solar wind (Hughes, 1994; McPherron, 2005). Such waves act as a conduit of energy and momentum distribution between the

## 2.2 Low- $m$ ULF Waves and Field Line Resonance

---

magnetosphere and ionosphere and can be classified in two types based on azimuthal scale structure as high- $m$  and low- $m$  waves (e.g., Yeoman *et al.*, 2006). Such classes of ULF waves are described in terms of the predominant wave polarisation as toroidal or poloidal modes (e.g., Klimushkin *et al.*, 2004; James *et al.*, 2013). Usually, low- $m$  (large azimuthal scale size) are thought to be of toroidal mode.

As discussed in the previous chapter, azimuthal wave number  $m$  of a ULF wave, commonly known as  $m$  number, is an important factor for determining the contribution of ULF wave-particle interactions to the dynamics internal to the magnetosphere (Murphy *et al.*, 2018). The azimuthal wave number  $m$  indicates the number of degrees of wave phase gradient per degree of magnetic longitude. It is inversely proportional to a ULF wave's azimuthal scale size.

## 2.2 Low- $m$ ULF Waves and Field Line Resonance

The majority of the ULF waves observed on the Earth's surface are thought to originate from sources external to the magnetosphere (Yumoto, 1988). Such waves generated from external sources such as the solar wind usually have an azimuthal scale structure that is large with  $m$  number of  $\sim 1$  (Yeoman *et al.*, 2006), and are known as low- $m$  waves. A common convention is that the sign preceding  $m$  number indicates the direction of the phase propagation of the wave. Here, positive  $m$  numbers denote waves with eastward phase propagation while negative  $m$  numbers are for waves with westward phase propagation.

The low- $m$  waves are toroidal modes primarily driven by sources external to the Earth's magnetosphere (e.g., Yeoman *et al.*, 2006; Agapitov & Cherenmykh, 2013). For example, via resonance of the Earth's magnetic field line with the fast mode propagating through the magnetopause (e.g., Yeoman *et al.*, 2006). Buffeting of the magnetosphere by variations in solar wind dynamic pressure can generate fast mode waves. Also, the rapid change in the solar wind velocity across the magnetopause can lead to processes such as the Kelvin-Helmholtz Instability that can drive a fast compressional wave in the magnetosphere (Lessard *et al.*, 1999; Rae *et al.*, 2005). The compressional waves from KHI or buffeting can couple with field-aligned Alfvén waves when their frequencies match the natural

frequencies of the field lines, driving toroidal Alfvén waves with a large azimuthal scale.

A field line resonance (FLR) is a shear Alfvén wave standing on the Earth’s magnetic field lines between the two conducting ionospheres (Samson *et al.*, 1992; Walker, 2005). The coupling of standing shear Alfvén waves on Earth’s magnetic field lines to fast-mode compressional MHD waves in the outer magnetosphere leads to field lines resonances (Fenrich & Samson, 1997). The field line resonance mechanism was first suggested in (Tamao, 1965). It has been applied in theoretical studies (e.g., Southwood, 1974; Chen & Hasegawa, 1974a,b) to describe ULF waves observed by (Samson *et al.*, 1971). Likewise, there are observations from ground-based instruments like magnetometers and HF radars (e.g., Walker *et al.*, 1979a; Fenrich *et al.*, 1995) and from spacecraft (e.g., Agapitov *et al.*, 2009) that support its existence. Apart from driving low- $m$  waves, field line resonance can generate high- $m$  waves (Fenrich & Samson, 1997). Some examples of features of field line resonances are a broad peak of wave amplitude at the resonant region and a  $180^\circ$  phase shift across the resonance region (e.g. Walker *et al.*, 1979a). The peak amplitude and  $180^\circ$  phase shift occur over the same region of latitudes. Field line resonance and ULF waves with low- $m$  number are not the main focus of the wave observations presented in Chapters 4 and 5 of this thesis.

## 2.3 High- $m$ ULF waves

High- $m$  ULF waves are usually poloidal modes and are understood as being driven by sources internal to the Earth’s magnetosphere (Yeoman *et al.*, 2016). Energetic particles are deposited in the magnetotail through processes such as magnetospheric reconnection between the interplanetary and terrestrial magnetic fields, which could lead to a subsequent substorm activity. Such energetic particles enter into the inner magnetosphere and will experience gradient-curvature drift. These gradient-curvature drifting particles move around the Earth and as such form part of the global ring current. Also, these particles can drive MHD wave modes in the inner magnetosphere, resulting in perturbations in the electric and magnetic fields both in the magnetosphere and ionosphere when free energy is available to the wave. Such energy sources due to wave-particle interactions in the

magnetosphere, commonly generate waves with high- $m$  values or small azimuthal scale sizes.

As stated in the above, high- $m$  waves can be excited by unstable particle populations by means of the drift-bounce or drift instability. Such unstable particles can be protons or electrons. Karpman *et al.* (1977) suggested that such unstable proton particles have energies of about 10 to 150 keV. ULF waves from such mechanisms can be due to a condition for which the part of the ion distribution function (IDF) feeds energy into the wave at the point where  $\partial f/\partial W > 0$ , with  $f$  representing the ion distribution function and  $W$  the energy (e.g., Southwood, 1976; Hughes *et al.*, 1978). These non-Maxwellian IDFs also referred to as “bump-on-tail” distributions can be created quite often by naturally-occurring processes in the magnetosphere. An example of such a process is a substorm-associated particle injection in the magnetosphere. Subsequent to such an injection, the ions (or electrons) species will gradient-curvature drift in the westward (or eastward) direction and occasionally, will match the local drift-bounce resonance condition (Southwood *et al.*, 1969),

$$\omega_{wave} - m_{wave}\omega_d = N\omega_b \quad (2.1)$$

where the integer  $N$  is either zero in the case of a drift resonance or  $\pm 1$  for drift-bounce resonance. The other parameters,  $\omega_{wave}$ ,  $m_{wave}$ ,  $\omega_d$  and  $\omega_b$  in either cases are the angular frequency of the wave, the effective azimuthal wave number, the proton (or electron) azimuthal drift and the proton bounce angular frequencies respectively. Conventionally, if the azimuthal wave propagation is eastward (westward),  $m$  number of wave is defined as positive (negative). Wave-particle interactions of this nature are a process of fundamental importance in collisionless astrophysical plasmas.

Previous studies have shown that such high- $m$  waves are observed both in in-situ spacecraft and ground-based measurements such as HF coherent ionospheric radars (James *et al.*, 2016). Also, ULF wave activities with a high- $m$  azimuthal signature have been observed from an imaging riometer system as reported in Beharrell *et al.* (2010). Analysis presented in Chapters 4 and 5 of this thesis are observations from ground-based HF radar and magnetometer instruments.

### 2.3.1 Ground-Based Observations

Ground based magnetometer datasets have been widely applied in ULF wave studies prior to more recent HF radar techniques. The magnetic perturbations observed on the ground using magnetometers have undergone modifications due to ionospheric rotation leading to wave polarisation and spatial integration and attenuation of the wave magnetic signature, which represent the differences between the magnetometer and radar measurements (Chisham *et al.*, 2007). The attenuation of the wave magnetic perturbation below the ionosphere is proportional to  $e^{-kz}$ , where  $k$  is the field-perpendicular component of the wave number and  $z$  represents the ionospheric E-region height (Hughes & Southwood, 1976). This screening action of the ionosphere makes high- $m$  wave detection in magnetometer data unlikely, which is not the case for satellites and radar instruments. For instance, magnetometer and radar measurements have relative advantages given that whilst HF radars have good spatial resolution, magnetometers have high temporal resolution. As such, both instruments and techniques complement each other and have been applied together for robust analysis and study of magnetospheric ULF waves (e.g., Mtumela *et al.*, 2015), which clearly demonstrates the benefit of multi-instrument wave studies. As a result of the high spatial resolution capabilities of SuperDARN radar measurements, they have shown to be useful in the study of high- $m$  waves of small azimuthal scale length (e.g., Wright & Yeoman, 1999; Baddeley *et al.*, 2002; Yeoman *et al.*, 2010; Pilipenko *et al.*, 2012; Mager *et al.*, 2015; Chelpanov *et al.*, 2016; James *et al.*, 2016).

### 2.3.2 Quiet Time Observations

A class of ULF waves that are relatively high- $m$  waves are giant pulsations (Pgs). Based on previous observations, giant pulsation occurrence is rare and usually in the morning sector with an azimuthal wave number,  $m$  in the range of 16 to 35 (e.g., Rostoker *et al.*, 1979; Takahashi *et al.*, 2011), propagating westward around the Earth. A statistical study by Chisham & Orr (1991) using 34 events observed by the EISCAT cross magnetometers showed that such pulsations are mainly poloidal mode with average azimuthal wave number of  $\sim 26$ .

Giant pulsations and associated phenomena have been observed from ground magnetometers (e.g., Rostoker *et al.*, 1979; Chisham *et al.*, 1990; Chisham & Orr, 1991; Chisham *et al.*, 1992; Takahashi *et al.*, 1992; Chisham & Orr, 1994; Glassmeier *et al.*, 1999; Wright *et al.*, 2001; Takahashi *et al.*, 2011; Watson *et al.*, 2016). Such observations have shown that Pgs are monochromatic oscillations of the Earth's magnetic field in the Pc4 band (45 - 150 s) frequency range. The structure of giant pulsations are highly sinusoidal with the wave amplitude modulating as a long duration wave packet. Such previous studies utilising ground magnetometer data have shown that Pg's amplitude is maximum in the magnetic perturbations in the D-coordinate and they also exhibit a resonant latitudinal phase profile. The east-west perturbation is an indication that the polarisation of Pgs in the magnetosphere is poloidal since the field lines oscillate radially. Mager & Klimushkin (2013) have suggested that the prevailing poloidal polarisation and the wave packet shape of modulating amplitude can be described by a trapping of Pg waves in a magnetospheric resonator.

Other instruments have also been employed for studying giant pulsations and their related wave observations. Pgs have been observed from spacecraft (e.g., Hughes *et al.*, 1979; Kokubun *et al.*, 1989; Takahashi *et al.*, 1992; Glassmeier *et al.*, 1999; Takahashi *et al.*, 2011; Watson *et al.*, 2016; Yamamoto *et al.*, 2018) and from HF radar (e.g., Chisham *et al.*, 1992). Such observations have similar wave characteristics as ground magnetometer observations. However, Mager & Klimushkin (2013) noted that they detect a considerable compressional magnetic field component as well in the case of (e.g., Hughes *et al.*, 1979; Kokubun *et al.*, 1989). In contrast, Takahashi *et al.* (2013) reported waves observed from spacecraft propagating westward azimuthally with a fundamental poloidal mode and attributes similar to Pgs but not detected in ground magnetometers due to a likely ionospheric screening given their large  $m$  number ( $\sim 70-200$ ). Takahashi *et al.* (2013) noted that such ground observations of Pgs shows that they are a subset of fundamental poloidal waves excited in the magnetosphere. While Watson *et al.* (2016) observed a Pc4 wave activity with characteristics associated with giant pulsation in the magnetic field data from magnetically connected ground magnetometer and satellite as well as in the variation of Total Electron Content (TEC) inferred from GPS data. Applying GPS TEC data in studying ULF waves

is a relatively new technique (Watson *et al.*, 2016). Likewise, poloidal pulsations with characteristics consistent with giant pulsations have been observed from ionospheric HF Doppler radar along with magnetometers (Wright *et al.*, 2001; Baddeley *et al.*, 2004, 2005) and optical instrumentation (Chisham *et al.*, 1992).

Many authors have now linked the generation mechanism of giant pulsations to wave-particle interactions of a second-harmonic poloidal mode as described in (e.g., Chisham & Orr, 1991; Chisham *et al.*, 1992; Baddeley *et al.*, 2005). These waves occur in a magnetosphere during quiet times or in a magnetosphere recovering from a prior activity (Rostoker *et al.*, 1979). Likewise, the rarity of giant pulsations during quiet time has been suggested as due to the low proton energy ( $\sim 5\text{-}30$  keV) driving these pulsations (Chisham, 1996). At undisturbed times, the proton particles of  $\sim 5\text{-}30$  keV injected into the inner magnetosphere on the nightside will drift westward around the Earth on enclosed paths for small  $\mathbf{E} \times \mathbf{B}$  drifts due to the magnetospheric convection and corotation electric fields (Chisham, 1996). (Takahashi *et al.*, 2011) ascribed a Pg wave activity observed from multisatellite observations to poloidal standing Alfvén waves with an odd fundamental mode structure along the field line. Chisham & Orr (1991) suggested that Pgs are second harmonic standing wave oscillations. Drift wave instability of the compressional Alfvén wave at the outward part of the quiet time ring current has been suggested as a possible generation mechanism especially for oscillations with odd mode and the bounce resonance mechanism, which requires the Pgs waves to be even mode oscillations (Chisham & Orr, 1991). Whether the structure of Pg oscillations is even or odd and the wave driving mechanisms are yet to be sufficiently addressed (Chisham & Orr, 1991; Takahashi *et al.*, 2011; Mager *et al.*, 2019). However, the wave characteristic features and the driving mechanism rather than the symmetric or antisymmetric structure is more of interest to this present study as it will be applied in interpreting a wave in the Pc4 frequency band detected in the magnetometer data in Chapter 4.

## 2.4 Intermediate- $m$ ULF waves

Yeoman *et al.* (2010) in a case study of ULF waves, classified waves with azimuthal wave number in the range of  $\sim 10$ -15 as intermediate- $m$  ULF waves. The wave event reported in Yeoman *et al.* (2010) was linked to energetic particles injected by substorm activity and it exhibited an equatorward latitudinal phase propagation with a predominant poloidal mode. Such observational features are consistent with behaviours associated with high- $m$  waves (e.g., Tian *et al.*, 1991; Grant *et al.*, 1992; Yeoman *et al.*, 1992; Fenrich *et al.*, 1995; Yeoman *et al.*, 2008a). As such, intermediate- $m$  waves can be likened to high- $m$  ULF waves, but with lower  $m$  values.

In a recent paper on ULF waves, Mager *et al.* (2019) reported a wave of 1.8 mHz, propagating westward in the ionosphere with  $m$  number of  $\sim 10$  as observed from a SuperDARN-type radar and the Van Allen Probes mission spacecraft data. During the interval they observed the wave event, the magnetospheric activity indices such as SYM-H of  $\sim -15$  nT, maximum planetary Kp index of 3+ as shown in Figure 2.1 suggested a weak perturbation of the magnetosphere but also showing an increased magnetic activity attributed to the IMF  $B_z$  changing southward in direction several times. The authors ascribed the wave event to a drift-compressional mode due to substorm-injected proton particles with energy of about 90 keV leading to drift wave-particle resonance.

Intermediate- $m$  ULF waves can be driven by the same wave-particle interactions inside the magnetosphere via drift-bounce instability process for high- $m$  waves as discussed in Section 2.3. They have also been generated by neither the mechanism espoused in the (Yeoman *et al.*, 2010; Mager *et al.*, 2019) nor the mechanism described in Section 2.3. For instance, a wave with  $m$  number of 14 observed by Hao *et al.* (2014) was attributed to interplanetary shock, which is a predominant generation mechanism for low- $m$  waves. Thus, the generation mechanisms of intermediate- $m$  waves are yet to be fully understood. Chapters 4 and 5 will discuss intermediate- $m$  ULF wave observations using SuperDARN radar and ground magnetometer datasets. As earlier noted, ground magnetometers and HF radars are synergistic instrument types for studying ULF waves (e.g., Mtumela *et al.*, 2015).

## 2.5 Substorm-injected Particles Driven ULF Waves

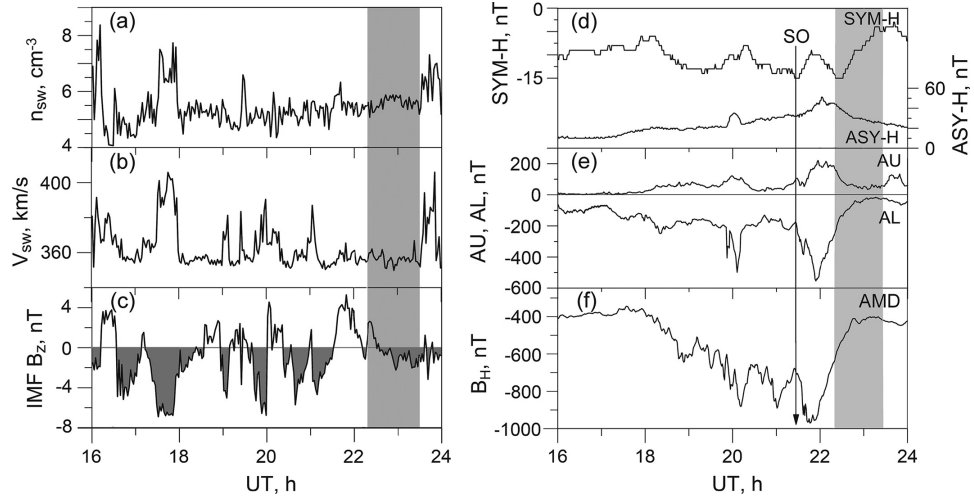


**Figure 2.1:** This figure, taken from Mager *et al.* (2019), shows the state of the solar wind and magnetosphere for 16–24 UT on 22 November 2014 during the interval in which they reported an intermediate- $m$  wave observed simultaneously from a radar and spacecraft. Where (a) and (b) represent the density ( $n_{sw}$ ) and velocity ( $V_{sw}$ ) of the solar wind; (c) the  $B_z$  component of the interplanetary magnetic field (IMF  $B_z$ ); (d) ASY-H and SYM-H geomagnetic indices (1 min high-resolution global storm indexes); (e) AU and AL auroral indices; (f) horizontal component of the magnetic field  $B_H$  according to AMD geomagnetic station (Mager *et al.*, 2019, and therein). The gray stripes denote the interval of the reported wave event and the arrow denotes the substorm onset.

## 2.5 Substorm-injected Particles Driven ULF Waves

Some previous ULF wave related observations by HF ionospheric radar (e.g., Yeoman *et al.*, 2010; James *et al.*, 2013, 2016) and from satellite data (e.g., Zolotukhina *et al.*, 2008; Chen *et al.*, 2017; Rubtsov *et al.*, 2018) have been attributed to energetic particles injected by substorms in the Earth’s magnetosphere. As stated in the last section, the substorm is a typical naturally-occurring process in the magnetosphere that can provide bump-on-tail distributions, which can give energy for ULF wave growth. Many of such substorm-injected particles driven waves have a poloidal mode. A possible driving mechanism of this kind of wave suggested by Mager & Klimushkin (2007, 2008); Mager *et al.* (2009), was that a

## 2.5 Substorm-injected Particles Driven ULF Waves

non-steady azimuthal current resulting from substorm-injected particles drifting azimuthally in the magnetosphere, generate the poloidal ULF waves.

Another feature observed in substorm particle-driven ULF waves (e.g., Zolotukhina *et al.*, 2008) was mixed polarisation. Wave polarisation tends to transform from poloidal to toroidal mode and vice versa. Likewise, Mager & Klimushkin (2007, 2008), proposed that such waves begin with mixed polarisation and progress to poloidal as the wave together with the energetic particles from the substorm propagate away from where the particles were injected. Subsequently, the waves will progress into a toroidal polarisation with a likely decrease in wave amplitude due to attenuation resulting from wave-particle interactions and a finitely conducting ionosphere.

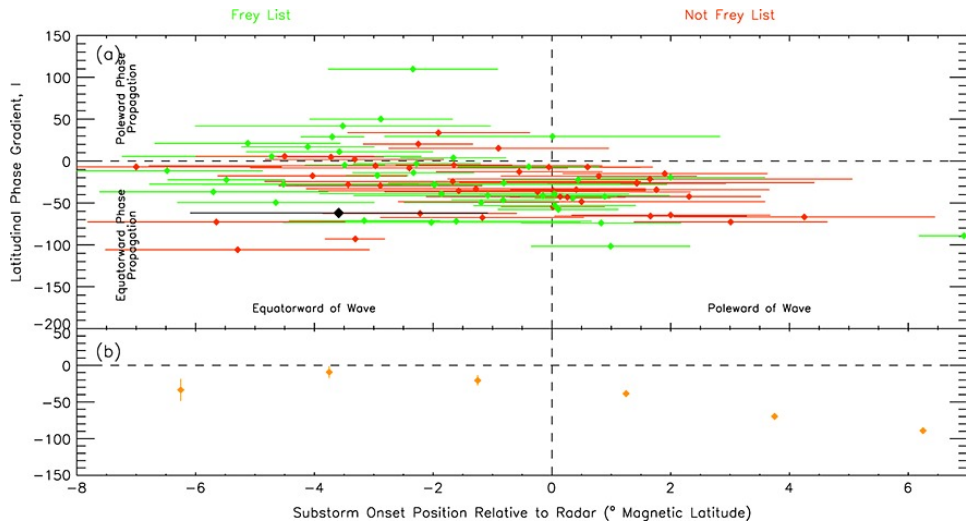


**Figure 2.2:** This figure, taken from James *et al.* (2013), shows that a clear majority of substorm-injected particles driven waves propagate equatorward as indicated by a plot of latitudinal phase gradient for the waves against the magnetic latitude separation of the waves from the substorm onset positions.

Substorm-injected particle driven ULF waves mostly exhibit equatorward phase propagation as shown, for example, in a statistical study of such waves by James *et al.* (2013). Studying 83 multiple SuperDARN radar observations of similar ULF wave events associated with energetic particles injected by substorms, many of which were earlier identified in (Frey *et al.*, 2004), James *et al.*

## 2.5 Substorm-injected Particles Driven ULF Waves

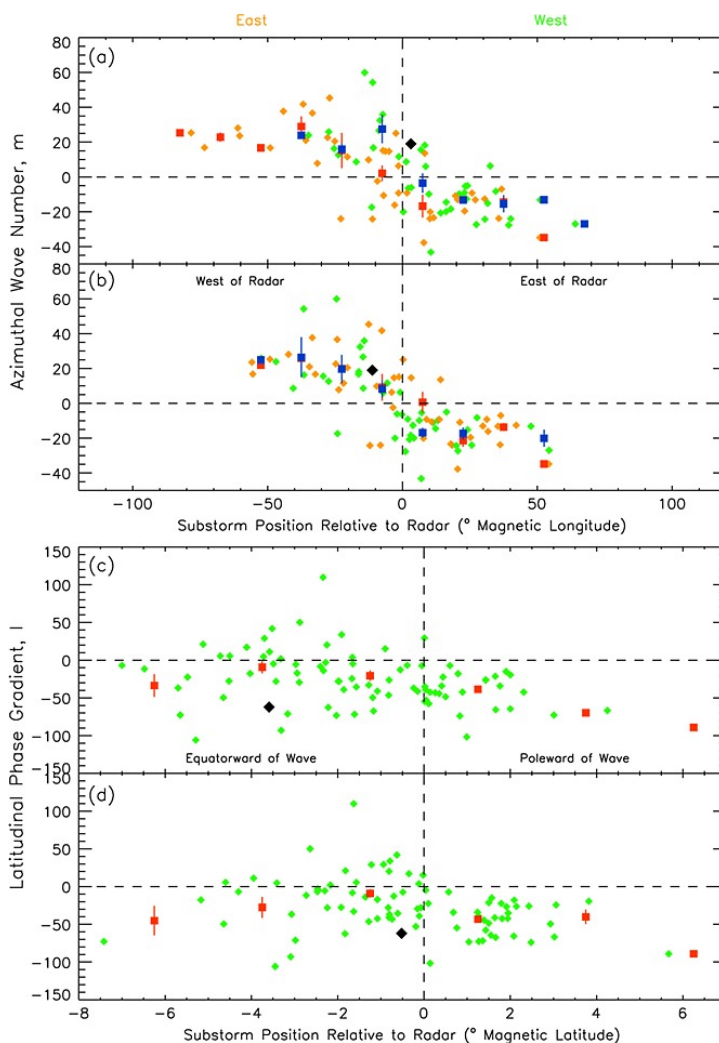


**Figure 2.3:** Variation of (a) Azimuthal wave numbers,  $m$  of ULF waves versus the distance from substorm onset position for comparison with (b)  $m$  relative to the substorm location when the substorms have expanded to their largest size. Where green data points denote events in which the substorms have expanded in the westward direction while orange data points denote eastward expansion. They (a and b) also show the eastward expanding (red) and westward expanding (blue) wave events placed into  $15^\circ$  bins shown by square symbols. Likewise, (c) and (d) show latitudinal phase gradient,  $l$ , against latitudinal separation of substorm UV aurora and observed wave in green at the substorm onset time (c) and after expansion (d). The red square points in (c) and (d) represent the green data points for  $2.5^\circ$  bins. From James *et al.* (2013)

---

## 2.6 Previous Studies Related to HF Ionospheric Ray Tracing

(2013) showed, as depicted in Figure 2.2 that the majority of such waves exhibited equatorward latitudinal phase propagation while those with poleward phase propagation were few in number. This paper also confirmed a prior suggestion by Yeoman *et al.* (2010) that the properties of these substorm-injected particle driven ULF waves such as azimuthal  $m$  number and the particle energy are dependent on the proximity of the wave observations to the substorm onset as shown in Figure 2.3, with higher energy particles (leading to lower  $m$ -number waves) resulting from smaller azimuthal separations between wave observations and substorm onset.

A suggestion in Mager *et al.* (2009) provides an explanation for the predominance of equatorward phase propagation of substorm-injected particle driven waves. From a model of wave excitation by an azimuthally drifting particle inhomogeneity during substorm activity, Mager *et al.* (2009) showed that as a cloud of particles is injected into the magnetosphere at some azimuthal position following substorm onset (the particles continue to drift azimuthally away from injection point), the cloud is elongated into a spiral in the equatorial plane, leading to a radial component of the phase velocity being directed towards the earth (equatorward phase propagation) if the angular drift frequency ( $\omega_d$ ) increases with the radial coordinate (L-shell) (Mager *et al.*, 2009).

## 2.6 Previous Studies Related to HF Ionospheric Ray Tracing

Ray tracing is a useful tool for studying and understanding the Earth's ionosphere and radio wave propagation through the ionosphere (Bennett *et al.*, 2004). There are many existing studies in which ray tracing has been used to model and interpret observations from experiments utilising radio propagation through the ionosphere. For instance, ray tracing has been applied for predicting the geographical locations where orthogonality between a HF radar wave vector and the geomagnetic field can be achieved under various ionospheric conditions at high latitude (e.g., Villain *et al.*, 1984) and mid latitude (e.g., Nishitani & Ogawa,

## 2.6 Previous Studies Related to HF Ionospheric Ray Tracing

---

2005). This is a clear indication of the importance and usefulness of ray tracing. This section presents some previous papers to highlight ray tracing applications.

Farges *et al.* (1999) used ray tracing to characterise possible sources of Type I and II equatorial electrojet irregularities from the structure of echoes observed by a broad-beam HF zenithal radar at equatorial latitudes. The characteristics of frequency spectra from a HF radar backscattering in the equatorial electrojet are classified as Types I and II based on the difference in their features (Sudan, 1983). For example, while the width of the Type I spectrum is narrower than its Doppler shift, that of Type II echoes is comparable to their Doppler shift (Sudan, 1983). They employed ionospheric parameters derived from ionogram measurements during a quiet activity period for the ray tracing modelling, while radar signatures of Type I and II irregularities were inferred from echo intensity and Doppler shift calculated as a function of range.

Ray tracing was used in (Stocker *et al.*, 1999) to synthesise variation of the F-region skip distance, which is a characteristic signature that can be observed in HF radar range time intensity (RTI) plots when travelling ionospheric disturbances (TIDs) are present. The authors compared the ray tracing results with experimental observation and found that the magnitude of the skip variation was a function of the peak electron density perturbation associated with the TID and radar frequency. Thus, they suggested the use of the skip-distance variation as an indicator of the TID perturbation density.

In a similar vein, numerical ray tracing was applied by Yeoman *et al.* (2001) to evaluate the range accuracy of the standard algorithm that SuperDARN radars used for determining ground range location of backscatter measurements. The authors found that the standard algorithm was accurate to within 16 km for direct backscatter and 60 km for  $1^{1/2}$ -hop backscatter. They suggested that in theory, an implication of such findings for SuperDARN measurements would be significant range errors for high elevation-angle backscatter from 2-hop and  $1^{1/2}$ -hop paths. However, such errors for direct backscatter would be within one range gate for SuperDARN radars, which typically operate with a range gate of 45 km.

In a later HF propagation study, Stocker *et al.* (2003) used ray tracing for simulations of HF off-great-circle propagation due to the mid-latitude azimuth trough. This paper studied two possible mechanisms that can lead to changes

## 2.6 Previous Studies Related to HF Ionospheric Ray Tracing

---

in azimuth, which are the propagation along the density gradients that form the equatorward wall of the trough and side scatter from regions of the sea well to the south of the trough, and showed that the simulation of the latter mechanism correlated well with experimental observation.

In a study describing an improved technique for identifying ground scatter and ionospheric scatter in mid latitude SuperDARN data, Ribeiro *et al.* (2011) illustrated the formation of ionospheric and ground scatter in a typical HF ionospheric radar using ray tracing.

de Larquier *et al.* (2011) used ray tracing method coupled with an ionospheric electron densities from the International Reference Ionosphere (IRI) to characterise observations by SuperDARN radar at mid latitude for features of evening enhancement in electron densities.

Warrington *et al.* (2016) used a ray tracing method with the main parameters of the ionosphere deduced from the IRI model and measurements of ionosonde and GPS total electron content (TEC), to model the effects of the polar ionosphere on HF signals. Such a study is important for improving techniques for nowcasting and forecasting HF propagation at polar latitudes, which is useful in airline operation.

Prior to the development of the Hokkaido SuperDARN radar (Nishitani *et al.*, 2019) at a mid latitude location, (Nishitani & Ogawa, 2005) used a ray tracing simulation to identify possible ionospheric backscatter areas at mid-latitude. Nishitani & Ogawa (2005) showed that local time and geomagnetic activity affect the distributions of possible areas where ionospheric backscatter can be realised for mid latitude HF coherent radars. This study is similar to the work presented in Chapter 6 but there we investigate three proposed SuperDARN radars at African equatorial latitude locations.

## 2.7 HF Radar Experiments at Equatorial African Longitudes

There are a few previous HF radar experiments performed over the equatorial latitude region in the African longitude sector. Some of these studies, which are fairly old, are discussed in this section. It is important to note here that as of February 10 2020, there are no currently existing HF coherent radars in this region.

Hanuse & Crochet (1977) reported a multiple frequency HF coherent radar study of plasma instabilities associated with the equatorial sporadic-E from experiments performed in Ethiopia, an equatorial African location. In a similar vein, plasma irregularities associated with the equatorial electrojet (EEJ) were studied by Hanuse & Crochet (1978) using a preliminary HF radar experiment carried out at Sart-Fort Archambault, Chad (long. 18°35E, lat. 09°20N, dip. -3°3); an equatorial location in Africa. At a radar operating frequency of 21.3 MHz, they observed Type I and II irregularities, linked to instabilities associated with the EEJ.

Blanc *et al.* (1996) observed kilometeric scale irregularities in the E and F region ionosphere during daytime from a vertical HF coherent radar experiment at a location in the present day Côte d'Ivoire (long. 5°37'38" W, lat. 9°24'62" N). They suggested a large sporadic E layer within the altitude range of 100-150 km as the origin of the observed irregularities. From a similar location, Blanc & Hounninou (1998) studied the daytime ionospheric structures using a HF zenithal radar.

Farges *et al.* (1999) investigated the possible source of Type I and II equatorial electrojet irregularities from backscatter measurements of a broad-beam HF zenithal radar taken during the International Equatorial Electrojet Year (1993-1994) at an equatorial location in Côte d'Ivoire. The authors reported that the radar operated at a frequency  $\sim 5$  MHz and their observations showed that Type II irregularities from both vertical and oblique directions in the 100-140 km range dominated the spectra from radar measurements while there were no definitive identifications of Type I irregularities. Figure 2.4 is RTI plot from Farges *et al.* (1999), which on the other hand, supports the presence of naturally occurring

## 2.7 HF Radar Experiments at Equatorial African Longitudes

ionospheric plasma irregularities capable of HF radar coherent scattering in the ionosphere in the African equatorial sector. For example, such consideration of the presence of irregularities is important for future development of a SuperDARN radar at an equatorial geographic location.

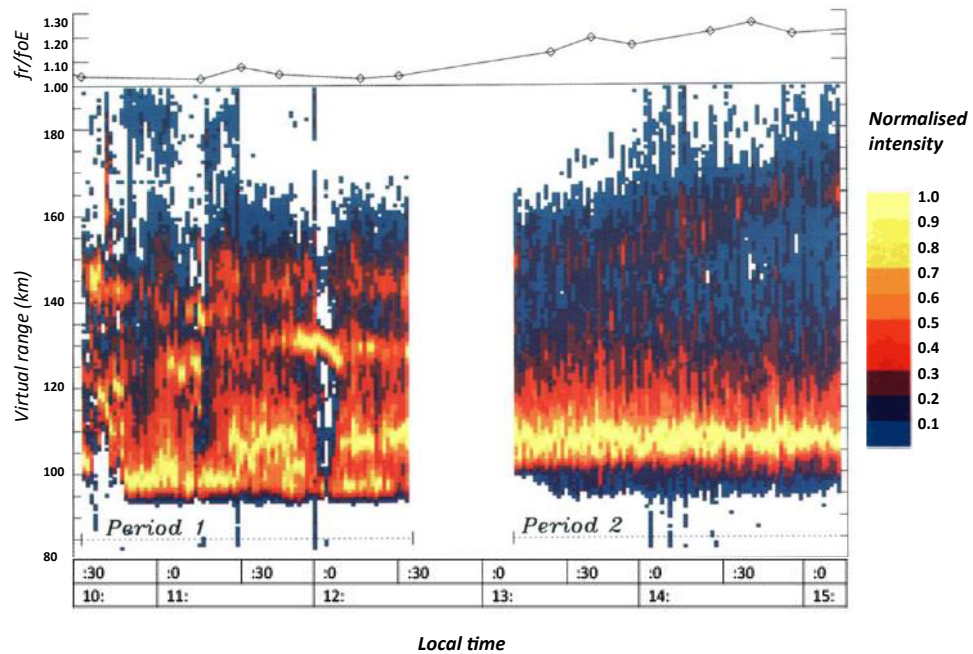


**Figure 2.4:** RTI plot from a broad-beam HF zenithal radar at Korhogo in Côte d'Ivoire, an African equatorial location. Note that the axes labels have been re-created after the original. From Farges *et al.* (1999)

# Chapter 3

## Instrumentation and Analysis Techniques

### 3.1 HF Ionospheric Radar

Radars operating in the HF, VHF and UHF frequency bands have been widely applied in studying the structure and dynamic processes of the Earth's ionosphere (e.g. Röttger, 2004). These scientific studies enhance our understanding of the complex phenomena of the Earth's atmosphere-ionosphere-magnetosphere system and also have useful applications, for example, in the satellite navigation and communication industries. The principles and techniques utilised for studying the ionosphere and magnetosphere using HF radar systems are discussed in this section.

The structure and composition of the ionised region of the Earth's atmosphere, known as the ionosphere, have been discussed in section 1.7 of this thesis. The ionosphere like other parts of the Earth's atmosphere is a dispersive medium with varying refractive indices, which influence waves transmitted from radars operating in any electromagnetic frequency range. The behaviours, such as reflection, refraction and absorption that the wave undergoes are affected by the plasma and critical frequency of the ionosphere. For instance, a typical global representation of the F<sub>2</sub> layer critical frequency will vary between 5 and 17 MHz (Davies, 1990). As a result, incoherent scatter from thermal motions of free elec-

trons in the ionosphere occur when the radar wave frequency far exceeds (up to 500 MHz and more) the critical frequency. This incoherent scattering from the ionosphere is a key principle that Incoherent Scatter Radars (ISRs) use for their operation. On the other hand, coherent scatter of the radar wave results from plasma turbulence, which is a perturbation of the ionisation structure, generated by instabilities in the ionosphere (Röttger, 2004). Coherent scattering occurs on HF and VHF electromagnetic frequencies and is applied for studying the E- and F-region ionospheric irregularities using coherent scatter radars (Greenwald *et al.*, 1995; Chisham *et al.*, 2007), which are the type of radars of primary interest in this thesis.

Coherent and incoherent scatter can also originate from other regions of the Earth's atmosphere. In the troposphere and stratosphere, air turbulence in the neutral atmosphere can cause small deviations of refractive index from variations in density, temperature and humidity, which results in irregularities leading to a coherent scatter. While at mesospheric altitudes, neutral air turbulence can result to mesosphere and D-region irregularities due to indirect perturbation of the ionisation, which then lead to coherent scatter (Röttger, 2004). This backscatter produced in different regions of the atmosphere is used in the mesosphere-stratosphere-troposphere radars operating in the VHF and HF band as well as in the incoherent scatter radars given that the ionosphere is coupled to the neutral atmosphere and the magnetosphere.

HF coherent scatter radars are radars operating on HF frequencies and observing backscatter from ionospheric irregularities that are aligned with Earth's magnetic field. The ionospheric irregularities producing backscatter that coherent radars detect are mainly from a spectrum of plasma waves generated by instabilities. This backscatter measurement has been applied in plasma physics research especially for studying a wide range of processes and dynamics in the magnetosphere, ionosphere, thermosphere and mesosphere (Chisham *et al.*, 2007). For example, a project dedicated to such coherent scatter radars is the Super Dual Auroral Radar Network (SuperDARN) (Greenwald *et al.*, 1995; Chisham *et al.*, 2007). The operation and technique used by the SuperDARN radar systems are discussed further in the following sections.

### 3.1.1 SuperDARN

SuperDARN is an international network of HF radars capable of measuring backscatter from plasma irregularities in the E- and F-regions of the Earth's ionosphere (Greenwald *et al.*, 1995; Chisham *et al.*, 2007). These radars measure the same parameters and also have similar operational techniques such as antenna design. Operating on HF frequencies, SuperDARN radars measure the Doppler velocity of F-region irregularity backscatter targets moving with the ambient plasma at the  $\mathbf{E} \times \mathbf{B}$  convection velocity, among other parameters (Chisham *et al.*, 2007). The accuracy of the SuperDARN radar measurements has been validated in previous studies (e.g. Ruohoniemi *et al.*, 1987; Davies *et al.*, 1999; Milan *et al.*, 1999; Koustov *et al.*, 2018) that compared velocity measurements of SuperDARN with the  $\mathbf{E} \times \mathbf{B}$  plasma drift measurements of simultaneously operating incoherent scatter radar systems. This kind of radar was primarily conceived for studying plasma convection in the high latitude region but has now become applicable in the study of various magnetosphere-ionosphere processes and interactions (e.g. Greenwald *et al.*, 1995; Ponomarenko *et al.*, 2003; Chisham *et al.*, 2007; Grocott *et al.*, 2009; Yeoman *et al.*, 2010; Lester, 2013). Also, the geographical spread of the SuperDARN network has expanded from its original high latitude to the mid and lower latitude regions of both northern and southern hemispheres (e.g. Chisham *et al.*, 2007; Nishitani *et al.*, 2019). Thus, SuperDARN has become a vital instrument for studying ionospheric and magnetospheric processes.

The evolution of HF radars that now constitute SuperDARN can be traced back to the VHF coherent radars under the umbrella of DARN, the Dual Auroral Radar Network (Greenwald *et al.*, 1985). The success of these early radars led to SuperDARN, which achieved its official status in 1995 (Nishitani *et al.*, 2019). As of 24 June, 2019, SuperDARN comprises 36 radars, 23 in the Northern Hemisphere and 13 in the Southern Hemisphere as shown in Figure 3.1 and the details of their geographic coordinates in Table 3.1.

Among the radars listed in Table 3.1, the Hankasalmi and Þykkvibær SuperDARN radars are a primary source of data used in this thesis and are located at Hankasalmi, Finland (62.3° N, 26.6° E) and at Þykkvibær, Iceland (63.8° N, 19.2°

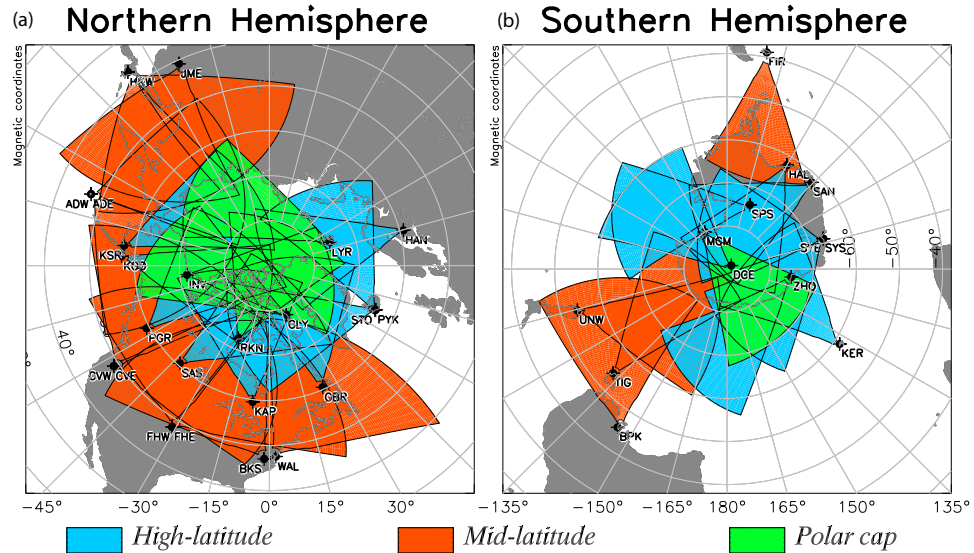


**Figure 3.1:** Fields of view of the SuperDARN radars as of 24 June 2018 in the (a) Northern and (b) Southern Hemispheres. Created from the VT-SuperDARN Radar FOVS tool

W) respectively. This pair of radars are commonly referred to as the Co-operative UK Twin Located Auroral Sounding System (CUTLASS) radars with each covering up to  $4 \times 10^6$  km<sup>2</sup> field of view. The large and increasing field of coverage that SuperDARN radars provide represents one of their advantages. A complete radar scan typically takes about 60 to 120 seconds, which means that the time resolution of the measurements is suitable for studying magnetosphere-ionosphere plasma processes from the dynamics of ionospheric convection.

The Hankasalmi SuperDARN radar for example, sounds a sequence of 16 beams forming a full 52° azimuth scan. For the common mode of operation, the radar performs a full scan every 120 s with a dwell time of 7 s per beam. While during the fast common mode the radar is synchronised to perform a full scan every 60 sec, with a dwell time of 3 s for each beam. Apart from common and fast common modes of operation, other operating modes, which allow for discretionary beam and range scanning are possible with SuperDARN radars. Along each beam, the radar measures 75 ranges gates after 180 km range. The standard gate length is 45 km with an angular separation of  $\sim 3.2^\circ$ . The effective azimuthal resolution due to the half power beam width, which is radar frequency

### 3.1 HF Ionospheric Radar

Radar Name	Code	PI* Insti- tution's Country	Geo. lat (°)	Geo. lon. (°)	Boresite
<i>Northern Hemisphere</i>					
Adak Island East	ade	USA	51.88	-176.63	46.0
Adak Island West	adw	USA	51.88	-176.63	-28.0
Blackstone	bks	USA	37.10	-77.95	-40.0
Christmas Valley East	cve	USA	43.27	-120.36	54.0
Christmas Valley West	cvw	USA	43.27	-120.36	-20.0
Clyde River	cly	Canada	70.49	-68.50	-55.6
Fort Hays East	fhe	USA	38.86	-99.39	45.0
Fort Hays West	fhw	USA	38.86	-99.39	-25.0
Goose Bay	gbr	USA	53.32	-60.46	5.0
Hankasalmi	han	UK	62.32	26.61	-12.0
Hokkaido East	hok	Japan	43.53	143.61	25.0
Hokkaido West	hkw	Japan	43.54	143.61	-30.0
Inuvik	inv	Canada	68.41	-133.77	26.4
Kapuskasing	kap	USA	49.39	-82.32	12.0
King Salmon	ksr	Japan	58.68	-156.65	-20.0
Kodiak	kod	USA	57.62	-152.19	30.0
Longyearbyen	lyr	Norway	78.153	16.074	23.7
Pykkvibaer	pyk	UK	63.77	-20.54	30.0
Prince George	pgr	Canada	53.98	-122.59	-5.0
Rankin Inlet	rkn	Canada	62.82	-92.113	5.7
Saskatoon	sas	Canada	52.16	-106.53	23.1
Stokkseyri	sto	UK	63.86	-21.03	-59.0
Wallops Island	wal	USA	37.93	-75.47	35.9
<i>Southern Hemisphere</i>					
Buckland Park	bpk	Australia	-34.62	138.46	146.5
Dome C	dce	Italy	-75.09	123.35	115.0
Falkland Islands	fir	UK	-51.83	-58.98	178.2
Halley	hal	UK	-75.52	-26.63	165.0
Kerguelen	ker	France	-49.22	70.14	168.0
McMurdo	mcm	USA	-77.88	166.73	300.0
SANAE	san	South Africa	-71.68	-2.85	173.2
South Pole Station	sps	USA	-90.00	118.29	75.7
Syowa East	sye	Japan	-69.00	39.58	106.5
Syowa South	sys	Japan	-69.00	39.58	159.0
Tiger	tig	Australia	-43.40	147.20	180.0
Unwin	unw	Australia	-46.51	168.38	227.9
Zhongshan	zho	China	-69.38	76.38	72.5

**Table 3.1:** The geographic co-ordinates to two decimal point accuracy, boresite and host institution's country of the SuperDARN radars as of 24 June 2019 for the northern and southern hemisphere. \*PI stands for principal investigator. Adapted from the VT-SuperDARN radar information table

dependent and adjustable, varies between  $2.5^\circ$  at 20 MHz and  $6^\circ$  at 8 MHz.

Given that the ionospheric plasma frequency varies diurnally, the Hankasalmi radar operating frequency (9 - 14 MHz) is usually different for daytime and night time. The lower frequencies are used at night for improved refraction through the F region with depleted ionisation at night time compared to during the day. The variation in the operating frequency produces an average angular resolution of  $4^\circ$  or a beam width of approximately 100 km at the half-range mark of 1500 km (McWilliams *et al.*, 2000) The radar consists of 16 log-periodic antennas, which form the beams and both transmit and receive signals. An electronically controlled phasing matrix allows for beam steering from the 16 antennas.

#### 3.1.1.1 Multiple Pulse Sequence in SuperDARN

SuperDARN radars use a multi-pulse transmission sequence in sounding the ionosphere. A multi-pulse sequence is characterised by four parameters. These parameters are pulse length ( $t_p$ ), lag time ( $\tau$ ), number of pulses ( $N_p$ ), and pulse table (ptab). The ptab consists of integers denoting the pulse spacing in multiples of the  $\tau$ . The SuperDARN radars operate with a typical individual pulse length of  $300 \mu\text{s}$ , corresponding to a range resolution of 45 km in a multi-pulse (normally seven to eight pulses) transmission sequence from which the auto-correlation function (ACF) is determined in normal mode for ranges from 180 to at least 3230 km, depending upon the number of gates (Lester *et al.*, 2004). For example, Figure 3.2 from McWilliams (2001), illustrates a seven-pulse sequence transmitted during a Hankasalmi normal mode operation. The pulses are separated by  $\tau$ , representing the integral multiples of the unit pulse separation and usually set to  $2400 \mu\text{s}$ . The seven-pulse are sampled as 0, 9, 12, 20, 22, 26 and 27 in a 100 ms transmission window. The transmitter is turned off after each pulse is emitted in order for the receiver to process the backscatter signal. This process entails deriving the ACF for each range as a function of lag time. Thus, the ACF of the received signal is used for determining, amongst others, the plasma drift velocity along the beam also known as line-of-sight (LOS) velocity, the backscattered power and the spectral width, representing the three main parameters measured

### 3.1 HF Ionospheric Radar

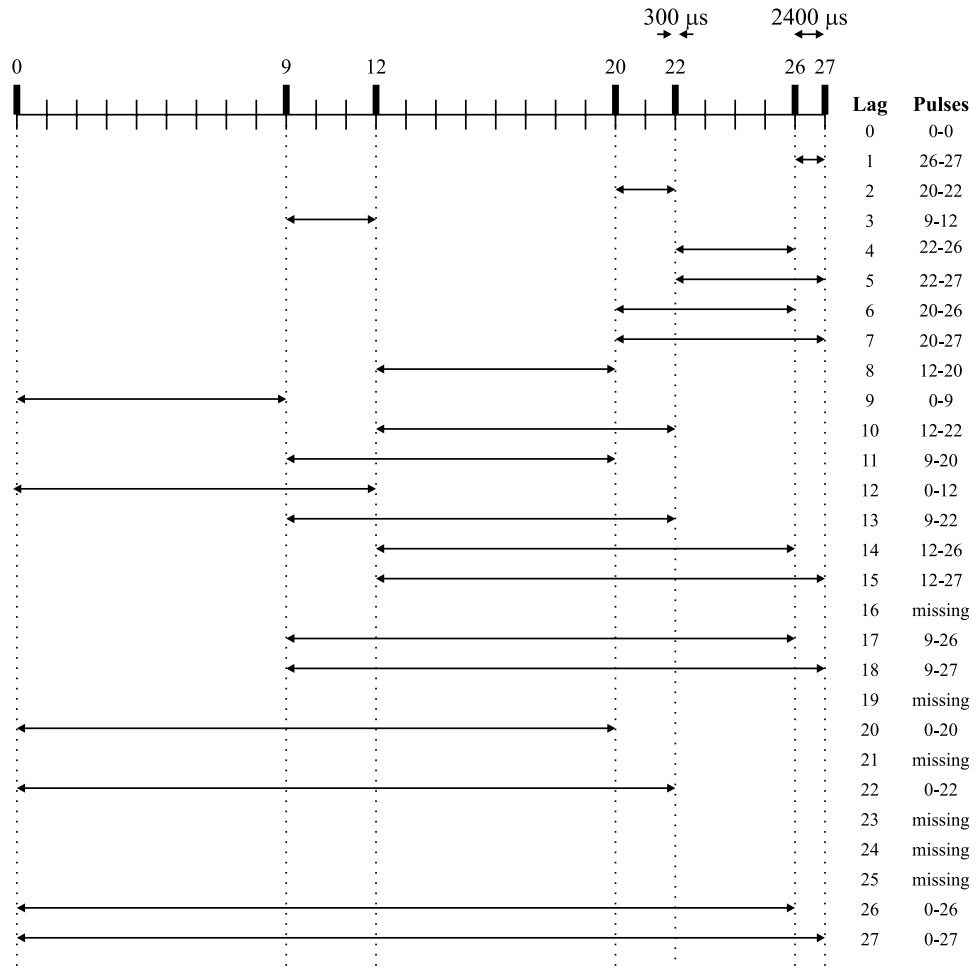


**Figure 3.2:** A diagram showing the seven-pulse sequence transmitted by the SuperDARN radars for normal operation mode (from McWilliams, 2001).

by SuperDARN. The subsequent parts of this section are a further discussion on the principles of ionospheric sounding by pulsed radar.

The basic schematic illustration below in Figure 3.3 shows how a typical radar works by transmitting a pulse and receiving backscatter from the target, which are plasma irregularities in the ionosphere. The time delay between transmission and reception, allows for the range of the target along a radar beam to be determined. The range  $R$  of the target for a pulse propagating at the speed of light  $c$  relate to the time delay between transmission and reception at the signal  $T$ , as:

$$R = \frac{cT}{2} \quad (3.1)$$

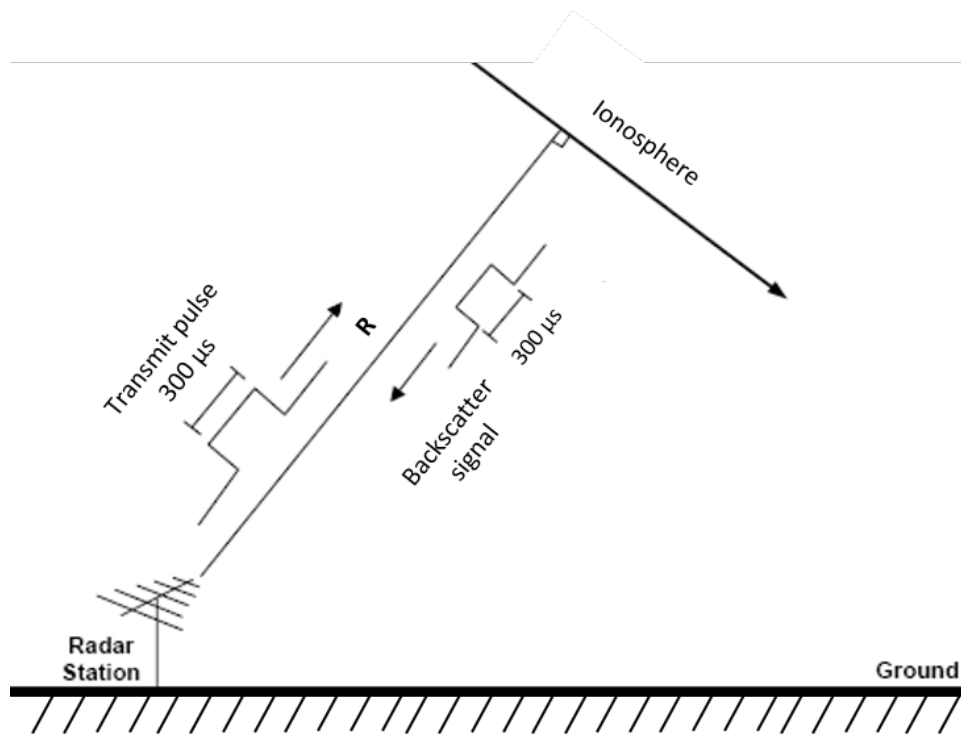


**Figure 3.3:** Simplified illustration of how a typical radar transmits pulse and receives echo (adapted from Bryson *et al.*, 2007).

SuperDARN radars receive backscatter from initial range of about 180 km up to 4000 km. Here, a two-pulse sequence is used as a simple approach to illustrate

multiple-pulse sounding of the ionosphere following the approach of McWilliams (2001). As depicted in a space-time diagram, Figure 3.4, the initial pulse ( $P_1$ ) is transmitted at time  $t_0$  then followed by a second pulse ( $P_2$ ) at  $t_0 + \tau$ , where  $\tau$  represents the lag time and  $d_0$ ,  $d_+$ , and  $d_-$  are distances from which the pulses are scattered back to the receiver. These distances are similar to range cells or gates of the SuperDARN radars. Here,  $P_1$  is transmitted at  $t_0$ , scattering back to the receiver at  $t_1$ , while  $P_2$  is transmitted at  $t_0 + \tau$  with the scatter arriving to the receiver at  $t_1 + \tau$ .

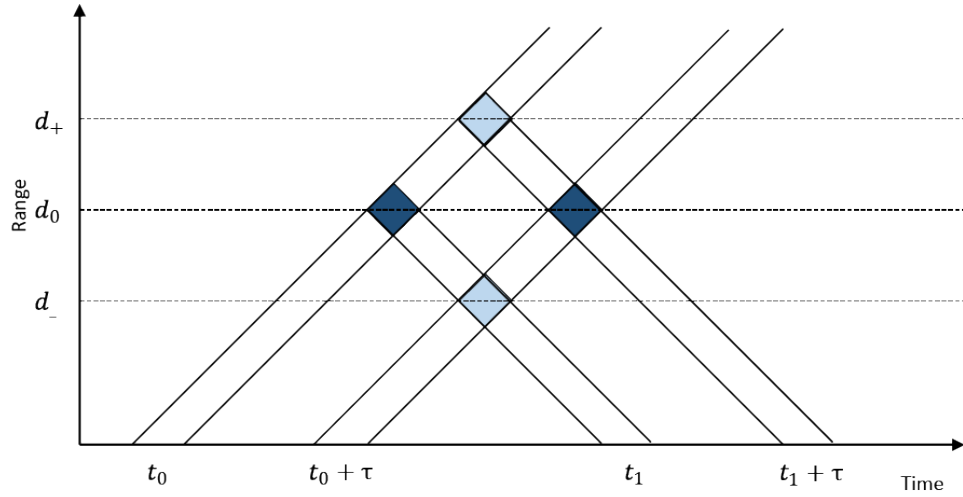


**Figure 3.4:** A schematic diagram of a two-pulse transmission sequence (adapted from McWilliams, 2001).

The backscatter signals received at  $t_1$ , which is equal to  $t_0 + \frac{2d_0}{c}$ , are from range  $d_-$  of  $P_2$  resulting to an amplitude of  $A_2(d_-)$  and  $d_0$  of  $P_1$  with an amplitude of  $A_1(d_0)$ . Conversely, the backscatter signals received at  $t_1 + \tau$  arrive from range  $d_+$  of  $P_1$  and  $d_0$  of  $P_2$  with amplitude of  $A_1(d_+)$  and  $A_2(d_0)$  respectively.

At both  $t_1$  and  $t_1 + \tau$ , there is a contribution to received backscatter signal from range  $d_0$ . Thus, the total received signal amplitude at  $t_1$  is

$$A(t_1) = A_1(d_0) + A_2(d_-) \quad (3.2)$$

while at  $t_1 + \tau$ , the total received signal amplitude is

$$A(t_1 + \tau) = A_1(d_+) + A_2(d_0) \quad (3.3)$$

The product of the total received amplitude at  $t_1$  and  $t_1 + \tau$ ,  $A(t_1)A(t_1 + \tau)$ , represents the ACF of lag  $\tau$ . Therefore, the ACF for lag  $\tau$  consists of four, out of which two emanated from range  $d_0$ . These ambiguities in the ACF, for SuperDARN, are reduced by transmitting the pulse sequence many times and averaging the backscattered signal (McWilliams, 2001). Therefore, the time-averaged contribution to the ACF at lag  $\tau$  is:

$$\begin{aligned} \langle A(t_1)A(t_1 + \tau) \rangle = & \langle A_1(d_0)A_2(d_0) \rangle + \langle A_1(d_0)A_1(d_+) \rangle \\ & + \langle A_2(d_-)A_1(d_+) \rangle + \langle A_2(d_-)A_2(d_0) \rangle \end{aligned} \quad (3.4)$$

By transmitting the pulse sequence many times with sufficient time averaging, uncorrelated terms tend to zero if there is good correlation at common range  $d_0$ . Thus equation 3.4 reduces to:

$$\langle A(t_1)A(t_1 + \tau) \rangle \approx \langle A_1(d_0)A_2(d_0) \rangle \quad (3.5)$$

The two-pulse sequence exemplified here produces ACF for a lag time  $\tau$  only. However, a multiple pulse sequence with varying pulse separation that is different integral values of  $\tau$ , as illustrated in Figure 3.2 will produce an ACF with many lags from the received signal, enough to compute the SuperDARN parameters. Eliminating noise from the returned signal, a SuperDARN radar with seven-pulse ACF will require a minimum of ten pulse sequences resulting in a 1 s shortest integration time since it takes 1 s to transmit and receive ten pulse sequences (McWilliams, 2001). In addition, the pulse separation are set to maximise the number of distinct lags (1-27) as shown in Figure 3.2. SuperDARN normally uses the first 18 lags to determine the ACFs for a pulse sequence. Because SuperDARN radars are monostatic, there are missing lags in the ACF arising from when the receiver is switched off and the transmitter is on. A SuperDARN ACF is exemplified in Figure 3.5 following McWilliams (2001). The solid line in Figure 3.5(a) shows the real part of the ACF, which peaks at lag zero, while the broken line is the imaginary part of the ACF with a phase offset from the real part as shown in Figure 3.5(b). The phase of the ACF denoted by crosses in Figure 3.5(b) aliases at  $\pm\pi$ , which makes it difficult to determine the fitted phase (solid line) of the complex ACF. The Doppler spectrum shown in Figure 3.5(c) is obtained from the Fast Fourier Transform (FFT) of the ACF from which the three main

parameters of SuperDARN radars are derived. Actual SuperDARN parameters

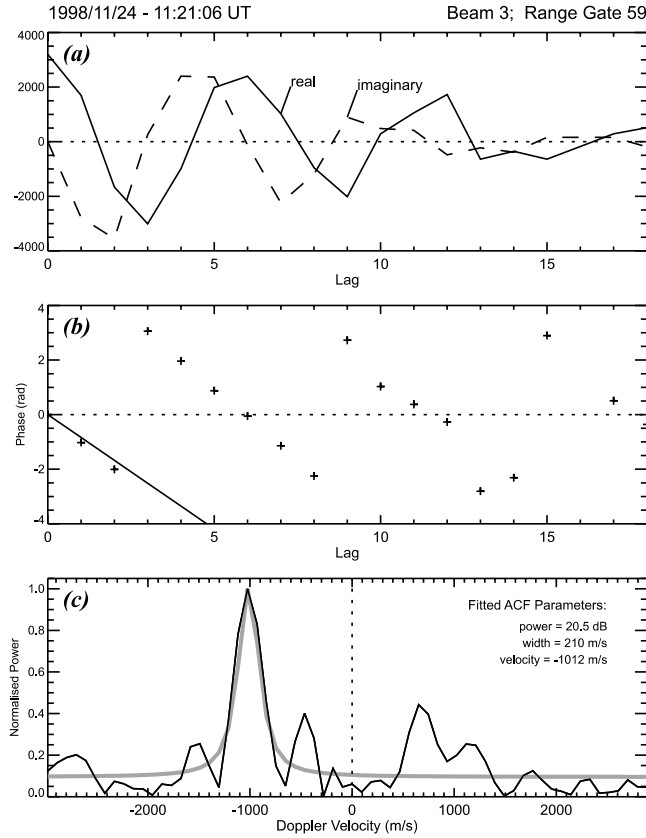


**Figure 3.5:** The top panel (a) shows a plot of a complex autocorrelation function (ACF) measurement from Þykkvibær SuperDARN radar (see Table 3.1), while the middle panel (b) shows the phase (crosses) and fitted phase (solid line) of the ACF which aliases at  $\pm\pi$ . The bottom panel (c) shows the Doppler spectrum obtained from a Fast Fourier Transform (FFT) of the ACF from which the three main parameters of SuperDARN radars (backscattered power, velocity and spectral width) are derived. Taken from McWilliams (2001).

(backscattered power, line-of-sight velocity and spectral width) are generated by such a fitting process to the ACF briefly described here using the fitACF routine in the radar software (Reimer *et al.*, 2018; Reimer, 2018).

### 3.1.2 SuperDARN Antennas

Antenna system design is a broad subject beyond the scope of this thesis. However, some aspects of the antenna system used by SuperDARN radars are discussed here to provide a background for chapter 7 of this thesis.

Antennas are transducers that convert electrical signals into radio frequency (RF) radiation and vice versa. An antenna is isotropic if it radiates power uniformly in all directions. However, antennas are mostly designed to radiate power in a particular direction. The amount of radiation power increases when two or more antennas are combined together in what is known as antenna array. An antenna array consists of radiators and elements. Each element is aligned close to the equivalent radiator's induction field, producing a radiation pattern, also known as directive gain, which represents the vector sum of the individual antennas. The radiation pattern ( $R(\theta, \phi)$ ) is an important parameter of the antenna system, usually represented as diagrams in polar coordinates. It describes the region where the radio frequency power is concentrated. For example, an antenna with a mean radiation intensity  $\bar{I}$  from the radiation intensity  $I(\theta, \phi)$  in a given azimuth  $\phi$ , radiation pattern is the ratio of the two terms denoted by

$$R(\theta, \phi) = \frac{I(\theta, \phi)}{\bar{I}} \quad (3.6)$$

The sum of the radiation of all the elements in a given array form the radiation beam. As a result, radiation beam has high gain and directivity. If the geometry and direction of a radiation pattern is determined by the relative phases and current present at each antenna of an array, then such an antenna array is referred to as a phased antenna array.

SuperDARN radars measure backscatter from ionospheric irregularities where there is a near-perpendicularity between radar wave vector and the target, a major requirement of SuperDARN operation. As such, antennas used for SuperDARN radars are directive. Early SuperDARN radars used Log-periodic Dipole Array (LPDA) antennas, given their efficient gain and high bandwidth (Chisham *et al.*, 2007). As stated in section 3.1.1, the antennas of SuperDARN are electronically phased, which allows for beam steering without moving physical parts (Sterne *et al.*, 2011). A typical SuperDARN log-periodic antenna is  $\sim 15$  m wide on

the longest element,  $\sim 12$  m long with 10 elements and  $\sim 15.5$  m above the ground (Sterne *et al.*, 2011). The main array, usually comprising 16 antennas, separated by 15 m, is accompanied by a second set of 4 antennas built parallel to the main array. Unlike the main array with both transmit and receive capability, the second set of 4 antennas, commonly known as the interferometer array, only has receive capability.

The interferometer arrays are essential in determining the angle of arrival of backscatter signal. This can be achieved by measuring the difference between the time a signal arrives at the main array and at the interferometer array (McDonald *et al.*, 2013; Burrell *et al.*, 2016; Reimer, 2018). By using the main array together with an interferometer array, SuperDARN elevation angles are inferred by

$$\Delta = \arcsin \sqrt{\cos^2 \alpha - \left( \frac{\Psi}{kd_{cor}} \right)^2} + \Delta_{cor} \quad (3.7)$$

where  $\alpha$  is the azimuthal angle of the beam off the radar boresight at zero elevation,  $k$  represents the wavenumber of the incoming signal,  $d_{cor}$  is the horizontal distance between the midpoints of the main and interferometer arrays,  $\Delta_{cor}$  is the difference in elevation caused by the altitude difference between the main and interferometer arrays, which also depends on the azimuthal angle of the beam, and  $\Psi$  is the phase lag between signals received at the main and interferometer arrays (Burrell *et al.*, 2016). As such, elevation angle determination is useful, for example, in characterising the geolocations of the backscatter measured by the SuperDARN radars (e.g. Chisham *et al.*, 2008; Yeoman *et al.*, 2008b; Burrell *et al.*, 2016)

Recent SuperDARN radars have been constructed with Twin Terminated Folded Dipole (TTFD) antennas (Custovic *et al.*, 2011). Some of the advantages of TTFD antenna over LPDA are lower construction cost, superior front-to-back ratio and beam-steering capability. More details of SuperDARN antenna systems can be found in (Milan *et al.*, 1997b; Sterne *et al.*, 2011; Greenwald, 2012; Custovic *et al.*, 2013), while the design and performance difference of the LPDA and TTFD antennas are detailed in (Custovic *et al.*, 2011; Sterne *et al.*, 2011; Custovic *et al.*, 2013).

### 3.1.3 Ionospheric Radar Backscatter

The backscatter that radars such as SuperDARN receive, results, as stated before, from naturally occurring wave structures in the ionospheric plasma, commonly known as irregularities. However, backscatter can be produced by artificially generated irregularities in radar experiments (e.g., Wright *et al.*, 2004). Radio waves propagating through the ionosphere can be described at the scattering point, by incident wave vector  $\vec{k}_i$ , scattered wavevector  $\vec{k}_s$  and the wavevector of the ionospheric medium  $\vec{k}_{med}$ . Following momentum conservation,

$$\vec{k}_s = \vec{k}_i + \vec{k}_{med} \quad (3.8)$$

then from the Bragg's condition

$$\lambda_{radar} = 2\lambda_{irr}\sin(\theta/2) \quad (3.9)$$

In a condition where  $|\vec{k}_i| = |\vec{k}_s| = 2\pi/\lambda_{radar}$  and  $|\vec{k}_{med}| = 2\pi/\lambda_{irr}$ ,  $\theta$  being the scattering angle, can result in a constructive interference, which leads to peak backscatter amplitude in a group of many scatterers with scale length  $\lambda_{irr}$  as shown in Figure 3.6 (Schlegel, 1996). Following equation 3.9, the scale size of the irregularities observable to radar is determined by the radar wavelength. The terms  $\lambda_{irr}$  and  $\lambda_{radar}$  denote the scale size of the irregularities and the radar wavelength respectively. In the case of monostatic backscatter such as the SuperDARN radars, where  $\theta$  is equal to  $180^\circ$ , for such,  $\lambda_{irr} = \lambda_{radar}/2$ . For example, the wavelengths for SuperDARN radars are in the range of 37.5 - 15 m (8 - 20 MHz).

Ionospheric irregularities are magnetic field-aligned, and for backscatter to occur the radio waves need to be perpendicular to the irregularities, requiring that the aspect angle, the angle between the radio wave propagation vector and the normal to the magnetic field has to be  $\sim \pm 1^\circ$ . As previously mentioned in Chapter 2, this is a vital requirement in the backscatter measured by SuperDARN radars. From the Doppler shift of the signal that returned to the radar, the phase velocity of the scattering plasma density irregularities can be deduced. The ionospheric scattering volume is of the order of several 1000  $km^3$ , and is

determined by the antenna characteristics and the pulse length of the transmitted signals for a monostatic, pulsed radar or the intersecting antenna beams for bistatic radars (Schlegel, 1996).

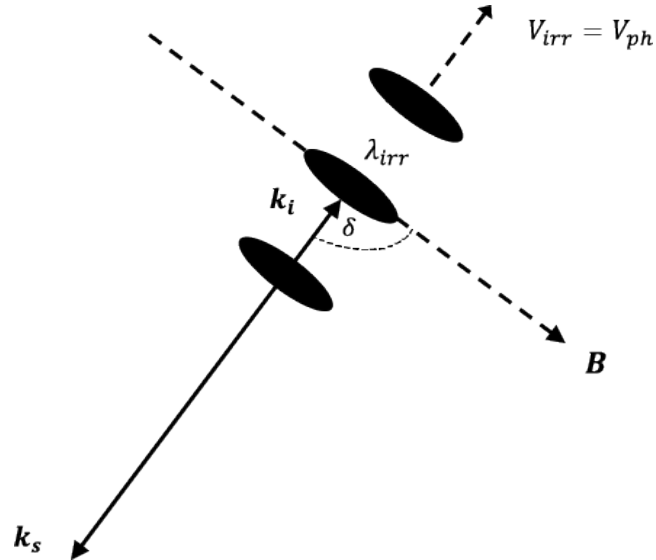


**Figure 3.6:** A schematic diagram describing the radar backscatter from field-aligned plasma irregularities for a monostatic system following Schlegel (1996).  $k_i$  and  $k_s$  denote the incident and scattered radar wave-vector,  $\delta = 90 \pm \alpha$ , where  $\alpha$  is the aspect angle and the  $\lambda_{irr}$  represent the scale size of the irregularities.

An illustration of the possible propagation paths of radio waves from where ionospheric backscatter (and backscatter from other sources such as the ground) received by SuperDARN radars are shown in Figure 3.7. Here, the orthogonality criteria are easily achieved where the magnetic field tilts horizontally towards the radar. For example, in the equatorial region, which is studied in Chapter 6, the field geometry is quite different, but the near-horizontal magnetic field will offer opportunities for orthogonality in the vertical and east-west directions. This potentially will make achieving orthogonality more likely at equatorial latitude. It also highlights the importance of refraction to achieving orthogonality in the high latitude where most of the existing SuperDARN radars lie with the field geometries at high latitude being more vertically inclined towards the radar.

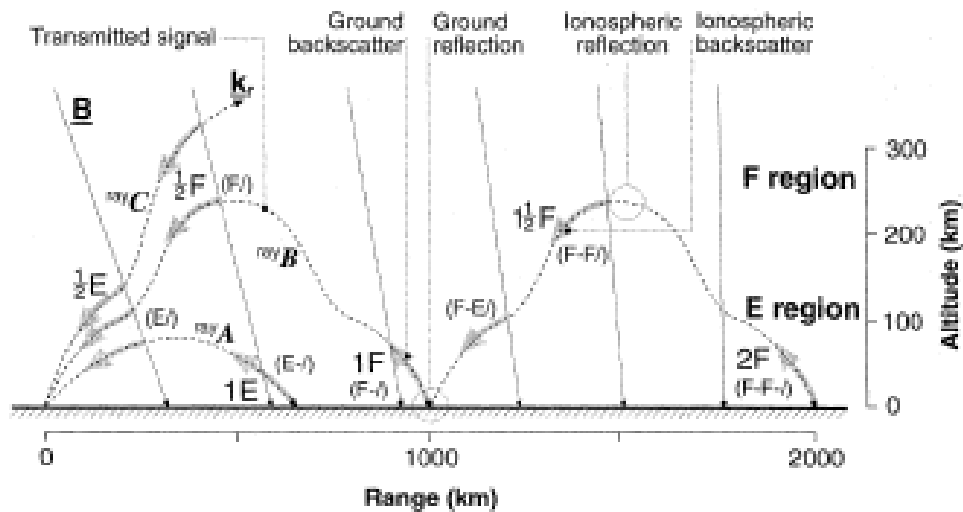


**Figure 3.7:** A schematic illustration of possible propagation modes and regions from where ionospheric backscatter (and other backscatter sources such as the ground) are received. From Milan *et al.* (1997a)

### 3.1.4 Time-Series Analysis of ULF Waves in SuperDARN measurement

As earlier noted in section 3.1.1, SuperDARN measurements are used for studying various ionospheric and magnetospheric subjects. An example of such subjects is the study of ULF waves. ULF waves were traditionally detected as a geomagnetic field variation from ground-based magnetometers with characteristic limitations, such as, restricted spatial resolution ( $\delta r \sim 200$  km) due to spatial integration effects, and amplitude, phase and polarisation distortion arising from E-region Hall and Pedersen currents in the ionosphere (e.g., Hughes & Southwood, 1976; Ponomarenko *et al.*, 2003). However, the periodic variations of the plasma motions in the ionosphere are detectable in the radar measurements from which ULF waves can be identified (e.g. Ponomarenko *et al.*, 2003; Yeoman *et al.*, 2006). Radar measurement is an effective alternative for remote sensing the magnetosphere and ionosphere by ULF waves since these radars can provide a large field of coverage of up to 2000 km with  $\delta r$  of about 15 - 45 km. The time resolution of radar data varies depending on the scan mode. For a typical common mode SuperDARN radar operation, the time resolution is 1 minute. Because the periods of

ULF waves are longer than the typical time resolution of Doppler velocity data measured by SuperDARN, periodic fluctuations can be observed. The procedure used in this thesis for characterising ULF waves from time-series measurement by SuperDARN radars are explained here.

After removing the mean from the data such that the remaining data has a zero mean, tapering using a window function is applied to the data to minimise spectral leakage given that the duration of ULF waves in a time-series data is finite. In this thesis, the preferred window function for pre-processing the time-series data is the split cosine bell function, which is written as:

$$w(t) = \begin{cases} \frac{1}{2}(1 - \cos\frac{\pi}{\alpha}t), & t \leq \alpha \\ 1, & \alpha \leq t \leq (T - \alpha) \\ \frac{1}{2}(1 - \cos\frac{\pi}{\alpha}(T - t)), & (T - \alpha) \leq t \leq T \end{cases} \quad (3.10)$$

where  $\alpha$  represents a fixed fraction of the total length of the time series  $T$ . In the analysis presented in sections 4 and 5,  $\alpha$  is set at 10% of  $T$ , as such, keeping all the data, but with 10% at each end being tapered. The data gaps within the time series radar measurement are removed by interpolating the data over a uniform time array before tapering to prevent noise spikes. Then, the pre-processed time series data is further processed using a Fast Fourier Transform (FFT), producing the power and phase spectra of the wave. The frequency accompanying the peak Fourier power spectrum is ascribed to the wave frequency and there is a phase value along with each frequency.

The power and phase values at the wave frequency are then used to characterise the wave propagation as a function of latitude and longitude using the spatial information of the radar beam and range gate cells. To do this, we use time series data in the cells consisting of a specific beam and several range gates along the beam or a specific range gate for several beams, to work out the latitudinal and longitudinal phase and amplitude variations of the wave depending on field-of-view of the radar. In the case of the Hankasalmi radar with a largely poleward FOV, range cells along a particular beam (with constant longitude) are used to determine whether a wave is propagating poleward or equatorward. In contrast, a few range cells from varying beams at a constant latitude are used to determine whether a wave is propagating eastward or westward and also to

compute the effective azimuthal wave number,  $m$  (or the azimuthal scale size) of the wave. The effective azimuthal wave number can be expressed as

$$\frac{\Delta\phi}{\Delta\lambda} \tag{3.11}$$

which is the number of degrees of wave phase change ( $\Delta\phi$ ) per degree of magnetic longitude ( $\Delta\lambda$ ). As earlier noted in Section 2.3, the effective azimuthal wave number,  $m$  is defined as positive (negative) where the azimuthal wave propagation is eastward (westward).

## 3.2 Ground Magnetometers

In order to determine the driving source of the ULF waves observed in the radar data, here ground magnetometer data from stations located across the FOV of the radar are used for a simultaneous study with radar and also to probe for substorm activity about and during the time of the wave event. ULF wave activity observed in the ionosphere can equally be seen on the ground by magnetometers when the effect of ionospheric screening is minimal.

Magnetometer data used here consist of the  $X$ ,  $Y$  and  $Z$  components in the geographic coordinate system, corresponding to  $H$ ,  $D$  and  $Z$  in the magnetic coordinate system respectively. As such,  $X$  indicates the north-south geographic component of magnetic perturbation,  $Y$  is the east-west geographic component and the vertical  $Z$  component pointing downward towards the centre of Earth. For the Scandinavian magnetometers used in this thesis, which are discussed in the next section, the geographic and magnetic coordinates are very closely aligned, so can be considered equivalent. The magnetic perturbation in the Pi2 band with a period between 40 and 150 s as earlier discussed in Section 1.6.2.1 of the mid latitude magnetometer data is a ULF wave signature of an Alfvén mode that indicates the onset of the field-aligned currents in the substorm current wedge (Rae *et al.*, 2009). Here we identify substorm onset by bandpass filtering the magnetometer data between 20 and 200 s to show the Pi2 pulsation that appears following the formation of the substorm current wedge (Mann *et al.*, 2008). The ULF wave and its frequency bands, such as the Pi2 are previously described in

Section 1.6.2. After establishing the onset of a substorm using the Pi2 waves, the gradient of the magnetic bay in the north-south and east-west components can be used infer the location of the substorm in latitude and longitude respectively with respect to locations of the magnetometer stations (e.g., James *et al.*, 2016). This method is used for inferring the location of substorms in the studies presented in Chapter 4 of this thesis.

#### 3.2.1 IMAGE

The magnetometer data employed here are provided by the International Monitor for Auroral Geomagnetic Effects (IMAGE). As of July 7, 2019, IMAGE consists of 41 magnetometer stations located in European countries such as Finland, Sweden, Norway and Germany (IMAGE, 2019a). The IMAGE array was originally set up for studying auroral electrojets and moving two-dimensional current systems over geographic latitudes between 51 and 79 degrees. The locations of the IMAGE stations currently providing data are shown in Figure 3.8, and are in close proximity with the Hankasalmi SuperDARN radar field of coverage making them suitable for the analysis here. The data from IMAGE array are sampled at 10 second resolution in a geographic coordinate system.

### 3.3 Ray Tracing Model

The time taken for an electromagnetic (EM) waves packet travelling between two points A and B can be written as:

$$T = \int_A^B \frac{ds}{v(s)} \quad (3.12)$$

where  $ds$  represents an infinitesimal element of the ray path  $s$ , and  $v(s)$  is the phase velocity of the wave packet along the ray path. This speed is a function of the local ionospheric electron density, and its spatial variation results in refraction of the wave packet. As such, a measurement or model of the electron density distribution is required for a ray tracing analysis. Such a model of the electron density distribution used here is described in section 3.4. If there is some

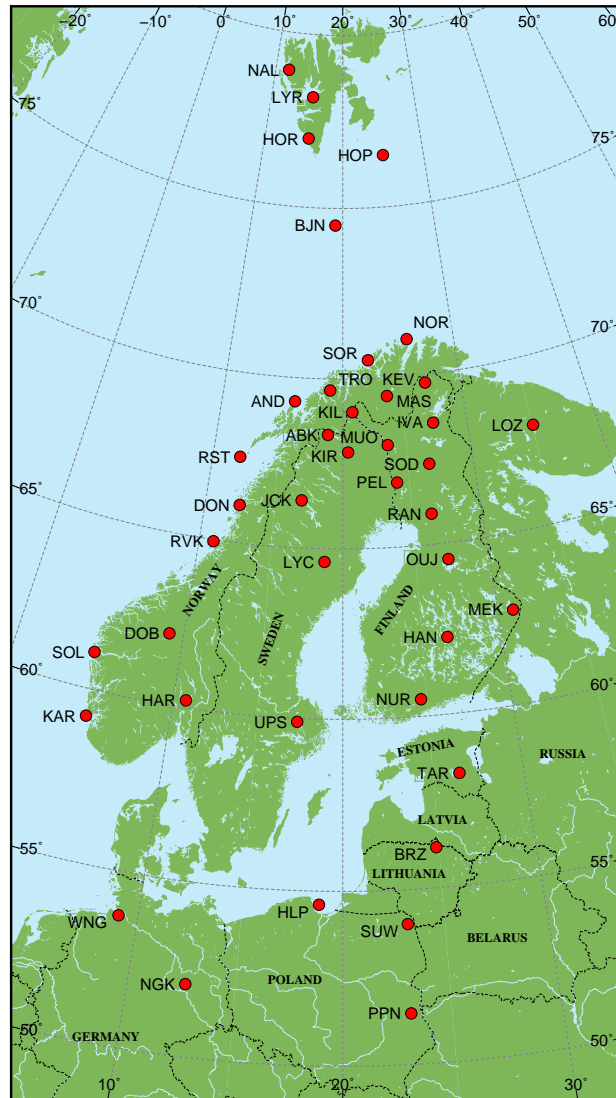


**Figure 3.8:** Map of IMAGE magnetometer stations in geographic coordinates. (Taken from IMAGE, 2019c)

functional form for the electron density, an analytic and equivalent numerical ray tracing solution, which predicts the ray trajectories and positions at varying altitudes in space can be realised from equation 3.12. Jones & Stephenson (1975) developed a widely used model for such ray tracing, which has been used for a ray tracing study in chapter 6 of this thesis.

## 3.4 International Reference Ionosphere

The International Reference Ionosphere (IRI) is an international project and model funded by the Committee on Space Research (COSPAR) and the International Union of Radio Science (URSI) aimed at developing an empirical standard model of the ionosphere from available data (Bilitza, 2018). The sources of data from which the IRI model is produced are, for example, ionosondes, incoherent scatter radars and in-situ instruments on board satellites. The model provides monthly averages of electron density, electron temperature, ion temperature and ion composition ( $O^+$ ,  $H^+$ ,  $He^+$ ,  $NO^+$ ,  $O_2^+$ , Cluster ions) in the altitude of 50-2000 km on the whole globe given location, time and date (Bilitza, 2018). The IRI model and software are updated periodically by the IRI Working Group. The recent IRI 2012 is one of the several improved editions of the model that has been released (Bilitza *et al.*, 2014).

The IRI 2012 model is employed in the ray tracing simulations presented in chapter 6 for estimating the ionospheric electron density over the African equatorial region. Because IRI is a data-based model, its accuracy and performance rely on the spatial and temporal coverage of the primary data base. For instance, it performs better at northern mid-latitudes with high data density than the polar and equatorial latitudes with a sparse data density (Bilitza, 2018). However, previous ionospheric studies have shown that the IRI 2012 model data for the equatorial ionosphere of the African longitude sector has a good correlation with measured data. For example, Tariku (2015) showed that the IRI-2012 model with the NeQuick topside option was generally good in estimating the total electron content (TEC) derived from GPS measurements.

## 3.5 IGRF

The need for orthogonality between waves transmitted by a HF radar and ionospheric irregularities, from which backscatter is measured, has been discussed earlier in section 3.1.3. Therefore, a model of the magnetic field direction is required in order to simulate typical SuperDARN radar backscatter using a ray tracing analysis.

The International Geomagnetic Reference Field (IGRF) is a global model that provides numerical values of the Earth's magnetic field vector (Thébault *et al.*, 2015). Given latitude and longitude information either in geodetic or geocentric coordinate systems, the IGRF model can calculate the geomagnetic field values and the rate of variation for the following field components:

- Declination ( $D$ ), which is the difference between true north and magnetic north of the Earth and it is positive if magnetic north is east of true north.
- The horizontal intensity of the geomagnetic field ( $H$ ).
- Inclination or dip, ( $I$ ), defined as the angle the field vector makes with the horizontal, positive below the horizontal.
- The north component of the field ( $X$ ).
- The east component of the field ( $Y$ ).
- The vertical component of the field ( $Z$ ), positive downwards.
- The total intensity of the field ( $F$ ).

Here, IGRF-12 (Thébault *et al.*, 2015), a recent version of the IGRF model, is coupled with the ray tracing model used in chapter 6 for determining the regions where a ray propagating through the ionosphere can achieve orthogonality with the Earth's magnetic field.

## Chapter 4

# Phase Evolution of Intermediate- $m$ ULF Waves Driven by Substorm-injected Particles: a case study

### 4.1 Introduction

Ultra-low frequency (ULF) waves provide a conduit for energy and momentum transfer in the magnetosphere-ionosphere system. Thus, they are an important diagnostic of magnetospheric structure and dynamics (Yeoman *et al.*, 2006). The classifications of such ULF waves based on their characteristic azimuthal wave number  $m$ , as low- $m$  and high- $m$  ULF waves have been discussed in Chapter 2. ULF waves of the same  $m$  number spectrum tend to have similar wave mode and energy source and vice versa. For example, the low- $m$  waves are generally thought to be from sources external to the magnetosphere (Agapitov & Cherenmykh, 2013).

Specifically, section 2.4 discussed a class known as intermediate- $m$  ULF waves with  $m$  number in the region of 10 (Yeoman *et al.*, 2010; Hao *et al.*, 2014; Mager *et al.*, 2019). They can be considered as an extension of the high- $m$  waves but

with lower  $m$  values and their features, driving mechanism and generation are not totally understood (Mager *et al.*, 2019).

In this chapter, we investigate a ULF wave event that occurred between 00:00 UT and 03:00 UT, May 13, 2016 observed by the Hankasalmi SuperDARN radar. Initial inspections of the line of sight (LOS) velocity data of beam 2 to beam 11 suggest that the phase propagation of the wave along the beams in latitude evolved from equatorward to poleward over time. Theoretical studies such as Klimushkin *et al.* (2004); Mager & Klimushkin (2008) have shown that waves identified as having poloidal polarisation can transform into the toroidal Alfvén mode. An observational case study of a phase propagation transformation from a mostly poleward to equatorward wave propagation was reported in (Chelpanov *et al.*, 2019) for an intermediate- $m$ . However, such observations of wave evolution are still rare. Thus, data from ground-based magnetometer stations of the IMAGE arrays that are closely located in geomagnetic latitude and longitude with the Hankasalmi SuperDARN radar coverage have been combined together with the radar data to investigate the ULF wave characteristics of this event and to verify a possible evolution in its phase behaviour. The instruments and techniques used in this study are presented in the next section, followed by the analysis, discussion and summary.

## 4.2 Data

The ionospheric velocities recorded by the SuperDARN radar at Hankasalmi, Finland were used to study the characteristics of ULF wave activity on 13th May 2016. Figure 4.1 shows the fields-of-view (FOV) of the radar scan modes. The Hankasalmi radar operated on two Channels A and B with the capability of utilising a full 16-beam scan of 45 km range gates, starting at 180 km. The operations of the SuperDARN radars have been discussed earlier in Chapter 3. In this study, the radar sounded the 16 beams, all pointing northwards on Channel A as outlined in Figure 4.1. Channel B was constrained to one beam across the entire range gates as highlighted inside the radar FOV outline. ULF wave activity is depicted by the oscillations in the velocity towards and away from the radar with insignificant ground scatter from range gates 24 up to 35 along the

beams. Beam 9 has 3 s resolution, and is a focus of the study, but the wave is also investigated in beams 5-10, where it is most clearly observed, with a time resolution of 1 min. The magnetometer data presented here were obtained from the International Monitor for Auroral Geomagnetic Effects (IMAGE) database, with a sampling interval of 20 s. The positions of the IMAGE magnetometer stations used in this study with respect to the radar FOV, are depicted in Figure 4.1 and their names and location coordinates are presented in Table 4.1.

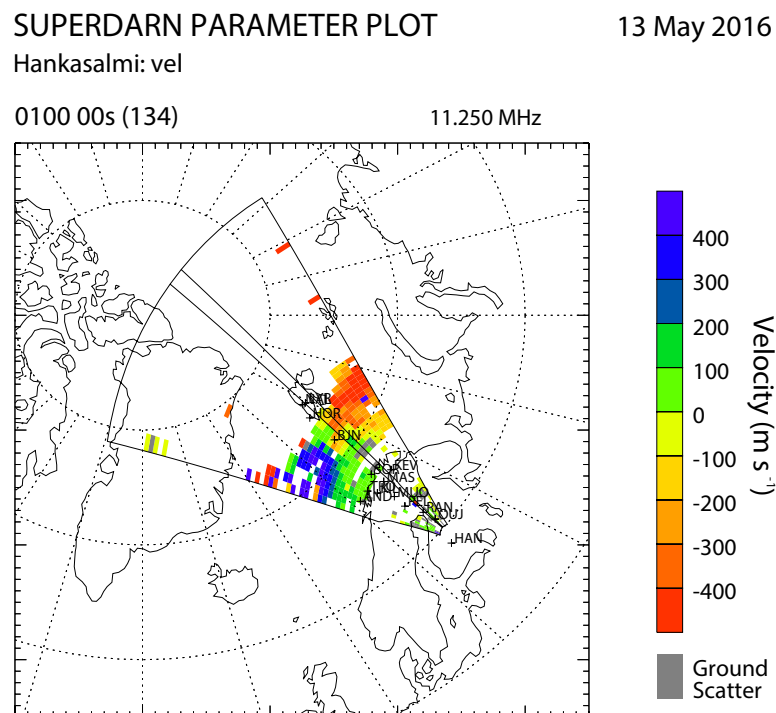


**Figure 4.1:** Field-of-view and data coverage from Channel A of the SuperDARN radar at Hankasalmi, Finland during the wave activity interval, onset at 01:00 UT in magnetic latitude-magnetic local time coordinates. The outline inside the FOV indicates the beam that Channel B is restricted to. The radial dashed lines are separated by 1 h local time, with local midnight being marked by the vertical dashed line. The positions of the IMAGE magnetometer stations used are highlighted. The ionospheric velocities are colour-coded such that red (negative) and blue (positive) represent velocities away from the radar and towards the radar respectively.

S/N	Code	Name	Geo. lat. (°)	Geo. lon. (°)	CGM lat. (°)	CGM lon. (°)
1	NAL	Ny Ålesund	78.92	11.95	75.25	112.08
2	LYR	Longyearbyen	78.20	11.82	75.12	113.00
3	HOR	Hornsund	77.00	15.60	74.13	109.59
4	BJN	Bear Island	74.50	19.20	71.45	108.07
5	SOR	Sørøya	70.54	22.22	67.34	106.17
6	KEV	Kevo	69.76	27.01	66.32	109.24
7	TRO	Tromsø	69.66	18.94	66.64	102.90
8	MAS	Masi	69.46	23.70	66.18	106.42
9	AND	Andenes	69.30	16.03	66.45	100.37
10	KIL	Kilpisjärvi	69.06	20.77	65.94	103.80
11	MUO	Muonio	68.02	23.53	64.72	105.22
12	PEL	Pello	66.90	24.08	63.55	104.92
13	RAN	Ranua	65.90	26.41	62.09	105.91
14	OUJ	Oulujärvi	64.52	27.23	60.99	106.14
15	HAN	Hankasalmi	62.25	26.60	58.69	104.54

**Table 4.1:** The geographic and geomagnetic location of the IMAGE magnetometer stations used in this study. CGM stands for Corrected Geomagnetic Coordinates. Taken from IMAGE (2019b)

To characterise the wave activity in the radar velocity data, a series of processes described earlier in Chapter 3 is followed. This includes using Fourier analysis to establish the dominant frequency of the ULF waves observed in both the radar and the magnetometer data. The values of the wave Fourier power and phase derived at the dominant frequency were selected for examining latitudinal and longitudinal variation of the amplitude and phase characteristics of the wave activity. The Fourier phase values selected from several range gates and beam combinations covering a range of geomagnetic longitudes at approximately constant geomagnetic latitude were used to determine the wave’s azimuthal phase propagation and the effective azimuthal wave number. In the case of the magnetometer measurements, wave amplitude and phase values derived from stations

with identical geomagnetic longitude but different latitude were used to study the latitudinal wave evolution and in the same vein for the longitudinal wave amplitude and phase variation. Magnetometer data of AND, TRO, KIL, MAS, KEV and SOR stations were used for examining the longitude profile of the ULF wave observations and the rest of the stations presented in Table 4.1, except AND, MAS and KEV for the latitude profile. The effective azimuthal wave number was derived in a similar process as in the case of the radar observations.

### 4.3 ULF Wave Event on May 13th 2016

The analysis done to characterise the ULF pulsations observed in the Hankalsami SuperDARN radar and ground magnetometer data of the May 13th 2016 wave event are presented in this section. The range-time-velocity plots (similar to Figure 4.2) suggest a wave activity from the radar velocity measurement during a 3-hour (00:00 - 03:00 UT) interval on May 13th 2016. The radar beams captured a noticeable trend where the latitudinal phase across the 3-hour interval that this wave event was observed appear to change into a poleward-like phase at about 01:40 UT, which also coincided with a backscatter bite-out lacking in data across almost all the beams. Here, the Fourier results obtained from the radar data over the 3-hour interval of this event are presented first. Thereafter, the 3-hour radar dataset is divided into two intervals to further investigate the nature of the apparent spatial and temporal evolution of the wave's phase propagation, followed by the results of some interesting backscatter bite-out features observed across most radar beams. Lastly, the results outlining substorm occurrence during the period of this wave event using magnetometer data are shown. Presented along with the magnetometer data is the Fourier analysis of a wave with similar frequency to the one observed in the radar data and another distinctive wave feature with different frequency using the IMAGE Y-component magnetometer data. The Y-component is used because the wave activities are clearer in this component than the X and Z-components.

Figure 4.2 shows ionospheric flow velocities of the Hankasalmi radar beam 9 measurements of the ULF wave activity that occurred on May 13th 2016. It displays the meridional view of the wave as a function of geomagnetic latitude,

### 4.3 ULF Wave Event on May 13th 2016

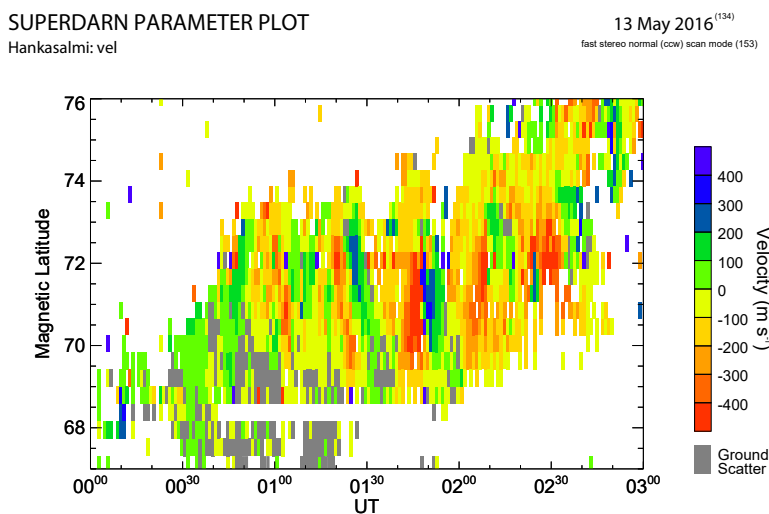


**Figure 4.2:** Hankasalmi beam 9 SuperDARN radar velocity measurements as a function of magnetic latitude. The ionospheric velocities are colour-coded such that red (negative) and blue (positive) represent velocities away from the radar and towards the radar respectively.

which corresponds to the radar range gates of about 20 to 40. The velocity flows between magnetic latitudes of  $69^\circ$  and  $74^\circ$  depict clear oscillations with a seeming equatorward phase propagation in the interval 00:00 UT to 01:30 UT, a wave signature associated with particle-driven ULF waves (Yeoman *et al.*, 2010). However, it appeared to evolve into a poleward-like phase around the interval of 01:40 UT to 03:00 UT, more prominent in the component of the velocity flowing away from the radar. Another interesting feature that can be observed is that there is a backscatter bite-out at about 01:40 UT and  $\sim 72^\circ$  latitude, more obvious in the next figure (Figure 4.3). Figure 4.3 presents the velocity data for beams 3-9, and shows the temporal and spatial evolution of the bite out. The spatial extent of this backscatter bite-out is illustrated in the middle panel of Figure 4.4. During the time of its appearance, the lower latitude limit is about  $71^\circ$  while the longitudinal width is  $\sim 10^\circ$ . Such radar backscatter bite-outs can be attributed to depletion of scattering structure of the ionospheric irregularities region observed by the radar due to energetic particle precipitation from substorms, changes on HF propagation due to changing electron density, or ionospheric absorption (e.g., Gauld *et al.*, 2002). Spatial structure of the injected particles from such substorms

### 4.3 ULF Wave Event on May 13th 2016

SUPERDARN PARAMETER PLOT 13 May 2016<sup>(134)</sup>  
Hankasalmi: vel fast stereo normal (ccw) scan mode (153)

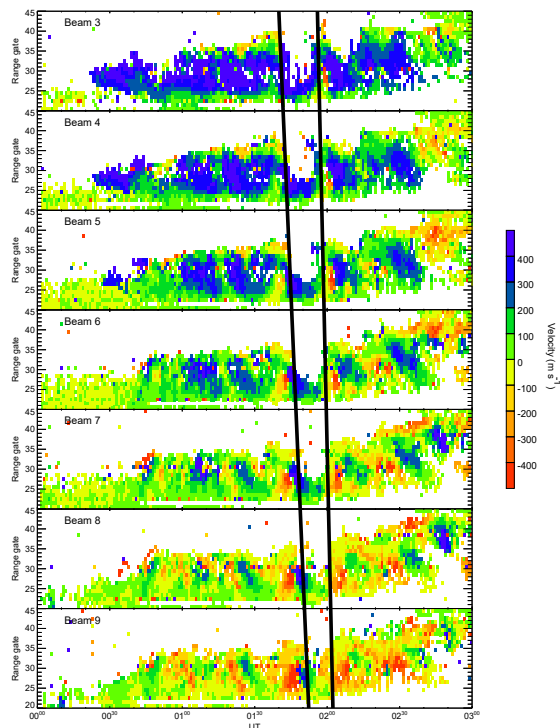


**Figure 4.3:** Hankasalmi beams 3 - 9 SuperDARN radar velocity measurements as a function of Radar range gate. The ionospheric velocities are colour-coded such that red (negative) and blue (positive) represent velocities away from the radar and towards the radar respectively, while the black lines indicate drifting bite-out features.

can determine the phase characteristics of ULF waves driven by the substorm-injected particles (Yeoman *et al.*, 2012). It is possible, following these previous studies, that the possible phase evolution in Figure 4.2 and the bite-out depicted in Figure 4.3 might both be linked to energetic particles generated by substorms. These preliminary observations about this wave event are investigated further in the subsequent sections of this chapter.

### 4.3 ULF Wave Event on May 13th 2016

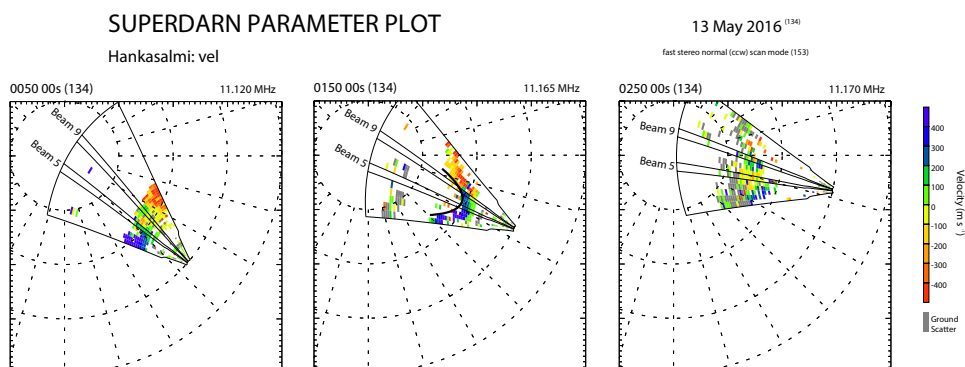


**Figure 4.4:** Similar to Figure 4.1 except that here shows wave activity onset at 00:50 UT before (left panel), 01:50 UT during (middle panel), and 02:50 UT after (right panel) the appearance of the bite-out. The vertical outlines inside the FOV indicates beams 5 and 9 while curved black outline in middle panel describes the spatial extent of bite-out.

Visualising ULF wave activity from radar velocity data can be problematic due to data gaps in the interval of a wave event. Usually, this problem is rectified through velocity data reprocessing that involves interpolating the gaps. Excessive interpolation of data gaps can alter the wave features or produce a wrong result during Fourier analysis. As such, a check to confirm that there is sufficient data over a period of a wave event before Fourier analysis is important. To ensure sufficient data for Fourier analysis, data availability is ascertained for each of the 1200 cells (that is 75 range gates multiplied by 16 beams) over the interval of a likely wave activity. The analysis shows percentage data occupancy in each cell over the interval of a wave event. This procedure is demonstrated in Figure 4.5, where the left pane is the velocity data for the 3-hour interval of the wave event (which is the same as Figure 4.2) from which the right pane was made, showing the percentage data occupancy in each cell during the interval.

In analysing the present ULF wave events, we use cells with data availability of 50% and above for Fourier analysis to determine the amplitude and phase behaviour of the wave. For example, as seen in Figure 4.5(a), key data required to analyse the 13th May 2016 activity measured by Hankasalmi radar are present as most gaps are at the start and end of the 3 hour length of the time-series data, part of which are tapered off before applying a Fast Fourier Transform (FFT).

SUPERDARN PARAMETER PLOT  
Hankasalmi: vel

13 May 2016

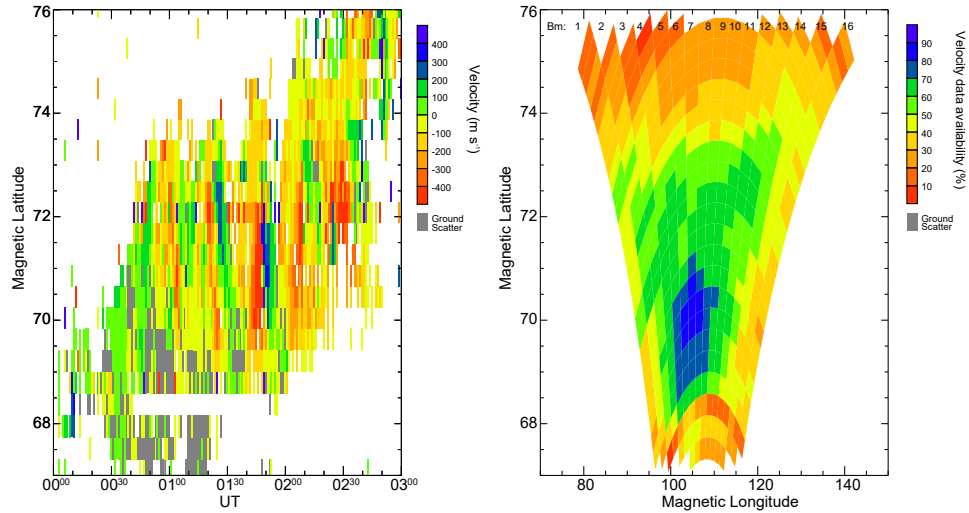


**Figure 4.5:** (a) SuperDARN radar velocity measurement from Hankasalmi beam 9 for the current ULF wave event. Red (negative) indicate ionospheric velocities away from the radar and blue (positive) for velocities towards the radar. (b) Velocity data availability. Colour code shows percentage data occupancy in each cell over the 3-hour wave activity interval.

Likewise, while the right edges representing beams 14 to 16 do not meet the criteria as there are no cells with  $\geq 50\%$  data (green and blue cells) occupancy as seen in Figure 4.5(b), beams 3 to about 11 consisting of the beams focused on here have sufficient data. The Fourier spectrum for each of the cells with  $\geq 50\%$  data was checked along with the time-series velocity, confirming that the unfavourable effect of data interpolation was insignificant and that the dominant frequency was present. Thus, there is sufficient coverage to get the wave parameters using 50% as a threshold.

Fourier analysis shows that there are two obvious frequencies of 0.10 mHz and 0.75 mHz (a period of 1340 s) as illustrated in Figure 4.6. The lower frequency is likely a linear trend in the velocity data. The 0.75 mHz peak is dominant and consistent between the latitude range of 68°-74° and longitude range of  $\sim 95^\circ$ -110° across all the cells with  $\geq 50\%$  data occupancy as shown in Figure 4.5. The

### 4.3 ULF Wave Event on May 13th 2016

---

dominant frequency of 0.75 mHz is about a 20 minute period, which is consistent with the appearance of the time series of the oscillation in Figure 4.2. The wave frequency is approximately in the range of a Pc5 pulsation and as such, has been designated as a Pc5 wave in subsequent analysis.

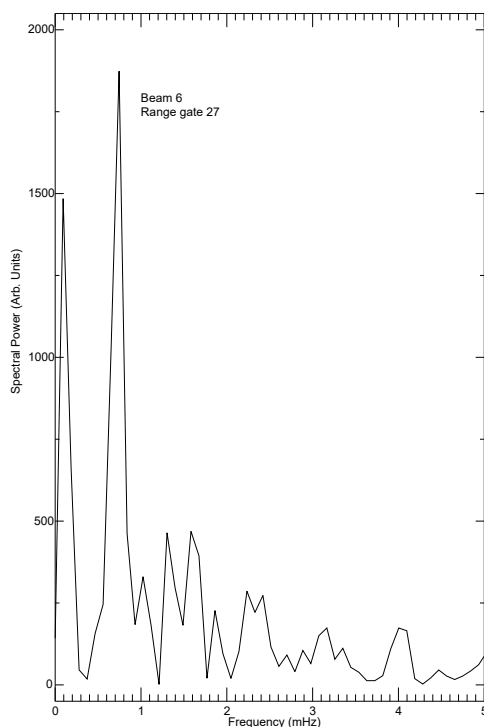


**Figure 4.6:** Fourier power spectrum of beam 6 range gate 27 showing two clear dominant frequencies.

The Fourier amplitude and phase characteristics of the wave over the 3-hour interval is now examined in more detail. Figure 4.7 shows the Fourier amplitude and phase characteristics of the wave at the dominant frequency of 0.75 mHz as a function of geomagnetic latitude and geomagnetic longitude. Each of the near-vertical columns of range cell data represents a beam, as highlighted by black outline for beam 9 which represents the beam used to examine the latitudinal phase profile. Figure 4.7(a) reveals a broad peak of the wave amplitude between the latitude range  $70^\circ$  and  $72^\circ$  and corresponding longitude range  $102^\circ$  and  $112^\circ$ . While Fourier phase varies from one range cell to another along the latitude range, the general trend mostly between beam 5 to about 10 where the wave activity is

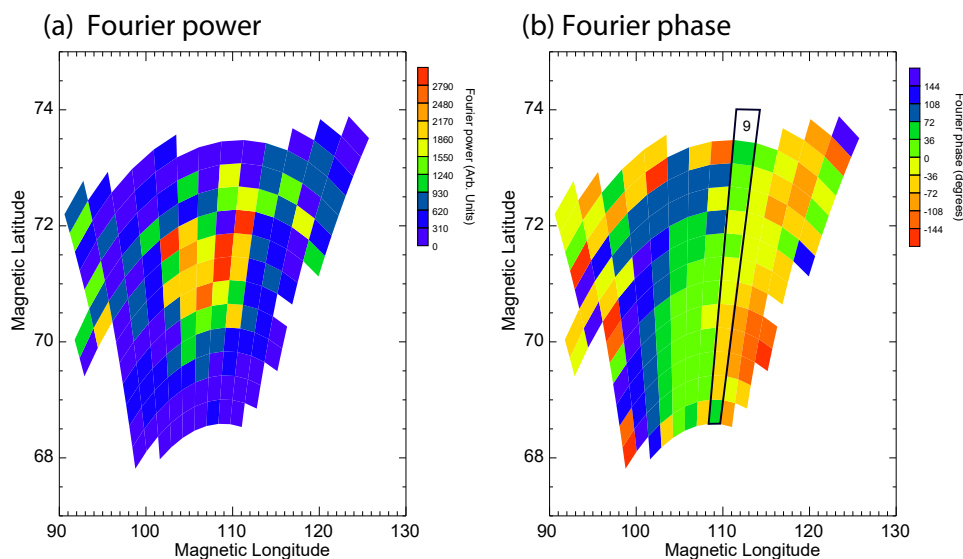


**Figure 4.7:** Fourier (a) amplitude and (b) phase at 0.75 mHz peak frequency of the ULF wave derived from the ionospheric drift velocity measurement for all the cells with 50% and above data availability over the 3-hour (00:00-03:00 UT) interval across all the beams as a function of geomagnetic latitude and longitude. The black outline indicates beam 9.

obvious, confirms an equatorward phase propagation over  $68^{\circ}$ - $74^{\circ}$  latitude range. The phase propagation is equatorward where the phase values are decreasing with latitude. The latitudinal amplitude variation and phase propagation can also be viewed in a one-dimensional plot as shown in Figures 4.8(a-b) along beam 9.

Longitudinal phase profile of the wave as shown in Figure 4.7 reveal an eastward phase propagation. This is indicated by a broad decrease in phase values from the west of longitude range (left) to the east of longitude range (right). Similarly, Figures 4.8(c-d), which are the one-dimensional equivalent of Figure 4.7 confirm an eastward phase propagation. Figures 4.8(c-d) show the Fourier power and phase derived from the dominant frequency (0.75 mHz) across beams 5 to 11 at radar range gate 25, which represents a latitude of  $\sim 70^{\circ}$ . From Figure 4.8(d), a corresponding effective azimuthal wave number,  $m$  of  $17 \pm 1$  is calculated for this Pc5 wave using linear least squares fit to the phase values as shown by the dotted lines in Figure 4.8(d).

### 4.3 ULF Wave Event on May 13th 2016

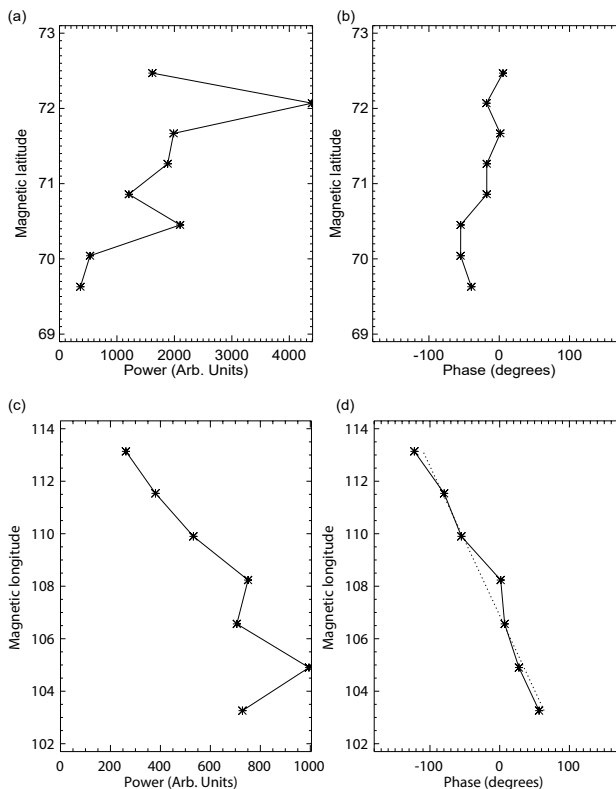


**Figure 4.8:** Fourier (a) amplitude and (b) phase at 0.75 mHz peak frequency of the ULF wave derived from the ionospheric drift velocity measurement along beam 9, and Fourier (c) amplitude and (d) phase across beams 5-11 of the Hankasalmi SuperDARN radar at  $\sim 70^\circ$  latitude as a function of geomagnetic longitude. The dotted line in (d) is a linear fit to the longitudinal phase variation.

The same process of determining  $m$  number was repeated for radar range gates 27 and 30, which represent magnetic latitude ranges of  $\sim 71^\circ$  and  $\sim 72^\circ$  respectively. The differences in  $m$  values at those latitude ranges, representing the region with peak wave amplitude, are equal within uncertainty. The azimuthal wave number,  $m$  of  $17 \pm 1$  calculated for this wave event represents an intermediate- $m$  wave (e.g., Yeoman *et al.*, 2010).

Furthermore, the longitudinal phase profile of the wave viewed as a function of magnetic local time (MLT) in Figure 4.9 clearly confirms an eastward phase propagation as illustrated by the black arrowhead pointing to the east of longitude range (right). In order to investigate the possible temporal latitudinal phase

## Fourier phase propagation in Magnetic Local Time (MLT)

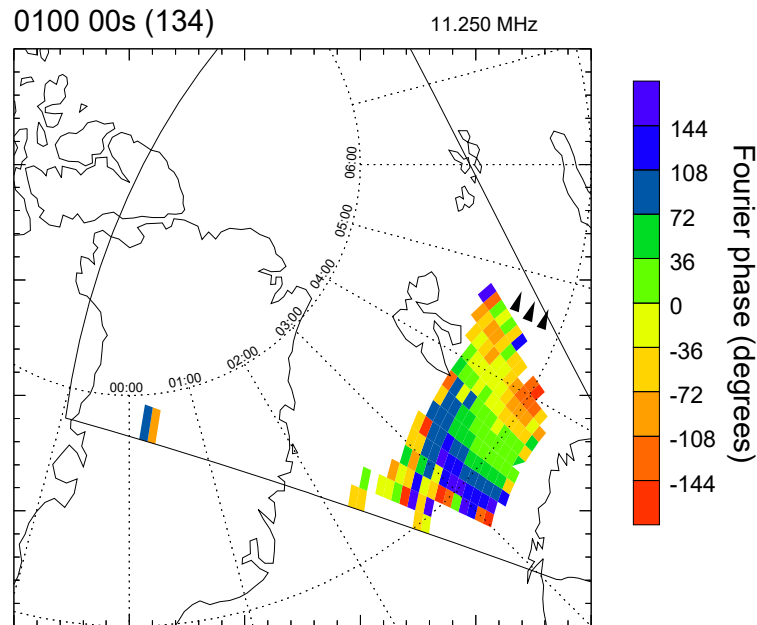


**Figure 4.9:** Fourier phase at 0.75 mHz peak frequency of the ULF wave derived from the ionospheric drift velocity measurement as a function of Magnetic Local Time (MLT). The figure is presented in magnetic latitude-magnetic local time coordinates. The bold outline inside indicates the radar FOV. The radial dashed lines are separated by 1 h local time, with local midnight being marked by the vertical dashed line, while the black arrowheads show azimuthal direction of wave propagation.

evolution of the ULF wave activity previously highlighted, the time series velocity data over the three hour of wave activity have been divided into two; 00:00 UT to 01:30 UT for Interval 1 analysis and 01:30 UT to 03:00 UT for Interval 2. The analysis for these two intervals investigating the possible phase evolution is presented in the next two sections.

### 4.3.1 Interval 1 (00:00 – 01:30 UT) Radar Observation

Fourier analysis of Interval 1 velocity data reveals that the same wave frequency of 0.75 mHz earlier described is detectable in Fourier spectra across the radar beams. The beams and range cells with  $\geq 50\%$  data occupancy and a clear wave activity features are used for the 2-dimensional Fourier amplitude and phase analysis as shown in Figures 4.10(a-b).

Figure 4.10(a) presents the Fourier power at the wave frequency as a function of geomagnetic latitude and longitude, derived from the ionospheric drift velocity measurements along the beams with clear wave activity features. Here, Fourier power peaks (red colour) at about  $72^\circ$  in latitude, while in longitude it peaks between  $\sim 100^\circ$  and  $110^\circ$ .

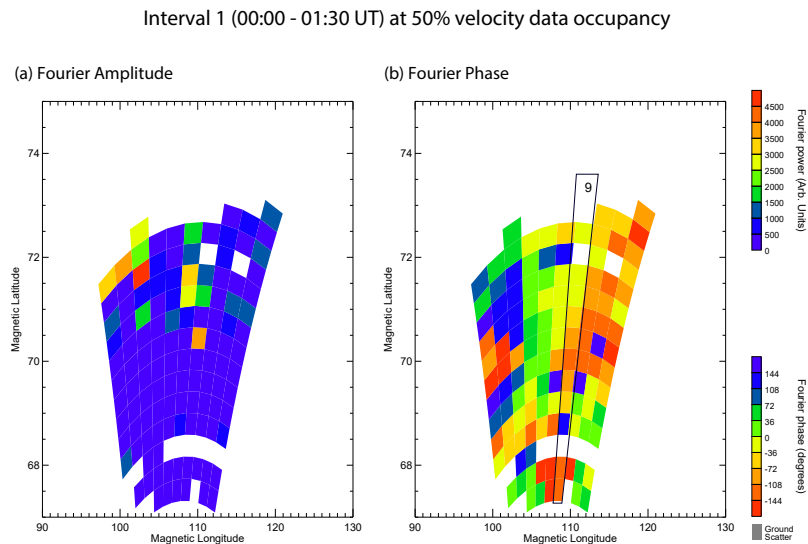


**Figure 4.10:** Interval 1 Fourier (a) amplitude and (b) phase as a function of geomagnetic latitude and longitude across beams with clear wave activity that meet the 50 percent data occupancy. The black outline in (b) indicates beam 9.

A clear trend of equatorward phase variation is observed as depicted by the near-vertical columns of range cells data for beam 9 (black outline) in Figure 4.10(b) and the corresponding one dimensional plot for beam 9 is shown in Figure 4.11. Whilst the phase propagation along beam 9 is equatorward, some beams follow the same trend and others have mixed equatorward and poleward phase

### 4.3 ULF Wave Event on May 13th 2016

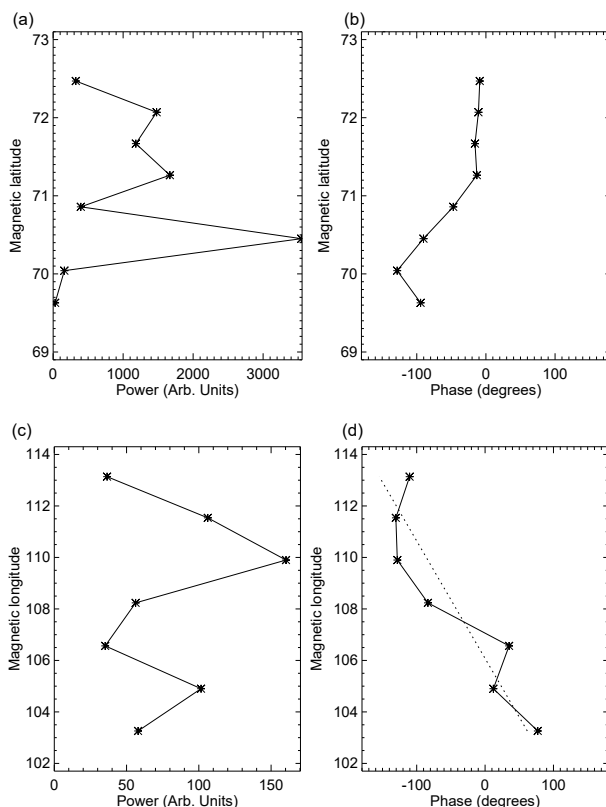


**Figure 4.11:** Interval 1 - Fourier (a) amplitude and (b) phase at 0.75 mHz frequency of the ULF wave derived from the ionospheric drift velocity measurement along beam 9, and Fourier (c) amplitude and (d) phase across beams 5-11 of the Hankasalmi SuperDARN radar at  $\sim 70^\circ$  latitude as a function of geomagnetic longitude. The dotted line in (d) is a linear fit to the longitudinal phase variation.

variation. The phase variation is considered to propagate equatorward where phase values are smaller at lower latitudes than at higher latitudes. Here, it can be seen that the equatorward phase variation is more obvious between  $70^\circ$  and  $71^\circ$  compared to the analysis over the 3-hour interval. The longitudinal phase variation in Figure 4.10(b), generally indicates a clear eastward phase propagation. Likewise, it can be seen in Figure 4.11(d) that longitudinal phase propagation depicts a curve in eastward direction. Following a similar azimuthal wave number calculation for the 3-hour wave observation, the  $m$  number is examined for Interval 1 at latitude of  $\sim 70^\circ$ , which is equivalent to radar range gate 25, along beams

5 – 11 and, it is determined as  $21 \pm 3$ . The value for  $m$  is the gradient estimated using linear least squares fit to the phase values as shown by the dotted lines in Figure 4.11(d). The eastward direction observed for the Interval 1 is consistent with the analysis for the 3-hour interval. However, the  $m$  value is slightly higher compared to the 3-hour interval analysis but still consistent within error.

#### 4.3.2 Interval 2 (01:30 – 03:00 UT) Radar Observation

In the last section, the wave behaviours at interval 1 showed a clearer equatorward latitudinal phase variation along beam 9 compared to the analysis over the 3-hour interval. Here, we repeat the same analysis but for interval 2 (01:30 – 03:00 UT). In a similar procedure to the previous time interval considerations, Fourier analysis was done where the percentage of data occupancy for each range cell across the beams meet the 50 percent criterion and have sufficient wave activity features. The same 0.75 mHz frequency is dominant as derived from Fourier spectra, similar to the analysis over the 3-hour of the wave activity. The equivalent wave amplitude and phase determined by Fourier analysis are presented in Figures 4.12(a-b).

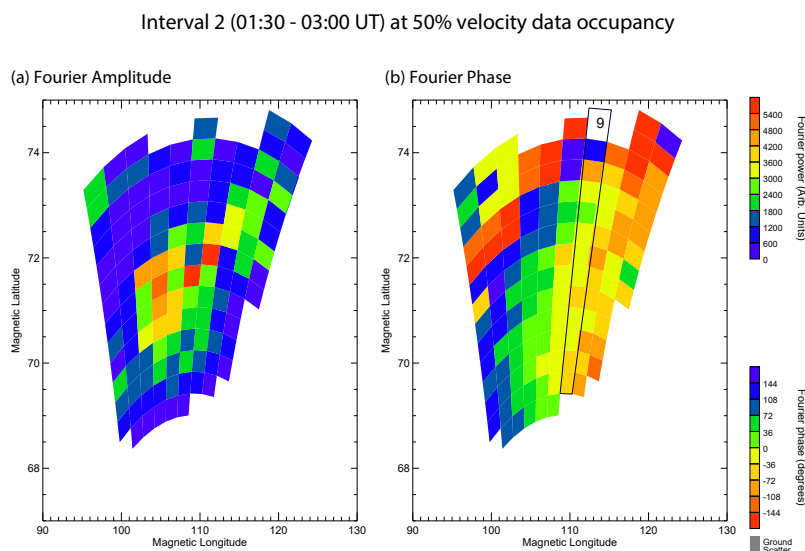


**Figure 4.12:** Similar to Figure 4.10, but for Interval 2 (01:30-03:00 UT) with peak frequency 0.74 mHz.

### 4.3 ULF Wave Event on May 13th 2016

The wave amplitude as shown in Figure 4.12(a), peaks (red colour) in latitude at about  $72^\circ$ , and in longitude between  $\sim 102^\circ$  and  $111^\circ$ . The Fourier phase in Figure 4.12(b) reveals little latitudinal phase propagation. This variation in latitudinal phase propagation is also shown in Figure 4.13(b). The degree per

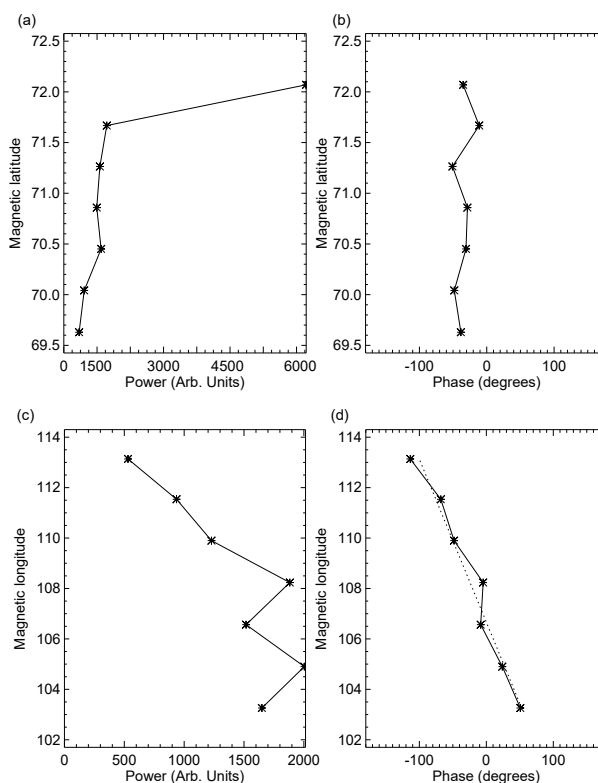


**Figure 4.13:** Similar to Figure 4.11 but for Interval 2 (01:30 - 03:00 UT) analysis.

latitude change of the wave phase variation over  $\sim 69^\circ$ - $72^\circ$  latitude range is small. The change in phase behaviour seen in the time domain is not clearly illustrated through the Fourier analysis in Figure 4.13(b) given the short length of time of the Interval 2 available for analysis, but it is different from the other intervals. Fourier phase variation in magnetic longitude follows a similar eastward phase propagation with azimuthal wave numbers of  $15 \pm 1$  determined using the same combination of radar range gate 25 (equivalent to  $\sim 70^\circ$  latitude) along beams 5–11. The  $m$  value is similar to that of the 3-hour interval and Interval 1.

## 4.4 Magnetometer Observations

Magnetic field data derived from the IMAGE magnetometer stations with close proximity to the Hankasalmi SuperDARN radar as presented in Table 4.1 have been employed to examine whether the wave observed by the radar is associated with a substorm, given that previous wave observations with a similar equatorward propagation in latitude and intermediate- $m$  azimuthal properties were linked to substorm-generated particles (e.g., Yeoman *et al.*, 2010). Also, the magnetometer measurements are examined for the signatures of the wave observed by the radar.

### 4.4.1 Substorm Occurrence

Figure 4.14 presents the unfiltered X-component the the IMAGE stations covering latitudes decreasing from top to bottom panels, with the last panel representing data from one of the stations (HAN, see Table 4.1) but band-pass filtered using a cut-off period between 20 s and 200 s to emphasise Pi2 pulsation activity. This figure shows that the interval between 18:00 UT and 20:10 UT on 12th May 2016 is magnetically quiet, followed by the onset of a substorm expansion phase characterised by sharp decrease in the X-component magnetic field at high latitudes as earlier discussed in Section 1.5.1.1, which is corroborated by the observation of a clear mid-latitude Pi2 pulsation. There are two clear subsequent Pi2 bursts around 20:50 UT and 23:30 UT on 12th May 2016. However, the substorm with the onset expansion phase at 20:10 UT may not be responsible for the wave activity detected by the Hankasalmi radar given the time lag of about 2.30 hours between the onset and the time (0000 – 0300 UT, May 13 2016) that the wave activity was clearly observed in the radar data. As such, the subsequent bursts at about 20:50 UT and 23:30 UT are the likely substorm candidates that can drive the ULF wave observed in the radar. Thus, the observed enhanced westward electrojet and substorm magnetic bay activity, up to -150 nT in the X-component data (equivalent here to the H-coordinate magnetic perturbation), confirm substorm occurrence and accompanying energetic particle injection at about 1-hour prior to the interval ULF wave activity is seen in the radar data.

## IMAGE x-component

Data from 18:00 UT 12th to 06:00 UT 13th, May 2016

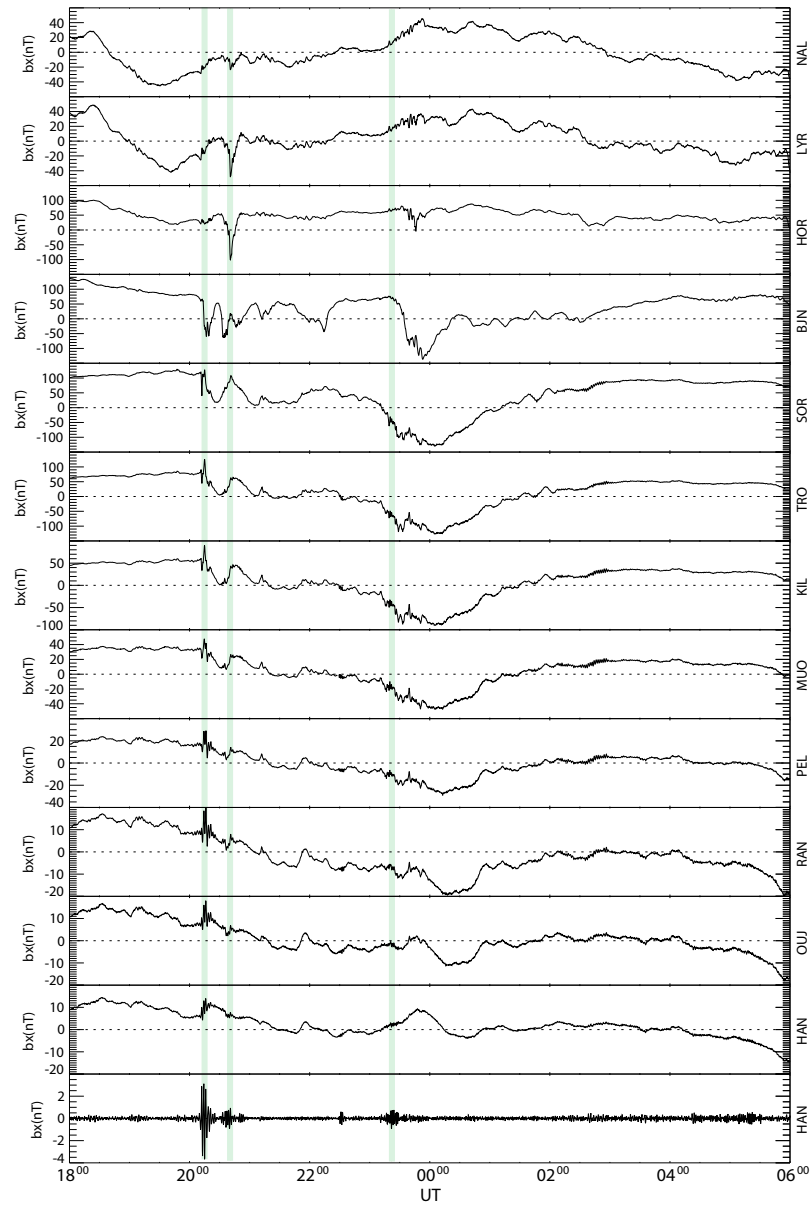


**Figure 4.14:** Unfiltered IMAGE X-component magnetometer data during the substorm interval. The IMAGE stations covering decreasing latitudes from top to bottom panels. The last panel shows HAN station data bandpass filtered between 20-200 s to highlight Pi2 pulsation activity. The light green outlines indicate onset of substorm expansion phase and subsequent bursts.

We cannot precisely identify the substorm location with only ground magnetometers and also considering that the Atlantic lies to the west with no magnetometers in contrast to, for example, James *et al.* (2013), where they used substorms located by their auroral signatures. However, Figure 4.15 depicting a positive and negative bay in the mid-latitude X- and Y-component magnetic field respectively, suggests that the substorm is near and to the west of the IMAGE magnetometers. As discussed earlier in Section 1.5.1.1, the variations of magnetic bays in the components of the geomagnetic field close to the substorm current wedge (SCW) can be used to deduce the location of the substorm. A negative gradient of the X-component coinciding with the Pi2 burst at higher latitude as shown previously in the top panels of Figure 4.14 indicates a westward electrojet. The upward and downward field-aligned currents from the SCW which feed this electrojet predict a symmetric peak in the X-component around the centre of the SCW, and an asymmetric pattern in the Y-component at lower latitudes as highlighted in Figure 4.15. Thus, the mid-latitude X- and Y-component data here are consistent with a substorm close to the wave observations, but to the west. The role of energetic particle population from the substorm in generating the Pc5 wave is considered in Section 4.5.1.

The Y-component of the magnetometer data as shown in Figure 4.16, reveals signatures of a long-period magnetic perturbation highlighted by light-blue outline and a seemingly narrowband short-period wave denoted by light-yellow outline. It is interesting to note here that the Y-component (east-west component at the earth's surface) of the magnetometer data is equivalent to north-south (direction of the Hankasalmi radar FOV) velocity of the ionospheric irregularities measured by the radar. Inspecting Figure 4.16 further, shows that for example, for the BJN station, there is a wave activity with a period of  $\sim 1350$  s (referred to as a Pc5 wave). This period is similar to the wave observed by the radar, which suggests that the magnetometer data may have detected the wave activity seen in the radar data.

Furthermore, analysis involving a band-pass filtering of the Y-component magnetometer data with a cut-off period between 20 and 150 s indicates another distinct wave activity as shown in Figure 4.17. On a closer look at magnetometer stations such as SOR and TRO (in the geomagnetic latitude range of  $63^\circ$ - $68^\circ$ ),

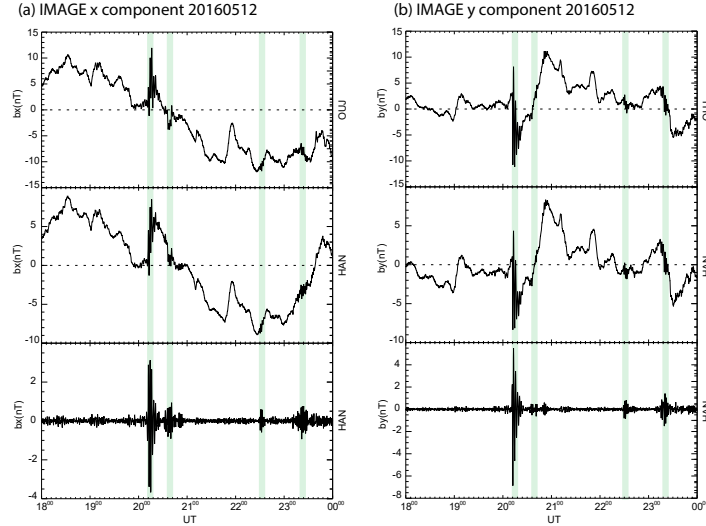


**Figure 4.15:** Magnetic field bay of mid-latitude IMAGE (a) X-component and (b) Y-components during the substorm. The data is the same as in previous Figure 4.14 and subsequent Figure 4.16 but for selected two mid-latitude stations between 18:00 and 23:59 UT interval on 12th May 2016. The top and middle panels are unfiltered X- and Y-components from the Ouj and HAN stations of the IMAGE array, while the bottom panels are HAN station but with a 200-20 s band-pass filter applied to illustrate the Pi2 pulsation activity (onset times marked with light green solid lines) associated with the substorm expansion phase onset at about 20:10 UT.

this distinct wave activity looked to have a period of  $\sim 120$  s, which is within the frequency band of a Pc4 ULF wave (Jacobs *et al.*, 1964). Thus, detailed investigation of the Pc5 and Pc4 ULF wave events in the magnetometer data are presented in the next two sections.

#### 4.4.2 Magnetometer Observation of the Pc5 ULF wave

The IMAGE magnetometers have been employed to analyse the low frequency ULF wave characteristics observed between 00:00 and 03:00 UT on 13 May 2016 using Fourier analysis. As earlier stated, magnetometer and radar instruments complement each other. Thus, studying a wave event with both instruments will lead to an enhanced understanding of the wave behaviour. Fourier spectra, calculated between 00:00 and 03:00 UT reveal a peak frequency of 0.77 mHz. This

## IMAGE y-component

Data from 23:00 UT 12th to 03:30 UT 13th, May 2016

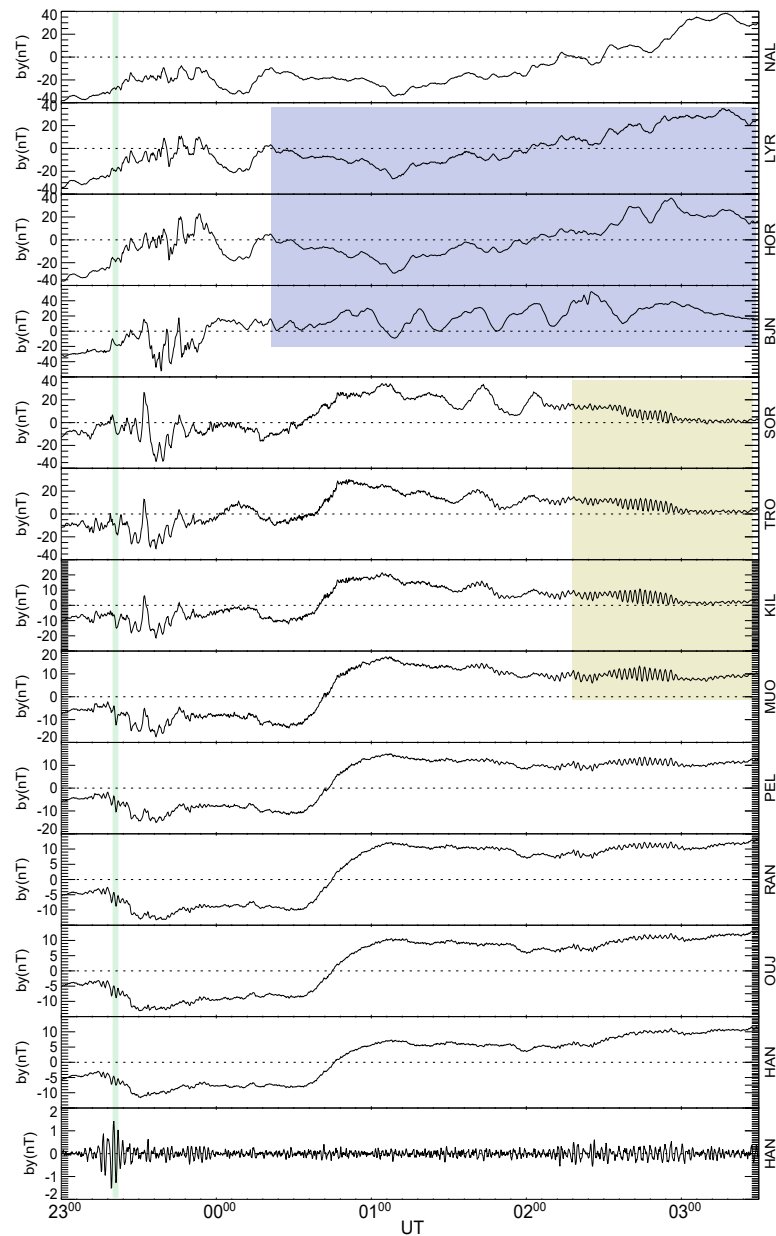


**Figure 4.16:** Similar to Figure 4.14 but for Y-component (east-west component at the earth's surface) and interval of 23:00 UT 12th to 03:30 UT 13th, May 2016. The last panel shows HAN station data bandpass filtered between 20-200 s to highlight Pi2 pulsation activity indicated by the light-green outline. The light-blue and yellow highlight a long period wave activity and a short period wave respectively.

## Filtered IMAGE y-component Data

Data from 02:00 UT to 03:00 UT, 13th May 2016

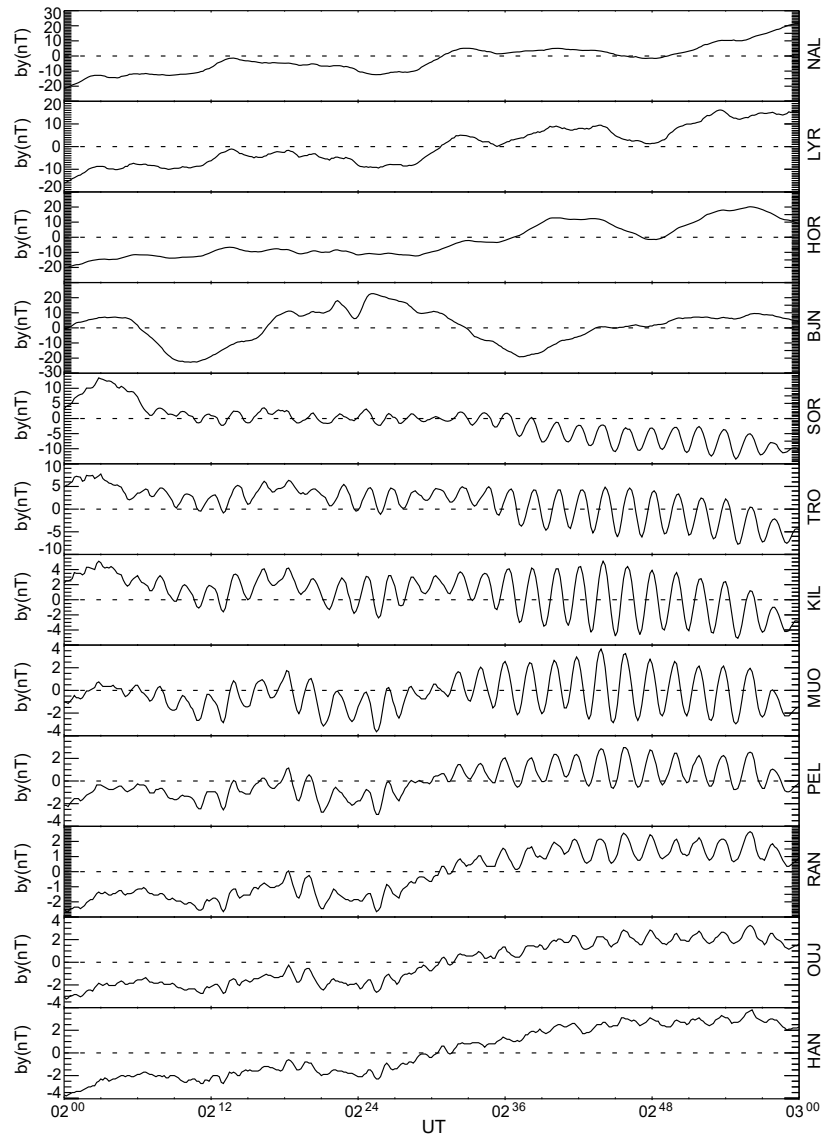


**Figure 4.17:** IMAGE Y-component magnetometer data between the intervals 02:00 UT – 03:00 UT on May 13th, 2016. The IMAGE stations covering decreasing latitudes from top to bottom panels. The data is bandpass-filtered between 20-150 s to highlight a Pc4 pulsation activity observed in the magnetometer data.

peak frequency observed in the magnetometer data is consistent with the initial inspection as well as being similar to the 0.75 mHz observed in the radar data. This is an indication that the same wave activity is detected in the ionosphere by the radar and on the earth's surface by closely located magnetometers.

The 0.77 mHz Fourier wave amplitude peaks between  $\sim 70^\circ$  and  $72^\circ$  in latitude and between  $\sim 102^\circ$  and  $106^\circ$  in longitude and respectively illustrated in Figures 4.19(a) and (c), which is consistent with the behaviours of the Pc5 wave as observed by the Hankasalmi radar. The phase variation determined with Fourier analysis suggests a latitudinal phase gradient of  $\sim 13.2^\circ$  per degree in the equatorward direction, from  $66.5^\circ$  to  $\sim 74.1^\circ$  latitude range as depicted in Figure 4.19(b). In longitudinal phase variation shown in Figure 4.19(d) reveals an effective azimuthal wave number,  $m$ , of  $\sim 16 \pm 1$  in the eastward direction. Note that the BJN station is the only magnetometer that lies close to the radar action, as such, the wave behaviour seen here from the magnetometer data is consistent with radar observation. However, we have not tried to split the wave in the same way that was possible with the radar data. Thus, the Pc5 wave observed by ground-based IMAGE magnetometers with an equatorward phase propagation in latitude and eastward propagation in longitude ( $m$  number of  $\sim 16 \pm 1$ ), have similar ULF wave characteristics to the wave observed in the radar.

### 4.4.3 Magnetometer Observation of a Pc4 ULF Wave

Apart from the Pc5 wave seen in the magnetometer data, which seems to be the same wave activity observed by Hankasalmi radar based on Fourier analysis, preliminary analysis in Section 4.4.1 indicated a distinct Pc4 wave. This Pc4 wave, which is clear in the magnetometer dataset between 02:00 - 03:00 UT is analysed in detail here.

Fourier spectra, calculated between 02:00 and 03:00 UT reveal a peak frequency of 8.3 mHz, a typical Pc4 ULF wave, which is consistent with initial inspection. At this peak frequency, Fourier wave amplitude and phase as function of magnetic latitude and longitude was determined as shown in Figure 4.18 in a similar way to Figure 4.19. In contrast to the Pc5 wave observed simultaneously in the Hankasalmi radar and IMAGE magnetometer dataset, here, Fourier

IMAGE y-component Data

Pc4 Fourier amplitude and phase variation from 02:00 to 03:00 UT on 13th, May 2016

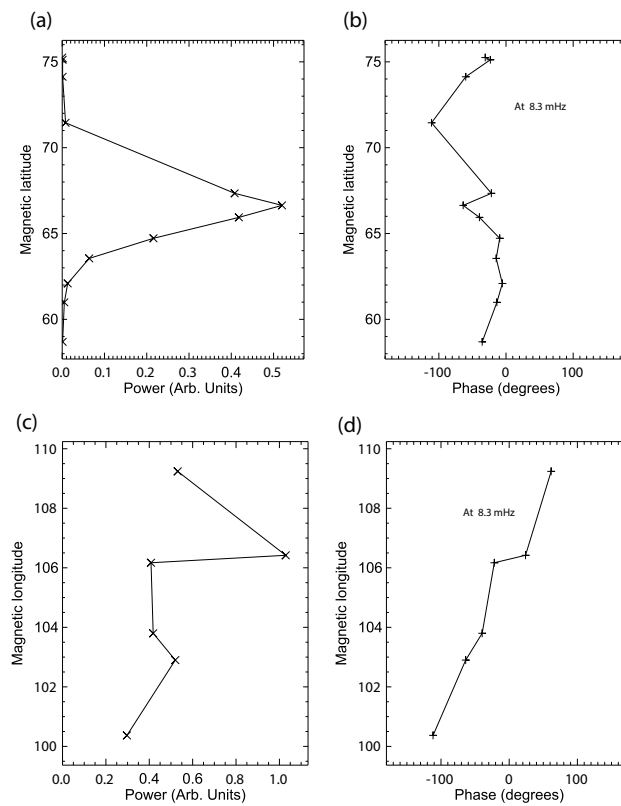


**Figure 4.18:** Similar to Figure 4.19 but for the Pc4 ULF wave observation at 8.3 mHz peak Fourier spectra in the IMAGE Y-component magnetometer data between the interval 02:00–03:00 UT on May 13th, 2016.

## IMAGE y-component Data

Fourier amplitude and phase variation over 00:00 to 03:00 UT on 13th, May 2016

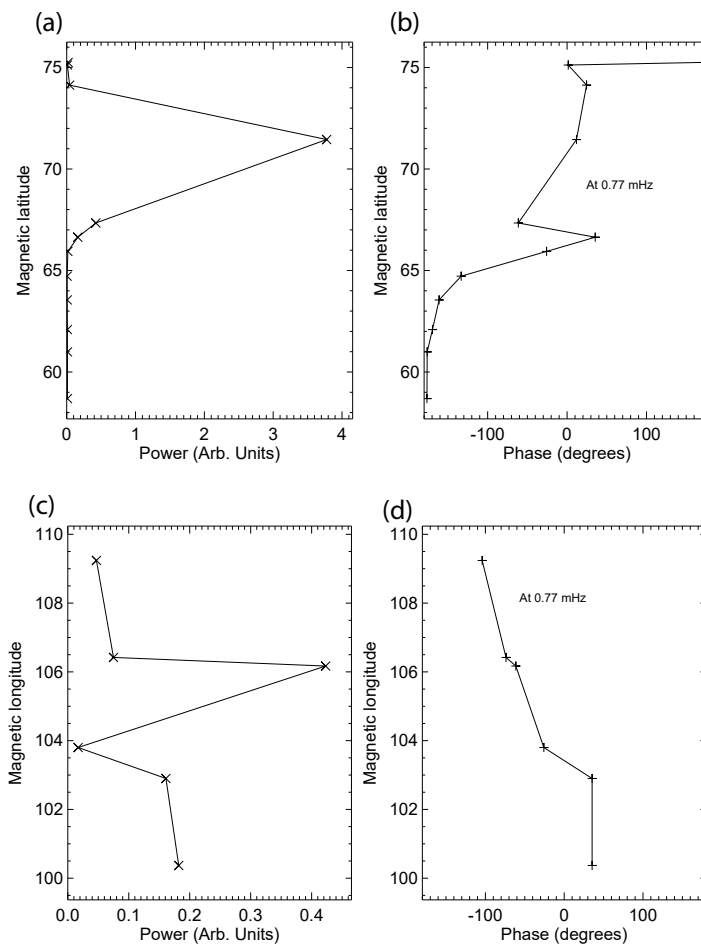


**Figure 4.19:** Latitudinal variation of (a) amplitude and (b) phase and equivalent longitudinal (c) amplitude and (d) phase profiles for the Pc5 ULF wave observation at 0.77 mHz peak Fourier spectra in the IMAGE Y-component magnetometer data between the interval 00:00–03:00 UT on May 13th, 2016.

analysis indicates a poleward latitudinal phase variation and a westward longitudinal phase propagation with an azimuthal wave number of  $-21 \pm 1$ . As such, the periodic perturbation with 8.3 mHz seen in the Y-component magnetic field data is very different from the Pc5 wave observed by both radar and magnetometers.

The likely source of the wave observations from the radar and magnetometer datasets are discussed along with observations of related previous studies in the next section.

## 4.5 Discussion

The oscillatory flow in the velocity data measured by the Hankasalmi SuperDARN radar on 13th May 2016 has been investigated for ULF wave activity using Fourier wave analysis as shown in the previous sections. This section presents the interpretation of the characteristic features observed for the case study ULF wave along with the magnetometer observations.

The wave activity studied using radar data between 00:00 and 03:00 UT is characterised by a frequency of 0.75 mHz, which is denoted as a Pc5 pulsation. The total equatorward latitudinal phase variation shown in Figure 4.2 slightly exceeded  $180^\circ$  in the radar FOV. As such, a field line resonance is ruled out as a possible wave mode. It is also characterised by eastward longitudinal phase propagation with an intermediate- $m$  effective azimuthal wave number (typically  $m = 10-15$ ) and a poloidal component. Equatorward phase propagation has been observed over part of the Hankasalmi radar FOV (e.g., Yeoman *et al.*, 2008a). Whilst the wave event in Yeoman *et al.* (2008a) and wave events observed in (e.g., Grant *et al.*, 1992; Yeoman *et al.*, 1992) using other ground-based instruments have a small azimuthal scale size (high- $m$  number), they are characterised by a westward longitudinal phase variation driven by drifting protons internal to the Earth's magnetosphere. Such observations of high- $m$  waves propagating in westward direction are sparse compared to observations of low- $m$  wave driven by external sources such as the solar wind. In contrast, the present observations of equatorward propagating ULF waves are more reminiscent based on wave's azimuthal scale size (intermediate- $m$  number) of waves observed by SuperDARN radars (Yeoman *et al.*, 2010), Van Allen Probes spacecraft (Hao *et al.*, 2014) and

simultaneously using radar and spacecraft (Mager *et al.*, 2019). However, the azimuthal direction found for the current wave is eastward, which is the same as Yeoman *et al.* (2010) but different from similar intermediate- $m$  ULF waves propagating westward in Hao *et al.* (2014); Mager *et al.* (2019). Therefore, there might be a difference in excitation mechanism between the Pc5 pulsation of the current case study and previous observations with intermediate- $m$  number.

### 4.5.1 Driving Particles and Wave Energy

The dissimilarities in the driving mechanism ascribed to previous observations of intermediate- $m$  waves (e.g., Yeoman *et al.*, 2010; James *et al.*, 2013; Hao *et al.*, 2014; Mager *et al.*, 2019) observed by radar and spacecraft, connotes the complexities in predicting processes driving such a wave.

In the present case study, magnetic perturbations in the H coordinate system recorded at a number of IMAGE magnetometer stations having a close proximity with Hankasalmi radar, confirmed that there were various substorm occurrences prior to the interval the waves are observed. One of such substorms occurred at  $\sim 23:30$  UT on 12th May 2016, which was about 1 hour to the time of the wave event. Due to the nearness of the substorm onset to the wave, there is a likelihood that energetic particles associated with the substorm might be driving the waves. This assumption is consistent with the interpretation of previous observations of intermediate and high- $m$  waves with similar wave characteristics observed by satellites (Kazue & McPherron, 1984) and ground-based radars (Baddeley *et al.*, 2005; Yeoman *et al.*, 2010). In such a case, the driving mechanism may be due to the drift-bounce Alfvénic instability. This instability develops when particles with a given angular drift frequency exchange energy with waves under the drift-bounce resonance (Southwood *et al.*, 1969) as discussed further below. Note that the drift and drift-bounce resonance can involve protons and westward propagation while drift resonance only is possible for electrons and eastward propagation, due to the very rapid electron bounce. In addition, a similar intermediate- $m$  wave reported by (Yeoman *et al.*, 2010) with equatorward latitudinal and eastward azimuthal phase propagation was associated with energetic particles generated by a substorm.

Following the substorm-particles being injected close to the time of wave observation, the energy in keV associated with these particles can be determined for a better understanding of the wave characteristics. The driving particle energy is predicted using the drift-bounce resonance condition. The equation

$$\omega_{wave} - m_{wave}\omega_d = N\omega_b \quad (4.1)$$

described in Section 2.3 can be solved with respect to whether the driving particle is an electron or an ion. The pulsation event is assumed to have either a fundamental (symmetric,  $N = 0$ ) or second harmonic (anti-symmetric,  $N = 1$ ) standing wave structure. Based on these assumptions, the technique expressed in (Chisham *et al.*, 1992; Chisham, 1996) and applied by Yeoman *et al.* (2010) and also by Yeoman & Wright (2001); Baddeley *et al.* (2005) are followed in predicting the energy of the driving particles given that the effective azimuthal wave number derived for the Pc5 wave observations and wave phase propagation are similar to (Yeoman *et al.*, 2010). Following Baddeley *et al.* (2005), the angular drift frequency of interacting particles are determined using

$$\omega_{drift} = \frac{6WL(0.35 + 0.15 \sin \alpha)}{B_s R_E^2} + \frac{2\Psi_0(0)L^3 \sin \varphi}{B_s R_E^2} \quad (4.2)$$

where  $W$  represents the particle energy in eV and  $L$  is the particle's L-shell.  $B_s$  is the equatorial surface magnetic field strength,  $\varphi$  is the azimuth of particle measured anticlockwise from local midnight,  $\alpha$  is the particle pitch angle,  $R_E$  is the Earth radius and  $\Psi_0(0) \sim 45(1 - 0.159K_p + 0.0093K_p^2)^{-3}$  is the Volland-Stern (Volland, 1973; Stern, 1975) representation of the convective dawn to dusk electric potential. The first term on the right hand side of Equation 4.2 written as positive here is negative for ions. This term represents the gradient-curvature drift and so is in the opposite direction for ions (westward) and electrons (eastward), whereas the second term on the right hand side of Equation 4.2 is that resulting from  $\mathbf{E} \times \mathbf{B}$  drift from the dawn to dusk electric field, and acts the same on both electrons and ions. But due to its relationship to  $\sin \varphi$  it is positive (eastward) in the morning sector, and negative (westward) in the afternoon sector (and so contributes a drift component towards the dayside for both ions and electrons, irrespective of location) (Chisham, 1996).

Likewise, the angular bounce frequency is determined using

$$\omega_{bounce} = \frac{\pi\sqrt{W}}{\sqrt{2m_p}LR_E(1.3 - 0.56 \sin \alpha)} \quad (4.3)$$

where  $m_p$  is the proton mass, while other parameters retain the same meaning. The L-shell values used for the Pc5 wave observation were in the range of 6.6 - 15, where the wave ranged, with a peak power at about L=7.5, which was used for the calculation, while the pitch angles used were 70° and 45° to 20° when considering a drift and a drift-bounce interaction respectively. As explained in Southwood & Kivelson (1982), drift resonance are likely to occur with particles of large pitch angles in the equatorial plane, whereas the drift-bounce resonance occur mainly with particles os smaller pitch angles. A single value (pitch angle) is used for drift-frequency calculation given that a range similar to the drift-bounce frequency calculation has very small effect. The Pc5 wave with eastward azimuthal phase propagation and equatorward phase motion is thought to be a fundamental poloidal mode (Yeoman & Wright, 2001). This coincided with the direction of gradient-curvature drifting electrons following substorm injection. As such, drift resonance is the only viable mode, which requires a large pitch angle for protons situated near the equator where the wave electric field is strongest (Southwood & Kivelson, 1982) and also applies to electrons (e.g., Yeoman *et al.*, 2010). The Pc5 wave observed by the Hankasalmi SuperDARN radar indicated particle's energy of  $35 \pm 5$  keV for a drift resonance interacting medium as graphically represented in Figure 4.20, showing the drift resonance condition ( $N = 0$  in the Equation 4.1). Figure 4.20 is a representation of the possible interacting energies (keV) of the particle population on the x-axis and the left hand side of Equation 4.1 (in radians per second) on the y-axis using the  $m$  number and frequency of the Pc5 wave. The spread in the blue shaded area is indicating maximum error due to uncertainties in the parameters used. The drift resonance condition is satisfied where the blue shaded area crosses the x-axis. The particles can provide energy to such a wave mode at those interaction energies where a non-Maxwellian ion distribution function has a positive gradient, indicating that the free energy is available (Southwood, 1976; Hughes & Southwood, 1976; Baddeley *et al.*, 2002).

The wave characteristics of the Pc5 ULF wave observations have some similarities with previous wave studies as illustrated in Table 4.2. The drift-time of

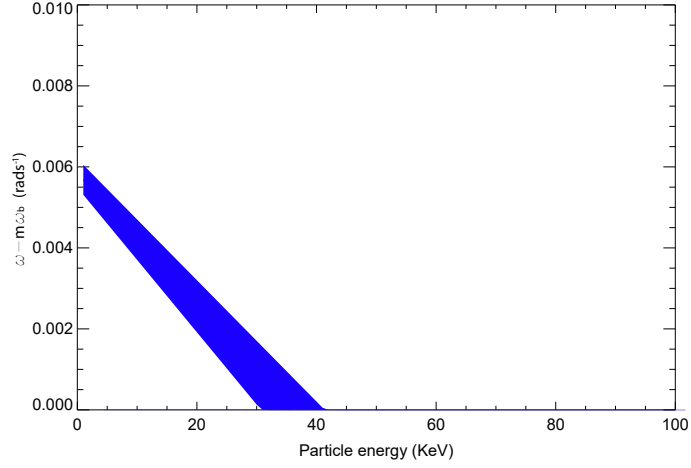


**Figure 4.20:** A graphical representation of the drift resonance condition for the Pc5 ULF wave event.

$\sim 8$  minutes per hour of Local Time (LT) is predicted for the Pc5 wave from the wave angular frequency of about  $6 \times 10^{-3}$  rads  $s^{-1}$ ,  $m$  number of  $17 \pm 1$  and drift angular frequency of  $\sim 5 \times 10^{-4}$  rads  $s^{-1}$  in drift resonance condition, which suggests that this wave is driven by particles associated with the 23:30 UT substorm expansion.

Study	Instrument	$m$ number	Period	L-Shell	W(keV)
This study	Radar	$+17 \pm 1$	1342	6.6-15	$35 \pm 5$
	Magnetometer	$+16 \pm 1$	1294	6.6-15	$35 \pm 5$
(Yeoman <i>et al.</i> , 2010)	Radar	+13	580	7-15	33
(James <i>et al.</i> , 2016) - Event 2	Radar	-12	1440	9.08	8-19

**Table 4.2:** A summary of the characteristics of the Pc5 ULF wave observations and a previous ULF wave observations with equatorward phase propagation.

### 4.5.2 Possible Phase Evolution

A possible evolution in the phase characteristics of the Pc5 wave activity observed by radar as seen in Figure 4.2. Initial investigation suggested that the wave evolved from an equatorward to poleward phase propagation, depicted by the velocity measurement away from the radar. The phase variation coincided with an eastward drifting bite-out observed across the radar beams. The 3-hour dataset is subdivided into interval 1 and 2 to further examine the wave phase behaviour. ULF wave driving mechanisms other than the drift-bounce instability explored in deriving the particle's energy as shown in the last section need to be considered to understand the possible phase evolution.

The investigation of a likely phase evolution seen in the ionospheric velocity data suggested that during Interval 1, the Pc5 wave is mostly equatorward along Beam 9. The equatorward signature is clearer at this interval compared to the analysis over 3-hours. The azimuthal wave propagation was eastward, which is consistent with the analysis over the 3-hour interval. However, the  $m$  number is higher compared to the analysis over the 3-hour interval but within the uncertainties. On the other hand, the analysis of the Interval 2 produced a mostly mixed latitudinal phase propagation along the radar beams, with Beam 9 showing a poleward phase variation with a small gradient as well as azimuthal wave characteristics reminiscent of the 3-hour interval and Interval 1. Thus, there is a likelihood that the particle injection responsible for the backscatter bite-out, which appeared at the beginning of Interval 2 resulted in the latitudinal phase transformation observed for the Pc5 wave.

In a similar substorm-driven ULF wave observed by Hankasalmi and Pykkvibær SuperDARN radars, Yeoman *et al.* (2010) following a moving wave source theory (e.g., Mager *et al.*, 2009), suggested that the azimuthal separation of a substorm onset and a wave excitation due to particle population from the substorm influences the particle energy and azimuthal wave number. Also, this assumption has been corroborated by other studies (e.g., James *et al.*, 2013). As such, lower energy particles (associated with higher- $m$  azimuthal wave number) are due to bigger azimuthal separations between substorm onset and the wave.

Going by this postulation, there is a possibility that the previous 20:50 UT substorm-injected particles are responsible for the behaviour exhibited by the Pc5 wave during Interval 2 while an earlier substorm onset with a larger azimuthal separation led to the higher  $m$  number observed for the wave during Interval 1. This possibility is ruled out given that the previous substorm was quite distant in time, so would not be a candidate for providing particles of the energy predicted by the wave parameters during Interval 1 and 2. Another possibility is that additional particles injected by a latter burst (e.g., the 23:30 UT) is responsible for the wave peculiarity during Interval 2 while particles from a sub-structure within the original substorm injection at  $\sim 20:50$  UT, farther in azimuthal separation, is responsible for Interval 1. This latter interpretation is in agreement with the inferred particle energy of  $35 \pm 5$  keV. In addition, a hint of more particle injection after 23:30 UT is seen from Figure 4.16. Therefore, it is suggested here that an additional particle injection drifting round the earth in MLT and arriving later in time, resulted in a phase mixing observed in the radar data. This additional particle injection may have caused the eastward drifting backscatter "bite-out" observed across the beams as seen in Figure 4.3 following (e.g., Gauld *et al.*, 2002), which can alter the wave structure observed by radar (Yeoman *et al.*, 2012).

According to Klimushkin *et al.* (2004), Alfvén waves can transform from poloidal to toroidal polarisation and vice versa. The condition required for such transformation is detailed in (Klimushkin *et al.*, 2004). Similarly, Mager & Klimushkin (2008); Zolotukhina *et al.* (2008); Mager *et al.* (2009) have demonstrated transformation of ULF wave activity between a mixed polarisation and poloidal. They showed theoretically that the wave transforms into a mixed polarization as it moves farther and farther away from the driving source. In another previous study, Yeoman *et al.* (2012) observed a ULF wave event with a high- $m$  and curved phase fronts, which they noted as a common action of the field line curvature, the plasma pressure and the equilibrium current, while some of the wave features agreed with a wave signature resulting from proton cloud drifting away from source in the magnetosphere. In another previous study, Chelpanov *et al.* (2019) reported a wave event observed by radar that transformed from a poleward to equatorward phase propagation. They attributed the wave mode to a drift-compressional mechanism described in (Chelpanov *et al.*, 2016; Kostarev

& Mager, 2017). In the case of Mager *et al.* (2009), which considered a wave propagating equatorward in latitude, the azimuthally drifting particle inhomogeneity injected during substorm activity was suggested as a likely excitation mechanism for an azimuthal direction of the phase velocity that coincides with the cloud of energetic particles from the substorm. Consequently, the equatorward phase propagation observed here, which is thought to be resulting from the spatial structure of the driving particles might be accompanied by an evolving wave polarisation as the particle populations themselves evolve. However, such an evolution of the wave polarisation would not obviously transform the latitudinal phase propagation from poleward to equatorward. On the other hand, new particle populations are a candidate for transforming the wave polarisation. This will be investigated here and in the next chapter.

### 4.5.3 Eastward Drifting Bite-out

An eastward drifting backscatter bite-out feature is observed in the ionospheric plasma velocity flow across the Hankasalmi radar beams as earlier shown in Figure 4.3. Interestingly, eastward direction of this backscatter bite-out matches with the longitudinal phase propagation of the Pc5 wave observed in both the radar and magnetometer data. Here, the measured azimuthal propagation of the bite out feature is compared with the calculated azimuthal propagation of the particles inferred from the wave observations, to establish whether the same energy particles might be associated with both. Following the time interval that this feature is observed are signatures of latitudinal phase mixing and evolution observed in the radar data, more prominent in the velocities away from the radar. As noted earlier, this is an indication that the processes driving the wave might be responsible for the backscatter bite-out. The velocity of the plasma flow associated with this feature has been determined from which the drifting particle energy is predicted. The time intervals between the onset and end of this feature for beam 5 is  $t_2 - t_1$  and for beam 9 is  $t_4 - t_3$ . The time gradient is estimated as 600 s with the longitudinal spatial gradient,  $\Delta long$  between beam 5 and beam 9 giving  $7.4^\circ$ . A drift velocity corresponding to an angular frequency of  $2.2 \times 10^{-4}$

rads s<sup>-1</sup> is determined by using

$$\frac{\Delta long \times \frac{\pi}{180}}{(t_4 - t_2) - (t_2 - t_1)} \quad (4.4)$$

This angular frequency is comparable to the predicted particle angular frequency of  $\sim 5 \times 10^{-4}$  rads s<sup>-1</sup> with energies of  $35 \pm 5$  keV derived from the Pc5 wave analysis. This provides a hint that the dynamic energetic particle interactions producing this backscatter bite-out feature are responsible for the evolution of the wave activity observed by the Hankasalmi radar on 13th May 2016 from 00.00UT to 03.00 UT.

#### 4.5.4 Ground Magnetometer Wave Signatures

##### 4.5.4.1 The Pc5 Wave

In the magnetometer data, a wave was detected with a frequency similar to the Pc5 wave observed by the Hankasalmi radar. In addition, this Pc5 wave observed in the magnetometer data followed a similar equatorward latitudinal phase propagation as well as an eastward azimuthal propagation. The effective azimuthal wave number at 70° is  $16 \pm 1$ , which is slightly less than  $17 \pm 1$  derived for the radar observation at the same latitude. This slight disparity in  $m$  number of the pulsation in the ionosphere as seen by Radar and on the Earth's surface measured by magnetometer might be due to attenuation of wave field by the ionospheric currents as described in (e.g., Hughes & Southwood, 1976). Such attenuation as shown by Hughes & Southwood (1976), is proportional to  $e^{-kz}$  where  $k$  is the field-perpendicular component of the wave number and  $z$  is the E-region height of the ionosphere. Due to ionospheric screening, the attenuation factor has to be small in order for the waves to be detected on the ground by magnetometers. Whilst ULF waves with a high  $m$  number have been simultaneously detected in the ionosphere by radar and in ground magnetometer data (e.g., Yeoman *et al.*, 2012; Mtumela *et al.*, 2015), such multi-instrument observations of intermediate- $m$  and high- $m$  waves are sparse. The same particle energy predicted for the Pc5 wave observed by the radar is applicable for the magnetometer data, clearly indicating that the same wave activity was observed simultaneously in the radar and magnetometer data.

#### 4.5.4.2 The Pc4 Wave

The Pc4 wave seen in the magnetometer data revealed different latitudinal and azimuthal properties to the Pc5 wave. The rapid poleward latitudinal phase propagation and westward azimuthal propagation (high- $m$  number of  $-21 \pm 1$ ) observed for this wave suggests a giant pulsation (Pg). The wave-particle energy for the Pc4 wave event is graphically shown in Figure 4.21, where the blue shaded area represents the left hand side of the wave resonance equation for a drift solution ( $N = 0$  in Equation 4.1) and the orange shaded curved areas represent the right hand side of Equation 4.1 for the bounce angular frequency ( $N = 1$ ). The interval where both drift and bounce solution intersect, representing a drift-bounce resonance, is highlighted by a dotted orange line. This wave-particle energy predicted by applying the same method earlier discussed in Section 4.5.1 indicated that the high (Pc4) frequency wave observed in the magnetometer data could either be driven through a drift resonance interaction (a fundamental mode) with ions of  $143 \pm 10$  keV or a second harmonic mode driven by a drift-bounce resonance interaction with ions of  $10 \pm 3$  keV. However, following the interpretations of previous observations (e.g., Baddeley *et al.*, 2005) of waves with similar frequency and azimuthal wave number suggests that a second harmonic mode through a drift-bounce resonance interaction is the likely process driving this wave and it is consistent with characteristics associated with giant pulsations (Pgs). Chisham & Orr (1991) in a statistical study of Pgs, observed that most Pg events occur between 02:00 LT and 06:30 LT with L-shell values ranging from 5.75 and 7.75. They suggested a drift-bounce resonance instability as the likely generation mechanism for Pgs, which involves energetic protons injected into the nightside to have drifted round the Earth in time to generate Pgs, dominantly of even-mode structure along the geomagnetic field-line. Various previous studies (e.g., Wright *et al.*, 2001) of Pgs using ground-based instruments, spacecraft in-situ measurements or both, have supported the mechanism described for Pgs in Chisham & Orr (1991).

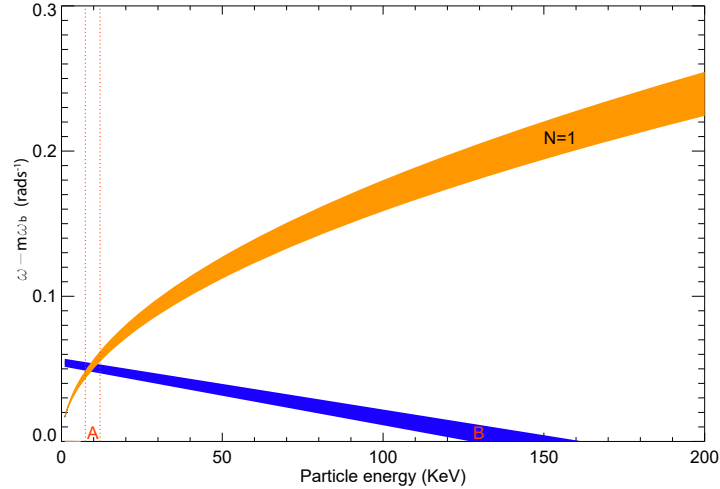


**Figure 4.21:** A graphical representation of the drift-bounce resonance condition for the Pc4 ULF wave event. The side labelled A represents wave particle energy driven through a drift-bounce resonance interaction while B represents wave driven through a drift resonance.

Another previous study of Pgs by Glassmeier *et al.* (1999) demonstrated a case of Pgs associated with drifting proton particles injected into the nightside magnetospheric ring current from a substorm activity using a ground-based and satellite instruments. Rostoker *et al.* (1979) alluded that Pc4 giant pulsations mainly occur in the magnetosphere that is quiet or recovering from magnetic activities such as a substorm. In the case of the Pc4 wave event presented here, particle drift time of about 2 minutes per hour of LT is predicted for a drift resonance solution. No evidence of such a substorm is observed east of the wave event. On the other hand, a particle drift time of about 87 minutes per hour of LT is calculated for a drift-bounce solution. This time is too long for any individual substorm to be associated with the particle injection proposed to be driving the wave activity. As such, none of the substorm events considered here is linked to the Pc4 wave following the particle drift time for both of these solutions. However, the substorm associated with the Pc5 wave cannot be associated with this Pc4 wave event, and there is no evidence of a nearby candidate substorm in the magnetometer data, supporting the idea that the substorm is distant and the  $10 \pm 3$  keV low energy solution is correct. This implies that the particles have

probably drifted a long way. In addition, the frequency (8.3 mHz, much higher than the nearby 0.75 mHz wave event) is strongly suggesting a second harmonic mode for the Pc4 wave event, hence supporting a drift-bounce resonance solution. Thus, it seems reasonable to suggest that the Pc4 wave described here is more from a drift-bounce resonance instability with a likely even-mode structure in the magnetosphere and proton energy of  $10 \pm 3$  keV given that time of occurrence,  $m$  number and the L-shell predicted for the wave is similar to Chisham & Orr (1991) than due to a drift resonance instability suggested in (e.g., Glassmeier *et al.*, 1999). However, the coincidence between the time it occurred and the interval in which a phase evolution was observed in the radar data requires further studies to ascertain whether the coincidence is a one-off or a recurrent event.

## 4.6 Summary

ULF wave activity observed by the Hankasalmi SuperDARN radar, as well as detected in the data of IMAGE magnetometers with close proximity to the radar has been studied using Fourier wave analysis. Denoted as a Pc5 pulsation, this wave followed an equatorward phase propagation in latitude and an eastward azimuthal propagation with an average  $m$  number of  $17 \pm 1$  making it an intermediate- $m$  class of ULF wave according to Yeoman *et al.* (2010). The disparity between the measurement of the wave activity in the ionosphere by Radar and on the Earth's surface by magnetometer is due to wave attenuation of the pulsation magnetic perturbation below the ionosphere. The Pc5 wave reported here is believed to be due to drifting energetic electrons via a kinetic instability caused by the non-Maxwellian electron distribution functions, commonly termed “bump-on-tail” distributions similar to proton particles reported by (e.g., Baddeley *et al.*, 2005). The generation mechanism is thought to be a drift resonance ( $N = 0$ ) wave-particle interaction (Southwood, 1976). On the other hand, the features of phase evolution observed by the radar may be due to an additional electron cloud drifting azimuthally in the magnetosphere. These additional energetic electrons are thought to be responsible for the evolving temporal latitudinal phase propagation, which is supported more by another possible ULF wave interpretation, the moving source theory Mager & Klimushkin (2007, 2008), which a similar case

study of an intermediate- $m$  wave by Yeoman *et al.* (2010) adopted as a candidate for driving the wave event in their work. Other mechanisms behind the transformation and mixing of ULF wave polarisation are addressed by previous studies (e.g., Klimushkin *et al.*, 2004; Mager & Klimushkin, 2008; Zolotukhina *et al.*, 2008; Mager *et al.*, 2009).

Furthermore, a backscatter bite-out drifting azimuthally in the same eastward direction as the Pc5 wave is observed in the ionospheric plasma velocity flow across the Hankasalmi radar beams. It is thought that the dynamic energetic particle interactions producing this backscatter bite-out feature might have triggered the temporal latitudinal phase evolution observed during the Pc5 wave activity by the Hankasalmi radar. At about the time the backscatter bite-out and temporal latitudinal phase evolution were seen in the radar data, a distinct narrowband wave feature with a 8.2 MHz peak frequency (a Pc4 wave) was observed in the magnetometer data. The high- $m$ , westward phase propagation and wave-particle characteristic of this Pc4 wave matched with waves interpreted in previous studies (e.g., Chisham & Orr, 1991) as giant pulsations.

The ULF wave analysis presented here has shown interesting features. For example, the phase evolution believed to be associated with the backscatter bite-out may be a one-off event or a recurrent event. Also, the energetic particles associated with the backscatter bite-out most likely have not generated the seeming giant pulsation given the difference in their propagation. Whilst the backscatter bite-out was propagating eastward, the high- $m$  Pg was propagating in the westward direction. This raises a question of whether such a narrowband wave could be applied as a tracer for identifying intermediate- $m$  waves with possible phase mixing or evolution in the radar and magnetometer measurements. In contrast, the narrowband (Pg) wave may be a one-off occurrence. Therefore, statistical analysis of similar wave events observed in radar measurements will be useful in confirming these possibilities. Observations of intermediate to high- $m$  ULF waves by radar and magnetometer are rare, making the case study presented here a useful analysis for further scientific understanding of this type of wave.

# Chapter 5

## A Statistical Study of Intermediate- $m$ ULF Waves Driven by Substorms

### 5.1 Introduction

In Chapter 4, we presented analysis of a Pc5 ULF wave with an intermediate- $m$  azimuthal wave number and evolving phase properties as observed by the Hankasalmi SuperDARN radar. The Pc5 wave was also detected by magnetometers in close proximity to the Hankasalmi radar. The analysis showed that the Pc5 wave is driven by substorm-associated particle injections. As such, it was suggested that the Pc5 wave was particle-driven, by eastward-drifting electrons with a predicted particle energy of  $35 \pm 5$  keV for a drift resonance. A kinetic instability caused by a bump-on-tail distribution similar to proton particles reported by (e.g., Baddeley *et al.*, 2005) is a candidate mechanism, while the evolving wave polarisation is supported more by the moving source theory Mager & Klimushkin (2007, 2008). There was also evidence that the backscatter bite-out observed in the radar data across the beams was drifting azimuthally in the same eastward direction as the Pc5 wave and is associated with energetic particles of a similar energy to those driving the Pc5 wave activity seen both in the radar and magnetometer datasets. Likewise, we presented an analysis of a Pc4 wave observed in

the magnetometer data at about the same interval the phase evolution and the backscatter bite-out were observed in the radar velocity data. The Pc4 wave with a westward phase propagation was interpreted as a likely giant pulsation following previous studies (e.g., Chisham & Orr, 1991) with similar wave characteristics.

Following the interesting characteristics observed in the case study ULF wave presented in the last chapter, a statistical analysis of similar wave events is conducted to examine these features. For example, there could be a relationship between the evolving phase features and the backscatter bite-out onset at about the time this phase transformation was seen in the radar. Also, the Pgs could be associated with the intermediate- $m$  waves with a possible relationship with the same driving particles, or the near-simultaneous occurrence of the two wave types could be a simple coincidence. Therefore, the statistical analysis presented here is aimed at confirming these interesting features as well as to provide a further understanding of this class of waves. A total of 18 wave events are used for this study.

As discussed earlier in chapters 1 and 4, magnetospheric ULF waves being a manifestation of magnetohydrodynamic wave activity in the frequency range of 1 to 100 mHz, are a major channel of energy and momentum in the dynamic interaction between the solar wind and the interplanetary magnetic field and the Earth's space environment. They are of intrinsic scientific interest, but also of societal and commercial importance as they form an important part of the space weather processes which impact on, for example, space hardware and communications systems. As such, the analysis presented here contribute to a better understanding of the characteristic features of ULF waves and the processes driving them.

## 5.2 Data

The instrumentation and procedure for ULF wave analysis employed in this section have earlier been described in Section 3.1.3 as well as applied to the case study wave analysis presented in Chapter 4. The Hankasalmi SuperDARN radar

employed here is located in Finland and sounded all its 16 beams, pointing northward. More detail of the operation, field-of-coverage (FOV) and measurements of this radar is discussed in Chapters 3 and 4 of this thesis.

The ionospheric velocity data of the Hankasalmi SuperDARN radar over the last ten years period before January 2018 were searched for likely ULF wave activity. As such, the statistics presented here used characteristic information of wave events selected based on a number of criteria. These wave events identified from the radar velocity data have been characterised by determining the frequencies, amplitudes and phase propagation of the waves. Then, such waves were selected for the following statistical analysis where they have effective azimuthal wave numbers in the intermediate- $m$  ULF wave range following the description, for example, in Section 2.4 and the generation mechanism can be attributed to substorm-injected particles. Furthermore, driving particle energies were predicted for the selected waves. An example wave event in the next section illustrates these selection criteria itemised below.

- Wave event with  $m$  number in the intermediate- $m$  range ( $10 \geq m < 20$ ).
- Wave event associated with substorm-injected particles.

### 5.2.1 Example Wave Event

Figure 5.1 presents line of sight velocity recorded by the Hanksalmi radar from which a ULF wave event is detected. The velocity data is colour coded such that red represents velocity flow away from the radar while blue represents velocity flow towards the radar over  $68^\circ - 74^\circ$  latitude range for about an hour after midnight on March 30th 2015. Fourier analysis similar to those applied for the case study wave in Chapter 4 is employed to characterise this example wave event and similar wave events used in the statistics as presented here. The dominant frequency of 0.83 mHz (a period of about 1200 s) is observed as revealed by Fourier spectra. The wave activity is obvious across beams 4 to 10 within a latitude range of about  $69^\circ - 74^\circ$ . As such, Fourier analysis is applied for range cells of those beams with obvious wave activity and percentage data occupancy

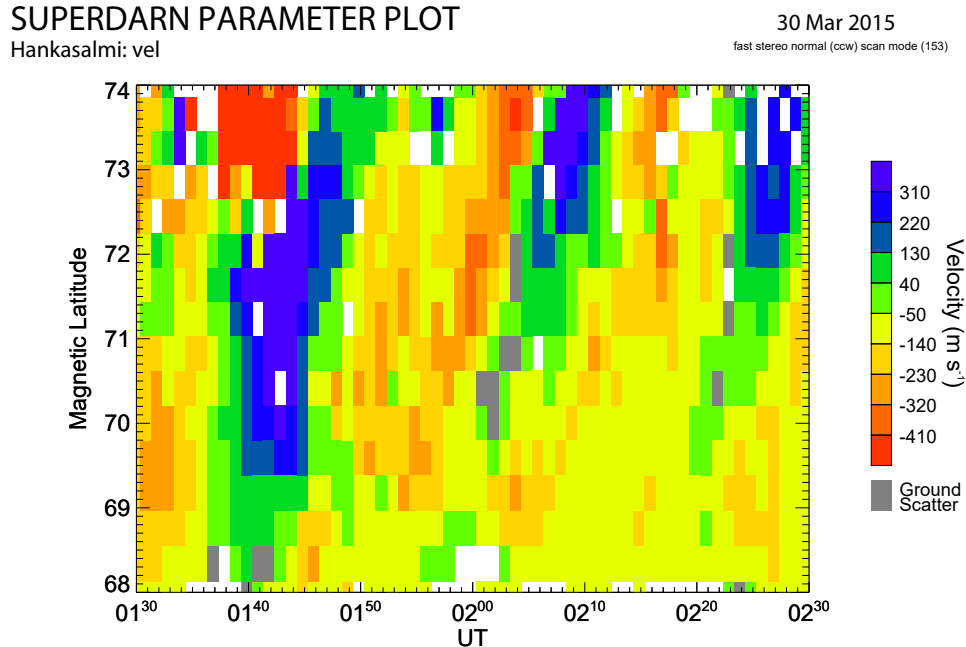


**Figure 5.1:** Hankasalmi beam 8 SuperDARN radar velocity measurements as a function of magnetic latitude. The ionospheric velocities are colour-coded such that red (negative) and blue (positive) represent velocities away from the radar and towards the radar respectively.

of  $\geq 50\%$  over the one hour interval of the wave observation for this example event. Note that a similar approach has been adopted for other events used in the statistical study. Values of Fourier power and phase for each range cell are plotted in a 2-dimensional latitude and longitude view as shown in Figure 5.2.

Figure 5.2 shows Fourier power and phase of the wave event shown in Figure 5.1 in a two dimensional analysis as a function of latitude and longitude. The near-vertical columns of range cell data correspond to radar beams and beam 8 is highlighted by a black outline. It can be seen in the left panel that the Fourier power is at a maximum value around  $73^\circ$  latitude and between  $\sim 111^\circ$  and  $113^\circ$  in longitude. The increasing phase values with decreasing latitude reveals a general poleward propagation as well as a westward propagation since the phase values tend to decrease to the west of longitude.

The 1-dimensional version of Figure 5.2 for beam 8 is shown as Figure 5.3. Fourier amplitude viewed in the 1-dimensional plot is consistent with the above

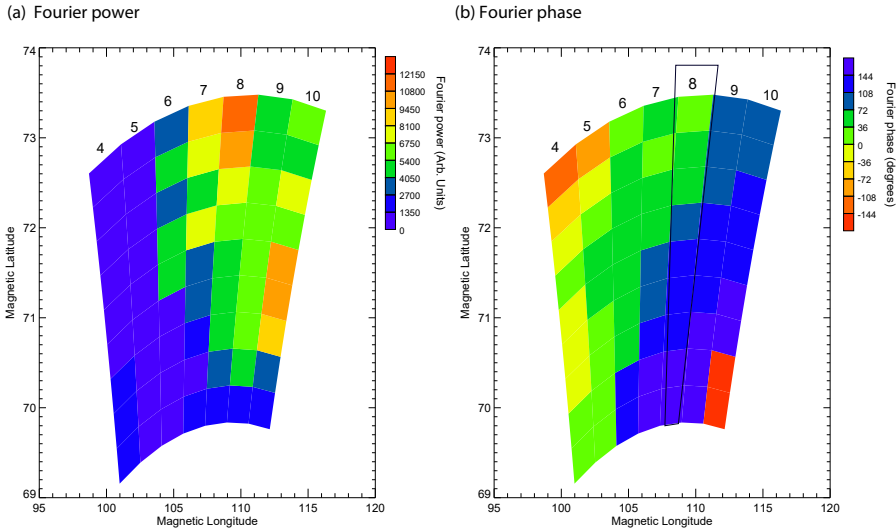


**Figure 5.2:** Fourier (a) power and (b) phase at dominant 0.83 mHz frequency of the wave event shown in Figure 5.1 across beams 4 to 10 as a function of geomagnetic latitude and longitude. The black outlines indicate beam 8.

2-dimensional view. Similarly, the Fourier latitudinal phase variation can be seen to propagate poleward with a gradient of about  $40^\circ$  per degree of latitude as depicted in 5.3(b) while (d) illustrates the Fourier phase variation in longitude. The  $m$  number of  $-12 \pm 2$  is calculated for the wave using linear least squares fit to the phase values, where the negative sign preceding it indicates a westward azimuthal propagation.

### 5.3 Substorm Observations

A similar analysis conducted in Chapter 4 to confirm substorm activity has been repeated for the wave events studied here. For example, Figure 5.4 demonstrates substorm activity that occurred not more than 150 minutes prior to the time interval during which the wave event shown in Figure 5.1 occurred. This can be seen as the light-green outline indicating a Pi2 pulsation activity at substorm onset. In Figure 5.4 the time interval between wave appearance shortly after the onset of the substorm suggests that the wave is associated with particle popula-

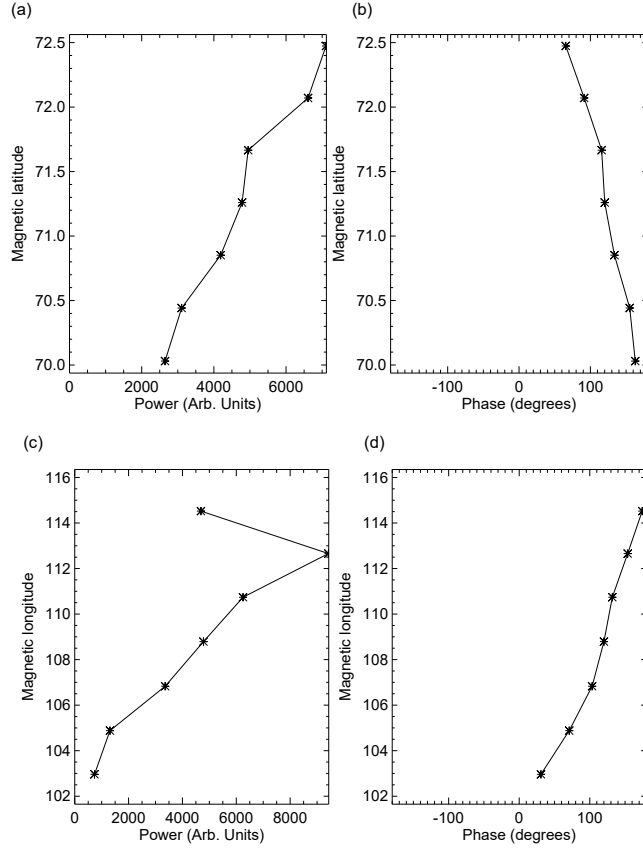


**Figure 5.3:** Similar to Figure 5.2 except that it is the one dimensional version of Fourier (a) power, (b) phase along beam 8 and Fourier (c) power and (d) phase across beams 5-10 at  $\sim 71^\circ$  latitude as a function of geomagnetic longitude.

tions injected by the substorm. In a similar vein, analysis of magnetometer data for each of the 18 events confirmed substorm onset and expansion, occurring at about 120 minutes on average to the time of the radar observations of the wave events.

Furthermore, magnetometer data were band-pass filtered to identify whether any Pc4 giant pulsations occurred during the interval of any of the wave events used in the statistical study. However, Pc4 giant pulsations were not seen during the interval of the wave events, which confirms the rarity of such giant pulsations (Rostoker *et al.*, 1979; Chisham & Orr, 1991), and suggests that the observation of two distinct waves types in the interval examined in Chapter 4 was purely coincidental.

## IMAGE x-component

Data from 21:30 UT 29th to 3:30 UT 30th, March 2015

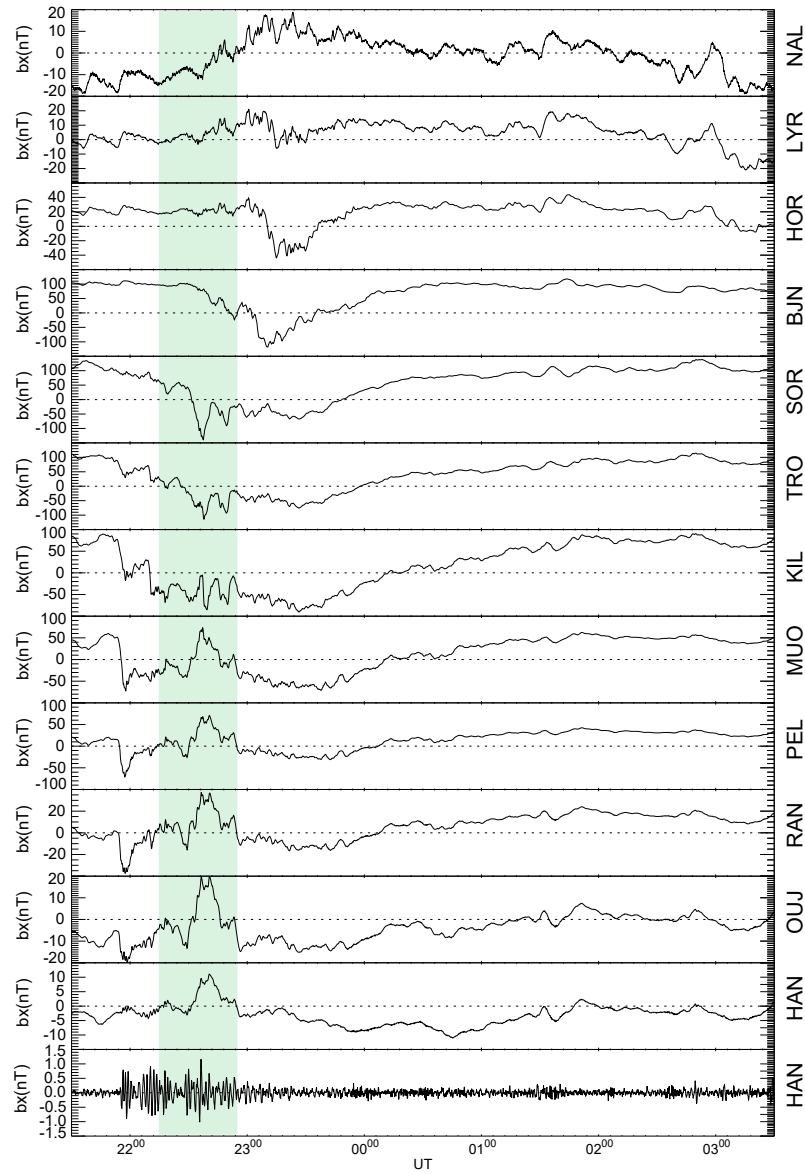


**Figure 5.4:** Unfiltered IMAGE X-component magnetometer data over the time interval of the wave event in Figure 5.1. The IMAGE stations are the same as those used in Chapter 4 (See Table 4.1). The last panel shows HAN station data bandpass filtered between 20-200 s to highlight Pi2 pulsation activity. The light green outline indicates substorm activity.

## 5.4 Statistical Observations

The procedure presented in the last section has been employed for all of the 18 wave events identified from the velocity data recorded by the Hankasalmi SuperDARN radar. Wave period, latitudinal phase propagation, azimuthal wave number, and predicted particle energy in keV the  $N = 0$  case as discussed in section 4.5.1) for these events are presented and discussed in subsequent sections.

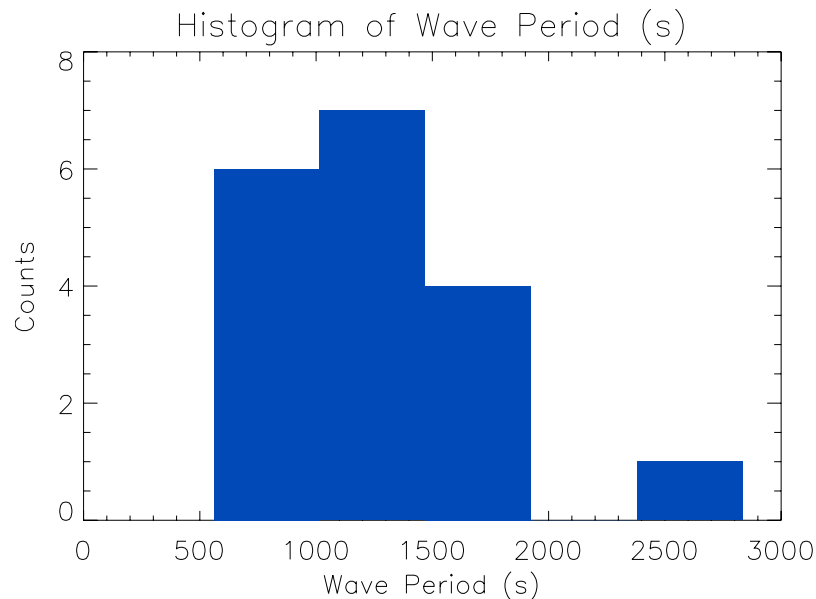


**Figure 5.5:** Histogram showing the periods of the waves studied placed into 500 s bins.

### 5.4.1 Wave Periods

The histogram in Figure 5.5 reveals that the periods of the waves studied here are dominantly in the region of 1000 to 1500 s across a population ranging from about 500 s to about 2500 s. Such wave periods are consistent with the Pc5 wave case study studied in the last chapter. Interestingly, they are also consistent with a similar statistical study of substorm-injected particle driven ULF waves reported by James *et al.* (2013), which they noted that such a long period wave can be a signature that the waves existed on stretched field lines in the nightside of the Earth's magnetosphere.

### 5.4.2 Wave Phase Propagation

The latitudinal and longitudinal phase propagation of the waves studied here are shown in Figure 5.6. Figure 5.6 shows a comparison of periods in the  $y$ -axis and azimuthal wave number,  $m$  in the  $x$ -axis of the waves, and the phase propagation in latitude indicated by different symbols. Waves with poleward phase propagation are shown by asterisks and those with equatorward phase propagation are depicted by black-shaded circles. Figure 5.6 shows that there are slightly more wave events with equatorward phase propagation, similar to the case study wave of the last chapter, than those with poleward phase propagation. This feature corresponds with some previously reported wave observations with intermediate to high- $m$  number recorded by SuperDARN radars (Yeoman *et al.*, 2010; James *et al.*, 2013). These previous observations were interpreted as particle-driven poloidal waves. The majority of the wave events have positive  $m$  values, indicating waves propagating eastward, compared to the wave events with  $m$  number characterised by a negative value, indicating waves propagating westward as defined earlier here and in the last chapter. The eastward propagating wave would be associated with electrons while the westward propagating wave is associated with protons as discussed further in the next section.

There is no clear difference in the wave period and the size of  $m$  number for both waves propagating equatorward and poleward as seen in Figure 5.6. However, the number of poleward phase propagation such as the example wave event presented here is 7 out of 18 wave events, which is a significant number. It is interesting to note that the latitudinal phase propagation in these 18 events was observed to be consistent throughout the duration of the event, and there is no evidence for any temporal latitudinal phase evolution over the wave events studied here. Note also that there is no evidence of any backscatter bite-outs in the radar velocity data similar to what was seen in the case study wave presented in Chapter 4 in any of these 18 wave events. Also, Figure 5.6 shows that equatorward propagating waves are mostly characterised by positive  $m$  values (eastward propagation) and poleward propagating waves mostly have negative  $m$  values (westward propagation). It reveals that waves propagating eastward are 10, which is slightly more than those propagating to the west of longitude. Such

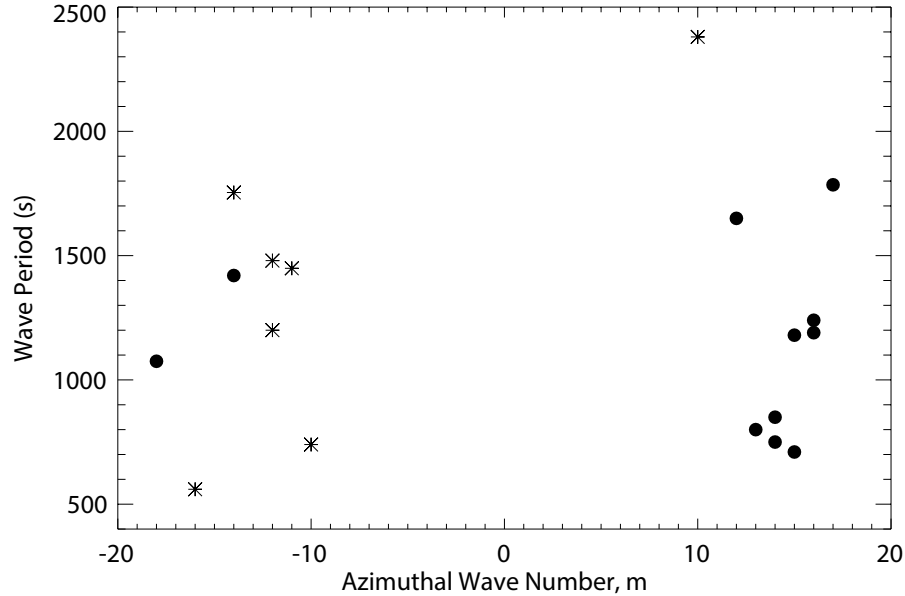


**Figure 5.6:** Wave periods as a function of azimuthal wave number of each of the waves. Waves with poleward phase propagation are shown by asterisk symbols while those with with equatorward phase propagation are shown by black-shaded circle symbols.

waves with intermediate- $m$  number ( $\sim \pm 10$ ), propagating both eastwards and westwards have been observed in previous studies as noted in the last chapter.

### 5.4.3 Driving Particle Energies

Figure 5.7 shows the estimated particle energies in keV for each of the 18 events in the  $x$ -axis and wave periods in the  $y$ -axis. Here, similar to Figure 5.6, wave events with poleward phase propagation are shown by asterisks and those with equatorward phase propagation are represented by circles, while the wave events associated with either resonance with an electron or proton are differentiated with a red or blue colour respectively. The error bars represent the approximate extent of the calculated particle energies. The energies of the drifting particles injected by substorms, which achieved a drift resonance using the equation described in section 2.4 is determined by the same approach applied for the case study wave presented in the last chapter. The estimated particle energies for a drift resonance

condition shown in Figure 5.7 are mostly in the region of 20 - 45 keV, which is similar to the energy predicted for the case study wave. The drift resonance condition employed here is consistent with the approach adopted by James *et al.* (2013) in which they used drift resonance condition regardless of whether the longitudinal wave phase propagation is eastward or westward. They noted in their study that the drift resonance condition is appropriate for both eastward and westward propagating waves because it does not negate the two driving mechanisms of instability or moving source theories suggested as driving their wave observations. This was also chosen due to the very similar nature of the waves irrespective of their azimuthal propagation direction. Thus, it is deemed appropriate to use the same approach here given that the waves explored here are considered to be driven by particles injected by substorms similar to James *et al.* (2013).

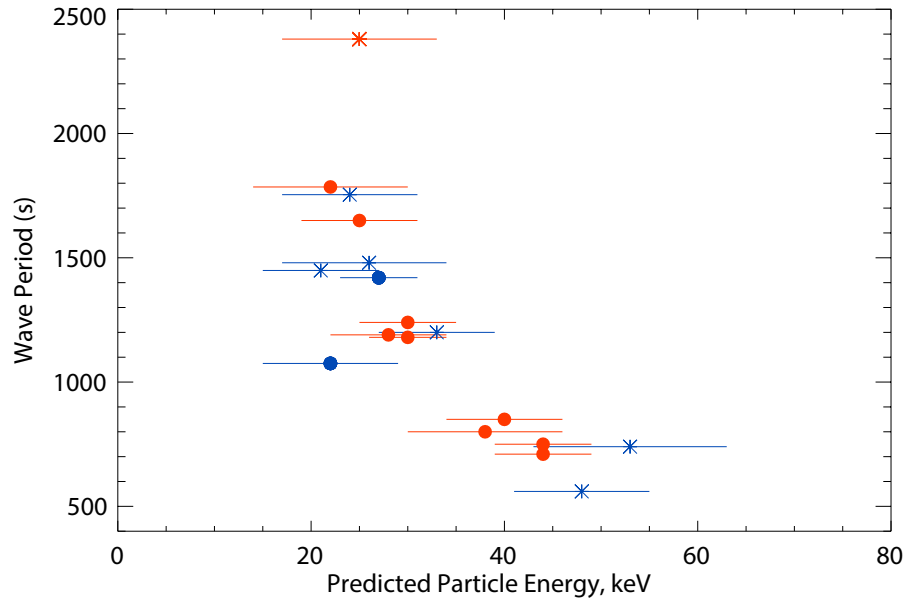


**Figure 5.7:** Wave periods as a function of calculated particle energies for each of the waves. Waves with poleward phase propagation are shown by asterisk symbols while those with equatorward phase propagation are shown by circle symbols. The red and blue symbols indicate waves driven by a resonance with electrons and protons respectively.

Figure 5.7 shows no clear difference in the comparison between wave periods

and the calculated particle energies regardless on whether such particles are associated with electron (red colour) or proton (blue colour) and on whether the wave events exhibit equatorward (circle) or poleward (asterisks) phase propagation. In a similar statistical study of waves driven by substorm-injected particles but more events, James *et al.* (2013) showed that where the azimuthal separation of the wave observations and the substorm onset is small, higher energy particles with corresponding lower  $m$  numbers were involved. However, a few number of events and a small range of  $m$  number waves ( $10 \geq m < 20$ ) are considered in this case, which might explain why there are no clear difference in the size of the particle energies observed here for waves associated with electron or proton as well as with the latitudinal phase propagation.

## 5.5 Discussion

The waves events studied here have shown dominant wave periods consistent with the Pc5 wave case study studied in the last chapter. Previous related studies have observed wave periods typical of the one dominant in this study. For example, the range of wave periods dominant in this study is similar to those reported by James *et al.* (2013) in a statistical study of substorm-injected particle driven waves. In an intermediate- $m$  observation reported in (Yeoman *et al.*, 2010), the wave period was about 600 s, a range of period also prominent in the present study. Yeoman *et al.* (2010) suggested that such a long period wave is a consequence of a wave situated in the stretched field lines of the nightside of the Earth's magnetosphere. The wave events reported here mostly occurred near midnight in UT, which is in the nightside to early morning in magnetic local time (MLT) given that the FOV of Hankasalmi radar is about 3 hours ahead of UT.

The latitudinal phase propagation is mostly equatorward. This is consistent with the observations for the case study in the last chapter and some previously reported waves observed by radar. For example, in a case study of intermediate- $m$  wave in (Yeoman *et al.*, 2010) and a statistical study by James *et al.* (2013), both of which were linked to particle populations from substorms through a wave-particle interaction. These previous ULF wave observations that exhibit equatorward phase propagation (e.g., Yeoman *et al.*, 1992; Fenrich *et al.*, 1995; Yeoman

*et al.*, 2010; James *et al.*, 2013), were interpreted as particle-driven poloidal waves. In contrast, an intermediate- $m$  ULF wave propagating poleward was reported in (Chelpanov *et al.*, 2019), which is similar to about seven wave observations in the present study. The latitudinal phase evolution seen in the case study reported in the last chapter, which is further studied here was not observed in any of the wave events presented in this chapter. As noted in the last chapter, previous theoretical (e.g., Klimushkin *et al.*, 2004; Mager & Klimushkin, 2008; Mager *et al.*, 2009) and observational (e.g., Zolotukhina *et al.*, 2008; Chelpanov *et al.*, 2019) studies have demonstrated the evolution from poloidal to toroidal polarisation of ULF waves, especially those of high- $m$  azimuthal wave number. There is no evidence here of such evolution, if it exists, changing the phase propagation from equatorward to poleward.

Interestingly, backscatter bite-outs seen in the case study were also not seen in the radar observations studied here. The lack of latitudinal phase evolution along with the absence of backscatter bite-out features in the radar data may be a further evidence that the phase evolution reported in Chapter 4 was due to energetic particles associated with the backscatter bite-out. The wave polarisation and the driving mechanism of the Pgs shown in the last chapter does not match with the interpretation of the longer period wave for the case study radar observation. As such, the lack of observation of Pgs from the ground magnetometer data is certainly due to the rarity of such waves on the ground (e.g. Chisham & Orr, 1991). This is an indication that the occurrence of giant pulsations during the wave event presented in Chapter 4 was a simple coincidence. The wave longitudinal phase propagation was mainly eastward, which is associated with electrons gradient-curvature drifting in the magnetosphere in the eastward azimuthal direction. Likewise, about 8 wave events showed a westward propagation, indicating westward drifting ions to be the source of the waves energy. The waves studied here are thought to be predominantly poloidal with estimated particle energy similar to the case study wave. The likely driving mechanisms of such modes were discussed in the last chapter.

## 5.6 Summary

A statistical analysis of 18 intermediate- $m$  ULF waves similar to the case study wave discussed in Chapter 4 have been presented here. These wave events are thought to be linked to substorm-injected particles. The statistical observations have shown that equatorward latitudinal and eastward longitudinal phase variations are dominant, which is similar to the observation by James *et al.* (2013). However, no latitudinal phase evolution and backscatter bite-outs were observed in these waves. The loss of radar backscatter is an indication of a new population of energetic drifting particles (e.g., Gauld *et al.*, 2002), and such new particles might have imposed a new phase structure on the wave studied in the last chapter, which agrees with a similar suggestion by Yeoman *et al.* (2012). Thus, the evolving phase and bite observed in the case-study might be related. The possible mechanisms leading to the generation of the observed wave phenomenon is similar to those discussed in the last chapter for the case study wave.

## Chapter 6

# A Ray Tracing Simulation of HF Ionospheric Radar Performance at African Equatorial Latitudes

### 6.1 Introduction

The SuperDARN field of coverage has been expanding in recent times, from its high latitude coverage at inception (e.g., Greenwald *et al.*, 1995; Chisham *et al.*, 2007; Berngardt *et al.*, 2019) to covering more mid-latitude ionosphere and towards the low-latitude ionosphere (Ribeiro *et al.*, 2012; Greenwald *et al.*, 2017; Nishitani *et al.*, 2019). In addition, there are ongoing discussions and proposition (e.g. Lawal *et al.*, 2018) for using SuperDARN-like HF radar techniques in studying the African low-latitude equatorial ionosphere. For instance, Lawal *et al.* (2018) suggested that establishing such a scientific project will lead to enhanced understanding of complex electrodynamics and physical processes such as the EEJ, predominant in this region, which are yet to be fully understood. The societal benefits from enhanced scientific understanding that such a project would provide are ever-increasing in today's world. For example, critical infrastructure like power grids and the Global Navigation Satellite System (GNSS) are impacted on by the space weather processes partly resulting from the near-earth terrestrial plasma dynamics. Therefore, extending the field of coverage of the

SuperDARN to the equatorial region, especially the African longitude sector that has remained virtually unstudied using a SuperDARN-like technique, will expand its usability and lead to an all-encompassing global ionospheric plasma convection map, studying related magnetospheric and ionospheric phenomena and enhanced understanding of electrodynamics predominant in the equatorial ionosphere.

As discussed earlier in Chapter 3.1.1, SuperDARN radars observe backscatter from the motion of plasma irregularities in the ionosphere. Such backscatter due to plasma density irregularities at E and F regions is commonly known as ionospheric scatter. Apart from observing ionospheric scatter, SuperDARN radars also see backscatter from the ground, known as ground scatter, and from other sources such as meteor trail echoes and the sea (Ribeiro *et al.*, 2011). Such ground scatter is due to rays reflecting from the ionosphere back to the Earth's surface. The capability of distinguishing ionospheric scatter from such ground scatter in existing SuperDARN data remains a work in progress. For example, Ribeiro *et al.* (2011) described an improved technique for identifying ground scatter and ionospheric scatter in mid latitude SuperDARN data. Burrell *et al.* (2015) presented an improved method for determining the return direction of backscatter, which is important for distinguishing ionospheric scatter from ground scatter. Such research is outside the scope of the present study. Likewise, a major difficulty encountered prior to SuperDARN and other ground-based radars used for studying ionospheric plasma irregularities was the determination of the raypaths of HF waves, which are strongly influenced by the ionosphere (Villain *et al.*, 1984). This difficulty meant that it was hard to precisely interpret the geolocation of the of the backscattered signals. In this regard, significant successes have been accomplished in rectifying and enhancing the geolocation accuracy of HF radar backscatter through application of ray tracing modelling of HF propagation through realistic ionospheres using modelled and measured data, and combinations of the two (e.g., André *et al.*, 1997; Yeoman *et al.*, 2001; Chisham *et al.*, 2008; Yeoman *et al.*, 2008b). However, a completely accurate way of determining backscatter geolocation is yet to be achieved.

There are a number of factors that need to be considered in order to develop a SuperDARN-like radar at an African equatorial location. For instance,

naturally occurring ionospheric irregularities are an essential requirement for SuperDARN radar measurements. This means that apart from a favourable orthogonality condition, for a SuperDARN operation, the ionosphere must support coherent scattering occurrence. Previous HF radar experiments at African equatorial ionosphere are discussed in section 2.7, for example Hanuise & Crochet (1977), corroborate the presence of naturally occurring plasma irregularities over the African equatorial ionosphere. However, these previous attempts at studying the ionosphere over the African equatorial latitude region using HF radar systems were largely short-lived scientific campaigns such as the International Equatorial Electrojet Year (IEEY). The implication of this is that the ensuing analyses in these studies may be limited in providing a broader understanding of for example, the long-term structure and evolution of the irregularities. Thus, it is safe to assume that naturally occurring ionospheric plasma irregularities required for the SuperDARN-type radar operation exist in the African equatorial latitude ionosphere, as such, it is important to consider the orthogonality requirement of the SuperDARN-type radars.

Determining the possible spatial distribution where the orthogonality requirement of the SuperDARN radar technique can be achieved is a major step towards the realisation of developing SuperDARN-type radars for studying the African low-latitude equatorial ionosphere. As such, an HF radio ray tracing discussed in section 1.8 can be applied in determining bespoke SuperDARN-like radar operating requirements over equatorial latitudes and also for a broader understanding of the behaviour of HF electromagnetic (EM) wave propagation through a realistic equatorial ionosphere. Also, given that the terrestrial magnetic field geometry varies in latitude, the high latitude analysis of probable locations where orthogonality between the HF radar wave vector and the geomagnetic field can be realised (e.g., Villain *et al.*, 1984) cannot easily predict system performance at the equatorial latitudes.

Therefore, a ray tracing simulation using a modified version of the algorithm developed by Jones & Stephenson (1975) and model equatorial ionospheric parameters deduced from the International Reference Ionosphere (IRI) 2012 model is presented in this chapter in order to predict HF ionospheric radar such as SuperDARN radars performance at African equatorial latitude locations. Such

ray tracing programs have been extensively applied for determining the probable locations that orthogonality between the HF radar wave vector and the geomagnetic field can be realised under various ionospheric conditions at high latitude (e.g., Villain *et al.*, 1984) and mid latitude (e.g., Nishitani & Ogawa, 2005). For example, prior to the development of Hokkaido SuperDARN radar at a mid latitude location (Nishitani *et al.*, 2019), a ray tracing simulation similar to the present study was performed in order to identify possible ionospheric backscatter areas at mid-latitude (Nishitani & Ogawa, 2005). Nishitani *et al.* (2019) showed that the distributions of possible areas of achieving ionospheric backscatter differ depending on the local time and geomagnetic activity. Given that the terrestrial magnetic field geometry varies enormously in latitude, the existing high latitude analysis cannot predict system performance at the equatorial latitudes.

This present analysis is devoted more on characterising possible areas of ionospheric backscatter for typical SuperDARN radars at African equatorial latitude. However, a section of the study provides a brief analysis of possible locations of ground scatter for such equatorial regions. In addition, it will provide a feasibility study for developing a SuperDARN-like radar for studying the equatorial ionosphere over the African latitude sector. For example, in determining technical radar characteristics such as preferable operating frequency and antenna bore-sight azimuths with optimal chances of achieving SuperDARN-type backscatter over the region.

## 6.2 Methods

Ray tracing simulations using representative ionospheric electron density profiles inferred from the IRI model are performed in order to predict the spatial region and the radar characteristics, such as frequency and bore-sight azimuth, with backscattering potential for a SuperDARN-like radar at equatorial latitudes. This section explains the method and models used for the analysis discussed in this chapter.

### 6.2.1 Ionospheric Models

The ionospheric electron density profiles used here have been deduced from the IRI 2012 model using the NeQuick option for the topside electron density (e.g., Bilitza *et al.*, 2014). The ionosphere as earlier stated is a continuously changing region of the terrestrial atmosphere due to photoionization and recombination mainly dictated by extreme ultra-violet (UV) rays from the Sun. As such, carrying out ray tracing modelling for this continuously varying region can best be done by producing an averaged profile that encapsulates the ionospheric electron density at the geographic location being studied.

A similar ray tracing simulation by de Larquier *et al.* (2011) based on the IRI ionospheric electron density profile for a mid-latitude ionosphere has shown good correlation for ground scatter during a geomagnetically quiet period. However, correlating radar measurements of ionospheric scatter with ray tracing are more problematic given that a typical ray-tracing model assumes uniform distribution of ionospheric irregularities. As such, it only predicts possible scatter distributions but cannot account for the presence or absence of the irregularities essential to observe ionospheric scatter (de Larquier *et al.*, 2013). Nonetheless, de Larquier *et al.* (2013) demonstrated that for a mid-latitude ionosphere the intrinsic uncertainties in the IRI model have an insignificant effect on the modelled ionospheric backscatter. The IRI being an empirical model, performs better at mid latitude with a large available database than for example the African equatorial latitude sector with a relatively sparse database (Bilitza *et al.*, 2014). However, previous ionospheric studies have shown that the IRI 2012 model data for the equatorial ionosphere of the African longitude sector have a good correlation with measured data. For example, Tariku (2015) showed that the IRI-2012 model with the NeQuick topside option was generally good in estimating the total electron content (TEC) derived from GPS measurements.

A double alpha-Chapman model (Chapman, 1931; Rishbeth & Garriott, 1969) has been fitted with the IRI model for different diurnal, seasonal and solar cycle periods in order to create broadly representative ionospheric conditions. Chapman layer is a theoretical model that describes the vertical profile of ionospheric electron density resulting from ionisation due to solar ultraviolet radiation from

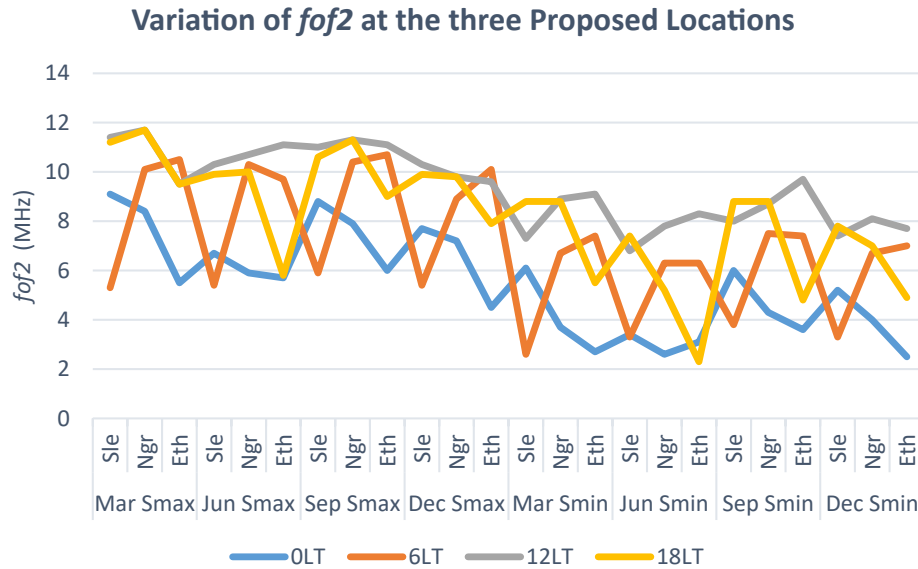


**Figure 6.1:** Variation of foF2 from IRI data at the three proposed locations. The  $x$ -axis indicates the three proposed location at different solar minimum and maximum intervals

the Sun (Chapman, 1931; Davies, 1990). The analysis (e.g., Figure 6.1) did not indicate any clear dissimilarity and pattern of variation of foF2, a key ionospheric parameter, at the three locations used for this study (See, Table 6.1 and Figure 6.2). On the other hand, the F2-layer critical frequencies are higher during a solar maximum year (2014) than a solar minimum year (2009) and during the local afternoon than at the local midnight and morning. These variations are nothing new as they are primarily controlled by ionisation and recombination of electrons. Considering that seasonal variability of ionospheric density and the variability at the three simulated radar locations are not significant, the ionospheric profiles shown in table 6.2, representing the general trends of peaks and troughs were selected and used in the present study regardless of the geographic location differences of the simulated radars. The ionospheric profiles shown in Table 6.2, include critical frequency of F-layer (foF2), height of maximum of F-layer (hmF2), scale height of F-layer (hF2), critical frequency of E-layer (foE), height of maximum of E-layer (hmE), scale height of E-layer (hE) parameters for varying

**Table 6.1:** Simulated Radar Locations

Country	Place	Geographic Coordinate	Label
Sierra Leone	Njala University	$7.93^{\circ}N, 11.76^{\circ}W$	Bo Njala Radar
Nigeria	University of Port Harcourt	$4.89^{\circ}N, 6.92^{\circ}E$	Port Harcourt Radar
Ethiopia	Bahir Dar University	$11.55^{\circ}N, 37.36^{\circ}E$	Bahir Dar Radar

diurnal and solar activity periods. In our ray tracing analysis, these ionospheric profiles represent a horizontally uniform ionosphere and there is no magnetic field. They are designated as ionospheric profile (A-H) in the subsequent analysis and discussions.

The simulated radar locations (Table 6.1) are selected to provide a broad coverage of the equatorial ionosphere over the African longitude sector. Also, locations such as university campuses are feasible locations for siting a SuperDARN-style radar in Africa.

**Table 6.2:** Characteristics of Ionospheric Density Profiles

Profile	Interval/solar activity	$F$ Region (Chapman Layer)	$E$ Region (Chapman Layer)
<i>A</i>	0 LT - minimum	foF2 = 3.9 MHz, hmF2 = 291 km, hF2 = 56 km	foE = 0.49 MHz, hmE = 110 km, hE = 10 km
<i>B</i>	6 LT - minimum	foF2 = 5.7 MHz, hmF2 = 290 km, hF2 = 60 km	foE = 2.68 MHz, hmE = 110 km, hE = 10 km
<i>C</i>	12 LT - minimum	foF2 = 8.2 MHz, hmF2 = 320 km, hF2 = 55 km	foE = 2.77 MHz, hmE = 110 km, hE = 10 km
<i>D</i>	18 LT - minimum	foF2 = 6.7 MHz, hmF2 = 308 km, hF2 = 57 km	foE = 1.45 MHz, hmE = 110 km, hE = 10 km
<i>E</i>	0 LT - maximum	foF2 = 7.0 MHz, hmF2 = 358 km, hF2 = 57 km	foE = 0.55 MHz, hmE = 110 km, hE = 10 km
<i>F</i>	6 LT - maximum	foF2 = 8.6 MHz, hmF2 = 360 km, hF2 = 60 km	foE = 3.30 MHz, hmE = 110 km, hE = 10 km
<i>G</i>	12 LT - maximum	foF2 = 10.8 MHz, hmF2 = 388 km, hF2 = 53 km	foE = 3.20 MHz, hmE = 110 km, hE = 10 km
<i>H</i>	18 LT - maximum	foF2 = 9.0 MHz, hmF2 = 376 km, hF2 = 50 km	foE = 1.30 MHz, hmE = 110 km, hE = 10 km

### 6.2.2 Description of Methods

In the ray tracing simulations performed here, realistic ionospheric electron densities profiles inferred from the IRI-2012 model (e.g., Bilitza *et al.*, 2014) and the latest International Geomagnetic Reference Field (IGRF-12) (Thébault *et al.*, 2015) are coupled with the three-dimensional (3-D) ray tracing model developed by Jones & Stephenson (1975). In this case, the IRI is used to calculate the refractive index using the non-collisional transverse Appleton-Hartree formula as a function of electron density and frequency (Davies, 1990). The refraction that a

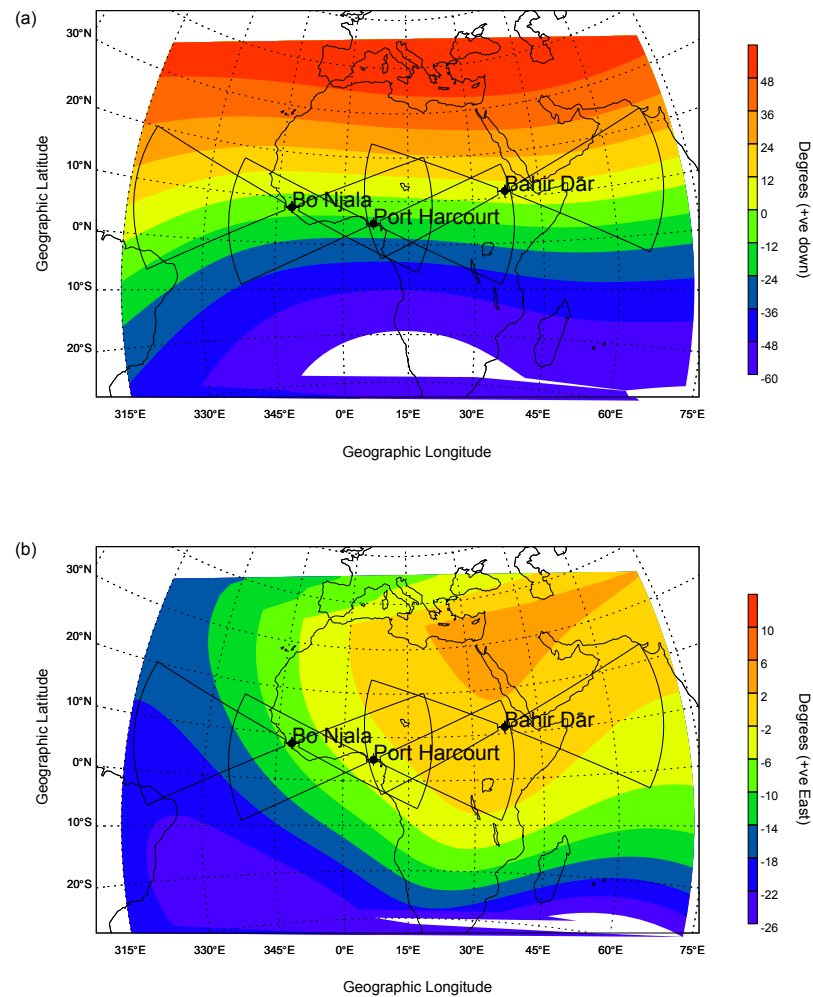


**Figure 6.2:** Map showing the Earth's magnetic (a) inclination (I), and (b) declination (D) over the locations and field-of-views (FOVs) of the simulated radars. Each side of the FOV range 3000 km from the radar location. The Earth's magnetic field is derived from IGRF model (Thébault *et al.*, 2015).

ray encounters as it propagates through the ionosphere is a determining factor of the locations where the ray has the potential of achieving orthogonality with the Earth's magnetic field. The orthogonality angle,  $\alpha = \text{mod}(90^\circ - \Omega)$ , where  $\Omega$  is the angle between the HF wave vector  $\mathbf{k}$  and the magnetic field vectors  $\mathbf{B}$ . This, in the case of HF SuperDARN radars, represents the region where backscatter from electron density irregularities may be observed as illustrated in Figure 6.3. The values of  $\alpha$  with the criterion being that  $\alpha \leq 1^\circ$ , are used to predict the spatial distribution of potential regions where backscatter can be achieved and such scattering regions are further analysed based on predicted elevation angle, altitude and ground range.

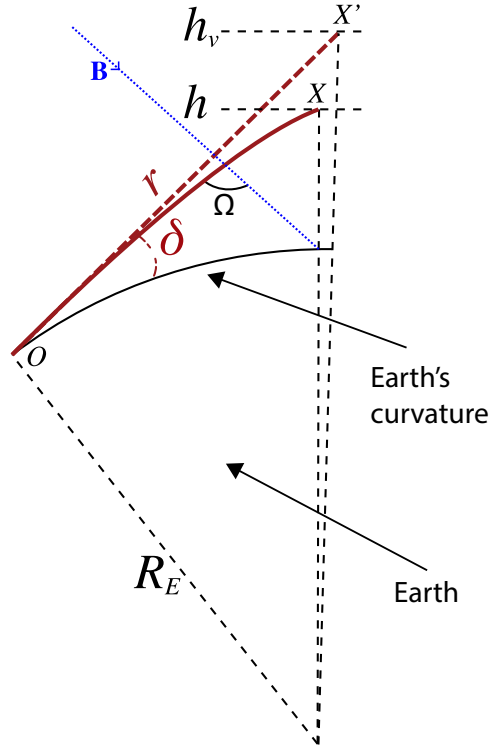


**Figure 6.3:** Schematic diagram illustrating ray propagation path traversing the ionosphere. The solid curve is a realistic path and the dashed line is the line-of-sight path,  $h$  and  $h_v$  represent the physical and virtual altitudes respectively. The angle between HF wave vector  $\mathbf{k}$  and vector of geomagnetic field  $\mathbf{B}$  is  $\Omega$ , such that the orthogonality angle,  $\alpha = \text{mod}(90^\circ - \Omega)$ , while  $\delta$  is the elevation angle,  $r$  is the slant range along the propagation path,  $R_E$  is the radius of the Earth and  $\mathbf{B}$  is the geomagnetic field (*After: de Larquier et al., 2013*).

We employed eight different ionospheric models (A-H) as presented in Table 6.2. These profiles include the E and F2 Chapman layers with associated scale heights (hF2 and hE). The derived critical plasma frequency is between 3.9 and 10.8 MHz for the F2-region (foF2) and between 0.5 and 3.3 MHz for the E-region (foE). For each of the ionospheric profiles, we performed ray tracings using multiple transmit frequencies (12, 16, 20 and 24 MHz) and elevation angles between  $1^\circ$  and  $90^\circ$  in steps of  $0.1^\circ$ . Although existing SuperDARN radars mainly operate from 8 to 20 MHz, here, we have selected 12, 15, 20, 24 MHz transmit frequencies because they represent a set of uniform workable frequencies for all the iono-

spheric conditions used in this study. For example, a ray tracing simulation using 8 MHz as shown in Figure 6.4 (top panel), reasonably achieved orthogonality for profile A, which is a weak ionosphere with a low foF2. In Figure 6.4 (middle panel) for ionospheric profile D with medium foF2, there is a possibility of ionospheric scatter with good orthogonality but it can be seen that it is collocated with densely-spaced 1-, 2-, and 3-hop ground scatter from  $\sim 500$ -2000 km ground range, and it is likely that the ground scatter will be more powerful (Milan *et al.*, 1997a), and dominate the measurements, preventing the collection of useful ionospheric scatter. In the event that the ionospheric critical frequency exceeds the radar transmit frequency, multiple reflections occur, and the radar field of view is saturated with ground scatter, making the detection of ionospheric backscatter unlikely. This is illustrated in Figure 6.4 (bottom panel) for ionospheric profile C (at noon with medium foF2) where many reflections occur when the critical frequency of the ionosphere is greater than the transmit frequency, which leads to a significant occurrence of ground scatter due to multiple hop propagation. Such profiles with medium and high foF2 are more typical of the profiles (see Table 6.2) employed in this study as deduced from the IRI model. It is not unexpected given that foF2 is usually large at equatorial latitude. A single antenna array cannot cover 8-24 MHz with an acceptable beam pattern, as a result, a frequency range of 12-24 MHz is optimal for the equatorial region, rather than 8-20 MHz typical of higher latitude SuperDARN radars and this frequency range is explored here.

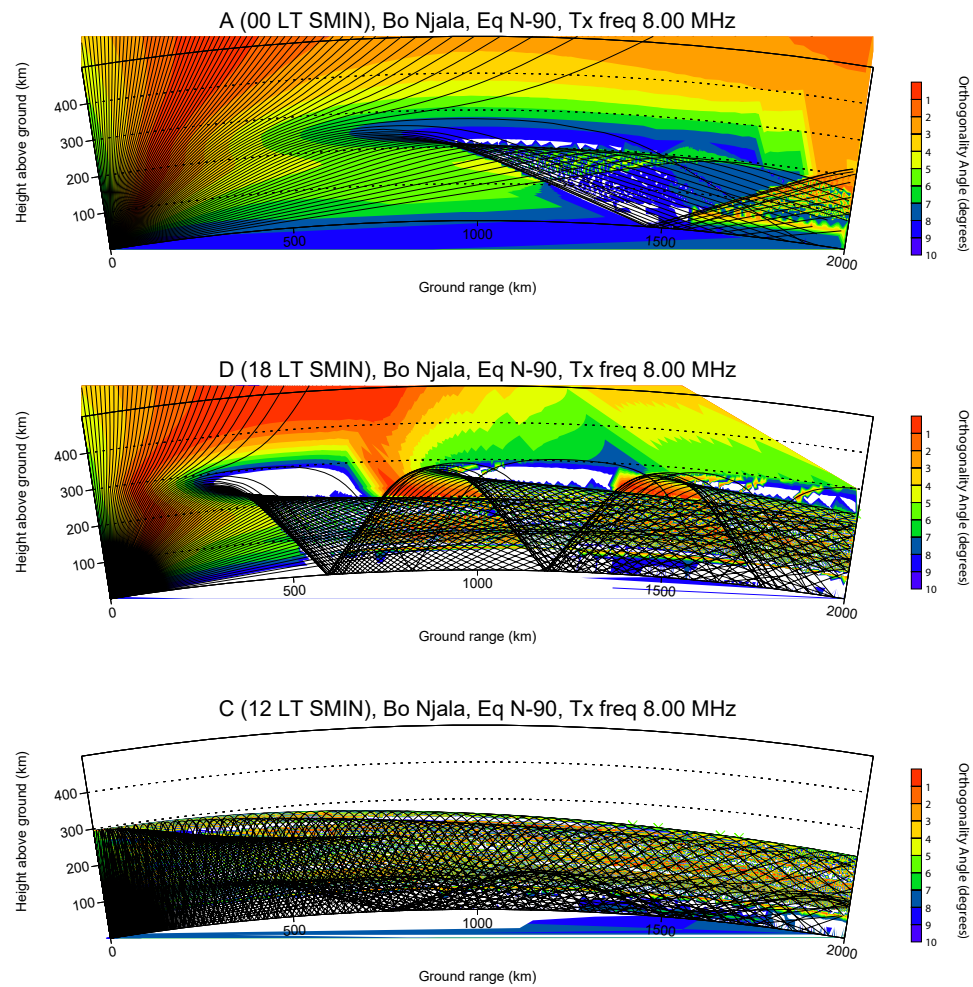


**Figure 6.4:** Ray tracing for simulated HF radars at Bo Njala location from an azimuth of  $90^\circ$  measured from North geographic coordinate at 8 MHz frequency and with elevation angle rays from  $0^\circ$  to  $90^\circ$ . The colour codes represent perpendicularity  $\leq 10^\circ$  between wave vector and the geomagnetic field. Plot derived using the ionospheric profiles A, D and C parameters as shown in the top, middle and bottom panels respectively.

Furthermore, collisions are ignored in the simulation since they mainly result in wave absorption. As such, transmitted rays follow trajectories influenced primarily by the gradients of the ionospheric electron density. This influence of the ionosphere is greater on the horizontally inclined rays than the vertically inclined rays. The orthogonality between the ray vector and the Earth's magnetic field is then deduced from the IGRF model. Given that the SuperDARN radars produce backscatter where the wave vector and geomagnetic field are orthogonal, the points on the simulated ray trajectory where  $\alpha \leq 1^\circ$  are selected with accompanying latitude, longitude, altitude, group path, elevation angle, and ground range parameters. The regions that meet these criteria are commonly referred to as simulated radar backscatter or backscatter in following analysis. In some of the analyses where there is need for spatial visualization, the orthogonality scales are expanded to  $\alpha \leq 10^\circ$  to allow easy illustration of variability but with emphasis placed on where  $\alpha \leq 1^\circ$ . The ray points are binned in group path in steps of 1 km and the projected angle is calculated using spherical trigonometry with the maximum horizontal range and altitude of raypaths set at 2500 km and 500 km respectively.

### 6.3 Raytracing

Figure 6.5 shows the results of ray tracing for one example simulation derived using profile C at noon with medium foF2 ionospheric parameters (see Table 6.2), an azimuth of  $90^\circ$  from geographic North and a 12 MHz transmit frequency and at the three different equatorial locations. Panels a - c represent Bo Njala, Port Harcourt and Bahir Dar radars respectively. The altitude above the ground and ground range both in kilometres are plotted along the y-axis and x-axis, respectively while the colour coding represents the variation in regions of perpendicularity  $\alpha \leq 10^\circ$  to the Earth's magnetic field across  $1^\circ$  to  $90^\circ$  elevation angles. The orthogonality is calculated for  $0.1^\circ$  steps of elevation angle while the rays are shown at 1 degree steps, for clarity.

As shown in Figure 6.5, at Bo Njala (panel a), there is more backscatter predicted from vertically inclined rays ( $\sim 44^\circ - 75^\circ$ ) as indicated in red regions than from lower elevation angles. The regions with orthogonality (deep red) are

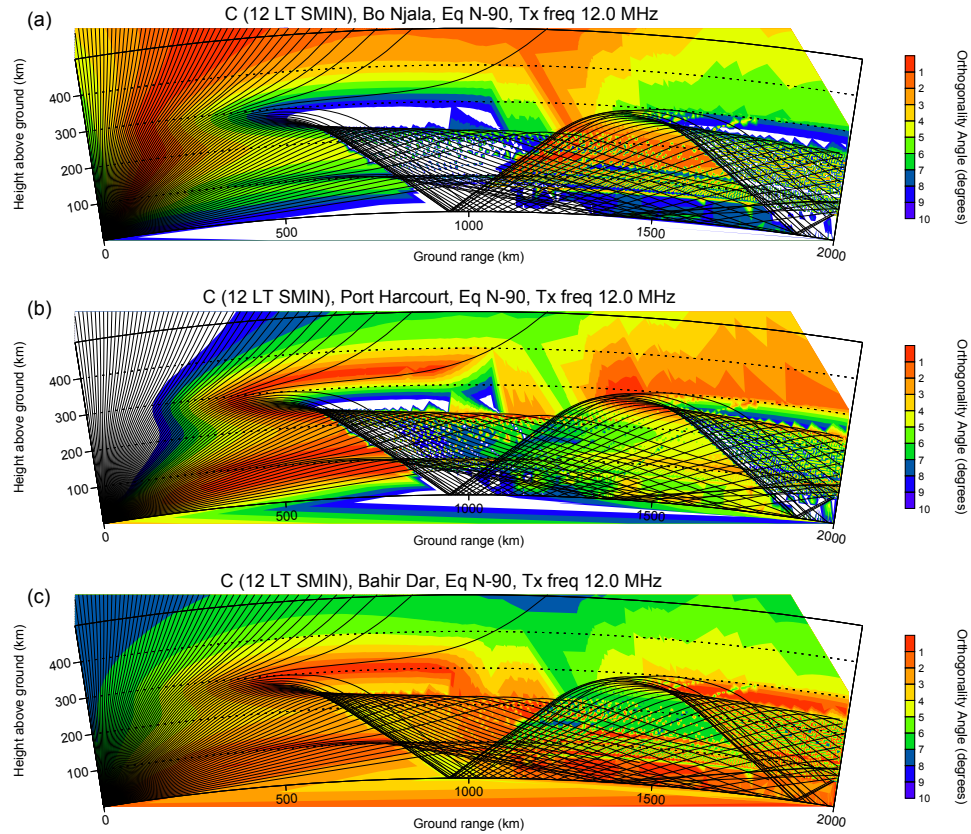


**Figure 6.5:** Ray tracing for simulated HF radars at Bo Njala (a), Port Harcourt (b) and Bahir Dar (c) locations, from an azimuth of  $90^\circ$  measured from North geographic coordinate at 12 MHz frequency and with elevation angle rays from  $0^\circ$  to  $90^\circ$ . The colour codes represent perpendicularity  $\leq 10^\circ$  between wave vector and the geomagnetic field. Plot derived using the ionospheric profile C parameters.

pronounced at altitudes above 100 km, spreading out at 200 km, the bottom side F region ionosphere, and above 300 km. At lower elevation angles, orthogonality is achieved up to 2000 km ground range. Also, a curved region that is depleted of orthogonality ( $\alpha \leq 5^\circ$ ) is apparent at about 350 km ground range and 300 km altitude, spreading out to 1200 km in range. This depleted region coincides with the F-region Pedersen rays from waves with elevation angles between  $38^\circ$  and  $41^\circ$ . Features of Pedersen rays, which represent rays that are at the limit between reflection off and penetration into the ionosphere, appear between  $9^\circ$  and  $11^\circ$  for the E-region. In addition, propagation from lower elevation angles produces

patches of backscatter below the F-region Pedersen rays at ground ranges between 1200 km and 1800 km. These patches arise due to rays between  $1^\circ$  and  $38^\circ$  reflecting off the ground at 1-hop  $\approx 950$  km and 2-hop  $\approx 1850$  km then radiating back to the ionosphere from where they achieve orthogonality. Therefore, at Bo Njala, regions that meet the orthogonality condition ( $\alpha \leq 1^\circ$ ) vary with the propagation angle. The locations where orthogonality seemed to be achieved at Bo Njala is corroborated by the Earth's magnetic field geometry shown in Figure 6.2. Here, Bo Njala lies almost under the magnetic equator with a near horizontal magnetic inclination angle of its FOV while the magnetic declination tilts to the west compared to at high latitude of the same longitude where it is almost zero degrees. Note here that the orthogonality associated with the near-vertical rays is predominantly due to Earth's magnetic field geometries rather than the influence of the ionospheric electron density gradients.

At Port Harcourt (Figure 6.5, panel b), vertically oriented rays above  $45^\circ$  elevation are depleted of backscatter. The lower elevation rays ( $\sim 1^\circ - 45^\circ$ ) have more backscatter compared to Bo Njala where vertical rays produced more backscatter than the oblique rays. Regions where orthogonality are achieved can be seen from 50 to 400 km altitude, covering both the E and F region ionosphere, which is different from Bo Njala which had little orthogonality below 100 km altitude. Moreover, regions with orthogonality ( $\alpha \leq 1^\circ$ ) appear from ground ranges of  $\approx 250$  km away from the radar to 2000 km maximum range. These features are slightly different from Bo Njala where propagation from near-vertical rays achieved orthogonality at ground ranges closer to the radar. Also, features of Pedersen rays from elevation angles between  $39^\circ$  and  $41^\circ$  for F-region,  $9^\circ$  and  $11^\circ$  for E-region are noticeable but with a smaller curved region depleted of orthogonality ( $\alpha \leq 5^\circ$ ) compared to Bo Njala. Similar to Bo Njala, there are also patches of backscatter from rays reflecting off the ground back to the ionosphere where they achieve orthogonality.

Figure 6.5 (panel c), representing Bahir Dar radar is similar to Port Harcourt radar in terms of structure of regions where orthogonality are achieved apart from having improved orthogonality. There is no curved region depleted of orthogonality ( $\alpha \leq 5^\circ$ ) at Bahir Dar. Both Port Harcourt and Bahir Dar radars, as shown from the Earth's magnetic field geometry (Figure 6.2), have almost horizontal

magnetic inclination, except that Port Harcourt radar is north of the equator while Bahir Dar is south. Therefore, despite the same ionospheric profile (C at noon with medium foF2), propagation azimuth and transmit frequency being used for the ray tracing in Figure 6.5, it can be seen that radar performance, in terms of where orthogonality with values ( $\alpha \leq 1^\circ$ ) are achieved, varies across the three different locations. The distribution of possible ground and ionospheric scatter at three equatorial locations in Figure 6.5 is quite typical of high and mid-latitude SuperDARN radar data (e.g., Milan *et al.*, 1997a; de Larquier *et al.*, 2013).

The preceding analysis demonstrates that the likelihood of achieving orthogonality will vary at the three different geographic locations. In other words, the potential of achieving orthogonality, which in practical terms translates to SuperDARN-type backscatter, will vary not only with radar locations but also with ionospheric electron density gradient, radar propagation azimuth and operating frequency. The ray tracing simulation in Figure 6.6 demonstrates the variation in radar performance as a result of different ionospheric conditions (different times of day). Figure 6.6 is the same azimuth as in Figure 6.5, but the location, Bo Njala, and 12 MHz transmit frequency are the same across the three panels, indicating from top to bottom, the A, F and H ionospheric profiles respectively (see Table 6.2). Profile A (top panel), a typical 00 LT solar minimum equatorial ionosphere, shows more backscatter from vertically inclined rays ( $\sim 44^\circ - 75^\circ$ ) than at lower elevation angles, which is similar to the ray tracing simulation in Figure 6.5 (top panel) derived from profile C at noon with medium foF2. Orthogonality ( $\alpha \leq 1^\circ$ ) from these vertical rays, is concentrated nearer to the radar, not detectable beyond 500 km ground range. From lower elevation rays, the curved region depleted of orthogonality ( $\alpha \leq 5^\circ$ ) emanates further in ground range at  $\approx 600$  km from the simulated radar. Due to poor orthogonality for ionospheric profile A at midnight with low foF2, only a  $\frac{1}{2}$ -hop propagation after 2000 km ground range is possible. In contrast, there is more backscatter in profile F (middle panel) and H (bottom panel) of Figure 6.6, representing typical 06 LT and 18 LT solar maximum ionospheres respectively. Both panels show similar  $1\frac{1}{2}$ -hop propagation to the simulation for Bo Njala in Figure 6.5 (top panel). Except that for profile F, the patches of backscatter from rays reflecting off the ground to the

## 6.3 Raytracing

ionosphere appear further out from the radar location at  $\frac{1}{2}$ -hop  $\approx 1000$  km and  $1\frac{1}{2}$ -hop  $\approx 1950$  km ground range. While for profile H, the patches of backscatter appear closer to the simulated radar location at  $\frac{1}{2}$ -hop  $\approx 900$  km and  $1\frac{1}{2}$ -hop  $\approx 1750$  km ground range compared to profile C in Figure 6.5 (top panel). The marked differences in where the  $\frac{1}{2}$ -hop and  $1\frac{1}{2}$ -hop reflect off the ground may be controlled by the E-region critical frequency ( $f_oE$ ). In this case, profile H has a lower  $f_oE$  value than profile F and C (Figure 6.5, top panel).

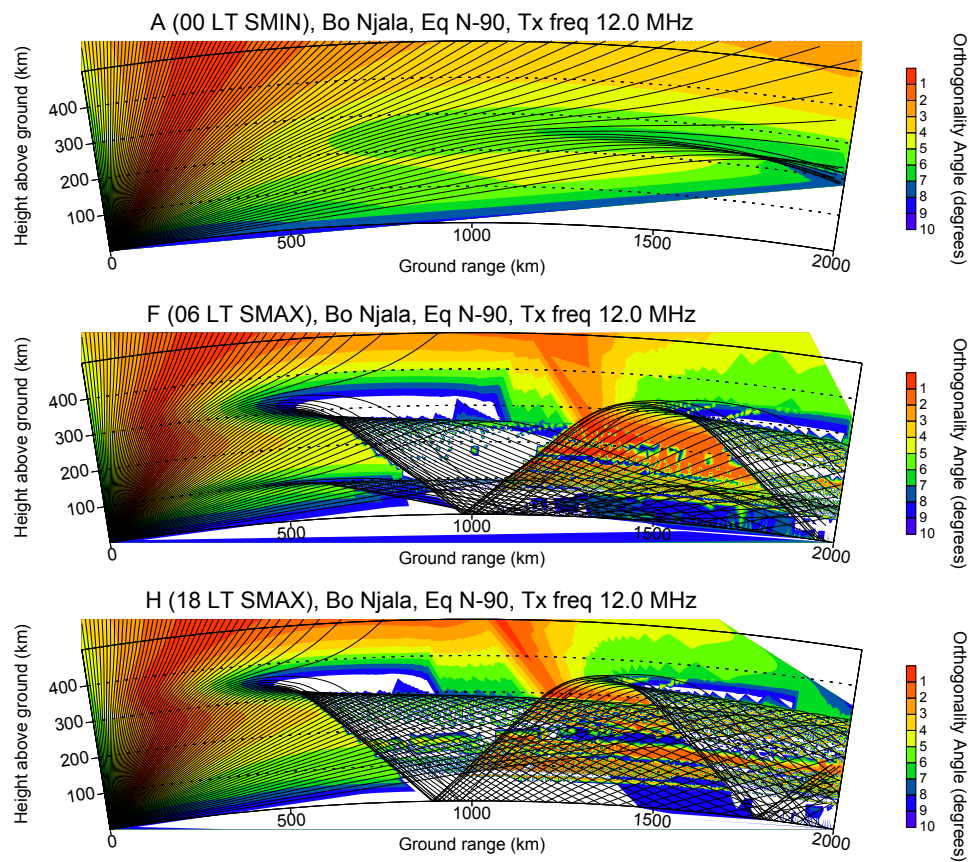


**Figure 6.6:** Same as Figure 6.5 except that it is for Bo Njala location only and the ionospheric profiles A, F and H parameters are used as shown in the top, middle and bottom panels respectively.

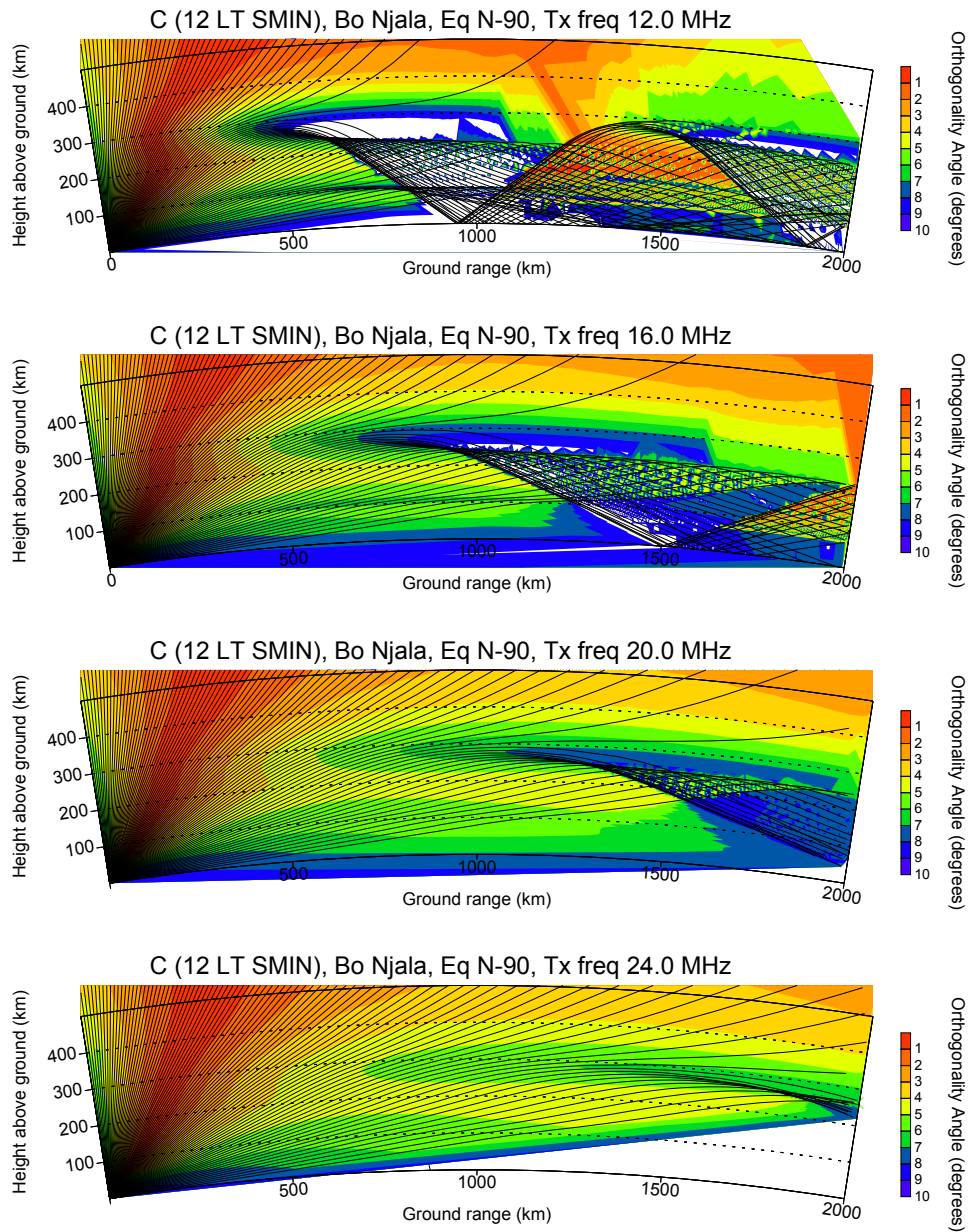


**Figure 6.7:** Same as Figure 6.5 except that it is for Bo Njala location only and the transmitted frequencies are 12, 16, 20 and 24 MHz as shown in first, second, third and fourth rows from top respectively.

Figure 6.7 is similar to Figure 6.5 (top panel) except that here the transmit frequencies are, from the top to bottom panels, 12, 16, 20 and 24 MHz respectively. The curved region, depleted of orthogonality ( $\alpha \leq 5^\circ$ ), tends to diminish with increasing frequency. This indicates that at higher transmit frequency, rays penetrate the ionosphere more, and as such, achieve orthogonality. But at lower transmit frequency, lower elevation rays are susceptible to both reflection and refraction, resulting in more orthogonality especially at lower altitudes.

Figures 6.5, 6.6 and 6.7 clearly show that the possibility of achieving backscatter for azimuth  $90^\circ$  (East-west propagation) in the equatorial latitude will vary at different locations due to deviation of the Earth's magnetic field across the radar field-of-view (FOV). The possibility of achieving backscatter will also be determined by the predominant ionospheric conditions and transmit frequency along with other controlling factors. As such, to determine the combinations of these radar operating parameters where achieving backscatter in a SuperDARN scenario is most feasible, we performed similar ray tracing simulations for all the possible azimuths. Backscatter observed by a SuperDARN-type radar as earlier noted, is classified mainly as the ionospheric scatter, which is the main consideration of this study, and the ground scatter. In subsequent sections, we briefly consider ground scatter then report the results of the analysis for these controlling factors in respect of the likelihood of achieving orthogonality for ionospheric scatter.

### 6.3.1 Ground Scatter Evaluation

The primary observations of the existing SuperDARN radars are ionospheric and ground scatter (Chisham *et al.*, 2007; Ribeiro *et al.*, 2011; Nishitani *et al.*, 2019). Ground scatter as earlier mentioned, is due to backscattering from the Earth's surface. Here, we consider the ranges where ground scatter features are likely to be observed. Such ground scatter features with respect to the present ray tracing analysis, are a function of the ionospheric model and transmit frequency but independent of the radar location. As such, the Bo Njala location out of the three locations used in this study (see Table 6.1) has been employed for this aspect of ground scatter evaluation.

Figure 6.8 examines the distribution of simulated ground scatter occurrence as a function of ground range and elevation angles for the same conditions in Figure 6.7. As seen in Figure 6.7, the two higher frequencies (20 and 24 MHz) in the third and fourth rows have either no ground scatter at less than 2000 km (24 MHz) or just achieve sufficient refraction for ground scatter close to 2000 km (20 MHz). Therefore, Figure 6.8 just looks at the lower two frequencies (12 and 16 MHz) in the first and second rows of Figure 6.7, where reflected rays have reached the ground within a ground range of 2000 km. Here, the ground range and elevation angle information has been collected for ray points where the altitude of a ray path reaches zero after it has reflected from the ionosphere.

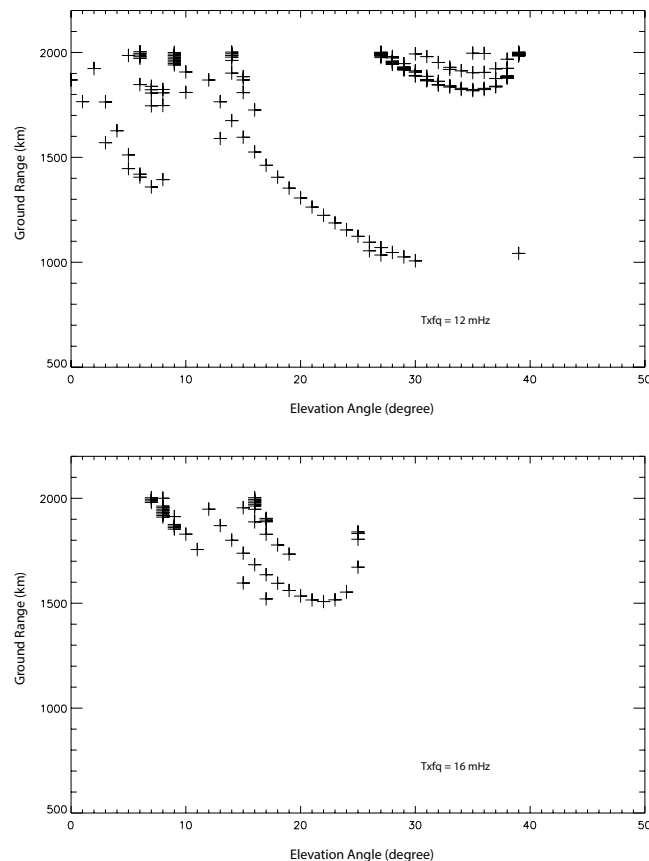


**Figure 6.8:** Ground scatter evaluation as a function of ground range and elevation angle for transmit frequency of 12 MHz (top panel) and 16 MHz (bottom panel) using the ionospheric Profile C (at noon with medium foF2) for the Bo Njala simulated radar.

## 6.4 Geographic distribution of orthogonality

---

Figure 6.8 (top panel) shows elevation angle vs ground range for ground scatter from the transmit frequency of 12 MHz and ionosphere in Figure 6.7 (first row). The 1-hop ground scatter propagation in Figure 6.7 (first row) can be seen in Figure 6.8 (top panel) to produce 1-hop ground scatter from the skip distance at 1000 km, 30° elevation angle out to 2000 km at close to 0° elevation angle. Also, a 2-hop ground scatter propagation from 27°-40° can be seen at ranges of about 1800-2000 km. Figure 6.8 (bottom panel) provides a similar analysis for transmit frequency 16 MHz, as shown in Figure 6.7 (second row). At 16 MHz, just 1-hop ground scatter propagation is produced from the skip distance at 1500 km,  $\sim 25^\circ$  elevation angle out to 2000 km at close to  $\sim 7^\circ$  elevation angle. The rays of larger elevation angles generate ground scatter at shorter ground range at both 12 and 16 MHz transmit frequency. Comparing the possible distribution of ground scatter described here with Figure 6.4 (bottom panel), indicates that for stronger ionospheres and lower transmit frequencies, we would expect ground scatter to dominate, hence our choice of 12-24 MHz for the equatorial radar.

## 6.4 Geographic distribution of orthogonality

We have performed ray tracing as demonstrated in Section 6.3 between 1° and 360° azimuth for 12, 16, 20 and 24 MHz radar operating frequency at each radar location. The ray tracing for each azimuth scanned through the elevation angles between 1° and 90° at 0.1° steps. The calculated performance characteristics, comprising orthogonality values with their latitude, longitude, group path, ground range and altitude were stored for each transmit frequency, simulated radar and ionospheric profile. The data were then binned by orthogonality ( $0 < \alpha < 10^\circ$ ), with emphasis on the regions where  $\alpha \leq 1^\circ$  in ensuing analysis as before. The altitude range is set between 100 km and 500 km, a region that encapsulates the E and F region ionosphere, while the maximum range from the simulated radar location is set at 2500 km. Uncertainties associated with the ray path and the regions indicated as perpendicular with the geomagnetic field increase with increasing ground range. So results obtained further from 2500 km are harder to simulate accurately, although radar backscatter is still expected from further ranges. The binned data are then gridded in steps of 1° of latitude and

## 6.4 Geographic distribution of orthogonality

---

longitude. In each grid, the minimum value of orthogonality is selected and the resulting data for the grids are presented in geographic stereo-graphic coordinates as shown for example in Figure 6.9, where radar ranges of 1000, 2000 and 3000 km from the simulated radar site are marked with concentric circles (corresponding to typical ground distances in Figures 6.5, 6.6 and 6.7, and radar azimuth is indicated radially from the radar site every 15 degrees. The minimum value of orthogonality recorded in each latitude-longitude cell is colour-coded with deep red indicating regions where  $\alpha \leq 1^\circ$ , which is synonymous with where there is a maximum likelihood of achieving backscatter in a SuperDARN radar.

The geographic distribution is discussed in two categories. The first category is the low elevation angle operations where all propagation including the low elevation angles are considered. The second category is the near-vertical operations, which consider propagation where the elevation angle is above  $45^\circ$  and therefore HF refraction is small. Such near-vertical propagation is possible in the equatorial region due to the near-horizontal local field geometry.

### 6.4.1 Low Elevation Angle Operations

Figures 6.9 and 6.10 derived using ionospheric profile A and C respectively are example plots of the low elevation angle operations. The top, middle and bottom rows represent the Bo Njala, Port Harcourt and Bahir Dar simulated radars respectively while the first, second, third and fourth columns represent 12, 16, 20 and 24 MHz radar operating frequencies.

As seen in Figure 6.9, the pronounced regions with simulated backscatter in each simulation are predominantly within the east-west azimuthal direction depicting a "bow-tie" shape. In Figure 6.9 (top panels), representing Bo Njala radar, the region with good orthogonality in 12, 16, 20 and 24 MHz radar operating frequencies, spreads across all radar ranges from close to the radar out to  $\approx 2500$  km between radar azimuth of  $75 - 100^\circ$  in the eastward direction and  $235 - 260^\circ$  in westward axis. Here, the azimuthal extent with good orthogonality is  $\sim 25^\circ$  in both eastward and westward direction. The sloped "bow-tie" feature is linked to the geometry of the Earth's magnetic field over Bo Njala FOV (see Figure 6.2).

## 6.4 Geographic distribution of orthogonality

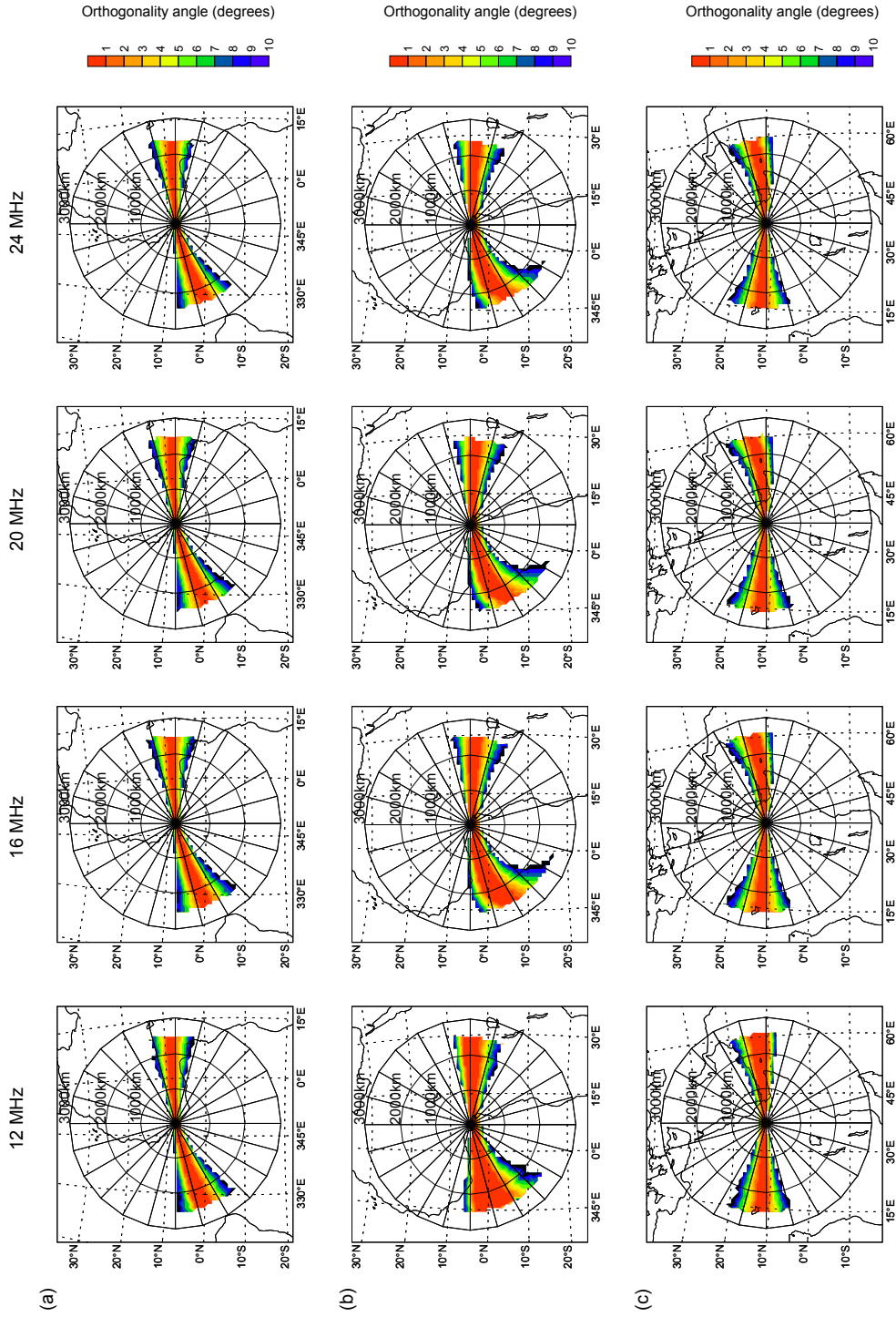


**Figure 6.9:** Spatial distribution of regions with perpendicularity,  $\alpha$  (colour-coded) between radar wave vector and the Earth's magnetic field within  $10^\circ$ . Plots derived from the ionospheric profile A (00 LT solar min) parameters, looking through  $1 - 360^\circ$  azimuths for transmit frequencies of 12 MHz (first column), 16 MHz (second column), 20 MHz (third column) and 24 MHz (fourth column). Rays propagate from the elevation angles of  $1^\circ$  to  $90^\circ$ . The rows a, b and c represent Bo Njala, Port Harcourt and Bahir Dar locations respectively.

## 6.4 Geographic distribution of orthogonality

---

The spatial distribution of backscatter for the Port Harcourt radar (Figure 6.9, row b) follows a similar pattern to Bo Njala, except that the azimuthal band in each of the transmit frequency covers  $80^\circ - 105^\circ$  in the eastward direction, which is  $\sim 25^\circ$  wide and correspondingly is  $230 - 270^\circ$  in the westward direction. At Port Harcourt, the azimuthal extent with good orthogonality in the westward direction broadened with increasing radar ranges, covering more northward and southward azimuths than at Bo Njala. The "bow-tie" configuration tilts horizontally, spreading out in a curve southward especially at 16, 20 and 24 MHz transmit frequencies. This feature is also due to the geometry of the Earth's magnetic field over Port Harcourt FOV as exemplified in Figure 6.2. On the other hand, the simulation of spatial distribution for the Bahir Dar radar, as seen in Figure 6.9 (bottom panels) is similar to Bo Njala and Port Harcourt radars. Here the radar azimuth covers  $70 - 95^\circ$  eastward and  $255 - 285^\circ$  westward, which represents  $\sim 25^\circ$  and  $\sim 30^\circ$  azimuthal coverage in eastward and westward direction respectively. The "bow-tie" feature shifts northwards, spreading further away from the simulated radar site in a curve shape in all the four transmit frequencies as a result of the geomagnetic field alignment.

Figure 6.10 is similar to Figure 6.9, but for the ionospheric profile C at noon with medium foF2. Figure 6.10 (top panels), shows the simulation for Bo Njala at transmit frequencies of 12, 16, 20 and 24 MHz. Simulated backscatter distribution for profile C, Bo Njala, similar to profile A at midnight with low foF2, depicts a "bow-tie" covering all radar ranges from the radar location out to  $\approx 2500$  km between radar azimuth of  $75^\circ - 100^\circ$  to the east and  $235^\circ - 260^\circ$  to the west. Also, we see a band of orthogonality at a distance of  $\sim 2200$  km radar range for all radar azimuthal angle, but with a better orthogonality in the southward axis. This orthogonality band is seen at 12, 16, 20 and 24 MHz transmit frequencies. Such band of orthogonality at  $\sim 2200$  km away from the simulated radar position might not be precise given that ray tracing simulations perform better at close ranges. The altitude where this band of orthogonality originates is much higher at a 24 MHz transmit frequency than at 12 MHz.

## 6.4 Geographic distribution of orthogonality

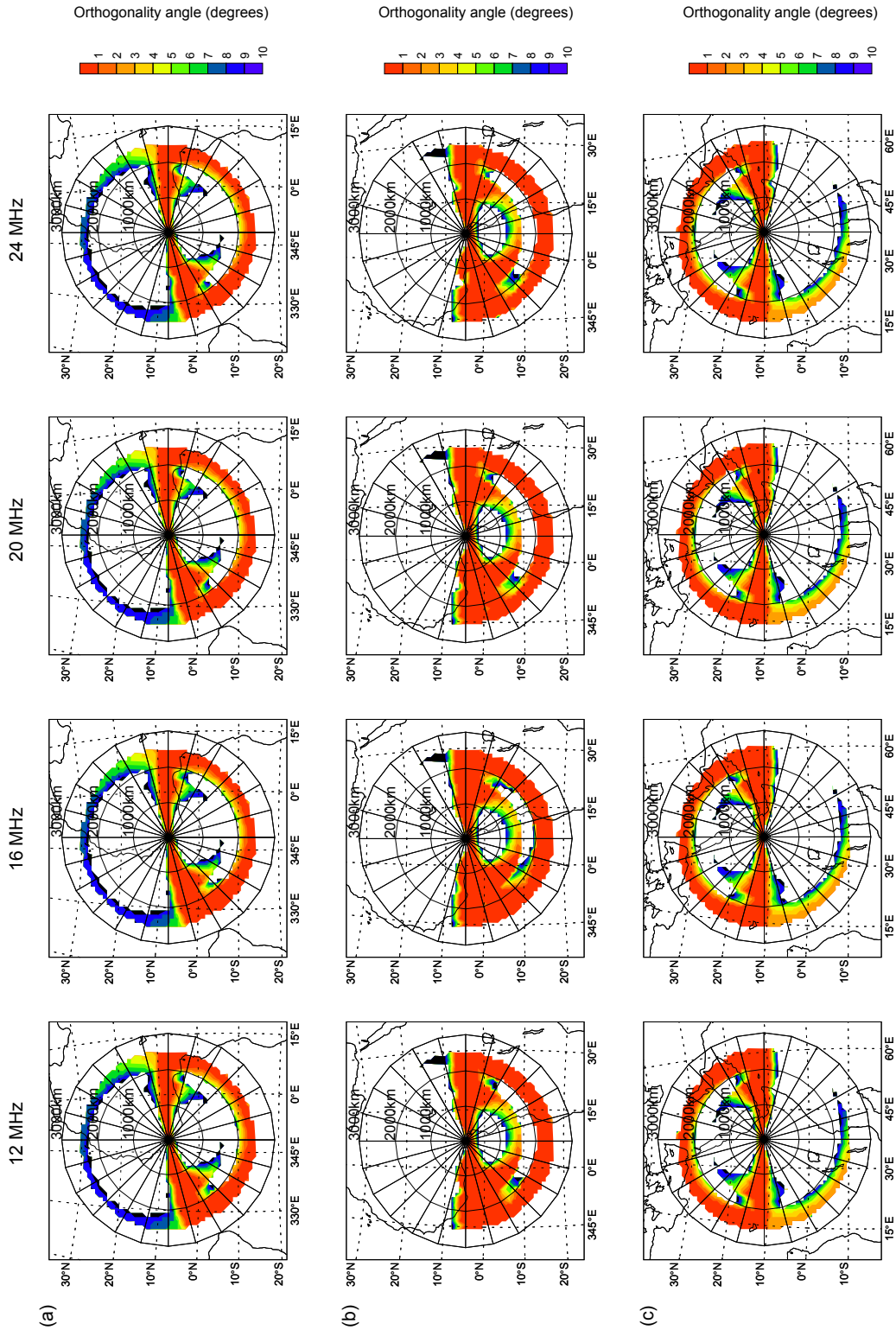


Figure 6.10: Same as Figure 6.9, but using ionospheric profile C (12 LT solar min) parameters.

## 6.4 Geographic distribution of orthogonality

---

Azimuthal geographic distribution of orthogonality for Port Harcourt simulated radar (ionospheric profile C at noon with medium foF2) shown in the second row of Figure 6.10, is similar to the Bo Njala radar. Here, we see a similar "bow-tie" characteristics covering all radar ranges from close to the radar out to  $\approx 2500$  km between radar azimuth of  $75 - 105^\circ$  and  $225 - 275^\circ$  in the eastward and westward direction respectively. Also, the band of orthogonality ( $\alpha \leq 1^\circ$ ) appears at distance of  $\sim 1500$  km and  $\sim 2200$  km, more in the south azimuth than in the north azimuth. This band of orthogonality as noted earlier, originates from high altitude.

Bahir Dar simulated radar for profile C (see Figure 6.10, bottom panels) follows the same pattern of azimuthal geographic distribution of orthogonality as Port Harcourt and Bo Njala radars. However, the "bow-tie" feature of Bahir Dar radar covers radar azimuth of  $70 - 95^\circ$  in the eastward direction and  $255 - 285^\circ$  in the westward direction while its band of orthogonality appear at a distance of  $\sim 2200$  km for azimuthal angles to the north. Similar to Port Harcourt and Bo Njala simulated radars, Bahir Dar radar shows  $\sim 25^\circ$  azimuthal extent with good orthogonality in the east-west direction.

The signature of Earth's magnetic field geometry is apparent in the azimuthal spatial distribution as shown in Figure 6.10 across the FOV of the three simulated radars. The magnetic field inclination (see Figure 6.2) is southward at Bo Njala and Port Harcourt but northward at Bahir Dar. Likewise, the slight east-west distortion seen in Bo Njala simulated backscatter distribution also corresponds with the shape of Magnetic declination over the Bo Njala radar FOV.

### 6.4.2 Near-vertical Operations

The geographic distribution of orthogonality for rays propagating from elevation angles between  $45^\circ$  and  $90^\circ$  are now considered in more detail. Figure 6.11 represents a zoomed-in version of Figure 6.10 but only for elevation angles of  $\delta > 45^\circ$ , where panels a, b, c are for Bo Njala, Port Harcourt and Bahir Dar radars respectively. The orthogonality distribution at Bo Njala (at the magnetic equator), peaks vertically. In contrast, Port Harcourt (south of the magnetic equator) peaks to the south, with Bahir Dar peaking slightly north. As previously pointed

## 6.4 Geographic distribution of orthogonality

out, the distortion of the geomagnetic field declination angle over the Bo Njala, Port Harcourt and Bahir Dar FOVs explains the slope in the spatial distributions between the east and west azimuths.

The spatial distribution of the near-vertical propagation is mainly governed by the geometry of the Earth's magnetic field, as such, it is not strongly controlled by the ionospheric plasma characteristics compared with propagation from lower elevation angles. In practice, a near-vertical ionospheric radar experiment could be applied for studying the structure and vertical velocity of EEJ over the African equatorial region.

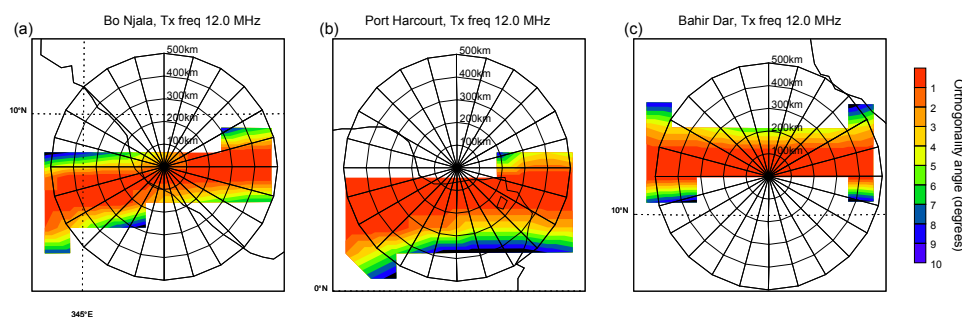


**Figure 6.11:** Spatial distribution of regions with perpendicularity (colour-coded) between radar wave vector and the Earth's magnetic field within  $10^\circ$ . Plots derived from the ionospheric profile C (12 LT solar min) parameters for near vertical elevation angles ( $45^\circ - 90^\circ$ ), looking through  $1 - 360^\circ$  azimuths for transmit frequency of 12 MHz. Panels a, b and c represent Bo Njala, Port Harcourt and Bahir Dar locations respectively.

Simulations for the azimuthal spatial distribution for lower elevation propagation as well as the performance of the near-vertical propagation of the other ionospheric profiles (see Table 6.2) follow the same pattern as for profile A in Figure 6.9 and profile C in Figures 6.10 and 6.11. The results of the near-vertical simulation is also in tandem with (Schlegel, 1996), which noted that based on the aspect angle conditions ( $\vec{k}_i \cdot \vec{B} \approx 0$ ) HF coherent radar installations at the equator can transmit almost vertically. In the subsequent sections, further propagation analysis of the simulated radars as a function of elevation angle, ground range and altitude are presented.

## 6.5 Propagation Analysis

The occurrence of  $\alpha < 1^\circ$  as a function of elevation angle, ground range and altitude are evaluated in more detail in this section. The analysis will be applied in determining the radar characteristics that can achieve useful backscatter in equatorial African region.

### 6.5.1 Orthogonality as a Function of Elevation Angle

The analysis of the backscatter occurrence as a function of elevation angles for all the eight representative ionospheric profiles used in this study are presented here. The azimuth is restricted to  $75^\circ - 100^\circ$ ,  $80^\circ - 105^\circ$  and  $70^\circ - 95^\circ$  from the North geographic coordinate for Bo Njala, Port Harcourt and Bahir Dar simulated radars respectively. We evaluate only the East FOVs in the subsequent analysis since the East and West azimuthal spatial performance were similar. For each transmit frequency (12, 16, 20 and 24 MHz), we performed a ray tracing using the appropriate azimuths from which orthogonality has been determined. The orthogonality values where  $\alpha \leq 1^\circ$  are selected and binned at altitudes between 100 km and 500 km and limited to a ground range of 2500 km.

As shown in Figure 6.12, the ionospheric profile A (00 LT solar minimum) in the first column, exhibits similar orthogonality performances at elevation angles between  $1^\circ$  and  $75^\circ$  for the Bo Njala simulated radar. Backscatter occurs from the horizontal elevation angles in 12, 16, 20 and 24 MHz radar frequencies. The occurrence level of 12 MHz for Bo Njala radar is slightly better than other frequencies at elevation angle between  $1^\circ$  and  $18^\circ$ . This occurrence level is likely from  $\frac{1}{2}$ -hop scatter at high altitude as exemplified in Figure 6.6a. Low elevation angles for Port Harcourt and Bahir Dar simulated radars (second and third row of Figure 6.12) performed similarly to Bo Njala but the extent of elevation angles with orthogonality occurrence for Port Harcourt and Bahir Dar radars is  $1^\circ - 50^\circ$  and  $1^\circ - 68^\circ$  respectively.

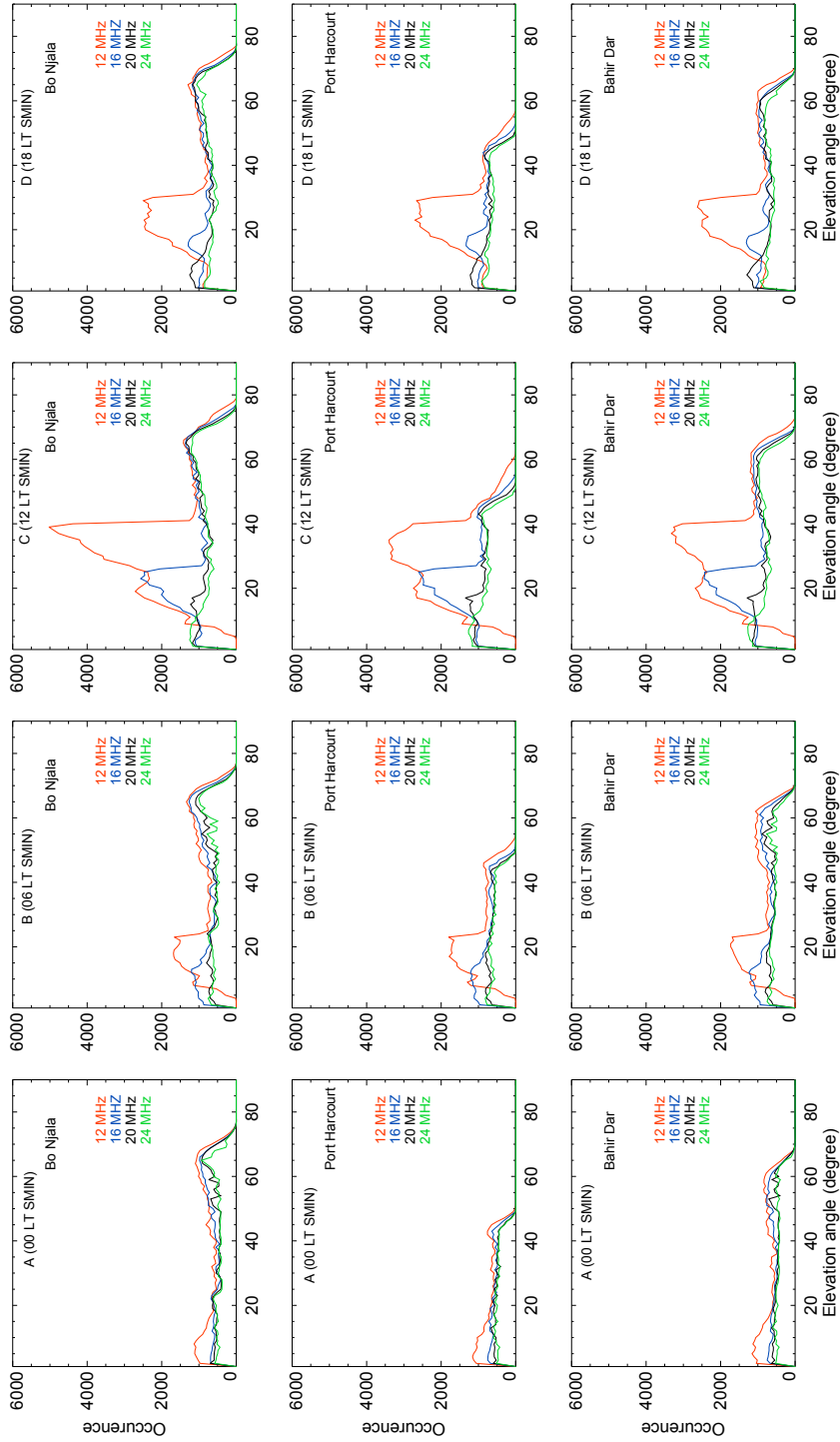


**Figure 6.12:** Evaluation of orthogonality ( $\alpha \leq 1^\circ$ ) as a function of elevation angle for transmit frequencies 12 MHz (red), 16 MHz (blue), 20 MHz (black) and 24 MHz (green). Plots derived from the solar minimum ionospheric profiles A (column 1), B (column 2), C (column 3) and D (column 4) parameters, looking through designated east-west azimuths measured from North geographic coordinate, top panels (Bo Njala,  $75 - 100^\circ$  azimuth), middle panels (Port Harcourt,  $80 - 105^\circ$  azimuth) and bottom panels (Bahir Dar,  $70 - 95^\circ$  azimuth).

Figure 6.12 (second column), represents simulations for ionospheric profile B, a typical 06 LT solar minimum equatorial ionosphere, at the three radar locations. Simulations for Bo Njala, show enhanced backscatter probability for 12 MHz transmit frequency from elevation angle of  $10^\circ$  and at about  $4^\circ$  for 16 MHz. Higher frequencies follow the same trend except that backscatter occurs from  $1^\circ$  horizontal elevation angle. Also, a rapid decrease in occurrence appears at  $\sim 24^\circ$  elevation angle for 12 MHz transmit frequency. This decrease was slight for 16 MHz and starts at  $\sim 14^\circ$  elevation angle while for 20 MHz and 24 MHz this feature is not obvious. The backscatter from more vertical elevation angles ( $\sim 45^\circ - 80^\circ$ ) follow the same trend regardless of the transmit frequency. As stated earlier, backscatter from such elevation angles is mainly due to the geomagnetic field orientation rather than due to the influence of refraction associated with ionospheric plasma density distributions. The vertically aligned ( $45^\circ - 80^\circ$ ) rays propagate through the ionosphere, achieving orthogonality where ray vectors are in the orientation that allow them to achieve orthogonality as illustrated in Figure 6.3 and in ray tracing shown in Figures 6.5, 6.6 and 6.7. The Port Harcourt simulated radar performance as function of elevation angle is similar to Bo Njala except that there is no backscatter beyond  $\sim 55^\circ$  elevation angle, an indication of poor performance of near-vertical elevation angles. At Bahir Dar, the elevation angle performances follow the same trend as Bo Njala and Port Harcourt radars but with a poorer performance for near-vertical elevation angles when compared to Bo Njala radar and a better performance compared to Port Harcourt radar. There is no backscatter for Bahir Dar radar beyond  $\sim 70^\circ$  elevation angle.

Profile C, a 12 LT solar minimum representative equatorial ionosphere, is shown as Figure 6.12 (third column). Backscatter occurrence, similar to profile B, is observed in 12 MHz frequency starting from elevation angle of  $\sim 10^\circ$  and from  $\sim 4^\circ$  in 16 MHz, while at higher frequencies backscatter starts from horizontal elevation. A slope in occurrence is noticeable at  $\sim 24^\circ$  elevation angle from rays transmitted at 12 MHz, which is similar to scatter occurrence for profile B. It then steadily increased up to  $41^\circ$  elevation angle, at which it rapidly decreased to  $10^\circ$  elevation angle level. The slope for 16 MHz radar frequency is seen at  $\sim 24^\circ$  elevation angle. Simulated backscatter for near-vertical rays ( $\sim 45^\circ - 80^\circ$ ) follows the same trend regardless of the radar frequency. Port Harcourt and Bahir radars

follow similar elevation angle performance as Bo Njala radar, except that there is no backscatter occurrence beyond  $\sim 55^\circ$  elevation angle for Port Harcourt and  $\sim 70^\circ$  elevation angle for Bahir Dar. The obvious increase in occurrence level of ionospheric profile C at noon with medium foF2 compared with B at dawn with low foF2 is due to the enhanced electron density associated with 12 LT diurnal ionosphere. Thus, for profile C, we see backscatter from the lower elevation angle  $\frac{1}{2}$ -hop E region and  $1\frac{1}{2}$ -hop F region dominating especially for lower transmit frequencies. The propagation resulting from this feature is illustrated in Figure 6.7.

The ionospheric profile D (18 LT solar minimum) is presented in the fourth column of Figure 6.12. The variation in backscatter occurrence for profile D follows similar trends observed in profile C at noon with medium foF2, because they have comparable ionospheric electron density. However, backscatter occurs from the horizontal elevation angles as seen in profile A with the occurrence level for 12 MHz slightly better than for other frequencies at elevation angle between  $\sim 11^\circ$  and  $32^\circ$ . The similarity in the occurrence of backscatter from horizontal elevation angle in profile A and D for rays transmitted at 12 MHz is as a result of depletion in electron density in E-region ionosphere that characterises 00 LT and 18 LT typical ionospheres compared to E region electron density enhancement of 06 LT and 12 LT ionospheres. A sharp fall in the level of backscatter occurrence appears at  $\sim 32^\circ$  elevation angle for 12 MHz and at  $\sim 20^\circ$  elevation angle for 16 MHz radar transmit frequency. The rapid decrease in the level of backscatter occurrence that we see for rays transmitted at 12 and 16 MHz frequencies, which is similar to profiles B and C previously discussed, may be associated with hop-propagation and Pedersen rays as seen for example in Figure 6.7.

In Figure 6.13, the evolution of orthogonality occurrence with respect to the elevation angles in 12, 16, 20 and 24 MHz transmit frequencies for ionospheric profiles E, F, G and H are presented respectively in column one to four for Bo Njala, Port Harcourt and Bahir Dar simulated radars respectively shown in the row panels, in the same format as Figure 6.12. In profile E (00 LT solar maximum), the orthogonality occurrence for Bo Njala radar originates from  $0^\circ$  up to  $\sim 76^\circ$  elevation angle across 12, 16, 20 and 24 MHz transmit frequencies. However, 12 MHz transmit frequency has more scatter from elevation angles between

$\sim 11 - 32^\circ$  than in 16, 20 and 24 MHz. The trend we see here is similar to what we saw for profile A, which is also a typical 00 LT ionosphere. Here, as expected, there is more backscatter because the ionosphere being a typical solar maximum ionosphere is stronger. Also, for Bo Njala, the near-vertical scatter varies similarly from elevation angle of about  $45^\circ - 76^\circ$  for all the transmit frequencies. Similar performances are observed for Port Harcourt radar in the second row and Bahir Dar radar in the last row but the vertical propagation only occurred from elevation angles between  $\sim 45^\circ - 55^\circ$  and  $\sim 45^\circ - 70^\circ$  respectively.

Profile F, a 06 LT solar maximum typical equatorial ionosphere, in Figure 6.13 (second column) shows orthogonality occurrence for Bo Njala, Port Harcourt and Bahir Dar radars in top, middle and bottom rows respectively. At Bo Njala, backscatter occurs from  $\sim 10^\circ$  elevation angle for 12 MHz, while in 16 MHz it starts from  $\sim 5^\circ$  but originates from  $0^\circ$  in 20 and 24 MHz transmit frequencies. The 12 MHz frequency has dominant occurrence from elevation angles between  $\sim 11$  and  $44^\circ$  compared to other frequencies. It increased from about  $11^\circ$  to  $\sim 24^\circ$ , decreased slightly and then increased steadily until an abrupt fall to  $\sim 11^\circ$  level at  $44^\circ$  elevation angle. This again demonstrates the trend we have seen so far, where high altitude  $\frac{1}{2}$ -hop scatter dominates for weaker ionospheres, illustrated in Figures 6.6 and 6.7, with lower elevation angle  $\frac{1}{2}$ -hop E region and  $1\frac{1}{2}$ -hop F region scatter becoming dominant for stronger ionospheres and lower frequencies. The near-vertical propagation from elevation angle of about  $45^\circ - 80^\circ$  follows the same trend for all the transmit frequencies. The performances of Port Harcourt and Bahir Dar radars are similar to Bo Njala radar. However, at Port Harcourt, the vertical propagation is small-scale, occurring only in elevation angles from  $\sim 45^\circ - 60^\circ$  for all transmit frequencies but stretching further between  $\sim 45^\circ$  and  $72^\circ$  elevation angles for the Bahir Dar radar.

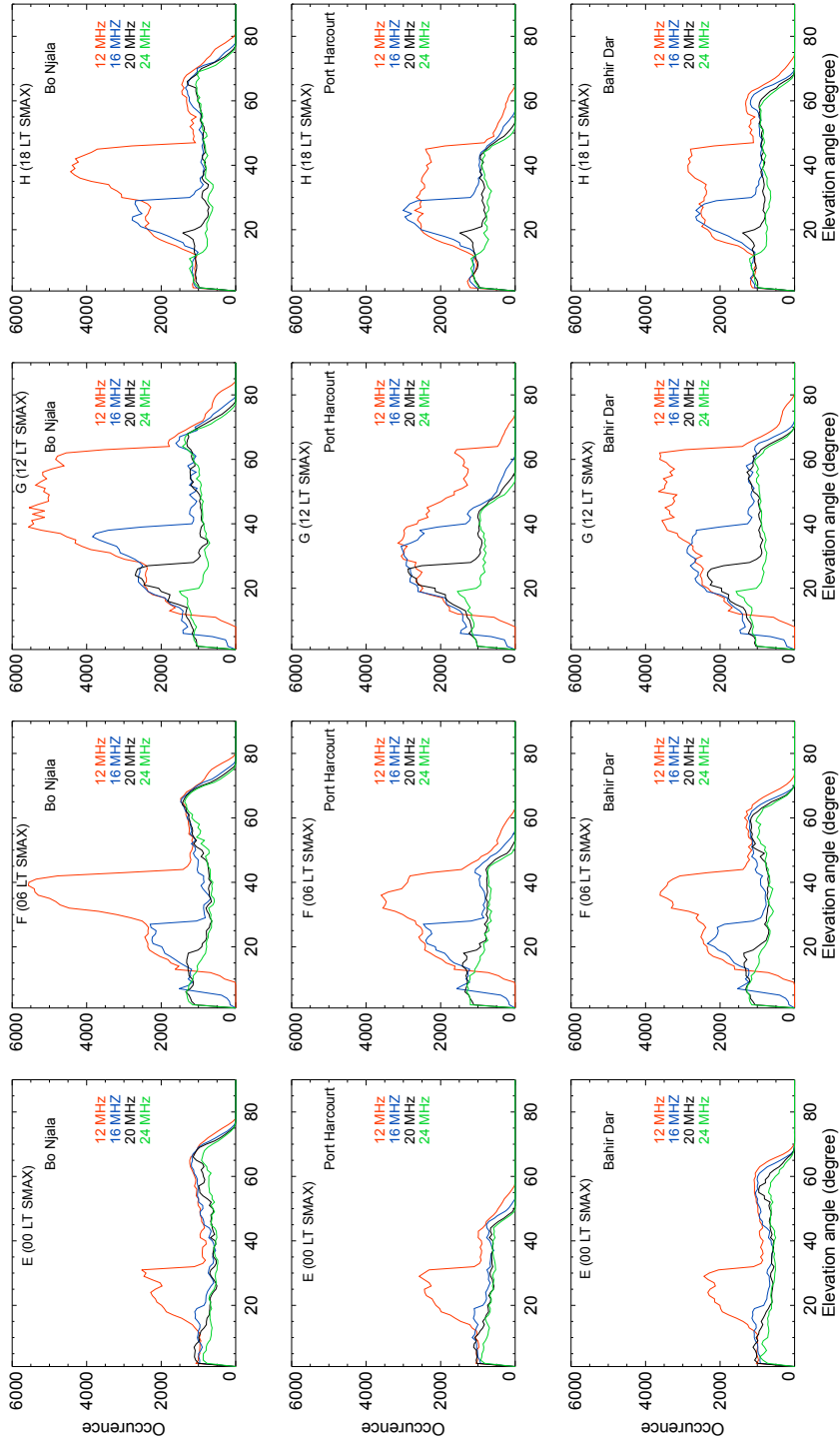


**Figure 6.13:** Same as Figure 6.12, but using solar maximum ionospheric profiles E (column 1), F (column 2), G (column 3) and H (column 4) parameters.

The performance characteristics during a 12 LT solar maximum representative equatorial ionosphere (profile G) is presented in Figure 6.13 (third column). Profile G share similarities with profiles F and C but the magnitude of backscatter occurrence for all the transmit frequencies and radars is seemingly largest in profile G due to its intense ionospheric density characteristics compared to other representative profiles. For the Bo Njala radar, backscatter is noticeable from elevation angle of  $\sim 10^\circ$  for 12 MHz and from  $\sim 4^\circ$  at 16 MHz. At 12 MHz, there is an upward slope from elevation angle of  $\sim 10^\circ$  up to  $\sim 27^\circ$ , where it slightly decreased before peaking at  $\sim 40^\circ$ . It fluctuates at the peak level and then falls to the  $10^\circ$  level at  $\sim 65^\circ$  elevation angle. 16 MHz followed the same trend, although it slightly performed better than 12 MHz between  $11^\circ$  and  $27^\circ$ , then dropped to  $10^\circ$  level at  $\sim 40^\circ$ . Unlike in other profiles, there is an obvious initial upward slope in 20 MHz and 24 MHz and rapid fall at  $\sim 27^\circ$  and  $\sim 20^\circ$  respectively. The backscatter population from the lower elevation angle  $\frac{1}{2}$ -hop E region and  $1\frac{1}{2}$ -hop F region and again for lower transmit frequencies explains the variation of scatter in profile G. Similar plots to Figure 6.7 not presented here confirms this assertion. The Port Harcourt radar followed the same trend as the Bo Njala radar except that there is no backscatter occurrence beyond  $\sim 71^\circ$  elevation for 12 MHz and  $\sim 60^\circ$  for other frequencies. At Bahir Dar, the elevation angle performance is similar to Bo Njala and Port Harcourt but there is no occurrence of backscatter beyond  $\sim 80^\circ$  elevation angle for 12 MHz and  $\sim 70^\circ$  for other frequencies.

Finally, in profile H (18 LT solar maximum), the backscatter occurrence for Bo Njala radar originates from horizontal elevation angle for all the transmit frequencies despite the relatively high foF2 of this profile. This feature, also seen in similar 18 LT ionosphere (profile D) could be as a result of profile H relatively small foE compared with profile G. In 12 MHz, there is an increase of occurrence from elevation angle of  $\sim 10^\circ$  up to  $\sim 27^\circ$ . This is followed by a slight decrease then increase to a peak level before falling to  $\sim 10^\circ$  elevation angle level at  $\sim 44^\circ$ . The near-vertical rays from elevation angle of about  $45^\circ - 80^\circ$  vary similarly for all the transmit frequencies. The orthogonality occurrences for Port Harcourt and Bahir Dar radars vary similarly to the orthogonality occurrences for Bo Njala radar. But at Port Harcourt, there is no occurrence beyond elevation angle of  $\sim 60^\circ$ , while at Bahir Dar orthogonality occurrence terminated at  $\sim 72^\circ$ .

As suggested earlier, the rapid fluctuation in the level of backscatter occurrence seen in all the solar maximum typical ionospheres, especially for 12 and 16 MHz frequencies could be due to multi-hop propagation and Pedersen rays exemplified in Figure 6.7.

### 6.5.2 Elevation Angle vs Ground Range

The simulated backscatter distributions as a function of ground range across  $1^\circ$  to  $90^\circ$  elevation angles is presented in detail here. Figure 6.14, derived from the ionospheric parameters of profiles A (top panels), C (middle panels) and G (bottom panels) for Bo Njala, shows that simulated backscatter is not distributed uniformly over the ground range in all the four transmit frequencies. The three ionospheres used for Figure 6.14 shown here, were selected because they provide a comprehensive representation of orthogonality distribution as a function of ground range and elevation angle for all the eight ionospheric profiles used in this study. To achieve Figure 6.14, we binned orthogonality value at ( $\alpha \leq 1^\circ$ ) and altitude between 100 km and 500 km.

Figure 6.14 (top panels) depicts orthogonality occurrence as a function of ground range and elevation angles for the profile A ionosphere for Bo Njala radar at transmit frequencies of 12, 16, 20 and 24 MHz. The near-vertical backscatter that originates from elevation angles of  $\approx 40^\circ - 70^\circ$  can be seen. This near-vertical backscatter that appears like a reddish "blob", covers from the simulated radar site to  $\approx 500$  km ground range in all the transmit frequencies. However, at lower frequencies 12 and 16 MHz, there is more backscatter than at 20 and 24 MHz. The frequency variation of backscatter is due to ionospheric profile A having low ionospheric density (e.g. foF2 is 3.9 MHz) relative to the transmit frequencies. For example, propagation for the near-vertical backscatter is typified in the top panels of Figure 6.6. At higher transmit frequencies there is no hop propagation so rays tend to penetrate the ionosphere producing less backscatter. Also, there is a backscatter region from the low elevation angles of  $\approx 1^\circ$  to about  $40^\circ$  across the transmit frequencies. Propagation from these low elevation angles produce oblique orthogonality, with the orthogonality occurring at above 2000 km range in 12 MHz due to  $\frac{1}{2}$ -hop as illustrated in Figure 6.6.

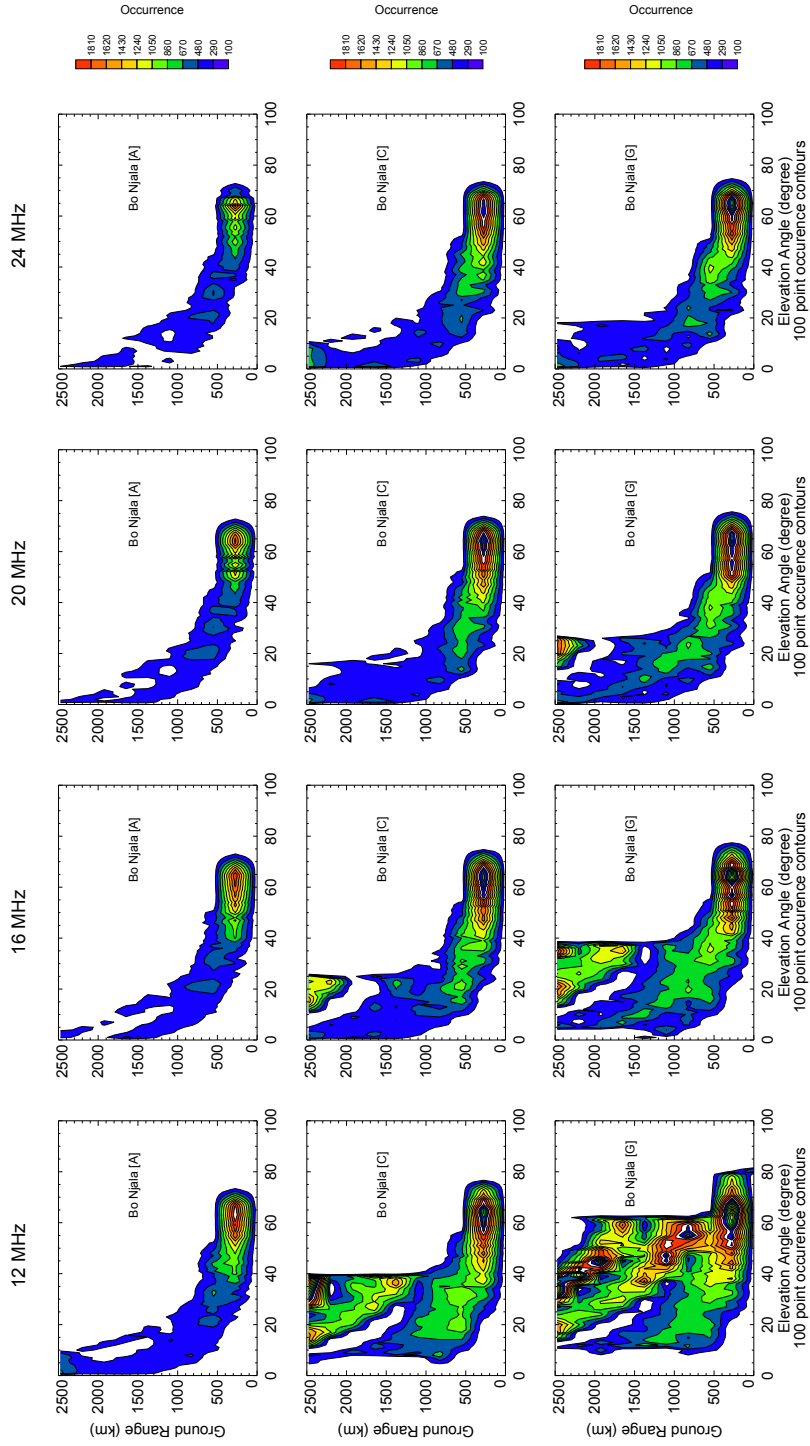


**Figure 6.14:** Evaluation of orthogonality ( $\alpha \leq 1^\circ$ ) as a function of ground range and elevation angles for transmit frequency 12 MHz (column 1), 16 MHz (column 2), 20 MHz (column 3) and 24 MHz (column 4). Plots derived from the ionospheric parameters of profiles A (top panels), C (middle panels) and G (bottom panels) for Bo Njala simulated radar looking through  $75 - 100^\circ$  eastward azimuths measured from North geographic coordinate.

Profiles C and G (middle and bottom panels of Figure 6.14) represent stronger ionospheres, which allows us to compare ionospheric effect on the orthogonality distribution as a function of ground range and elevation angles. Here, the near-vertical backscatter is similar to profile A, extending from the simulated radar site to  $\approx 500$  km ground range but with no clear difference in 12, 16, 20 and 24 MHz transmit frequencies. In contrast, the low elevation angles produced more backscatter across the ground ranges in profiles G and C than in profile A. The increasing scatter from the E-region  $\frac{1}{2}$ -hop and F-region  $1\frac{1}{2}$ -hop propagation account for the more backscatter especially in the 12 MHz transmit frequency. This hop feature is demonstrated in Figures 6.5 and 6.6 and appears more at lower transmit frequencies as shown in Figure 6.7. Here in Figure 6.14, multi-hop features as well as Pedersen rays can be seen as the longer ground range distributions appearing from 950 km to 2500 km ground range. Also, the backscatter distribution for profile C and G in 12 MHz transmit frequency is different from profile A. For example, we do not see backscatter from the horizontal elevation angle in 12 MHz transmit frequency due to large E-region ionospheric critical frequency ( $f_oE$ ) associated with 12 LT ionosphere. However, at higher transmit frequencies, rays from the horizontal elevation angles as exemplified in Figure 6.7 penetrate the E-region then refract in the F-region and produce backscatter at high altitude. Thus, Figure 6.14 confirms that the likelihood of achieving orthogonality is not uniformly distributed in ground range but depends on the radar frequency and the elevation angle of propagation. Simulations of ground range distributions of orthogonality for Port Harcourt and Bahir Dar radars (not presented here) are similar to the Bo Njala radar.

### 6.5.3 Orthogonality as a Function of Altitude

A detailed analysis of the altitude structure of orthogonality occurrence has been performed. Here the altitude is set between 1 km and 500 km, which represents an altitude range that encompasses the E- and F-region ionospheric plasma irregularities features predominant in equatorial latitude such as Sporadic E observed by Blanc *et al.* (1996) at altitude range of 100 - 150 km. It is also a reasonable

altitude range to focus our analysis using a delineation of the equatorial electrojet region to (100 - 110 km in altitude) and within a few degrees of latitude at the magnetic equator (Richmond, 1973). Note that the conventional SuperDARN signal processing currently does not estimate the altitude of backscatter, although there are models for example by Chisham *et al.* (2008) and Yeoman *et al.* (2008b) that can provide altitude information of backscatter closer to the radar.

Figure 6.15 depicts simulated altitude distributions of orthogonality occurrence for the Bo Njala radar, derived from the profiles A (top panels), C (middle panels) and G (bottom panels) representative ionospheres for transmit frequencies of 12, 16, 20 and 24 MHz. The analysis for orthogonality distribution as a function of altitude shown here are restricted to three ionospheres as seen Figure 6.15 because they provide a comprehensive picture of orthogonality distribution as a function of altitude for all the eight ionospheric profiles used in this study. In Figure 6.15, the altitude region (1-500 km) is binned at 5 km interval, from which the total occurrence of orthogonality ( $\alpha \leq 1^\circ$ ) was recorded at each interval over the  $1^\circ - 90^\circ$  elevation angle ( $\delta$ ) (black line in Figure 6.15). The same analysis was repeated at  $1^\circ - 30^\circ$ ,  $31^\circ - 60^\circ$  and  $61^\circ - 90^\circ$  elevation angle ( $\delta$ ) classifications (red, blue and green lines in Figure 6.15).

As shown in Figure 6.15, for profile A, significant populations of E and F region scatter are predicted at all frequencies for elevation angles less than  $60^\circ$ . The populations of E and F region scatter are even because profile A is a weak ionosphere, a typical 00 LT ionosphere. Backscatter from the elevation angles of  $61^\circ - 90^\circ$  dominates other groupings above 350 km altitude. In other words, we have seen features of such high altitude backscatter for example, in Figures 6.5 and 6.6 from the near-vertical rays spreading out to over 1500 km ground range as highlighted in Figure 6.10 (especially in 24 MHz) and Figure 6.14.

The altitude distributions of orthogonality for profiles C and G, representing stronger ionospheres, are in the middle and bottom panels of Figure 6.15. Here, significant populations of E and F region scatter are also predicted at all frequencies. However, the populations of E region ionospheric scatter outweigh the F region because both profiles C and G are a 00 LT representative ionosphere with a strong E region ionisation. Similar to simulations for profile A, backscatter originating from the elevation angles of  $61^\circ - 90^\circ$  are more significant at altitudes

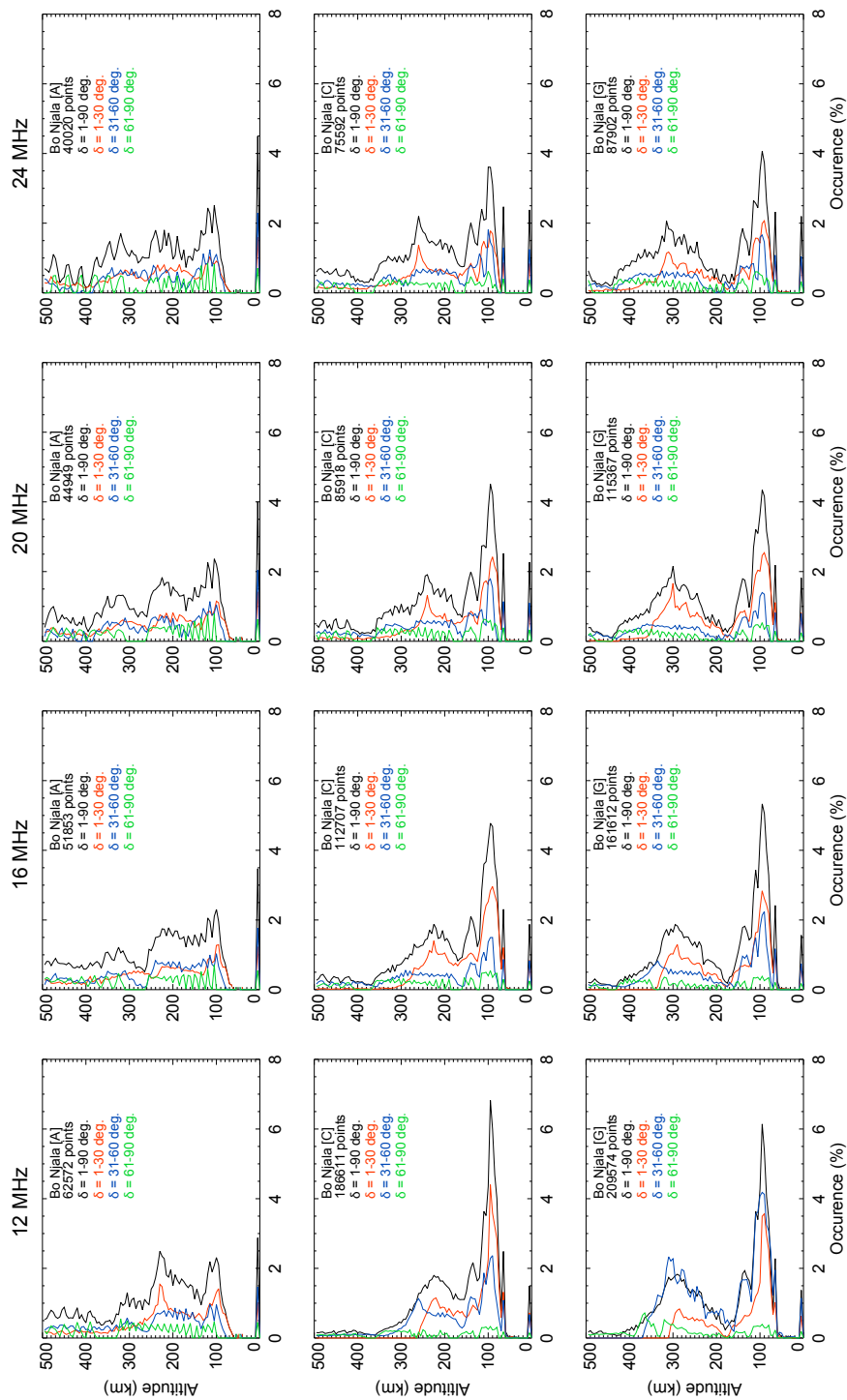


**Figure 6.15:** Evaluation of orthogonality ( $\alpha \leq 1^\circ$ ) as a function of altitude range  $\leq 500$  km for transmit frequencies 12 MHz (column 1), 16 MHz (column 2), 20 MHz (column 3) and 24 MHz (column 4). Plot derived from the parameters of ionospheric profiles A (top panels), C (middle panels) and G (bottom panels), for Bo Njala simulated radar looking through  $75 - 100^\circ$  azimuths from North geographic coordinate and at different classifications of elevation angles ( $\delta$ ). Altitude bins are 5 km wide.

beyond 350 km. The low elevation angles ( $1^\circ - 30^\circ$ ) dominate the E region altitude while the elevation angles of  $31^\circ - 60^\circ$  are significant at  $\sim 300 - 350$  km, typical of the topside F region ionosphere, especially for 12 MHz transmit frequency. Simulations of altitude distributions of orthogonality for Port Harcourt and Bahir Dar radars are not presented here, but follow similar trends to the Bo Njala radar.

Many HF ray tracing studies involve examining observed measurements of existing HF radars with ray tracing modelling. Unfortunately, there is no currently existing SuperDARN-like radar at the locations focused on in this present analysis. As such, the results presented here are discussed in the next section based on previous related studies, many of which are for the high latitude ionosphere. Also, the results presented here represent average expected performance under a variety of ionospheric conditions. Not all ionospheric conditions have been studied here, thus, the observations provided here will be subjected to further validation when SuperDARN-like radar measurements over this region become available.

## 6.6 Discussion

Ray tracing simulations have been extensively applied for determining the contours of perpendicularity of the HF radar wave vector with the Earth's magnetic fields at high latitudes under varying ionospheric conditions prior to inception of the SuperDARN Network (Villain *et al.*, 1984). These earlier studies formed a building block for SuperDARN. Refractive effects from ionospheric electron density distributions influence HF raypaths propagating through the ionosphere. Consequently, the spatial location where the HF wave vectors propagating through the ionosphere achieve orthogonality with the Earth magnetic field varies in latitude. The implication of this latitudinal variation is that results from HF ray tracing modelling for high latitude cannot be easily applied to equatorial latitude. Thus, this study was motivated by the need for a feasibility study towards the development of SuperDARN-like radars at equatorial latitude of the African sector given the rapid expansion of the SuperDARN Network from its original high latitude coverage to the lower latitude sector. In addition, the least studied equatorial African ionosphere is predominated by interesting electrodynamicics

such as EEJ, which is yet to be fully understood (Akala *et al.*, 2013; Yizengaw *et al.*, 2014) due to a lack of instrumentation to record data. As such, a long-term application of SuperDARN-like HF radar technique will lead to enhanced understanding of these terrestrial plasma dynamics peculiar to the equatorial ionosphere.

The study presented in this chapter used a modified version of the three-dimensional ray tracing computer program developed by Jones & Stephenson (1975). The modification entails the coupling of an up to date IGRF magnetic field model and representative equatorial ionospheric parameters deduced from the IRI model.

Results presented in section 6.4 have clearly shown that where orthogonality can be achieved for equatorial SuperDARN-like radars will be dependent on the azimuthal direction of the radar beam. In this simulation, the azimuth in the regions of  $75^\circ - 105^\circ$  east and  $230^\circ - 288^\circ$  west from geographic north performed best across the three simulated radars. The azimuthal extent in each of the simulated radars with good performance is  $\sim 25^\circ$ . The apparent paucity of backscatter for azimuths in the north and south axes is due to the configuration of the equatorial geomagnetic field. This north-south decreasing deviation in performance appears to be higher in the azimuths lying in the northern hemisphere than the southern hemisphere, a signature possibly due to the effect of the South Atlantic Anomaly as simulations, not presented here, further down the southern hemisphere at latitudes up to  $-15^\circ$  have suggested. The superior performance of the east-west azimuthal direction relative to the north-south azimuth at different radar operating frequencies and realistic equatorial ionospheres applied in this study is primarily due to the horizontal configuration of the Earth's magnetic field at equatorial African latitude. This horizontally inclined field geometry means that, the influence of refraction resulting from the non-uniform electron density gradient of the ionosphere where perpendicularity between wave vector and geomagnetic field exist is relatively small when compared with the high latitude where in order to achieve orthogonality sufficient refraction is required to bend propagating rays. This is not to say that the HF wave trajectories at equatorial latitudes are not susceptible to refractive effects from the ionospheric electron

density distribution. Going by the azimuthal performance, to construct a SuperDARN radar in the equatorial African latitude entails a choice of radar beams with a boresite location that allows coverage of the east-west azimuthal field-of-view, which has shown a striking probability of achieving useful backscatter.

The 12 MHz radar frequency generally has more occurrences of simulated scatter, with the majority apparently distributed within the E region ionosphere from rays in the region of  $1^\circ - 30^\circ$  elevation. Multi-frequency analysis suggests that more backscatter can be achieved in the topside F region relative to the E region ionosphere by operating the radar at higher HF frequency. In such a scenario, rays from elevation angles above  $30^\circ$  perform well. Simulated scatter at E region altitudes, especially for a typical afternoon ionosphere may be similar to features observed in radar measurement in Blanc *et al.* (1996), attributed to the effect of the solar zenith angle and the solar zenith radiation penetrating deeper into the atmosphere and producing more ionisation at lower altitudes. This large-scale E-region simulated scatter distribution is also reminiscent of the distributions found by Milan & Lester (2001) who employed the Pykkvibær SuperDARN radar measurements to study the E region backscatter associated with the auroral electrojets.

The elevation angles at about  $1^\circ - 10^\circ$  produced no simulated scatter for 06 LT and 12 LT typical ionospheres when the rays are transmitted at 12 MHz as illustrated for example in Figures 6.12 and 6.13. This feature is due to comparatively large foE associated with the 06 LT and 12 LT diurnal periods. Consequently, simulated backscatter occurrence is seen at higher transmit frequencies. There are more simulated backscatter occurrences for a typical afternoon and solar maximum ionosphere than in a realistic morning and solar minimum ionosphere respectively. This characteristic diurnal and solar variability variations in the level of simulated scatter could be dependent on the differences in ionospheric electron densities. The different distributions of regions with the possibility of ionospheric backscatter due to variability of ionospheric plasma density profiles and local time seen here are similar to the findings in (Nishitani & Ogawa, 2005) for mid latitude following a similar ray tracing analysis.

Rays of lower elevation angles show features of simulated scatter, and they appear up to the maximum range of 2500 km considered here. At such ranges

( $\geq 1000$  km), backscatter seen for example in Figure 6.10 for higher transmit frequencies originates from the high altitude as highlighted in Figure 6.15. Although, features in a modelled distribution of echoes have shown to appear much further in range than in measured data and are susceptible to greater uncertainties (de Larquier *et al.*, 2013) and are not simulated here. Therefore, in this study, backscatter above 1000 km in ground range, may be giving a less precise picture of the ground range backscatter distribution for a practical setup. Contrary to the range distribution of scatter for the lower elevation angles, scatter from the near-vertical elevation angles are confined to  $\sim 500$  km ground range away from the simulated radars. The electron density distribution may not be linked with the simulated scatter from vertical rays. Such backscatter is predominantly due to the magnetic field geometry favouring perpendicularity between the radar wave vector and the Earth's magnetic field. Accurate measurements of the elevation angle will be particularly important in the equatorial region, where both low and high elevation angles are likely to produce significant quantities of ionospheric backscatter.

Apart from ionospheric backscatter that requires orthogonality, SuperDARN-type radars also measure ground scatter as previously noted. Such ground scatter is useful for studying, for example, the characteristics of travelling ionospheric disturbances (TIDs) (e.g., Ribeiro *et al.*, 2011). The possible ground scatter region has been predicted for 12 and 16 MHz transmit frequencies where there are multiple hop propagation modes within the ground range of 2000 km. The likelihood of ground scatter occurrence depends on the transmit frequency and the ionosphere. For ionospheric profile C (at noon with medium foF2) at transmit frequency 20 and 24 MHz, no ground scatter is predicted at ranges less than 2000 km. Here, simulated ground scatter for the 12 MHz for ionospheric profile C (at noon with medium foF2) is mainly from low elevation angles that are below  $40^\circ$  for both 1 and 2 hop propagation modes. At the 16 MHz, simulated ground scatter is between  $\sim 7^\circ$  and  $25^\circ$  elevation angles due to the 1 hop propagation mode. At the same transmit frequency, simulated ground scatter is generated at shorter ground range for the ionospheric profiles with a medium and high foF2, typical of the daytime ionosphere, which is similar to the observation noted in Nishitani & Ogawa (2005) for a mid latitude SuperDARN radar. Identifying ground scatter

from ionospheric scatter in existing SuperDARN radars measurements is usually possible (Milan & Lester, 2001; Ribeiro *et al.*, 2011). However, the algorithm used for such identification of ground scatter from ionospheric scatter for SuperDARN measurement is still not always accurate, and as such remains an issue under investigation with SuperDARN data (e.g., Ribeiro *et al.*, 2011; Burrell *et al.*, 2015, 2016; Reimer *et al.*, 2018).

The analysis here has shown that a SuperDARN-type radar looking in the east-west azimuthal direction has the potential of achieving ionospheric backscatter at African equatorial latitudes. Therefore, such analysis needs to be considered in designing a suitable antenna for this equatorial sector. For instance, an antenna with beams that can provide a  $25^\circ$  scan coverage ( $\frac{1}{2}$  a normal SuperDARN scan) will be a good match for the proposed radars. The front-to-back ratio has been identified as a likely limitation that HF Antennas operating in the east-west azimuths will have, which needs to be considered in the design of the antenna's elevation radiation pattern, height and separation. This would entail constructing an antenna with a large front-to-back ratio to allow for distinguishing scatter from east and west azimuths, which is crucial for a SuperDARN measurement (Custovic *et al.*, 2011, 2013).

Most HF radars designed to study ionospheric irregularities are working at frequencies between 10 MHz and 30 MHz and the effects of the electron density on the ray path diminish considerably with increasing radar operating frequency (Villain *et al.*, 1984). Interesting signatures of Pederson rays at about  $8^\circ - 10^\circ$  in the E-region and  $32^\circ - 34^\circ$  in the F-region,  $\frac{1}{2}$ -hop and  $1\frac{1}{2}$ -hop from our simulation are features that can be validated using analysis from actual radar measurements.

## 6.7 Summary

In this chapter, a ray-tracing program has been applied in simulating the backscattering performance of a typical SuperDARN radar at equatorial African latitude locations. The simulated radar backscatter is consistent with the major SuperDARN radar's requirement that HF rays propagate nearly perpendicular to the geomagnetic field ( $\alpha \leq 1^\circ$ ). The spatial distributions of the eight different representative ionospheric profiles studied, following this criterion, have shown that

there is a likelihood of achieving backscatter in the east-west looking beams ( $25^\circ$  azimuthal range). This result shows that building a SuperDARN radar at the equatorial African latitude location, would require a choice of radar boresite that allows the beams to sweep the regions covering the east-west azimuthal direction. Interestingly, this azimuthal region represents the plane where field-aligned irregularities such as the equatorial electrojet flow.

The transmit frequency of 12 MHz followed by 16 MHz has the highest occurrence of simulated backscatter with most of this distribution from the low elevation rays in the E region ionosphere. The mid and near-vertically aligned rays achieved orthogonality better at higher frequencies of 20-24 MHz with a simulated distribution confined in the vicinity of  $\sim 500$  km ground range away from the simulated radar site. Contrarily to the vertically aligned rays, features of simulated scatter from the lower elevation angles appear up to the maximum range of 2500 km.

Backscatter measurements of SuperDARN-like HF radars located in the equatorial African latitude sector should provide important data for studying E and F region field-aligned irregularities and equatorial electrodynamic phenomena such as the equatorial electrojet. Other wide ranging terrestrial plasma research such as ULF waves may benefit from such data. The ionospheric profiles used in this present study are based on IRI modelled data for a quiet geomagnetic periods. As such, future studies could employ realistic electron density profiles derived from experimental ionogram data during a quiet geomagnetic period and a disturbed period like geomagnetic storms. Also, the relationships between the vertical and latitudinal structures of backscatter seen from different simulated radar locations could be examined using ray tracing simulation.

A HF ray tracing has been employed in this chapter to show simulations of probable distributions of complex echo structures from rays at varying elevation angles in a SuperDARN radar setup. The results presented here will be applied to radar antenna designs in chapter 7. This analysis, apart from its importance as a feasibility study for building HF radars at equatorial African latitudes, will also provide a basis for future interpretations of results obtained from data measured from such radars.

# Chapter 7

## Recommendations on Antenna Patterns and Array Design

### 7.1 Introduction

Chapter 6 has described the differences in, for example, optimal frequency, bore-site and azimuthal coverage required for an equatorial SuperDARN-type radar, compared with previous deployments at higher latitudes. The characteristics or performance parameters of an antenna system is essential for designing the antenna for a specific application. Previous studies such as Sterne *et al.* (2011); Custovic *et al.* (2011, 2013) have discussed the characteristics and designs of the antenna systems used for SuperDARN radars. As noted earlier in chapter 3, existing SuperDARN radars use two types of antennas, the log-periodic dipole array (LPDA) antennas and twin-terminated folded dipole (TTFD) antennas.

The limitations of the LPDA used by the early radars led to the TTFD antennas. For example, while an LPDA antenna operating across its frequency band (8 - 20 MHz) produces beams that can be steered beyond  $\pm 26^\circ$  from the boresite that is mostly applied in SuperDARN, it can also generate a backward pointing radiation beam with sufficient power to return backscatter signals from unwanted directions, which complicates data analysis (Custovic *et al.*, 2011). This disadvantage of the LPDA antennas, described as size of the front-to-back ratio, was improved on in the TTFD antennas. However, the LPDA antennas have some

advantages over the TTFD, for instance, they have more gain at operating frequency band of about 8-11 MHz even though the TTFD antennas have higher gain at higher frequencies (Custovic *et al.*, 2011). Therefore, it is important to factor in the differences of the parameters required for optimal operation of respective SuperDARN radars into the design of their antenna system.

The magnetic field geometries and ionosphere of the equatorial region is different from the high and mid latitude regions where there are already existing SuperDARN radars. Following this peculiarity, the geographic locations and radar characteristics such as frequency, bore-sight azimuth where useful backscatter can be achieved for a SuperDARN radar have been demonstrated in Chapter 6. On the other hand, at the existing high latitude SuperDARN radars, echoes are not expected at very high elevation angles even though they can sometimes be seen (Greenwald *et al.*, 1985; Chisham *et al.*, 2007). However, the analysis in Chapter 6 has shown that, for example, the Bo Njala simulated radar at African equatorial latitudes has high chances of achieving substantial backscatter from very high elevation angles. More specifically, distinguishing high elevation angle backscatter for (e.g., Bo Njala radar) from those at lower elevation angles will pose some difficulties given the operational technique of existing SuperDARN radars at high latitude (Chisham *et al.*, 2007). As such, choosing which elevation angle echoes to screen out in favour of the other will affect the choice of antenna gain pattern.

In this chapter, a number of recommendations for radar antenna design and technical parameters are presented based on the results of the ray tracing simulations in the last chapter. The simulations and analysis presented in that chapter have shown that a SuperDARN-type radar looking in the east or west azimuthal direction has the potential of achieving ionospheric backscatter at African equatorial latitudes. The east-west azimuths and other controlling factors such as transmit frequency and elevation angle with a good performance plausibility have been applied in designing antenna patterns that will be suitable for equatorial latitude SuperDARN radars. In addition, it was shown that higher radar frequencies of 12 - 24 MHz compared to the 8 - 20 MHz most existing SuperDARN radars use would be good for the African equatorial radars. These higher radar frequencies potentially mean smaller antenna arrays to reduce the cost of developing SuperDARN-type radar at African equatorial latitudes. This is because the use

of higher frequencies (smaller wavelengths) suggests that narrower and shorter antenna arrays might be possible, allowing for cost savings. These frequencies are compared with several azimuthal beamforming plans and antenna separations in order to determine suitable antenna and array designs for equatorial African SuperDARN radars. The analysis of such antenna patterns and array designs are discussed in the subsequent sections of this chapter. This chapter is an initial consideration at addressing some peculiarities identified so far for the African equatorial SuperDARN radars with respect to antenna array construction.

## 7.2 Elevation Radiation Pattern

The elevation radiation pattern of varying antenna height and separation are considered. Given that interpreting the backscatter from a typical SuperDARN radar looking in either east or west azimuth at the African equatorial region will be problematic with an antenna system that has an inferior front-to-back ratio, a Rankin-type antenna model was employed for the analysis due to its preferable front-to-back ratio (Custovic *et al.*, 2011, 2013). The radar at Rankin Inlet in Canada is one of the newer versions of SuperDARN radars (Chisham *et al.*, 2007).

Elevation radiation pattern of the Antenna models presented in this thesis were derived using EZNEC PRO2 (W7EL, 2019), a Numerical Electromagnetics Code (NEC) based software. This software is a CAD (computer aided design) package that allows for constructing a model of the antenna in three-dimensions (3D). The model is made up of lines which are broken down into segments. The software is then used to calculate impedance and current in each segment from which the NEC calculating software works out near and far fields, which can then be plotted out as 3D, vertical and azimuth plots.

### 7.2.1 Antenna Height

As shown in Figure in 7.1(a), a good elevation pattern is realised with a 12 MHz transmit frequency and a normal height (7.5 m, 12.5 m masts), depicted as black oval outline. Reducing the height to 5 m and 10 m masts, altered the peak of the elevation, impeding the front-to-back ratio. The EZNEC program determines

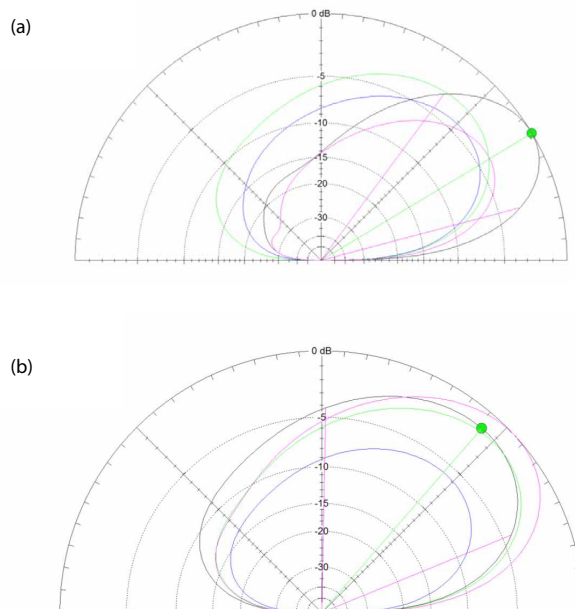


**Figure 7.1:** Elevation radiation pattern for a Rankin-type single type antenna using radar frequency of 12 MHz. (a) Antenna height for a normal height (black - 7.5 m, 12.5 m masts), reduced height (blue - 5 m, 10 m masts), reduced height with lower reflector (green), and reduced height tilted (red). The green dot indicates cursor elevation of 31°. (b) Antenna separation for a normal separation (black - 12 m), reduced separation (blue - 8.3 m), compromise separation one (green - 9.6 m), and compromise separation two (red - 12 m). The green dot indicates cursor elevation of 49°.

front-to-back ratio by calculating the difference in the gain between the main lobe and the pattern gain 180° in azimuth from the main lobe. An increased ratio is important in practice to allow the radar to radiate signals mostly toward a particular azimuth direction and reject those from other noisier directions (Sterne *et al.*, 2011). Further reduction of height with a lower reflector and a tilted masts produced an improved peak elevation but not as good as the normal height. However, reducing the height for higher average transmit frequencies would reduce cost and raise elevation pattern slightly, but at the expense of front-to-back ratio ( $\sim 6$  dB vs  $\sim 20$  dB). Thus, the normal height used in typical SuperDARN radars

provides the most suitable elevation radiation pattern as a function of antenna height in this scenario.

### 7.2.2 Antenna Separation

Following the antenna height consideration, the effects of different antenna separations to elevation radiation pattern has been evaluated as shown in Figure 7.1(b). For a normal separation of 12 m, the antenna model produced a good elevation pattern and an efficient radiator, while a reduced separation of 8.3 m produced an acceptable elevation pattern but is an inefficient radiator. Modifying the separation to 9.6 m produced a reasonable elevation pattern and also a better radiator than the normal separation from the analysis in Figure 7.1(b). Likewise, reducing antenna separation for higher average transmit frequencies will lead to reduction in cost. Therefore, the compromise separation of 9.6 m would be a good choice for an equatorial latitude SuperDARN radar from an elevation angle point of view. The next section considers possible azimuthal patterns for the elevation patterns discussed here.

## 7.3 Azimuthal Radiation Pattern

Models of azimuthal pattern that will be suitable for a SuperDARN-like radar in African equatorial latitudes are considered using the design of a standard 16 beam SuperDARN radar. In this case, the model for the CUTLASS (collaborative UK twin located auroral sounding system) SuperDARN radars (e.g., Jones *et al.*, 2001; Lester *et al.*, 2004) was used. It is noteworthy to mention that the Rankin Inlet radar antenna construction (TTFD) is different from the antenna employed by CUTLASS SuperDARN radars. As such, the radiation patterns might look different in practice.

The radiation pattern for a single antenna can be defined as a function  $R(\theta, \phi)$  as discussed in Section 3.1.2, where  $\theta$  in degrees represents the elevation angle radiation discussed in the last section and  $\phi$  also in degrees indicates azimuth. The SuperDARN radars utilise array antenna, which implies combining a set of identical  $N$  number of antennas oriented in the same desired direction and

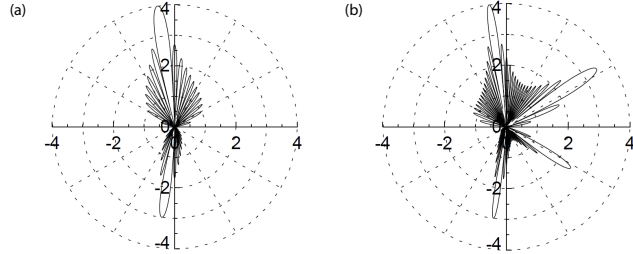


**Figure 7.2:** Azimuthal pattern for a Standard CUTLASS radar, beam 5 and azimuth  $-8.1^\circ$  off boresite with (a) 12 MHz that has a width of  $8^\circ$  and (b) 20 MHz that has a width of  $4.8^\circ$ .

suppressed in other unwanted directions for improved directivity over each of such antennas (Skolnik, 2001). For a linear array of  $N$  individual antennas that radiate isotropically, the total field intensity can be expressed as

$$R_{array} = R_{element} \times R_{AF} \quad (7.1)$$

where  $R_{element}$  is the field radiated by a single element and  $R_{AF}$  is the array factor, which is the pattern of an array for isotropic individual antennas (Balanis, 1997). The individual antenna element performance is approximated to a Hertzian dipole, with an azimuthal radiation pattern varying as  $R_{element} = \sin^2\theta$ , with a front-to-back ratio of 10 dB applied by attenuating the radiation pattern for angles  $180^\circ < \theta < 360^\circ$ . If the radiation from individual antennas is directive, the total field can be formed by multiplying the array factor of the isotropic sources by the field of an individual element and where such elements are identical, the array factor following Balanis (1997) can be calculated as

$$R_{AF} = \sum_{n=1}^N e^{-j(n-1)(kd \cos \theta + \beta)} \quad (7.2)$$

representing the sum of  $n$  from  $n = 1$  to  $N$  elements, where  $k$  is wave number ( $K = 2\pi/\lambda$ ,  $\lambda$  being the wavelength),  $d$  is antenna separation,  $\beta$  is phase offset and angle  $\theta$  defining a full circle array. The azimuth  $\phi$  for a specific angle ( $x_\theta$ ) from the boresite can be determined by  $\phi = 90^\circ - x_\theta$  and the complex array factor

### 7.3 Azimuthal Radiation Pattern

convolved to simulate the antenna radiation pattern for a given frequency, beam direction and antenna spacing.

Figure 7.2(a) was made using Equation 7.1 for a radar frequency of 12 MHz ( $\approx 25$  m radar wavelength) and 15.24 m spacing, which is typical of the 16 antennas used for CUTLASS SuperDARN radars. It produced a beamwidth of  $8^\circ$  for azimuth steered to  $-8.1^\circ$  off the boresite for a typical beam 5 of the CUTLASS radars. For a higher frequency (20 MHz), the beamwidth becomes smaller ( $4.8^\circ$ ) but more side lobes are generated as seen in Figure 7.2(b). This presents a problem for the equatorial radars, where operation at 20 MHz is expected to be common, even though it is rare at higher latitudes.

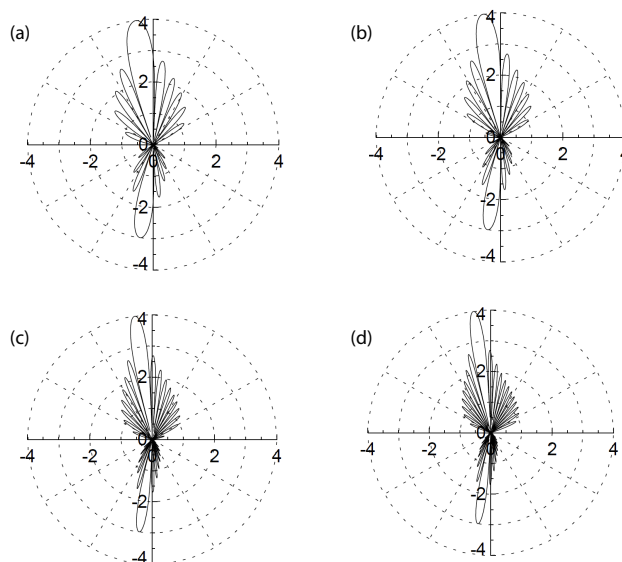


**Figure 7.3:** Azimuthal pattern for a Standard CUTLASS radar, beam 5 and azimuth  $-8.1^\circ$  off boresite with (a) 12 MHz and 8.3 m separation resulting in a width of  $14.6^\circ$ , (b) 12 MHz and 9.6 m separation giving  $12.6^\circ$  width, (c) 20 MHz and 8.3 m separation giving  $8.8^\circ$  width, and (d) 20 MHz and 9.6 m separation giving  $7.6^\circ$  width.

Different azimuthal beamforming versus frequency and antenna separation are further compared in the following analysis. For example, in Figure 7.3, antenna separation and frequency are varied. At 8.3 m antenna separation and 12 MHz

### 7.3 Azimuthal Radiation Pattern

---

combination in Figure 7.3(a) with beamwidth output of  $14.6^\circ$ , good azimuthal patterns are realised but such a configuration is not good for elevation pattern as seen in the previous section. The beamwidth reduces to  $12.6^\circ$  using the same frequency of 12 MHz but an increased separation of 9.6 m as shown in 7.3(b). Using an increased frequency of 20 MHz and the 8.3 m separation as shown in Figure 7.3(c) produces a reduced  $8.8^\circ$  width and similar azimuthal pattern to 12 MHz. However, this higher frequency of 20 MHz and reduced separation of 8.3 m produced an improved sidelobe power compared to the Figure 7.2 setup. In a similar vein, the same 20 MHz frequency but with the 9.6 m separation as shown in Figure 7.3(d) produced a reduced  $7.6^\circ$  width and improved sidelobe power. The antennas become inefficient if you make the separation too small as earlier seen. Thus, increasing antenna separation to 9.6 m as seen in Figures 7.3(b) and (d) with a  $12.6^\circ$  width for 12 MHz and  $7.6^\circ$  width for 20 MHz, give superior azimuthal radiation patterns compared to 7.3(a) and (c). In practice, a separation as small as possible is desirable, but the sidelobes at high frequency here are much better, so overall a better choice.

Patterns produced by a single antenna phase offset as seen in Figure 7.3 are combined for the phase offsets ( $\beta$  in Equation 7.2) used in each beam of a standard SuperDARN radar as depicted in Figure 7.4. A model of a CUTLASS SuperDARN radar with 15.24 m antenna separation, 12 MHz and 16 beams combination, which has a  $8^\circ$  width is shown in Figure 7.4(a). In Figure 7.4(b) a similar beam pattern is shown, but now with a reduced antenna separation of the favourable 9.6 m at a frequency of 16 MHz, 8 beams of separation  $3.24^\circ$  and  $10^\circ$  width will produce good antenna pattern that can be steered to cover the azimuth of interest for a SuperDARN radar operating at African equatorial latitudes. This configuration in Figure 7.4(b) can give more than 8 beams, but we anticipate from the previous study in Chapter 6 that using only 8 beams will be sufficient to cover the azimuths of interest.

Further modifications to the model with 9.6 m antenna separation and 16 MHz but now with the number of transmit antennas increased to 24 antennas are shown in Figure 7.5. Figure 7.5(a) uses a standard CUTLASS SuperDARN radar beam separation ( $3.24^\circ$ ), but extra antennas and only showing 8 beams. From the azimuthal range where orthogonality could be achieved at African equatorial

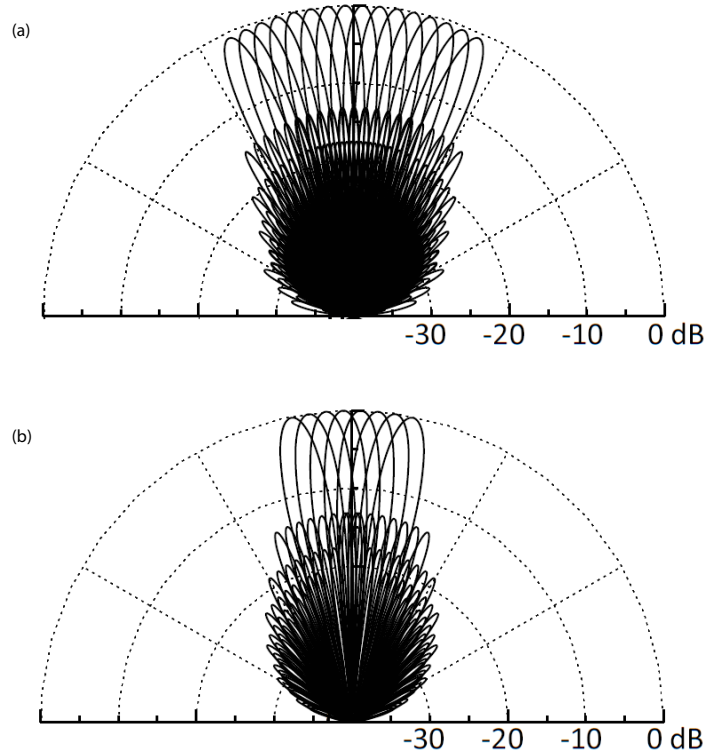


**Figure 7.4:** Azimuthal pattern for (a) 12 MHz 16 beams with 15.24 m separation giving a width of  $8^\circ$ , and (b) 16 MHz 8 beams with 9.6 m separation and a width of  $10^\circ$ .

latitude as demonstrated in Chapter 6, the 8 beams would be a good match for a  $25^\circ$  scan ( $\frac{1}{2}$  normal scan). Also, a reduced antenna separation gives potential of more antennas for a fixed array size. Therefore, a 12 beams,  $6.6^\circ$  width with the phase offset ( $\beta$ ) adjusted to give a reduced  $2.08^\circ$  beam separation in Figure 7.5(b) is possible. The 12 beams,  $6.6^\circ$  width and  $2.08^\circ$  beam separation combination would produce a superior azimuthal pattern for a SuperDARN radar operating at African equatorial latitude. However, a trade-off between a radar with this combination and a standard SuperDARN radar would be the increased high cost of developing such a radar.

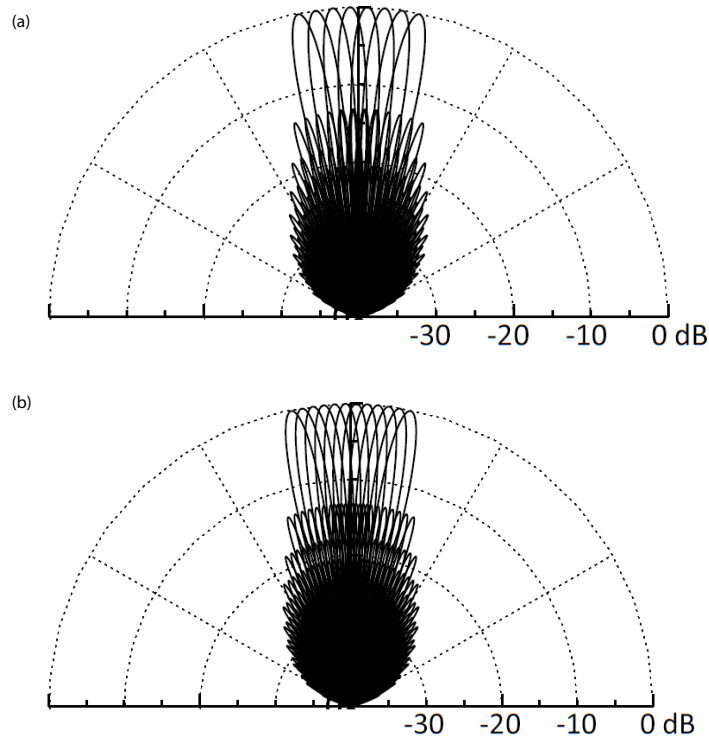


**Figure 7.5:** Same as Figure 7.4b except that here (a) has 16 MHz 24 antennas, 8 beams at  $3.24^\circ$ , resulting in a width of  $6.6^\circ$  and (b) 16 MHz 24 antennas, 12 beams at  $2.08^\circ$  giving a width of  $6.6^\circ$ .

## 7.4 Summary

The equatorial African region is a viable location for the development of SuperDARN-type radars for studying many geophysical phenomena such as the equatorial electrojet as demonstrated in Chapter 6. Some of the implications for antenna design with respect to the radiation pattern for the proposed African equatorial radars were evaluated in this chapter. The compromise antenna separation of 9.6 m was a better radiator for the same frequency of 12 MHz and produced a reasonable elevation pattern compared to the normal separation of 12 m in a typical Rankin-type antenna model. With reduced antenna separation of 8.3 m, the elevation pattern was acceptable but an inefficient radiator. The 9.6 m is a good alternative for SuperDARN-type radars at the equatorial region, which require antennas with improved front-to-back ratio. The front-to-back ratio can

be maximised with the TTFD antennas of standard height (e.g., Sterne *et al.*, 2011; Custovic *et al.*, 2011, 2013).

The 8.3 m and 9.6 m antenna separations were used for modelling antenna azimuthal radiation patterns. It was shown that reducing the antenna separation produced increased beamwidths. For example, at 12 MHz frequency the 9.6 m antenna separation produced a beamwidth of  $12.6^\circ$  while 8.3 m antenna separation produced a larger beamwidth of  $14.6^\circ$ . In addition, the sidelobes improved at a higher frequency of 20 MHz with reducing antenna separations. However, the antennas become inefficient if the separation is made too small. This is a trade-off between using antenna separation as small as possible and achieving desirable sidelobes at high frequency. Therefore, here the intermediate antenna separation of 9.6 m is the best solution. Whilst the 9.6 m antenna separation produced a smaller beamwidth than the 8.3 m separation, this compact beamwidth might not be a huge trade-off in the equatorial region where smaller azimuthal extent  $\sim 25^\circ$  can cover the region with likelihood of useful backscatter as shown in Chapter 6 compared to the high latitude region in which most of the existing SuperDARN radars are located. The analysis here has equally shown that improved sidelobes at high frequency are achievable compared to the traditional separation of 15.24 m with about  $8^\circ$  width for a radar frequency of  $\sim 12$  MHz. Thus, apart from the standard SuperDARN pattern, the following two azimuthal radiation patterns are possible for the proposed radars based on this initial antenna array analysis.

- A narrowed equatorial azimuth with 9.6 m antenna separation, 16 MHz central transmit frequency, 8 beams at the typical  $3.24^\circ$  separation and  $10^\circ$  beamwidth operation. This reduces the size and hence cost of the antenna array.
- An improved equatorial azimuth pattern with 9.6 m antenna separation, 16 MHz central transmit frequency, 24 antennas, 12 beams at  $2.08^\circ$  separation and beamwidth  $6.6^\circ$ . This increases the antenna array size back to the standard SuperDARN footprint, and increases cost due to additional antenna and transmitters (and receivers if using a digital receiver per antenna system).

# Chapter 8

## Conclusions and Future Work

This thesis has discussed the analysis of ULF wave observations from SuperDARN datasets in Chapters 4 and 5, and SuperDARN-style HF radar performance at African equatorial latitudes using ray tracing method in Chapter 6 and its application to antenna array design in Chapter 7. ULF waves provide vital information about the structure, evolution and dynamics of the Earth's magnetosphere while the ray tracing analysis of ionospheric HF radar performance is important, for example, in developing a SuperDARN radar in such an equatorial latitude region.

This chapter provides a summary and areas of future work for the studies in this thesis. It is subdivided into two sections. The first section treats the case-study and statistical analysis of a temporal phase evolution in latitude of observed ULF waves with  $m$  number in the intermediate- $m$  range while the last section is on the ray tracing analysis and application.

### 8.1 Intermediate- $m$ ULF Wave Observations

ULF wave activity has been identified in the velocity data of measurements by the Hankasalmi SuperDARN radar in the high latitude region. Such radar measurements are due to velocity variations of small-scale field-aligned ionospheric irregularities along the radar beam direction. Fourier analysis of this wave activity, which occurred on May 13<sup>th</sup> 2016 between 00:00 and 03:00 UT, revealed a seemingly Pc5 pulsation with a frequency of 0.75 MHz. This wave activity

## 8.1 Intermediate- $m$ ULF Wave Observations

---

also detected in the datasets of magnetometers with close proximity to the Han-kasalmi radar further revealed an equatorward phase propagation over the 3-hr interval. A preliminary inspection of this case study wave event depicted a temporal evolution of the latitudinal phase propagation behaviour along with a clear backscatter bite-out across radar beams 3 to 11. This radar backscatter bite-out can be caused by energetic particle precipitation from a substorm as suggested by Gauld *et al.* (2002), due to depletion of the scattering structure of the ionospheric irregularities observed by the radar, and ionospheric absorption. On the other hand, Yeoman *et al.* (2012) suggested that the spatial structure of the injected particles from such a substorm can determine the phase characteristics of ULF waves driven by the substorm-injected particles. Based on the preliminary investigation, we thought that the phase evolution might be associated with energetic particles in the likely event that this case-study ULF wave activity is generated by substorm-injected particles.

Fourier wave analysis showed that the case-study ULF wave possesses an intermediate- $m$  azimuthal wave number of 17, propagating eastward. The wave has been interpreted as resulting from drifting electrons of energies of  $35 \pm 5$  KeV in a drift resonance condition linked to particle populations from a substorm onset at about 1 hour prior to the wave occurrence. This driving mechanism of wave-particle interactions is due to energy exchange between the drifting particle populations in the magnetosphere due to substorm occurrence and Alfvén wave modes on the Earth’s magnetic field. On the other hand, the evolution in the wave polarisation can equally be explained by the moving source theory (e.g., Klimushkin *et al.*, 2004; Mager & Klimushkin, 2008; Zolotukhina *et al.*, 2008; Mager *et al.*, 2009) suggested in a similar intermediate- $m$  wave observed by Yeoman *et al.* (2010). A possible explanation suggested for the temporal evolution observed in the latitudinal phase propagation characteristics was that a new population of energetic drifting particles indicated by the loss of radar backscatter (e.g., Gauld *et al.*, 2002) imposed a new phase structure on the wave, similar to the suggestion by Yeoman *et al.* (2012). This mechanism might have caused the evolution from equatorward to poleward propagation of the latitudinal phase behaviour observed during the interval of this wave activity.

## 8.1 Intermediate- $m$ ULF Wave Observations

---

A statistical analysis of 18 similar intermediate- $m$  ULF wave events linked to substorm-injected particles revealed a dominant equatorward latitudinal and eastward longitudinal phase propagation consistent with a similar statistical study by James *et al.* (2013). Here, the statistical study showed that there are no latitudinal phase evolution or backscatter bite-outs in those similar waves, which provides evidence of a relationship between the evolving phase and radar backscatter bite-out observed in the case-study. Another interesting Pc4 wave driven by a different mechanism was also observed in the magnetometer data within the 3 hour interval during which the case study wave was observed. Further statistical analysis in Chapter 5 supports the idea that the wave suggested to be a giant pulsation is not connected to the evolving phase observed in the case study wave, with the occurrence of the two events near-simultaneously being coincidental.

A broader statistical study is needed to better understand the phase behaviour of intermediate- $m$  ULF waves. Also, observations from more radars may have to be involved in future studies in order to extend the study presented in Chapters 4 and 5 of this thesis. Such extended studies would prove or disprove the generality of the present results and enhance our present understanding of intermediate- $m$  ULF waves. Furthermore, conjugate observations (e.g., Mager *et al.*, 2019) from radar and the spacecraft such as Van Allen Probes that directly observe particles driving ULF wave activity can provide more explanations on the type of phase evolution experienced by intermediate- $m$  ULF wave activity studied in this thesis.

## 8.2 Ray Tracing Analysis of SuperDARN-style Radar Performance at African Equatorial Latitudes and Applications

The ray-tracing analysis in Chapter 6 has shown that there is a likelihood of achieving backscatter in the east-west looking beams ( $25^\circ$  azimuthal range) for the proposed SuperDARN-style radars at equatorial latitudes in the African longitude sector. There is a clear difference in performance at the three different geographic locations employed in the study, primarily because of their varying geomagnetic field geometries. Similarly, the ionisation characteristics due to diurnal, seasonal and sunspot number variations have noticeable effects in the analysis, such as, more orthogonality occurrence for an ionosphere of a typical afternoon with a high FoF2 than that of the morning. Whilst the lower elevation angle propagation has shown more likelihood of achieving orthogonality, the near-vertical elevation angle propagation can achieve orthogonality because of the near-horizontal configuration of the geomagnetic fields at the equatorial region. The results in that chapter have shown, among other technical radar parameters, that a choice of radar boresite should be such that it allows the beams to sweep the regions covering the east-west azimuthal direction. Radar technical parameters relating to antenna array design have been demonstrated, as shown in Chapter 7.

Geolocating radar echoes is difficult with existing SuperDARN systems. However, geolocating such echoes at the African equatorial latitudes explored in this thesis will be more problematic due to a number of reasons. The front-to-back ratio could become a likely problem for the radar antenna system given that irregularities will be observed to the east and west. Some of the locations studied here have shown that sufficient echoes can be achieved from high elevation angles as well as from the lower elevation angles. This will pose a challenge on deciding which category of echoes to screen out given that existing SuperDARN radars at high latitudes operate in such way that echoes from high elevation angles are not envisaged. Preferentially observing the lower elevation angle echoes over those from the high elevation angles would require a suitable antenna pattern in

## 8.2 Ray Tracing Analysis of SuperDARN-style Radar Performance at African Equatorial Latitudes and Applications

---

elevation or alternatively a reliable way of measuring the elevation angle. Contrarily, preferentially observing the high elevation angle echoes would require an antenna array design different from those utilised in existing radars such as the Rankin-type that does not not favour the high elevation angle echoes. An initial analysis on antenna array design has been presented in this thesis. Future work will involve building such a radar to look at the electrodynamics of the equatorial ionosphere, and before that simpler HF propagation experiments to test, for examples, the accuracy of the ionospheric models, the performance of some antenna designs and the occurrence of irregularities at the equatorial locations explored here.

## References

- AGAPITOV, O. & CHEREMNYKH, O. (2013). Magnetospheric ULF waves driven by external sources. *Advances in Astronomy and Space Physics*, **3**, 12–19. 45, 82
- AGAPITOV, O., GLASSMEIER, K.H., PLASCHKE, F., AUSTER, H.U., CONSTANTINESCU, D., ANGELOPOULOS, V., MAGNES, W., NAKAMURA, R., CARLSON, C.W., FREY, S. *et al.* (2009). Surface waves and field line resonances: A themis case study. *Journal of Geophysical Research: Space Physics*, **114**, <https://doi.org/10.1029/2008JA013553>. 46
- AKALA, A.O., SEEMALA, G.K., DOHERTY, P.H., VALLADARES, C.E., CARRANO, C.S., ESPINOZA, J. & OLUYO, S. (2013). Comparison of equatorial GPS-TEC observations over an African station and an American station during the minimum and ascending phases of solar cycle 24. *Ann. Geophys.*, **31**, 2085–2096, <https://doi.org/10.5194/angeo-31-2085-2013>. 175
- AKASOFU, S.I. (1964). The development of the auroral substorm. *Planetary and Space Science*, **12**, 273–282, [https://doi.org/10.1016/0032-0633\(64\)90151-5](https://doi.org/10.1016/0032-0633(64)90151-5). 23
- AKASOFU, S.I. (1977). *Physics of magnetospheric substorms*. Reidel, Dordrecht. 29
- ANDRÉ, R., HANUISE, C., VILLAIN, J.P. & CERISIER, J..C. (1997). HF radars: Multifrequency study of refraction effects and localisation of scattering. *Radio Sci.*, **32**, 153–168, <https://doi.org/10.1029/96RS02987>. 136
- BADDELEY, L., YEOMAN, T., WRIGHT, D., TRATTNER, K. & KELLET, B. (2004). A statistical study of unstable particle populations in the global ringcurrent and their relation to the generation of high  $m$  ULF waves. *Ann. Geophys.*, **22**, 4229–4241, <https://doi.org/10.5194/angeo-22-4229-2004>. 50
- BADDELEY, L., YEOMAN, T. & WRIGHT, D. (2005). HF doppler sounder measurements of the ionospheric signatures of small scale ULF waves. **23**, 1807–1820, <https://doi.org/10.1029/2004JA010500>. 1807

## REFERENCES

- org/10.5194/angeo-23-1807-2005. 50, 109, 110, 117, 119, 121
- BADDELEY, L.J., YEOMAN, T.K., WRIGHT, D.M., DAVIES, J.A., TRATTNER, K.J. & ROEDER, J.L. (2002). Morning sector drift-bounce resonance driven ulf waves observed in artificially-induced hf radar backscatter. *Ann. Geophys.*, **20**, 1487–1498, <https://doi.org/10.5194/angeo-20-1487-2002>. 24, 48, 111
- BAKER, D.N., PULKKINEN, T., ANGELOPOULOS, V., BAUMJOHANN, W. & MCPHERRON, R. (1996). Neutral line model of substorms: Past results and present view. *Journal of Geophysical Research: Space Physics*, **101**, 12975–13010, <https://doi.org/10.1029/95JA03753>. 23, 24
- BAKER, D.N., LI, X., PULKKINEN, A., NGWIRA, C., MAYS, M., GALVIN, A. & SIMUNAC, K. (2013). A major solar eruptive event in july 2012: Defining extreme space weather scenarios. *Space Weather*, **11**, 585–591, <https://doi.org/10.1002/swe.20097>. 1
- BALANIS, C.A. (1997). *Antenna theory: analysis and design*. John wiley & sons. 185
- BAUMJOHANN, W. & TREUMANN, R.A. (1997). *Basic Space Plasma Physics*. Imperial College Press. xii, 2, 11, 12, 22
- BEHARRELL, M., KAVANAGH, A.J. & HONARY, F. (2010). On the origin of high  $m$  magnetospheric waves. *Journal of Geophysical Research: Space Physics*, **115**, <https://doi.org/10.1029/2009JA014709>. 47
- BENNETT, J., DYSON, P. & NORMAN, R. (2004). Progress in radio ray tracing in the ionosphere. *URSI Radio Science Bulletin*, **2004**, 81–91. 42, 43, 55
- BERNGARDT, O., RUOHONIEMI, J., STMAURICE, J.P., MARCHAUDON, A., KOSCH, M., YUKIMATU, A., NISHITANI, N., SHEPHERD, S., MARCUCCI, M., HU, H. *et al.* (2019). Global diagnostics of Ionospheric Absorption During X-Ray Solar Flares Based on 8-to 20-MHz Noise Measured by Over-the-Horizon Radars. *Space Weather*, **17**, 907–924, <https://doi.org/10.1029/2018SW002130>. 135
- BILITZA, D. (2018). IRI the International Standard for the Ionosphere. *Adv. Radio Sci.*, **16**, 1–11, <https://doi.org/10.5194/ars-16-1-2018>. 80
- BILITZA, D., ALTADILL, D., ZHANG, Y., MERTENS, C., TRUHLIK, V., RICHARDS, P., MCKINNELL, L. & REINISCH, B. (2014).

## REFERENCES

- The International Reference Ionosphere 2012 - a model of international collaboration. *J. Space Weather Space Clim.*, **4**, <https://doi.org/10.1051/swsc/2014004>. 80, 139, 141
- BLANC, E. & HOUNGNINOU, E. (1998). Typical disturbances of the daytime equatorial f region observed with a high-resolution HF radar. *Ann. Geophys.*, **16**, 721–730, <https://doi.org/10.1007/s00585-998-0721-6>. 58
- BLANC, E., MERCANDALLI, B. & HOUNGNINOU, E. (1996). Kilometric irregularities in the E and F regions of the daytime equatorial ionosphere observed by a high resolution HF radar. *Geophys. Res. Lett.*, **23**, 645–648, <https://doi.org/10.1029/96GL00415>. 58, 171, 176
- BOROVSKY, J.E. & DENTON, M.H. (2006). Differences between CME-driven storms and CIR-driven storms. *Journal of Geophysical Research: Space Physics*, **111**, <https://doi.org/10.1029/2005JA011447>. 28
- BRYSON, G., BRISTOW, W. & PARRIS, T. (2007). An introduction to Radar and the Super Dual Auroral Radar Network. Tech. rep., Geophysical Institute University of Alaska Fairbanks. xv, 67
- BUCHERT, S. (2007). Introduction to ionospheric physics. In *IRF, Swedish Institute of Space Physics, Uppsala, Sweden*. 35
- BURRELL, A.G., MILAN, S.E., PERRY, G.W., YEOMAN, T.K. & LESTER, M. (2015). Automatically determining the origin direction and propagation mode of high-frequency radar backscatter. *Radio Science*, **50**, 1225–1245, <https://doi.org/10.1002/2015RS005808>. 136, 178
- BURRELL, A.G., YEOMAN, T.K., MILAN, S.E. & LESTER, M. (2016). Phase calibration of interferometer arrays at high-frequency radars. *Radio Sci.*, **51**, 1445–1456, <https://doi.org/10.1002/2016RS006089>. 72, 178
- CHAPMAN, S. (1931). The absorption and dissociative or ionizing effect of monochromatic radiation in an atmosphere on a rotating earth. *Proceedings of the Physical Society*, **43**, 26–45. 139, 140
- CHAPMAN, S. & BARTELS, J. (1940). Geomagnetism, vol. i: Geomagnetic and related phenomena. *Geomagnetism, Vol. I: Geomagnetic and Related Phenomena, by S. Chapman and J. Bartels. London: Oxford Univ. Press, 1940*, **1**. xii, 19

## REFERENCES

- CHAPMAN, S. & FERRARO, V.C. (1931). A new theory of magnetic storms. *Terrestrial Magnetism and Atmospheric Electricity*, **36**, 77–97, <https://doi.org/10.1029/TE036i002p00077>. 18
- CHELPANOV, M., MAGER, P., KLIMUSHKIN, D. & MAGER, O. (2019). Observing magnetospheric waves propagating in the direction of electron drift with Ekaterinburg Decameter Coherent Radar. *Solar-Terrestrial Physics*, **5**, 51–57, <https://naukaru.ru/en/nauka/article/28052/view>. 83, 114, 133
- CHELPANOV, M.A., MAGER, P.N., KLIMUSHKIN, D.Y., BERNGARDT, O.I. & MAGER, O.V. (2016). Experimental evidence of drift compressional waves in the magnetosphere: An Ekaterinburg coherent decameter radar case study. *Journal of Geophysical Research: Space Physics*, **121**, 1315–1326, <https://doi.org/10.1002/2015JA022155>. 48, 114
- CHEN, L. & HASEGAWA, A. (1974a). A theory of long-period magnetic pulsations: 1. Steady state excitation of field line resonance. *Journal of Geophysical Research*, **79**, 1024–1032, <https://doi.org/10.1029/JA079i007p01024>. 46
- CHEN, L. & HASEGAWA, A. (1974b). A theory of long-period magnetic pulsations: 2. impulse excitation of surface eigenmode. *Journal of Geophysical Research*, **79**, 1033–1037, <https://doi.org/10.1029/JA079i007p01033>. 46
- CHEN, X.R., ZONG, Q.G., ZHOU, X.Z., BLAKE, J.B., WYGANT, J. & KLETZING, C. (2017). Van Allen Probes observation of a 360° phase shift in the flux modulation of injected electrons by ULF waves. *Geophysical Research Letters*, **44**, 1614–1624, <https://doi.org/10.1002/2016GL071252>. 52
- CHISHAM, G. (1996). Giant pulsations: An explanation for their rarity and occurrence during geomagnetically quiet times. *Journal of Geophysical Research: Space Physics*, **101**, 24755–24763, <https://doi.org/10.1029/96JA02540>. 50, 110
- CHISHAM, G. & MANN, I. (1999). A Pc5 ulf wave with large azimuthal wavenumber observed within the morning sector plasmasphere by Sub-Auroral Magnetometer Network. *Journal of Geophysical Research: Space Physics*, **104**, 14717–14727, <https://doi.org/10.1029/1999JA900147>. 2
- CHISHAM, G. & ORR, D. (1991). Statistical studies of giant pulsations (Pgs): harmonic mode.

## REFERENCES

- Planetary and Space Science*, **39**, 999–1006, [https://doi.org/10.1016/0032-0633\(91\)90105-J](https://doi.org/10.1016/0032-0633(91)90105-J). 48, 49, 50, 117, 119, 120, 122, 126, 133
- CHISHAM, G. & ORR, D. (1994). The association between giant pulsations (Pgs) and the auroral oval. *Annales Geophysicae*, **12**, 649–654, <https://doi.org/10.1007/s00585-994-0649-4>. 49
- CHISHAM, G., ORR, D., TAYLOR, M.J. & LUHR, H. (1990). The magnetic and optical signature of a Pg pulsation. *Planetary and space science*, **38**, 1443–1456, [https://doi.org/10.1016/0032-0633\(90\)90119-B](https://doi.org/10.1016/0032-0633(90)90119-B). 49
- CHISHAM, G., ORR, D. & YEOMAN, T. (1992). Observations of a giant pulsation across an extended array of ground magnetometers and on auroral radar. *Planetary and space science*, **40**, 953–964, [https://doi.org/10.1016/0032-0633\(92\)90135-B](https://doi.org/10.1016/0032-0633(92)90135-B). 49, 50, 110
- CHISHAM, G., LESTER, M., MILAN, S.E., FREEMAN, M.P., BRITOW, W.A., GROCOTT, A., MCWILLIAMS, K.A., RUOHONIEMI, J.M., YEOMAN, T.K., DYSON, P.L., GREENWALD, R.A., KIKUCHI, T., PINNOCK, M., RASH, J.P.S., SATO, N., SOFKO, G.J., VILLAIN, J.P. & WALKER, A.D.M. (2007). A decade of the Super Dual Auroral Radar Network (SuperDARN): scientific achievements, new techniques and future directions. *Surv. Geophys.*, **28**, 33–109, <https://doi.org/10.1007/s10712-007-9017-8>. 34, 38, 48, 61, 62, 71, 135, 153, 181, 182
- CHISHAM, G., YEOMAN, T.K. & SOFKO, G.J. (2008). Mapping ionospheric backscatter measured by the SuperDARN HF radars - Part 1: A new empirical virtual height model. *Ann. Geophys.*, **26**, 823–841, <https://doi.org/10.5194/angeo-26-823-2008>. 42, 72, 136, 172
- CLAUER, C.R. & MCPHERRON, R.L. (1974). Mapping the local time-universal time development of magnetospheric substorms using mid-latitude magnetic observations. *Journal of Geophysical Research*, **79**, 2811–2820, <https://doi.org/10.1029/JA079i019p02811>. xiii, 26, 27
- COWLEY, S.W.H. (2000). Magnetosphere-Ionosphere Interactions: A Tutorial Review. In M.H. S.-I.Ohtani R. Fujii & R. Lysak, eds., *Magnetospheric Current Systems*, vol. 81 of *Geophysical Monograph Series*, 91–106, American Geophysical Union

- (AGU), Washington, D. C, <https://doi.org/10.1029/GM118p0091>. 21
- CROFT, T.A. (1972). Sky-wave backscatter: A means for observing our environment at great distances. *Reviews of Geophysics*, **10**, 73–155, <https://doi.org/10.1029/RG010i001p00073>. 39, 42
- CUSTOVIC, E., NGUYEN, H., DEVLIN, J., WHITTINGTON, J., ELTON, D., CONSOLE, A., YE, H., GREENWALD, R., ANDRE, D. & PARSONS, M. (2011). Evolution of the superdarn antenna: Twin terminated folded dipole antenna for HF systems. In *7th International Conference on Broadband Communications and Biomedical Applications*, 24–29, IEEE, <https://doi.org/10.1109/IB2Com.2011.6217936>. 72, 178, 180, 181, 182, 190
- CUSTOVIC, E., McDONALD, A.J., WHITTINGTON, J., ELTON, D., KANE, T.A. & DEVLIN, J.C. (2013). New antenna layout for a superdarn HF radar. *Radio Sci.*, **48**, 722–728, <https://doi.org/10.1002/2013RS005156>. 72, 178, 180, 182, 190
- DAVIES, J., LESTER, M., MILAN, S.E. & YEOMAN, T. (1999). A comparison of velocity measurements from the CUTLASS Finland radar and the EISCAT UHF system. *Ann. Geophys.*, **17**, 892–902, <https://doi.org/10.1007/s00585-999-0892-9>. 62
- DAVIES, K. (1990). *Ionospheric Radio*. The Institution of Engineering and Technology, London, U.K. 39, 40, 41, 42, 60, 140, 141
- DAVIS, T.N. & SUGIURA, M. (1966). Auroral electrojet activity index AE and its universal time variations. *Journal of Geophysical Research*, **71**, 785–801, <https://doi.org/10.1029/JZ071i003p00785>. 24
- DE LARQUIER, S., RUOHONIEMI, J.M., BAKER, J.B.H., VARRIER, N.R. & LESTER, M. (2011). First observations of the midlatitude evening anomaly using Super Dual Auroral Radar Network (SuperDARN) radars. *J. Geophys. Res.*, **116**, <https://doi.org/10.1029/2011JA016787>. 57, 139
- DE LARQUIER, S., PONOMARENKO, P., RIBEIRO, A.J., RUOHONIEMI, J.M., BAKER, J.B.H., STERNE, K.T. & LESTER, M. (2013). On the spatial distribution of decameter-scale subauroral ionospheric irregularities observed by SuperDARN radars. *J. Geophys. Res.*, **118**, 5244–5254, <https://doi.org/10.1002/jgra.50475>. xx, 42, 139, 144, 150, 177

## REFERENCES

- DUNGEY, J.W. (1961). Interplanetary Magnetic Field and the Auroral Zones. *Physical Review Letters*, **6**, 47. 21
- FARGES, T., BLANC, E. & VILLAIN, J.P. (1999). Interpretation of equatorial electrojet irregularities observed with a broad beam HF zenithal radar. *Radio Sci.*, **34**, 1141–1152, <https://doi.org/10.1029/1999RS900049>. xiv, 56, 58, 59
- FEJER, B.G. & KELLEY, M. (1980). Ionospheric irregularities. *Reviews of Geophysics*, **18**, 401–454, <https://doi.org/10.1029/RG018i002p00401>. 39, 43
- FENRICH, F. & SAMSON, J. (1997). Growth and decay of field line resonances. *Journal of Geophysical Research: Space Physics*, **102**, 20031–20039, <https://doi.org/10.1029/97JA01376>. 46
- FENRICH, F., SAMSON, J., SOFKO, G. & GREENWALD, R. (1995). ULF high- and low- $m$  field line resonances observed with the Super Dual Auroral Radar Network. *Journal of Geophysical Research: Space Physics*, **100**, 21535–21547, <https://doi.org/10.1029/95JA02024>. 46, 51, 132
- FRASER, B. (2006). ULF waves: A historical note. In K. TAKAHASHI, P.J. CHI, R.E. DENTON & R.L. LYSAK, eds., *Magnetospheric ULF waves: synthesis and new directions*, vol. 169 of *Geophysical Monograph Series*, 5–10, American Geophysical Union (AGU), Washington, D. C., <https://doi.org/10.1029/169GM03>. 33
- FRASER, B. (2009). ULF waves: exploring the earth’s magnetosphere. In *Advances in Geosciences: Volume 14: Solar Terrestrial (ST)*, 1–32, World Scientific. 31
- FREY, H., MENDE, S., ANGELOPOULOS, V. & DONOVAN, E. (2004). Substorm onset observations by IMAGE-FUV. *Journal of Geophysical Research: Space Physics*, **109**, <https://doi.org/10.1029/2004JA010607>. 23, 53
- FREY, H.U. (2007). Localized aurora beyond the auroral oval. *Reviews of Geophysics*, **45**, <https://doi.org/10.1029/2005RG000174>. xii, xiii, 20, 21, 22
- GAULD, J., YEOMAN, T., DAVIES, J., MILAN, S. & HONARY, F. (2002). SuperDARN radar HF propagation and absorption response to the substorm expansion phase. <https://doi.org/10.5194/angeo-20-1631-2002>. 87, 114, 134, 192
- GLASSMEIER, K.H., BUCHERT, S., MOTSCHMANN, U., KORTH, A. &

## REFERENCES

- PEDERSEN, A. (1999). Concerning the generation of geomagnetic giant pulsations by drift-bounce resonance ring current instabilities. *Annales Geophysicae*, **17**, 338–350, <https://doi.org/10.1007/s00585-999-0338-4>. 49, 118, 119
- GONZALEZ, W., JOSELYN, J.A., KAMIDE, Y., KROEHL, H.W., ROSTOKER, G., TSURUTANI, B. & VASYLIUNAS, V. (1994). What is a geomagnetic storm? *Journal of Geophysical Research: Space Physics*, **99**, 5771–5792, <https://doi.org/10.1029/93JA02867>. 28, 29
- GRANT, I., MCDIARMID, D. & MCNAMARA, A. (1992). A class of high-m pulsations and its auroral radar signature. *Journal of Geophysical Research: Space Physics*, **97**, 8439–8451, <https://doi.org/10.1029/92JA00434>. 51, 108
- GREENWALD, R. (2012). Steering SuperDARN radars. Tech. rep., Virginia Tech, [http://vt.superdarn.org/tiki-download\\_file.php?fileId=1060](http://vt.superdarn.org/tiki-download_file.php?fileId=1060) Last accessed 17 July, 2019. 72
- GREENWALD, R., BAKER, K., HUTCHINS, R. & HANUISE, C. (1985). An HF phased-array radar for studying small-scale structure in the high-latitude ionosphere. *Radio Sci.*, **20**, 63–79, <https://doi.org/10.1029/RS020i001p00063>. 62, 181
- GREENWALD, R.A., BAKER, K.B., DUDENEY, J.R., PINNOCK, M., JONES, T.B., THOMAS, E.C., VILLAIN, J.P., CERISIER, J.C., SENIOR, C., HANUISE, C., HUNSUCKER, R.D., SOFKO, G., KOEHLER, J., NIELSEN, E., PELLINEN, R., WALKER, A.D.M., SATO, N. & YAMAGISHI, H. (1995). DARN/SuperDARN: a global view of the dynamics of high-latitude convection. *Space Sci. Rev.*, **71**, 761–796, <https://doi.org/10.1007/BF00751350>. 61, 62, 135
- GREENWALD, R.A., FRISSELL, N. & DE LARQUIER, S. (2017). The importance of elevation angle measurements in HF radar investigations of the ionosphere. *Radio Sci.*, **52**, 305–320, <https://doi.org/10.1002/2016RS006186>. 135
- GROCOTT, A., WILD, J., MILAN, S.E. & YEOMAN, T.K. (2009). Superposed epoch analysis of the ionospheric convection evolution during substorms: Onset latitude dependence. *Ann. Geo-*

## REFERENCES

- phys.*, **27**, 591–600, <https://doi.org/10.5194/angeo-27-591-2009>. 62
- HANUISE, C. & CROCHET, M. (1977). Multifrequency HF radar studies of plasma instabilities in Africa. *J. Atmos. Terr. Phys.*, **39**, 1097–1101, [https://doi.org/10.1016/0021-9169\(77\)90018-6](https://doi.org/10.1016/0021-9169(77)90018-6). 58, 137
- HANUISE, C. & CROCHET, M. (1978). Oblique HF radar studies of plasma instabilities in the equatorial electrojet in Africa. *J. Atmos. Terr. Phys.*, **40**, 49–59, [https://doi.org/10.1016/0021-9169\(78\)90107-1](https://doi.org/10.1016/0021-9169(78)90107-1). 58
- HAO, Y., ZONG, Q.G., WANG, Y., ZHOU, X.Z., ZHANG, H., FU, S., PU, Z., SPENCE, H.E., BLAKE, J., BONNELL, J. *et al.* (2014). Interactions of energetic electrons with ULF waves triggered by interplanetary shock: Van Allen Probes observations in the magnetotail. *Journal of Geophysical Research: Space Physics*, **119**, 8262–8273, <https://doi.org/10.1002/2014JA020023>. 51, 82, 108, 109
- HOCKING, W. (2011). A review of Mesosphere–Stratosphere–Troposphere (MST) radar developments and studies, circa 1997–2008. *Journal of Atmospheric and Solar-Terrestrial Physics*, **73**, 848–882, <https://doi.org/10.1016/j.jastp.2010.12.009>. 43
- HUGHES, W. (1974). The effect of the atmosphere and ionosphere on long period magnetospheric micropulsations. *Planetary and Space Science*, **22**, 1157–1172, [https://doi.org/10.1016/0032-0633\(74\)90001-4](https://doi.org/10.1016/0032-0633(74)90001-4). 37
- HUGHES, W., SOUTHWOOD, D., MAUK, B., MCPHERRON, R. & BARFIELD, J. (1978). Alfvén waves generated by an inverted plasma energy distribution. *Nature*, **275**, 43, <https://doi.org/10.1038/275043a0>. 47
- HUGHES, W., MCPHERRON, R., BARFIELD, J. & MAUK, B. (1979). A compressional Pc4 pulsation observed by three satellites in geostationary orbit near local midnight. *Planetary and Space Science*, **27**, 821–840, [https://doi.org/10.1016/0032-0633\(79\)90010-2](https://doi.org/10.1016/0032-0633(79)90010-2). 49
- HUGHES, W.J. (1983). Hydromagnetic waves in the magnetosphere. In R.L. Carovillano & J.M. Forbes, eds., *Solar-Terrestrial Physics*, 453–477, Springer Netherlands, Dordrecht, [https://doi.org/10.1007/978-94-009-7194-3\\_18](https://doi.org/10.1007/978-94-009-7194-3_18). xiii, 32
- HUGHES, W.J. (1994). Magnetospheric ULF waves: A tutorial with a histor-

## REFERENCES

- ical perspective. In M.J. Engebretson, K. Takahashi & M. Scholer, eds., *Solar Wind Sources of Magnetospheric Ultra-Low-Frequency Waves*, vol. 81 of *Geophys. Monogr. Ser.*, 1–11, AGU, Washington, D. C, <https://doi.org/10.1029/GM081p0001>. 33, 44
- HUGHES, W.J. & SOUTHWOOD, D.J. (1976). The screening of micropulsation signals by the atmosphere and ionosphere. *J. Geophys. Res.*, **81**, 3234–3240, <https://doi.org/10.1029/JA081i019p03234>. xiii, 34, 37, 38, 48, 75, 111, 116
- IMAGE (2019a). International Monitor for Auroral Geomagnetic Effects (IMAGE) - Home web page. Online; last accessed 07 July 2019. <https://space.fmi.fi/image/www/index.php?page=home>. 78
- IMAGE (2019b). International Monitor for Auroral Geomagnetic Effects (IMAGE) Stations Coordinates. Online; last accessed 07 July 2019. <https://space.fmi.fi/image/www/index.php?page=stations>. xxiv, 85
- IMAGE (2019c). International Monitor for Auroral Geomagnetic Effects (IMAGE) Stations Map. Online; last accessed 07 July 2019. <https://space.fmi.fi/image/www/index.php?page=maps>. xv, 79
- JACOBS, J., KATO, Y., MATSUSHITA, S. & TROITSKAYA, V. (1964). Classification of geomagnetic micropulsations. *Journal of Geophysical Research*, **69**, 180–181, <https://doi.org/10.1029/JZ069i001p00180>. xxiv, 33, 34, 102
- JAMES, M.K. (2015). *ULF Waves Driven by Recently-injected Energetic Particle Populations*. Ph.D. thesis, University of Leicester. xiii, 25
- JAMES, M.K., YEOMAN, T.K., MAGER, P.N. & KLIMUSHKIN, D.Y. (2013). The spatio-temporal characteristics of ULF waves driven by substorm injected particles. *Journal of Geophysical Research: Space Physics*, **118**, 1737–1749, <https://doi.org/10.1002/jgra.50131>. xiv, 23, 24, 45, 52, 53, 54, 101, 109, 113, 128, 129, 131, 132, 133, 134, 193
- JAMES, M.K., YEOMAN, T., MAGER, P. & KLIMUSHKIN, D.Y. (2016). Multiradar observations of substorm-driven ULF waves. *Journal of Geophysical Research: Space Physics*, **121**, 5213–5232, <https://doi.org/10.1002/2015JA022102>. 47, 48, 52, 78, 112
- JONES, R.M. & STEPHENSON, J.J. (1975). A versatile three-dimensional ray tracing program for radio waves in the ionosphere. vol. 75-76, *Rep.* 75-76,

## REFERENCES

- Office of Telecommun., U.S. Dep. of Commerce, Boulder, Colo. 43, 80, 137, 141, 175
- JONES, T.B., LESTER, M., MILAN, S.E., ROBINSON, T.R., WRIGHT, D.M. & DILLON, R.S. (2001). Radio wave propagation aspects of the cutlass radar. *J. Atmospheric Sol.-Terr. Phys.*, **63**, 99–105, [https://doi.org/10.1016/S1364-6826\(00\)00134-6](https://doi.org/10.1016/S1364-6826(00)00134-6). 184
- KANGAS, J., GUGLIELMI, A. & POKHOTELOV, O. (1998). Morphology and physics of short-period magnetic pulsations. *Space Science Reviews*, **83**, 435–512, <https://doi.org/10.1023/A:1005063911643>. 33
- KARPMAN, V., MEERSON, B., MIKHAILOVSKY, A. & POKHOTELOV, O. (1977). The effects of bounce resonances on wave growth rates in the magnetosphere. *Planetary and Space Science*, **25**, 573–585, [https://doi.org/10.1016/0032-0633\(77\)90064-2](https://doi.org/10.1016/0032-0633(77)90064-2). 47
- KAZUE, T. & MCPHERRON, R.L. (1984). Standing hydromagnetic oscillations in the magnetosphere. *Planetary and Space Science*, **32**, 1343–1359, [https://doi.org/10.1016/0032-0633\(84\)90078-3](https://doi.org/10.1016/0032-0633(84)90078-3). 109
- KIVELSON, M.G. & RUSSELL, C.T. (1995). *Introduction to Space Physics*. Cambridge university press. xii, xiii, 12, 22, 25, 29, 30
- KLIMUSHKIN, D.Y., MAGER, P.N. & GLASSMEIER, K.H. (2004). Toroidal and poloidal Alfvén waves with arbitrary azimuthal wavenumbers in a finite pressure plasma in the Earth’s magnetosphere. *Ann. Geophys.*, **22**, 267–287, <https://doi.org/10.5194/angeo-22-267-2004>. 45, 83, 114, 120, 133, 192
- KOKUBUN, S., ERICKSON, K., FRITZ, T. & MCPHERRON, R. (1989). Local time asymmetry of pc 4-5 pulsations and associated particle modulations at synchronous orbit. *Journal of Geophysical Research: Space Physics*, **94**, 6607–6625, <https://doi.org/10.1029/JA094iA06p06607>. 49
- KOSTAREV, D. & MAGER, P. (2017). Drift-compression waves propagating in the direction of energetic electron drift in the magnetosphere. *Solar-Terrestrial Physics*, **3**, 18–27. 114
- KOUSTOV, A., GILLIES, R. & BANKOLE, P. (2018). Validation of Clyde River SuperDARN radar velocity measurements with the RISR-C incoherent scatter radar. *Ann. Geophys.*,

- 36**, 1657–1666, <https://doi.org/10.5194/angeo-36-1657-2018>. 62
- LAM, H.L. (2017). On the predictive potential of Pc5 ULF waves to forecast relativistic electrons based on their relationships over two solar cycles. *Space Weather*, **15**, 163–179, <https://doi.org/10.1002/2016SW001492>. 1
- LAM, H.L., BOTELER, D., BURLTON, B. & EVANS, J. (2012). Anik-E1 and E2 satellite failures of January 1994 revisited. *Space Weather*, **10**, <https://doi.org/10.1029/2012SW000811>. 1
- LANZEROTTI, L.J. (2017). Space weather: historical and contemporary perspectives. *Space Science Reviews*, **212**, 1253–1270, <https://doi.org/10.1007/s11214-017-0408-y>. 1
- LAWAL, H.A., LESTER, M., COWLEY, S.W.H., MILAN, S.E., YEO-MAN, T.K., PROVAN, G., IMBER, S. & RABIU, A.B. (2018). Understanding the global dynamics of the equatorial ionosphere in africa for space weather capabilities: A science case for AfrequaMARN. *J. Atmos. Terr. Phys.*, <https://doi.org/10.1016/j.jastp.2018.01.008>. 135
- LESSARD, M., HUDSON, M. & LÜHR, H. (1999). A statistical study of Pc3–Pc5 magnetic pulsations observed by the AMPTE/Ion Release Module satellite. *Journal of Geophysical Research: Space Physics*, **104**, 4523–4538, <https://doi.org/10.1029/1998JA900116>. 45
- LESTER, M. (2013). The Super Dual Auroral Radar Network (SuperDARN): an overview of its development and science. *Advances in Polar Science*, **24**, 11. 62
- LESTER, M., HUGHES, J.W. & SINGER, H.J. (1983). Polarization patterns of pi 2 magnetic pulsations and the substorm current wedge. *Journal of Geophysical Research: Space Physics*, **88**, 7958–7966, <https://doi.org/10.1029/JA088iA10p07958>. 26
- LESTER, M., CHAPMAN, P., COWLEY, S., CROOKS, S., DAVIES, J., HAMADYK, P., MCWILLIAMS, K., MILAN, S.E., PARSONS, M., PAYNE, D. *et al.* (2004). Stereo CUTLASS-A new capability for the superDARN HF radars. *Ann. Geophys.*, **22**, 459–473, <https://doi.org/10.5194/angeo-22-459-2004>. 65, 184
- MAGER, O.V., CHELPANOV, M.A., MAGER, P.N., KLIMUSHKIN, D.Y. & BERNGARDT, O.I. (2019). Conjugate Ionosphere-Magnetosphere Observations of a Sub-Alfvénic

## REFERENCES

- Compressional Intermediate-m Wave: A Case Study Using EKB Radar and Van Allen Probes. *Journal of Geophysical Research: Space Physics*, **124**, 3276–3290, <https://doi.org/10.1029/2019JA026541>. xiv, 50, 51, 52, 82, 83, 109, 193
- MAGER, P. & KLIMUSHKIN, D.Y. (2007). Generation of alfvén waves by a plasma inhomogeneity moving in the earth’s magnetosphere. *Plasma Physics Reports*, **33**, 391–398, <https://doi.org/10.1134/S1063780X07050042>. 52, 53, 119, 121
- MAGER, P. & KLIMUSHKIN, D.Y. (2008). Alfvén ship waves: high- $m$  ULF pulsations in the magnetosphere generated by a moving plasma inhomogeneity. *Ann. Geophys.*, **26**, 1653–1663, <https://doi.org/10.5194/angeo-26-1653-2008>. 35, 52, 53, 83, 114, 119, 120, 121, 133, 192
- MAGER, P. & KLIMUSHKIN, D.Y. (2013). Giant pulsations as modes of a transverse Alfvénic resonator on the plasmopause. *Earth, Planets and Space*, **65**, 3, <https://doi.org/10.5047/eps.2012.10.002>. 49
- MAGER, P.N., KLIMUSHKIN, D.Y. & IVCHENKO, N. (2009). On the equatorward phase propagation of high- $m$  ULF pulsations observed by radars. *Journal of Atmospheric and Solar-Terrestrial Physics*, **71**, 1677–1680, <https://doi.org/10.1016/j.jastp.2008.09.001>. 52, 55, 113, 114, 115, 120, 133, 192
- MAGER, P.N., BERNGARDT, O.I., KLIMUSHKIN, D.Y., ZOLOTUKHINA, N.A. & MAGER, O.V. (2015). First results of the high-resolution multibeam ULF wave experiment at the Ekaterinburg SuperDARN radar: Ionospheric signatures of coupled poloidal Alfvén and drift-compressional modes. *Journal of Atmospheric and Solar-Terrestrial Physics*, **130**, 112–126, <https://doi.org/10.1016/j.jastp.2015.05.017>. 48
- MANN, I., MILLING, D., RAE, I., OZEKE, L., KALE, A., KALE, Z., MURPHY, K., PARENT, A., USANOVA, M., PAHUD, D. *et al.* (2008). The upgraded CARISMA magnetometer array in the THEMIS era. *Space Science Reviews*, **141**, 413–451, <https://doi.org/10.1007/s11214-008-9457-6>. 26, 77
- MCDONALD, A.J., WHITTINGTON, J., DE LARQUIER, S., CUSTOVIC, E., KANE, T.A. & DEVLIN, J.C. (2013). Elevation angle-of-arrival determina-

## REFERENCES

- tion for a standard and a modified superDARN HF radar layout. *Radio Sci.*, **48**, 709–721, <https://doi.org/10.1002/2013RS005157>. 72
- MCMNAMARA, L.F. (1991). *The ionosphere: communications, surveillance, and direction finding*. Krieger Publishing Company. 35
- MCPHERRON, R., RUSSELL, C., KIVELSON, M. & COLEMAN, P. (1973). Substorms in space: The correlation between ground and satellite observations of the magnetic field. *Radio Science*, **8**, 1059–1076, <https://doi.org/10.1029/RS008i011p01059>. 23, 26
- MCPHERRON, R.L. (1970). Growth phase of magnetospheric substorms. *Journal of Geophysical Research*, **75**, 5592–5599. 22
- MCPHERRON, R.L. (1979). Magnetospheric substorms. *Reviews of Geophysics*, **17**, 657–681, <https://doi.org/10.1029/RG017i004p00657>. 23
- MCPHERRON, R.L. (2005). Magnetic pulsations: Their sources and relation to solar wind and geomagnetic activity. *Surveys in Geophysics*, **26**, 545–592, <https://doi.org/10.1007/s10712-005-1758-7>. 22, 23, 24, 29, 34, 44
- MCWILLIAMS, K., YEOMAN, T. & PROVAN, G. (2000). A statistical survey of dayside pulsed ionospheric flows as seen by the CUTLASS Finland HF radar. *Ann. Geophys.*, **18**, 445–453, <https://doi.org/10.1007/s00585-000-0445-8>. 65
- MCWILLIAMS, K.A. (2001). *Ionospheric signatures of dayside reconnection processes*. Ph.D. thesis, Department of Physics and Astronomy, University of Leicester, UK, <http://hdl.handle.net/2381/30652>. xv, 65, 66, 68, 69, 70
- MILAN, S., YEOMAN, T., LESTER, M., THOMAS, E. & JONES, T. (1997a). Initial backscatter occurrence statistics from the CUTLASS HF radars. *Ann. Geophys.*, **15**, 703–718, <https://doi.org/10.1007/s00585-997-0703-0>. xv, 75, 145, 150
- MILAN, S., DAVIES, J. & LESTER, M. (1999). Coherent hf radar backscatter characteristics associated with auroral forms identified by incoherent radar techniques: a comparison of CUTLASS and EISCAT observations. *J. Geophys. Res.*, **104**, 22591–22604, <https://doi.org/10.1029/1999JA900277>. 62
- MILAN, S., GOSLING, J. & HUBERT, B. (2012). Relationship between in-

## REFERENCES

- terplanetary parameters and the magnetopause reconnection rate quantified from observations of the expanding polar cap. *Journal of Geophysical Research: Space Physics*, **117**, <https://doi.org/10.1029/2011JA017082>. 21
- MILAN, S.E. & LESTER, M. (2001). A classification of spectral populations observed in HF radar backscatter from the E region auroral electrojets. *Ann. Geophys.*, **19**, 189–204, <https://doi.org/10.5194/angeo-19-189-2001>. 176, 178
- MILAN, S.E., JONES, T.B., ROBINSON, T.R., THOMAS, E.C. & YEOMAN, T.K. (1997b). Interferometric evidence for the observation of ground backscatter originating behind the CUTLASS coherent HF radars. *Ann. Geophys.*, **15**, 29–39, <https://doi.org/10.1007/s00585-997-0029-y>. 72
- MTUMELA, Z., STEPHENSON, J.A. & WALKER, A.D. (2015). An investigation of the nature of a Pc5 pulsation event using Superdarn and magnetometer data. *South African Journal of Science*, **111**, 1–7, <http://dx.doi.org/10.17159/sajs.2015/20130391>. 48, 51, 116
- MURPHY, K.R., INGLIS, A.R., SIBECK, D.G., RAE, I.J., WATT, C.E., SILVEIRA, M., PLASCHKE, F., CLAUDEPIERRE, S.G. & NAKAMURA, R. (2018). Determining the mode, frequency, and azimuthal wave number of ULF waves during a HSS and moderate geomagnetic storm. *Journal of Geophysical Research: Space Physics*, **123**, 6457–6477, <https://doi.org/10.1029/2017JA024877>. 2, 45
- NEWELL, P.T. & MENG, C.I. (1994). Ionospheric projections of magnetospheric regions under low and high solar wind pressure conditions. *Journal of Geophysical Research: Space Physics*, **99**, 273–286, <https://doi.org/10.1029/93JA02273>. 22
- NEWELL, P.T., GREENWALD, R.A. & RUOHONIEMI, J.M. (2001). The role of the ionosphere in aurora and space weather. *Reviews of Geophysics*, **39**, 137–149, <https://doi.org/10.1029/1999RG000077>. 18
- NISHITANI, N. & OGAWA, T. (2005). Model calculations of possible ionospheric backscatter echo area for a mid-latitude HF radar. *Advances in Polar Upper Atmosphere Research*, **19**, 55–62. 55, 57, 138, 176, 177
- NISHITANI, N., RUOHONIEMI, J.M., LESTER, M., BAKER, J.B.H., KOUSTOV, A.V., SHEPHERD, S.G.,

## REFERENCES

- CHISHAM, G., HORI, T., THOMAS, E.G., MAKAREVICH, R.A., MARCHAUDON, A., PONOMARENKO, P., WILD, J.A., MILAN, S.E., BRISTOW, W.A., DEVLIN, J., MILLER, E., GREENWALD, R.A., OGAWA, T. & KIKUCHI, T. (2019). Review of the accomplishments of mid-latitude Super Dual Auroral Radar Network (SuperDARN) HF radars. *Progress in Earth and Planetary Science*, **6:27**, 1–57, <https://doi.org/10.1186/s40645-019-0270-5>. 57, 62, 135, 138, 153
- ODENWALD, S. (2007). Newspaper reporting of space weather: End of a golden age. *Space Weather*, **5**, <https://doi.org/10.1029/2007SW000344>. 1
- ONWUMECHIKLI, C.A. (1997). *Equatorial Electrojet*. CRC Press. 39
- PERKINS, F. (1975). Ionospheric irregularities. *Reviews of Geophysics*, **13**, 884–884, <https://doi.org/10.1029/RG013i003p00884>. 39
- PILIPENKO, V. (1990). ULF waves on the ground and in space. *Journal of atmospheric and terrestrial physics*, **52**, 1193–1209, [https://doi.org/10.1016/0021-9169\(90\)90087-4](https://doi.org/10.1016/0021-9169(90)90087-4). 37
- PILIPENKO, V., BELAKHOVSKY, V., KOZLOVSKY, A., FEDOROV, E. & KAURISTIE, K. (2012). Determination of the wave mode contribution into the ULF pulsations from combined radar and magnetometer data: Method of apparent impedance. *Journal of Atmospheric and Solar-Terrestrial Physics*, **77**, 85–95, <https://doi.org/10.1016/j.jastp.2011.11.013>. 48
- PONOMARENKO, P.V., MENK, F.W. & WATERS, C.L. (2003). Visualization of ulf waves in superdarn data. *Geophys. Res. Lett.*, **30**, <https://doi.org/10.1029/2003GL017757>. 62, 75
- PONOMARENKO, P.V., F. W. MENK, F.W., WATERS, C.L. & SCIFFER, M.D. (2005). Pc3-4 ulf waves observed by the superdarn tiger radar. *Annales Geophysicae*, **23**, 1271–1280, <https://www.ann-geophys.net/23/1271/2005/>. 1
- RAE, I., DONOVAN, E., MANN, I., FENRICH, F., WATT, C., MILLING, D., LESTER, M., LAVRAUD, B., WILD, J.A., SINGER, H. *et al.* (2005). Evolution and characteristics of global Pc5 ULF waves during a high solar wind speed interval. *Journal of Geophysical Research: Space Physics*, **110**, <https://doi.org/10.1029/2005JA011007>. 1, 45

## REFERENCES

- RAE, I.J., MANN, I.R., ANGELOPOULOS, V., MURPHY, K.R., MILLING, D.K., KALE, A., FREY, H.U., ROSTOKER, G., RUSSELL, C.T., WATT, C.E. *et al.* (2009). Near-earth initiation of a terrestrial substorm. *Journal of Geophysical Research: Space Physics*, **114**, <https://doi.org/10.1029/2008JA013771>. 77
- RATCLIFFE, J.A. (1959). *The magnetospheric theory and its applications to the ionosphere*. University Press. 42
- REIMER, A., HUSSEY, G. & MCWILLIAMS, K. (2018). Statistically self-consistent and accurate errors for superdarn data. *Radio Science*, **53**, 93–111, <https://doi.org/10.1002/2017RS006450>. 70, 178
- REIMER, A.S. (2018). *Improved SuperDARN radar signal processing: A first principles statistical approach for reliable measurement uncertainties and enhanced data products*. Ph.D. thesis, University of Saskatchewan, <http://hdl.handle.net/10388/8534> Last accessed 17 July, 2019. 70, 72
- RIBEIRO, A., RUOHONIEMI, J., BAKER, J., CLAUSEN, L., DE LARQUIER, S. & GREENWALD, R. (2011). A new approach for identifying ionospheric backscatter in midlatitude SuperDARN HF radar observations. *Radio Sci.*, **46**, <https://doi.org/10.1029/2011RS004676>. 57, 136, 153, 177, 178
- RIBEIRO, A., RUOHONIEMI, J., BAKER, J., CLAUSEN, L., GREENWALD, R. & LESTER, M. (2012). A survey of plasma irregularities as seen by the midlatitude Blackstone SuperDARN radar. *J. Geophys. Res.*, **117**, <https://doi.org/10.1029/2011JA017207>. 135
- RICHMOND, A.D. (1973). Equatorial electrojet - II. Use of the model to study the equatorial ionosphere. *J. Atmos. Terr. Phys.*, **35**, 1105–1118, [https://doi.org/10.1016/0021-9169\(73\)90008-1](https://doi.org/10.1016/0021-9169(73)90008-1). 172
- RISHBETH, H. (1988). Basic physics of the ionosphere: a tutorial review. *Journal of the Institution of Electronic and Radio Engineers*, **58**, S207–S223, <https://doi.org/10.1049/jiere.1988.0060>. xiii, 35, 36, 37
- RISHBETH, H. & GARRIOTT, O.K. (1969). *Introduction to ionospheric physics*, vol. 14. Academic Press New York. 139
- ROSTOKER, G. (1994). Commentary on the Anik satellite upsets. *Report to Telesat Canada, Canadian Network for Space Research Report*. 1

## REFERENCES

- ROSTOKER, G., LAM, H.L. & OLSON, J.V. (1979). Pc 4 giant pulsations in the morning sector. *Journal of Geophysical Research: Space Physics*, **84**, 5153–5166, <https://doi.org/10.1029/JA084iA09p05153>. 48, 49, 50, 118, 126
- RÖTTGER, J. (2004). Ionosphere and atmosphere research with radars. *Max-Planck-Institut, Lindau, UNESCO Encyclopedia of Life Support Systems, Geophysics and Geochemistry, Paris*. 43, 60, 61
- RUBTSOV, A., AGAPITOV, O., MAGER, P., KLIMUSHKIN, D.Y., MAGER, O., MOZER, F. & ANGELOPOULOS, V. (2018). Drift resonance of compressional ULF waves and substorm-injected protons from multipoint THEMIS measurements. *Journal of Geophysical Research: Space Physics*, **123**, 9406–9419, <https://doi.org/10.1029/2018JA025985>. 52
- RUOHONIEMI, J., GREENWALD, R., BAKER, K., VILLAIN, J. & MCCREADY, M. (1987). Drift motions of small-scale irregularities in the high-latitude f region: An experimental comparison with plasma drift motions. *J. Geophys. Res.*, **92**, 4553–4564. 62
- SAKAO, T., KANO, R., NARUKAGE, N., KOTOKU, J., BANDO, T., DELUCA, E.E., LUNDQUIST, L.L., TSUNETTA, S., HARRA, L.K., KATSUKAWA, Y. *et al.* (2007). Continuous plasma outflows from the edge of a solar active region as a possible source of solar wind. *Science*, **318**, 1585–1588, <https://doi.org/10.1126/science.1147292>. 18
- SAKURAI, T. & SAITO, T. (1976). Magnetic pulsation pi2 and substorm onset. *Planetary and Space Science*, **24**, 573–575, [https://doi.org/10.1016/0032-0633\(76\)90135-5](https://doi.org/10.1016/0032-0633(76)90135-5). 24
- SAMSON, J., JACOBS, J. & ROSTOKER, G. (1971). Latitude-dependent characteristics of long-period geomagnetic micropulsations. *Journal of Geophysical Research*, **76**, 3675–3683, <https://doi.org/10.1029/JA076i016p03675>. 46
- SAMSON, J.C., HARROLD, B.G., RUOHONIEMI, J.M., GREENWALD, R.A. & WALKER, A.D.M. (1992). Field line resonances associated with MHD waveguides in the magnetosphere. *Geophys. Res. Lett.*, **19**, 441–444, <https://doi.org/10.1029/92GL00116>. 46
- SCHLEGEL, K. (1996). Coherent backscatter from ionospheric E-region plasma irregularities. *J. Atmospheric Sol.-Terr. Phys.*, **58**, 933–941, <https://doi.org/10.1016/>

## REFERENCES

- 0021-9169(95)00124-7. xv, 39, 73, 74, 161
- SKOLNIK, M.I. (2001). *RADAR systems*. McGraw-Hill, NY. 185
- SMITH, M. & LOCKWOOD, M. (1996). Earth's magnetospheric cusps. *Reviews of Geophysics*, **34**, 233–260, <https://doi.org/10.1029/96RG00893>. 21
- SOUTHWOOD, D. (1974). Some features of field line resonances in the magnetosphere. *Planetary and Space Science*, **22**, 483–491, [https://doi.org/10.1016/0032-0633\(74\)90078-6](https://doi.org/10.1016/0032-0633(74)90078-6). 46
- SOUTHWOOD, D. & HUGHES, W. (1983). Theory of hydromagnetic waves in the magnetosphere. *Space Science Reviews*, **35**, 301–366, <https://doi.org/10.1007/BF00169231>. 33
- SOUTHWOOD, D.J. (1976). A general approach to low-frequency instability in the ring current plasma. *J. Geophys. Res.*, **81**, 3340–3348, <https://doi.org/10.1029/JA081i019p03340>. 47, 111, 119
- SOUTHWOOD, D.J. & KIVELSON, M.G. (1982). Charged particle behavior in low-frequency geomagnetic pulsations, 2. graphical approach. *Journal of Geophysical Research: Space Physics*, **87**, 1707–1710, <https://doi.org/10.1029/JA087iA03p01707>. 111
- SOUTHWOOD, D.J., DUNGEY, J.W. & ETHERINGTON, R.J. (1969). Bounce resonant interaction between pulsations and trapped particles. *Planetary and Space Science*, **17**, 349–361, [https://doi.org/10.1016/0032-0633\(69\)90068-3](https://doi.org/10.1016/0032-0633(69)90068-3). 47, 109
- STERN, D.P. (1975). The motion of a proton in the equatorial magnetosphere. *Journal of Geophysical Research*, **80**, 595–599, <https://doi.org/10.1029/JA080i004p00595>. 110
- STERNE, K.T., GREENWALD, R.A., BAKER, J.B. & RUOHONIEMI, J.M. (2011). Modeling of a twin terminated folded dipole antenna for the Super Dual Auroral Radar Network (SuperDARN). In *2011 IEEE Radar-Con (RADAR)*, 934–938, IEEE, <https://doi.org/10.1109/RADAR.2011.5960673>. 71, 72, 180, 183, 190
- STOCKER, A., ARNOLD, N. & JONES, T. (1999). The synthesis of traveling ionospheric disturbance (tid) signatures in hf radar observations using ray tracing. *Annales Geophysicae*, **18**, 56–64, <https://doi.org/10.1007/s00585-000-0056-4>. 56
- STOCKER, A., WARRINGTON, E.M. & JONES, T. (2003). A comparison of observed and modeled deviations from the great circle direction for a 4490

## REFERENCES

- km hf propagation path along the mid-latitude ionospheric trough. *Radio Science*, **38**, 20–1, <https://doi.org/10.1029/2002RS002781>. 56
- SUDAN, R. (1983). Unified theory of type I and type II irregularities in the equatorial electrojet. *Journal of Geophysical Research: Space Physics*, **88**, 4853–4860, <https://doi.org/10.1029/JA088iA06p04853>. 56
- SWRI (2020). Solar wind, contained in glossary of Southwest Research Institute (swri) IMAGE HomePage. [http://pluto.space.swri.edu/image/glossary/solar\\_wind.html](http://pluto.space.swri.edu/image/glossary/solar_wind.html), accessed: 2020-03-11. 18
- TAKAHASHI, K., SATO, N., WARNECKE, J., LÜHR, H., SPENCE, H.E. & TONEGAWA, Y. (1992). On the standing wave mode of giant pulsations. *Journal of Geophysical Research: Space Physics*, **97**, 10717–10732, <https://doi.org/10.1029/92JA00382>. 49
- TAKAHASHI, K., GLASSMEIER, K.H., ANGELOPOULOS, V., BONNELL, J., NISHIMURA, Y., SINGER, H.J. & RUSSELL, C.T. (2011). Multisatellite observations of a giant pulsation event. *Journal of Geophysical Research: Space Physics*, **116**, <https://doi.org/10.1029/2011JA016955>. 48, 49, 50
- TAKAHASHI, K., HARTINGER, M.D., ANGELOPOULOS, V., GLASSMEIER, K.H. & SINGER, H.J. (2013). Multispacecraft observations of fundamental poloidal waves without ground magnetic signatures. *Journal of Geophysical Research: Space Physics*, **118**, 4319–4334, <https://doi.org/10.1002/jgra.50405>. 49
- TAMAO, T. (1965). Transmission and coupling resonance of hydromagnetic disturbances in the non-uniform earth's magnetosphere. *Science reports of the Tohoku University. Ser. 5, Geophysics*, **17**, 43–72, <http://hdl.handle.net/10097/44669>. 46
- TARIKU, Y.A. (2015). TEC prediction performance of the IRI-2012 model over Ethiopia during the rising phase of solar cycle 24 (2009–2011). *Earth, Planets and Space*, **67**:140, <https://doi.org/10.1186/s40623-015-0312-1>. 80, 139
- W7EL (2019). EZNEC Antenna Software (EZNEC PRO2). Last accessed 07 July 2019. <https://www.eznec.com/>. 182
- THÉBAULT, E., FINLAY, C.C., BEGGAN, C.D., ALKEN, P., AUBERT, J., BARROIS, O., BERTRAND, F., BONDAR, T., BONESS, A., BROCCO,

## REFERENCES

- L. *et al.* (2015). International geomagnetic reference field: the 12th generation. *Earth, Planets and Space*, **67**, 79, <https://doi.org/10.1186/s40623-015-0228-9>. xx, 81, 141, 142
- TIAN, M., YEOMAN, T., LESTER, M. & JONES, T. (1991). Statistics of Pc 5 pulsation events observed by SABRE. *Planetary and space science*, **39**, 1239–1247, [https://doi.org/10.1016/0032-0633\(91\)90037-B](https://doi.org/10.1016/0032-0633(91)90037-B). 51
- VILLAIN, J.P., GREENWALD, R.A. & VICKREY, J.F. (1984). HF ray tracing at high latitudes using measured meridional electron density distribution. *Radio Sci.*, **19**, 359–374, <https://doi.org/10.1029/RS019i001p00359>. 55, 136, 137, 138, 174, 178
- VOLLAND, H. (1973). A semiempirical model of large-scale magnetospheric electric fields. *Journal of Geophysical Research*, **78**, 171–180, <https://doi.org/10.1029/JA078i001p00171>. 110
- VORONKOV, I., DONOVAN, E. & SAMSON, J. (2003). Observations of the phases of the substorm. *Journal of Geophysical Research: Space Physics*, **108**, <https://doi.org/10.1029/2002JA009314>. 24
- WALKER, A. (2005). Excitation of field line resonances by sources outside the magnetosphere. *Ann. Geophys.*, **23**, 3375–3388. 46
- WALKER, A., GREENWALD, R., STUART, W. & GREEN, C. (1979a). Stare auroral radar observations of Pc 5 geomagnetic pulsations. *Journal of Geophysical Research: Space Physics*, **84**, 3373–3388, <https://doi.org/10.1029/JA084iA07p03373>. 46
- WALKER, A., GREENWALD, R., STUART, W. & GREEN, C. (1979b). STARE auroral radar observations of Pc 5 geomagnetic pulsations. *Journal of Geophysical Research: Space Physics*, **84**, 3373–3388, <https://doi.org/10.1029/JA084iA07p03373>. 37
- WARRINGTON, E.M., STOCKER, A., SIDDLE, D., HALLAM, J., AL-BEHADILI, H., ZAALOV, N., HONARY, F., ROGERS, N.C., BOTELER, D. & DANSKIN, D. (2016). Near real-time input to a propagation model for now-casting of HF communications with aircraft on polar routes. *Radio Science*, **51**, 1048–1059, <https://doi.org/10.1002/2015RS005880>. 57
- WATSON, C., JAYACHANDRAN, P., SINGER, H.J., REDMON, R.J. & DANSKIN, D. (2016). GPS TEC response to Pc4 “giant pulsations”. *Journal of Geophysical Research: Space Physics*,

## REFERENCES

- 121**, 1722–1735, <https://doi.org/10.1002/2015JA022253>. 49, 50
- WRIGHT, D. & YEOMAN, T. (1999). Cutlass observations of a high- $m$  ULF wave and its consequences for the DOPE HF Doppler sounder. **17**, 1493–1497, <https://doi.org/10.1007/s00585-999-1493-3>. 48
- WRIGHT, D.M., YEOMAN, T.K., RAE, I., STOREY, J., STOCKTON-CHALK, A.B., ROEDER, J.L. & TRATTNER, K.J. (2001). Ground-based and Polar spacecraft observations of a giant (Pg) pulsation and its associated source mechanism. *Journal of Geophysical Research: Space Physics*, **106**, 10837–10852, <https://doi.org/10.1029/2001JA900022>. 1, 49, 50, 117
- WRIGHT, D.M., YEOMAN, T.K., BADDELEY, L.J., DAVIES, J.A., DHILLON, R.S., LESTER, M., MILAN, S.E. & WOODFIELD, E. (2004). High resolution observations of spectral width features associated with ULF wave signatures in artificial HF radar backscatter. *Ann. Geophys.*, **22**, 169–182, <https://doi.org/10.5194/angeo-22-169-2004>. 73
- YAMAMOTO, K., NOSÉ, M., KASAHARA, S., YOKOTA, S., KEIKA, K., MATSUOKA, A., TERAMOTO, M., TAKAHASHI, K., OIMATSU, S., NOMURA, R. *et al.* (2018). Giant pulsations excited by a steep earthward gradient of proton phase space density: Arase observation. *Geophysical Research Letters*, **45**, 6773–6781, <https://doi.org/10.1029/2018GL078293>. 49
- YEOMAN, T., TIAN, M., LESTER, M. & JONES, T. (1992). A study of Pc5 hydromagnetic waves with equatorward phase propagation. *Planetary and space science*, **40**, 797–810, [https://doi.org/10.1016/0032-0633\(92\)90108-Z](https://doi.org/10.1016/0032-0633(92)90108-Z). 51, 108, 132
- YEOMAN, T., JAMES, M., KLIMUSHKIN, D.Y. & MAGER, P. (2016). Energetic Particle-Driven ULF Waves in the Ionosphere. In A. Keiling, D. Lee & V. Nakariakov, eds., *Low-Frequency Waves in Space Plasmas*, vol. 216 of *Geophysical Monograph Series*, 1–14, American Geophysical Union (AGU), Washington, D. C, <https://doi.org/10.1002/9781119055006.ch1>. 1, 24, 46
- YEOMAN, T.K. & WRIGHT, D. (2001). ULF waves with drift resonance and drift-bounce resonance energy sources as observed in artificially-induced HF radar backscatter. **19**,

## REFERENCES

- 159–170, <https://doi.org/10.5194/angeo-19-159-2001>. 110, 111
- YEOMAN, T.K., WRIGHT, D.M., STOCKER, A.J. & JONES, T.B. (2001). An evaluation of range accuracy in the Super Dual Auroral Radar Network over-the-horizon HF radar systems. *Radio Sci.*, **26**, 801–813, <https://doi.org/10.1029/2000RS002558>. 56, 136
- YEOMAN, T.K., WRIGHT, D.M. & BADDELEY, L.J. (2006). Ionospheric signatures of ULF waves: Active radar techniques. In K. Takahashi *et al.*, eds., *Magnetospheric ULF Waves: Synthesis and New Directions*, vol. 169 of *Geophys. Monogr. Ser.*, 273–288, AGU, Washington, D. C, <https://agupubs.onlinelibrary.wiley.com/doi/10.1029/169GM18>. 34, 45, 75, 82
- YEOMAN, T.K., BADDELEY, L., DHILLON, R., ROBINSON, T. & WRIGHT, D. (2008a). Bistatic observations of large and small scale ULF waves in SPEAR-induced HF coherent backscatter. **26**, 2253–2263, <https://doi.org/10.5194/angeo-26-2253-2008>. 51, 108
- YEOMAN, T.K., CHISHAM, G., BADDELEY, L.J., DHILLON, R.S., KARHUNEN, T.J.T., ROBINSON, T.R., SENIOR, A. & WRIGHT, D.M. (2008b). Mapping ionospheric backscatter measured by the SuperDARN HF radars - Part 2: Assessing SuperDARN virtual height models. *Ann. Geophys.*, **26**, 843–852, <https://doi.org/10.5194/angeo-26-843-2008>. 42, 72, 136, 172
- YEOMAN, T.K., KLIMUSHKIN, D.Y. & MAGER, P.N. (2010). Intermediate-m ulf waves generated by substorm injection: A case study. *Ann. Geophys.*, **28**, 1499–1509, <https://doi.org/10.5194/angeo-28-1499-2010>. 26, 48, 51, 52, 55, 62, 82, 87, 93, 99, 108, 109, 110, 111, 112, 113, 119, 120, 129, 132, 192
- YEOMAN, T.K., JAMES, M., MAGER, P.N. & KLIMUSHKIN, D.Y. (2012). SuperDARN observations of high-*m* ULF waves with curved phase fronts and their interpretation in terms of transverse resonator theory. *Journal of Geophysical Research: Space Physics*, **117**, <https://doi.org/10.1029/2012JA017668>. 2, 88, 114, 116, 134, 192
- YIZENGAW, E., MOLDWIN, M., ZESTA, E., BIOUELE, C., DAMTIE, B., MEBRAHTU, A., RABIU, B., VALADARES, C. & STONEBACK, R.A.

## REFERENCES

---

- (2014). The longitudinal variability of equatorial electrojet and vertical drift velocity in the african and american sectors. <https://doi.org/10.5194/angeo-32-231-2014>. 175
- YUMOTO, K. (1988). External and internal sources of low-frequency MHD waves in the magnetosphere: A review. *Journal of geomagnetism and geoelectricity*, **40**, 293–311, <https://doi.org/10.5636/jgg.40.293>. 45
- ZOLESI, B. & CANDER, L.R. (2014). The general structure of the ionosphere. In *Ionospheric Prediction and Forecasting*, 11–48, Springer, [https://doi.org/10.1007/978-3-642-38430-1\\_2](https://doi.org/10.1007/978-3-642-38430-1_2). 35
- ZOLOTUKHINA, N., MAGER, P. & KLIMUSHKIN, D.Y. (2008). Pc5 waves generated by substorm injection: a case study. *Ann. Geophys.*, **26**, 2053–2059, <https://doi.org/10.5194/angeo-26-2053-2008>. 52, 53, 114, 120, 133, 192